



**HAL**  
open science

# Ultrasound Induced Blood-brain Barrier Opening on Rodents: from Nanoparticles Delivery to a Therapy for Alzheimer's Disease

Matthieu Gerstenmayer

► **To cite this version:**

Matthieu Gerstenmayer. Ultrasound Induced Blood-brain Barrier Opening on Rodents: from Nanoparticles Delivery to a Therapy for Alzheimer's Disease. Biological Physics [physics.bio-ph]. Université Paris Saclay (COMUE), 2018. English. NNT : 2018SACLS424 . tel-02015610

**HAL Id: tel-02015610**

**<https://theses.hal.science/tel-02015610>**

Submitted on 12 Feb 2019

**HAL** is a multi-disciplinary open access archive for the deposit and dissemination of scientific research documents, whether they are published or not. The documents may come from teaching and research institutions in France or abroad, or from public or private research centers.

L'archive ouverte pluridisciplinaire **HAL**, est destinée au dépôt et à la diffusion de documents scientifiques de niveau recherche, publiés ou non, émanant des établissements d'enseignement et de recherche français ou étrangers, des laboratoires publics ou privés.

# Ultrasound-Induced Blood-Brain Barrier Opening on Rodents: from Nanoparticles Delivery to a Therapy for Alzheimer's Disease

Thèse de doctorat de l'Université Paris-Saclay  
Préparée à l'université Paris Sud

École doctorale n°575 : Electrical, Optical, Bio – physics and Engineering (EOBE)  
Spécialité de doctorat: Imagerie et Physique Médicale

Thèse présentée et soutenue à Gif-sur-Yvette, le 12 Novembre 2018, par :

**Matthieu GERSTENMAYER**

Composition du Jury :

<b>M. Hervé Boutin</b> Directeur de recherche, University of Manchester (DNEP)	Président
<b>M. Cyril Lafon</b> Directeur de recherche, Université Lyon 1 (LabTAU)	Rapporteur
<b>M. Chrit Moonen</b> Professeur, University Medical Center Utrecht (Imaging Division)	Rapporteur
<b>Mme. Karine Cambon</b> Ingénieur chercheur, CEA (MIRcen)	Examineur
<b>Me. Marie Sarazin</b> Professeur, Centre hospitalier Sainte-Anne (NML)	Examineur
<b>M. Cyril Poupon</b> Directeur de recherche, CEA (NeuroSpin)	Directeur de thèse
<b>M. Benoît Larrat</b> Ingénieur chercheur, CEA (NeuroSpin)	Encadrant



*« Voyage dans le temps et inverse le sens des flots de mon sang  
Noyé dans l'océan, je caresse le flanc du grand Leviathan »*

***Flavien Berger, Leviathan***

# Remerciements

Je tiens tout d'abord à remercier Benoit Larrat, qui m'a encadré au quotidien durant ma thèse. Toujours bouillant d'idées, merci de m'avoir conseillé scientifiquement et soutenu moralement. Merci d'avoir été présent et disponible quand j'avais besoin de toi. Enfin merci pour ta bonne humeur et ton encadrement attentif qui m'ont permis de m'épanouir durant ces trois années.

J'exprime ma gratitude à l'égard de Cyril Poupon qui a accepté d'être mon directeur de thèse. J'adresse tous mes remerciements à Cyril Lafon et Chrit Moonen qui m'ont fait l'honneur d'être rapporteurs de ma thèse. Merci à Karine Cambon, Marie Sarazin et Hervé Boutin qui ont bien voulu en être examinateurs.

Je remercie également Sébastien Mériaux pour avoir patiemment répondu à toutes mes questions de reconstructions d'images et pour m'avoir finement conseillé lors de nombreuses répétitions de présentations. Enfin, un grand merci pour ton management constructif et bienveillant de l'équipe MIDAS.

Un grand merci à Erwan Selingue pour avoir subi avec moi les longues semaines d'expérimentation, pour ces journées au son de France Inter et pour ses mythiques blagues. Un grand merci à Françoise pour m'avoir gentiment approvisionné en images histologiques et pour nous avoir fait de délicieux gâteaux.

Un grand merci à tous mes collègues de l'open-space qui ont rendu l'ambiance de travail chaleureuse et agréable, Solenne, Jacques, Pauline, Laura, Anthony, Pavel, Benjamin, Hermès, Marianne, Gabrielle, Ashley, Ricardo. Merci pour toutes ces discussions à la pause-café et à la cantine 2, mais aussi pour ces pique-niques et ces gouters à l'ombre du grand châtaignier.

Merci Rémi de m'avoir formé, un début de thèse n'aurait pas pu se passer mieux. Merci Allegra de m'avoir guidé dans le monde de la recherche, qu'aurais-je fais sans toi perdu dans ces conférences internationales. Merci Venetia pour ton aide précieuse et merci de t'attaquer à toutes les questions auxquelles je n'ai pas pu répondre.

Merci à Sébastien, Sylvain, Emilie, Maud, Nicolas et Charles pour m'avoir chaleureusement accueilli au Service Hospitalier Frédéric Joliot. Merci à Denis et Jérémy pour m'avoir dépanné de nombreuses fois. Merci à Jonathan, Christel, Elena, Philippe, Florian, Florence, Jean-Christophe, Serge pour l'aide apportée sans laquelle ce travail n'aurait pas pu se faire.

Merci à tous mes amis de BSY, d'Orsay et de Paris, merci d'avoir été présents quand les résultats, eux, tardaient à venir. Merci à ma famille de m'avoir toujours fait confiance et de m'avoir toujours soutenu. Enfin, Alice, merci pour tout.

Je dédicace cette thèse à Théophile Parjadis de Larivière qui nous a quitté récemment. Esprit libre, classe incomparable, toujours à fond sur le terrain de rugby, toujours à fond pour faire la fête. Tu vas nous manquer.

# Résumé en Français

## Contexte de la thèse : l'ouverture transitoire de la barrière hémato-encéphalique par ultrasons

Mon travail de thèse a consisté à développer des outils pour l'ouverture de la barrière-hémato-encéphalique chez le rat et la souris, soit dans le but de délivrer des molécules dans le cerveau soit comme thérapie pour la maladie d'Alzheimer, qui se caractérise au niveau moléculaire par le dépôt de plaques amyloïdes et par la dégénérescence neuro-fibrillaire. Dans le reste du corps, pour permettre les échanges moléculaires entre le sang et les organes, les vaisseaux sanguins sont relativement perméables. Le cerveau est un organe à part. Les vaisseaux sanguins qui l'irriguent sont beaucoup plus imperméables. Cette barrière, limitant le transport de molécules entre le sang et le cerveau est appelée la barrière hémato-encéphalique (BHE). Son rôle est de maintenir l'homéostasie du cerveau, de finement réguler l'apport en sucre et en oxygène et de protéger le cerveau de pathogènes. Les cellules endothéliales constituant la BHE sont liées les unes aux autres par les jonctions serrées. L'espace entre ces cellules est très réduit, ce qui limite fortement le passage vers le cerveau des molécules ayant un poids moléculaire supérieur à 400 Da. La BHE est donc essentielle au bon fonctionnement du cerveau, mais devient une limite pour y délivrer des médicaments. En effet, la plupart des molécules thérapeutiques ont une taille nanométrique ce qui ne leur permet pas de franchir la BHE une fois injectées dans le sang.

L'action combinée de microbulles et d'ultrasons focalisés permet la perméabilisation transitoire de la BHE. Cette technique de perméabilisation de la BHE par ultrasons est une piste sérieuse pour la délivrance de médicaments, par exemple anti-tumoraux, qui ne peuvent pas ou trop peu franchir naturellement la BHE. Les variations de pression générées par les ultrasons compriment et dilatent les microbulles injectées dans le sang. Ce phénomène, appelé « cavitation », génère un stress mécanique sur les cellules endothéliales qui se contractent et relâchent leur jonctions serrées. L'espace entre les cellules endothéliales s'agrandit ce qui permet le passage de molécules de taille nanométrique. Cette technique peut être guidée par IRM. Avant la perméabilisation de la BHE, l'IRM peut informer sur la position du faisceau d'ultrasons dans le cerveau et choisir la région de perméabilisation. Après perméabilisation, l'injection d'un agent de contraste IRM, qui ne franchit pas naturellement la BHE mais qui peut la franchir après sa perméabilisation par ultrasons, permet de visualiser et de quantifier l'intensité de la perméabilisation.

L'imagerie précoce de la maladie est un enjeu majeur tant pour la prise en charge des patients que pour la planification et le suivi des essais thérapeutiques. Les plaques amyloïdes, chargées en fer, produisent un effet  $T_2^*$  qui permet de les visualiser avec des IRM haut champ. L'ouverture de la BHE permet aussi de délivrer dans le cerveau des agents de contraste fonctionnalisés se liant aux plaques amyloïde pour améliorer leur détection. Enfin, l'ouverture la BHE par ultrasons, pourrait permettre en elle-même de diminuer la charge en plaques amyloïdes et d'améliorer les performances cognitives chez des souris modèles de la maladie.

## Développements autour des ultrasons transcrâniens

La première partie de ma thèse a été consacrée à des développements relatifs à la perméabilisation de la BHE par ultrasons. Cette technique nécessite de précisément doser l'intensité du faisceau ultrasonore dans le cerveau. Une intensité trop élevée peut causer des lésions alors qu'une intensité trop basse ne perméabilise pas la BHE. C'est pourquoi j'ai commencé par méthodiquement calibrer les émetteurs ultrasonores que j'allais utiliser. J'ai également développé un protocole pour perméabiliser la BHE dans une large région en déplaçant le transducteur pendant les tirs grâce à des moteurs. Sans déplacer le transducteur, la zone de perméabilisation est typiquement de  $1 \times 1 \times 5 \text{ mm}^3$ . En déplaçant le transducteur, il est possible de perméabiliser soit un hémisphère soit le cerveau entier (environ  $15 \times 10 \times 10 \text{ mm}^3$  chez la souris).

J'ai ensuite étudié le passage des ultrasons à travers le crâne. En effet, le crâne atténue les ultrasons et diminue leur intensité dans le cerveau. Pour atteindre une intensité voulue dans le cerveau, il faut donc augmenter l'intensité des ultrasons par rapport aux calibrations en cuve. Pour ce faire, les crânes sont placés dans une cuve entre le transducteur et l'hydrophone et la pression acoustique mesurée à travers le crâne est comparée à la pression sans le crâne. J'ai mené une étude extensive chez le rat où j'ai démontré une augmentation linéaire de l'atténuation des crânes avec la masse des animaux et une dépendance avec la région du crâne intersectée par le faisceau. Cette corrélation entre l'atténuation et la masse des animaux semble être due à une troisième variable, l'épaisseur des crânes, qui est proportionnelle à la fois à la masse des animaux et à l'atténuation.

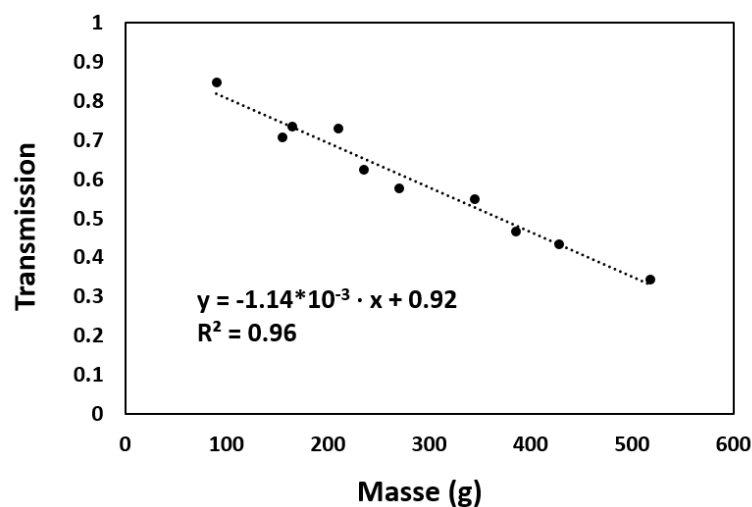


*Figure 1: Facteur de transmission des ultrasons à travers le crâne à 1.5 MHz en position « centrale » pour des rats Sprague Dawley.*

J'ai investigué l'influence de l'intensité des ultrasons sur la perméabilisation de la BHE. J'ai proposé une nouvelle méthode pour mesurer l'intensité minimum nécessaire pour la perméabilisation grâce à une corrélation entre l'intensité utilisée lors de la sonication et la quantité d'agent de contraste pénétrant dans le cerveau. Enfin, je me suis penché sur une relation pas ou encore peu étudiée, l'influence de l'intensité des ultrasons sur la durée de la perméabilisation. En utilisant plusieurs conditions d'intensité et en injectant des agents de contraste à différents moments après la

perméabilisation, j'ai démontré que plus la pression acoustique était élevée, plus la perméabilisation était intense et longue.

### **Délivrance de nanoparticules dans le cerveau grâce à la perméabilisation de la BHE**

Grâce à ces développements, j'ai pu participer à de nombreuses études portant sur la délivrance de molécules dans le cerveau.

En partenariat avec l'équipe de Nicolas Tournier du Service Hospitalier Frédérique Joliot (SHFJ), nous avons montré que la perméabilisation de la BHE par ultrasons chez le rat n'était pas suffisante pour délivrer des médicaments si ceux-ci étaient substrats des pompes d'efflux, qui transfèrent les molécules substrats du cerveau vers le sang. En collaboration avec plusieurs équipes du projet GRAVITY, nous avons pu délivrer des nanoparticules d'or dans le cerveau de souris et j'ai montré que le contraste des images IRM était proportionnel à la quantité d'agent de contraste mesurée par spectrométrie de masse. En collaboration avec Charles Truillet au SHFJ, nous avons également démontré que le passage d'un anticorps thérapeutique labellisé radioactivement était augmenté après perméabilisation de la BHE par ultrasons chez la souris, ceci mesuré par tomographie par émission de positrons.

Finalement, au sein de notre équipe, j'ai participé à des projets portés par Allegra Conti, postdoctorante dans notre équipe. Un premier projet dédié à l'étude de la diffusion d'agents de contraste dans le tissu cérébral après une perméabilisation localisée de la BHE. A l'aide d'une imagerie quantitative du  $T_1$ , nous avons pu suivre la concentration en agent de contraste au cours du temps et remonter à la tortuosité cérébrale. Nous avons observé, comme attendu, une diffusion plus rapide des agents de contraste de plus petite taille. Enfin, nous avons montré que perméabiliser la barrière hémato-tumorale permettait d'augmenter la quantité d'agent de contraste, et donc possiblement de médicaments, délivrée dans des tumeurs cérébrales.

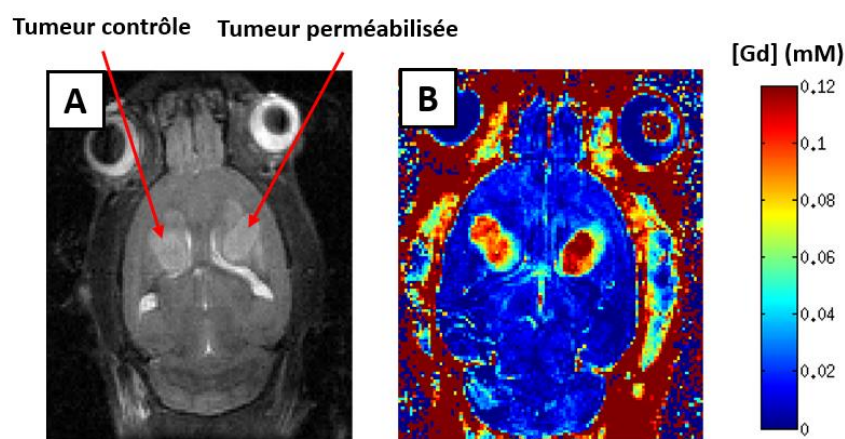


*Figure 2: A – Image anatomique montrant la double implantation de tumeurs dans le cerveau d'un rat. B – Carte de concentration en agent de contraste gadoliné après perméabilisation par ultrasons de la tumeur de droite. La concentration dans la tumeur perméabilisée est plus importante et persiste plus longtemps.*

### Imagerie des plaques amyloïdes

Une partie significative de mon travail fut dédiée à l'imagerie des plaques amyloïdes dans des modèles rongeurs de la maladie d'Alzheimer que nous élevons à NeuroSpin. Grâce à la perméabilisation de la BHE par ultrasons, j'ai pu délivrer des agents de contraste fonctionnalisés pour cibler les plaques amyloïdes. De nouveaux agents de contraste, les AgulX, produits par l'équipe de François Lux et Olivier Tillement à l'Institut Lumière-Matière à Lyon, ont été greffés avec du PEG pour augmenter leur biocompatibilité et avec du PIB pour qu'ils ciblent les plaques amyloïdes. J'ai procédé à leur délivrance, validée par IRM, dans le cerveau de souris modèles de la maladie d'Alzheimer. Nos partenaires, Jonathan Pansieri and Christel Marquette du CEA Grenoble, ont réalisé l'histologie de ces cerveaux et ont confirmé la présence d'AgulX greffées PIB dans le cerveau.

Une autre approche, cette fois-ci sans agent de contraste, a été développée par mes soins. J'ai optimisé une séquence IRM  $T_2^*$  *ex vivo* très haute résolution (40  $\mu\text{m}$  isotrope) pour l'imagerie des plaques amyloïdes, à 11,7 Telsa. Avec un traitement d'image approprié, cette séquence permet de quantifier la charge en plaques amyloïdes dans le cortex de souris modèle de la maladie d'Alzheimer. Cette technique mesure bien une charge en plaques plus élevée chez les souris plus âgées (qui ont de fait plus de plaques que les jeunes) et une charge quasiment nulle chez les souris sauvages (qui ne développent pas de plaques).

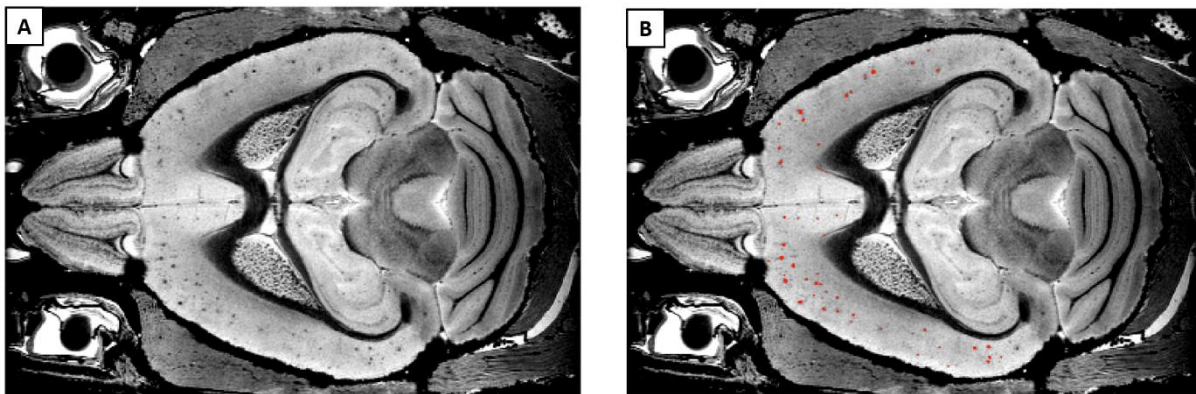


*Figure 3 : A – Image anatomique haute résolution  $T_2^*$  (40  $\mu\text{m}$  isotrope) d'un cerveau de souris modèle de la maladie d'Alzheimer. Les hypo-signaux noirs dans le cortex sont des plaques amyloïdes. B – Détection automatique des plaques amyloïdes (en rouge) dans le cortex.*

En collaboration avec Elena Longo et Philippe Zeitoun de l'ENSTA, nous avons étudié la délivrance de nanoparticules grâce à de l'imagerie par rayons X en contraste de phase. Après avoir délivré des nanoparticules dans le cerveau de souris de la maladie d'Alzheimer, nous avons amené ces cerveaux à l'European Synchrotron Radiation Facility à Grenoble pour l'imagerie. Cette technique s'est révélée très efficace pour l'imagerie des plaques. Des nanoparticules ont pu être retrouvées dans le tissu cérébral et j'ai pu corrélérer ces images avec des images IRM *ex vivo* haute résolution.

Pour finir, plusieurs marquages histologiques ont été mis au point par Françoise Geoffroy, la responsable histologie de notre équipe, pour imager les plaques amyloïdes, la protéine tau et la neuroinflammation. J'ai mis au point le traitement d'image nécessaire pour quantifier la charge en

plaques amyloïdes. Ces développements pour quantifier les plaques amyloïdes ont ensuite été utilisés lors des protocoles de thérapie par perméabilisation répétée de la BHE de nos rongeurs modèles de la maladie d'Alzheimer.

### **Perméabilisations répétées de la BHE chez des modèles rongeurs de la maladie d'Alzheimer**

Durant la dernière partie de ma thèse, je me suis servi de l'ensemble de ces développements pour étudier la perméabilisation répétée de la BHE par ultrasons comme thérapie pour la maladie d'Alzheimer. En effet, de récentes études ont montré que chez des souris modèles de la maladie d'Alzheimer, cette technique, utilisée de façon répétée (par exemple une perméabilisation par semaine pendant 2 mois), pouvait diminuer la charge en plaques amyloïdes et améliorer les performances cognitives. Cela serait vraisemblablement dû à une neuroinflammation protectrice induite par les ultrasons.

Grâce au protocole de perméabilisation global développé précédemment, j'ai testé cette hypothèse sur un modèle rat et un modèle souris de la maladie. Après six semaines, avec une perméabilisation par semaine, les souris ont montré des signes d'amélioration lors des tests de comportement basés sur la mémoire. De plus, une analyse histologique montre une tendance vers une diminution de la taille des plaques amyloïdes chez les souris traitées par ultrasons. Les rats traités par ultrasons ont également montré des signes d'amélioration de leur mémoire ainsi qu'une diminution de leur anxiété. L'analyse histologique et biochimique n'est pas encore terminée.

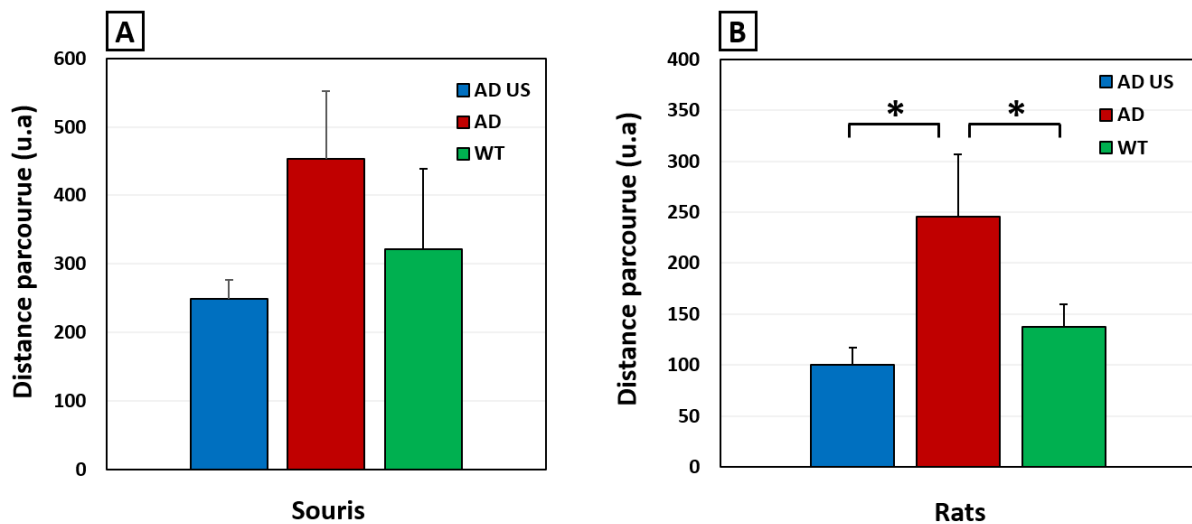


*Figure 4 : Distance parcourue pour retrouver la sortie du labyrinthe après 5 jours d'entraînement pour les souris (A) et 8 jours d'entraînement pour les rats (B). Dans les deux cas, les animaux modèles d'Alzheimer traités par ultrasons (AD US) parcourent moins de distance que les animaux modèles d'Alzheimer non-traités (AD). Les animaux traités par ultrasons ont des performances semblables aux animaux de type sauvage. Une distance parcourue plus courte indique une meilleure mémorisation de la sortie par rapport aux indices visuels extérieurs. Ces résultats montreraient un effet bénéfique des ultrasons sur la mémoire des animaux.*

En collaboration avec Charles Truillet au service hospitalier Frédéric Joliot, nous avons étudié, par tomographie par émission de positrons, la neuroinflammation induite par la perméabilisation de la BHE par ultrasons. Grâce un radio-traceur de la neuroinflammation marqué au <sup>18</sup>Fluor, nous avons montré une augmentation significative de la neuroinflammation après six semaines, avec une augmentation plus importante chez les souris modèles de la maladie d'Alzheimer que chez les souris de type sauvage.

### **Conclusions et perspectives**

En conclusion, cette thèse fut l'occasion d'approfondir les précédents développements de notre équipe en ce qui concerne la perméabilisation de la barrière hémato-encéphalique par ultrasons et de développer de nouvelles techniques telles que la perméabilisation globale. Ces nouvelles techniques m'ont permis de délivrer de diverses familles d'agents dans le cerveau de rongeurs dans le cadre de collaborations. Je me suis ensuite concentré sur la maladie d'Alzheimer en développant des techniques d'imagerie des plaques ainsi qu'en testant la perméabilisation de la barrière hémato-encéphalique par ultrasons comme thérapie pour cette maladie.

Les techniques de perméabilisation globale de la BHE et d'imagerie des plaques amyloïdes seront de nouveau utilisées lors d'études plus approfondies, en particulier sur les effets des perméabilisations répétées de la barrière hémato-encéphalique sur la maladie d'Alzheimer, dont l'étude que j'ai menée servira de base.



## Table of Contents

<b>CHAPTER 1. INTRODUCTION .....</b>	<b>1</b>
<b>1.1. Focused ultrasound: a promising tool to deliver drugs to the brain.....</b>	<b>1</b>
1.1.1. Medical use of ultrasound.....	1
1.1.2. The blood-brain barrier.....	3
1.1.3. Improving drug delivery to the brain .....	4
1.1.4. Ultrasound to increase the drug delivery to the brain .....	6
1.1.5. Optimum experimental parameters .....	7
1.1.6. Safety .....	11
1.1.7. Protocol for blood-brain barrier opening.....	13
<b>1.2. Alzheimer's disease.....</b>	<b>14</b>
1.2.1. Epidemiology of Alzheimer's disease .....	14
1.2.2. Physiopathology of AD and the amyloid cascade hypothesis.....	16
1.2.3. A difficult therapy.....	18
1.2.4. Animal models to study AD.....	20
1.2.5. Ethics of animal research .....	23
<b>1.3. Magnetic resonance imaging .....</b>	<b>23</b>
1.3.1. A brief history of MRI .....	23
1.3.2. Basic principles of MRI .....	25
1.3.3. Anatomical images.....	28
1.3.4. Imaging contrast agents .....	30
1.3.5. Imaging the ultrasound beam.....	32
1.3.6. Presentation of the preclinical MR scanner of NeuroSpin.....	33
<b>1.4. Conclusion .....</b>	<b>34</b>
<b>CHAPTER 2. METHODOLOGICAL ADVANCEMENTS ON ULTRASOUND-INDUCED BBB OPENING ..</b>	<b>37</b>
<b>2.1. Acoustic field calibration .....</b>	<b>37</b>
2.1.1. Transducer calibration .....	37
a) Transducers to emit ultrasound.....	37
b) Setup for calibration.....	38
c) Single element transducer.....	40
d) Multi element transducer.....	40
2.1.2. Transmission through rat skulls .....	42
a) Context and methods.....	42
a) Transmission factor decreases with frequency and body mass .....	45
b) Correlation with skull thickness .....	46
c) Spatial variation of the transmission factor.....	47
d) The different components of the insertion loss: aberration, attenuation and impedance mismatch.....	47
e) Other transmission factor measurements .....	48

2.1.3.	<i>In vivo estimation of the transmission factor with MR-ARFI.....</i>	49
a)	<i>MR-ARFI mapping .....</i>	49
b)	<i>Simulation of the viscoelastic response of the brain.....</i>	51
c)	<i>Acoustic transmission mapping .....</i>	52
<b>2.2.</b>	<b>Control of the position of the focal spot .....</b>	<b>54</b>
2.2.1.	<i>MR-guided displacement of the transducer.....</i>	54
a)	<i>Thermoguide .....</i>	54
b)	<i>MR-guided global BBB opening in rats .....</i>	55
2.2.2.	<i>Motorized trajectories outside the MR scanner.....</i>	57
a)	<i>Motorized positioning system.....</i>	57
b)	<i>Validation and safety of a global BBB opening protocol in mice .....</i>	58
2.2.3.	<i>Mapping of a rat skull with a transducer in pulse-echo mode.....</i>	60
<b>2.3.</b>	<b>Influence of the acoustic pressure on BBB opening .....</b>	<b>61</b>
2.3.1.	<i>An acoustic pressure threshold .....</i>	61
a)	<i>Co-registration of MR-ARFI and concentration maps.....</i>	62
b)	<i>Estimation of the acoustic pressure threshold.....</i>	63
c)	<i>Different acoustic pressures in an unique BBB opening experiment .....</i>	64
2.3.2.	<i>Higher pressures open the BBB longer.....</i>	66
a)	<i>Square trajectory.....</i>	66
b)	<i>Opening and follow-up of the permeabilisation .....</i>	67
c)	<i>Estimation of a closing time constant depending on the pressure .....</i>	68
<b>2.4.</b>	<b>Conclusion .....</b>	<b>70</b>
<b>CHAPTER 3. PHYSICAL AND FUNCTIONAL PROPERTIES OF THE BRAIN AFTER ULTRASOUND-INDUCED BBB OPENING .....</b>		
<b>73</b>		
<b>3.1.</b>	<b>Tortuosity of the brain .....</b>	<b>73</b>
3.1.1.	<i>Free diffusion of contrast agent.....</i>	74
3.1.2.	<i>In vivo restricted diffusion.....</i>	76
<b>3.2.</b>	<b>Activity of the efflux pumps .....</b>	<b>78</b>
3.2.1.	<i>Reminders on Positron Emission Tomography and efflux pumps .....</i>	79
3.2.2.	<i>Protocol to follow erlotinib extravasation .....</i>	80
a)	<i>Chemicals and radiochemicals.....</i>	80
b)	<i>The ultrasound protocol.....</i>	80
c)	<i><sup>11</sup>C-erlotinib PET study.....</i>	82
d)	<i><sup>11</sup>C-N-desmethyl-loperamide PET study .....</i>	83
e)	<i>Image analysis.....</i>	83
3.2.3.	<i>FUS-induced BBB opening did not increase the brain exposure to <sup>11</sup>C-erlotinib and <sup>11</sup>C-N-desmethyl-loperamide .....</i>	83
3.2.4.	<i>Not only size matter .....</i>	87
<b>3.3.</b>	<b>Increased delivery of therapeutic compounds with ultrasound.....</b>	<b>88</b>
3.3.1.	<i>Delivery of gold nanoparticles followed by MRI .....</i>	88

a) BBB opening .....	89
b) Correlation between MRI and ICPMS.....	90
3.3.2. Delivery of an anti-cancer antibody followed by PET imaging.....	91
a) BBB opening .....	91
b) PET imaging .....	92
3.4. FUS-induced blood-tumor barrier opening.....	93
3.4.1. Symmetrical double implantation of tumors in rats' brains. ....	93
3.4.2. Ultrasound-induced opening of the blood-tumor barrier .....	94
3.4.3. An increased permeability after FUS-induced BTB opening.....	95
3.5. Conclusion .....	97
CHAPTER 4. IMAGING OF ALZHEIMER'S DISEASE .....	99
4.1. A new functionalized contrast agent: AgulX-Peg-PIB .....	99
4.1.1. Characterization of AgulX .....	100
4.1.2. Delivery of AgulX-Peg-PIB in the brain of APP/PS1 mice .....	102
a) Context.....	102
b) Ultrasound protocol for AgulX-Peg-PIB delivery.....	103
c) MR imaging.....	103
4.1.3. Validation of the targeting with histology.....	104
4.2. Ex vivo imaging of Alzheimer's disease .....	106
4.2.2. Automatic plaque detection.....	107
a) Optimization of sum of the echoes .....	108
b) Cortex segmentation.....	109
c) Detection of the hyposignals.....	110
4.2.3. Amyloid plaque load quantification.....	111
a) On mice .....	111
b) On rats.....	112
4.2.4. In vivo imaging.....	113
4.2.5. An efficient method to quantify amyloid load .....	115
4.3. Imaging AD with X-ray phase-contrast at the ESRF .....	115
4.3.1. Phase-contrast imaging .....	116
4.3.2. AgulX delivery.....	116
4.3.3. Imaging of Alzheimer's mouse brains .....	118
4.3.4. Correlation with MRI.....	120
4.4. Imaging Alzheimer's disease with histology .....	121
4.4.1. Amyloid plaques imaging.....	121
a) Imaging of A $\beta$ deposits: Thioflavin-S.....	121
b) Imaging of iron deposits: Perls'.....	122
c) Correlation between iron and amyloid plaques.....	123
4.4.2. Other stains related to Alzheimer's disease.....	125
a) Tau protein imaging.....	125

b) Neuroinflammation imaging.....	125
4.5. Conclusion .....	126
<b>CHAPTER 5. BLOOD-BRAIN BARRIER OPENING AS A THERAPY FOR ALZHEIMER’S DISEASE .....</b>	<b>129</b>
5.1. <b>Ultrasound as a therapy for Alzheimer’s disease: promising studies .....</b>	<b>129</b>
5.1.1. <i>Preclinical studies</i> .....	129
5.1.2. <i>The first clinical trial</i> .....	133
5.2. <b>Assessment of memory deficits with behavior tests .....</b>	<b>134</b>
5.2.1. <i>The Open Field test</i> .....	135
5.2.2. <i>The Y-maze test</i> .....	137
5.2.3. <i>The Barnes Maze test</i> .....	140
5.3. <b>Therapeutic trials on mice .....</b>	<b>144</b>
5.3.1. <i>A first trial without motorization .....</i>	<i>144</i>
a) <i>Protocol</i> .....	144
b) <i>Safety</i> .....	146
c) <i>Behavior test</i> .....	146
d) <i>Ex-vivo imaging</i> .....	149
e) <i>Limits of this study</i> .....	150
5.3.2. <i>A safety study</i> .....	150
a) <i>Protocol and follow-up of the weights</i> .....	150
b) <i>Results of the behavior tests</i> .....	152
5.3.3. <i>A second trial on APP/PS1 mice .....</i>	<i>153</i>
a) <i>Behavior tests</i> .....	154
b) <i>Histology</i> .....	157
5.4. <b>Therapeutic trial on rats .....</b>	<b>160</b>
5.4.1. <i>Ultrasound protocol</i> .....	160
5.4.2. <i>Behavior tests results</i> .....	161
5.5. <b>Study of the neuroinflammation with PET.....</b>	<b>164</b>
5.5.1. <i>How to detect neuroinflammation</i> .....	164
a) <i>Neuroinflammation in Alzheimer’s disease</i> .....	164
b) <i>A marker of neuroinflammation: the TSPO protein</i> .....	165
5.5.2. <i>Ultrasound and PET protocol</i> .....	166
5.5.3. <i>Follow-up of the neuroinflammation</i> .....	167
5.6. <b>Conclusion .....</b>	<b>169</b>
<b>GENERAL CONCLUSION .....</b>	<b>170</b>
<b>SCIENTIFIC COMMUNICATIONS .....</b>	<b>172</b>
<b>BIBLIOGRAPHY .....</b>	<b>174</b>



# Chapter 1. Introduction

In this introduction chapter, I introduce the needed background knowledge to understand my PhD work. It starts with an overview of therapeutic ultrasound with a specific focus on the ultrasound-induced blood-brain barrier opening technique. I explain the functioning of this technique, list its possible applications and discuss its safety. Then, I continue with a broad introduction to Alzheimer's disease and the possible underlying mechanisms. I present the animal models which are used to study the disease. Finally, I introduce Magnetic Resonance Imaging, its basic principles and how it can be used to study Alzheimer's disease or to investigate ultrasound-induced BBB opening and even guide it.

## 1.1. Focused ultrasound: a promising tool to deliver drugs to the brain

### 1.1.1. Medical use of ultrasound

The French physicist Paul Langevin was the first person to ever use ultrasound when he designed the first sonar in the 1910's, a technique that the animal kingdom has long mastered with dolphins or bats. A military technique at first, ultrasound became an industrial technique for detecting flaws in solid materials. In the 1940's the Dussik brothers suggested that ultrasound could be used as a medical tool for detecting brain tumors by measuring the absorption through the head, so in a non-invasive way! Even if their images were mainly artifacts, they paved the way for ultrasound as an imaging tool for diagnosis. In 1957, the engineer Tom Brown and the gynecologist Ian Donald designed what can be named the first clinical ultrasound scanner for breast cancer imaging. To avoid fully immersing patients they used olive oil to ensure a good acoustic coupling between the skin and the transducer. Commercially developed during the 1960's, ultrasound imaging is the best known clinical technique using ultrasound. Practiced routinely to follow pregnancies, cardiac diseases or liver diseases for example, this technique allows real-time imaging of moving structures in a non-invasive and safe way. Nowadays, ultrasound imaging provides not only tissue imaging but also blood flow imaging with Doppler, elastography to measure tissue stiffness, contrast enhanced perfusion imaging or it can be used to guide surgery. Its affordability, its portability and its ease of use make ultrasound imaging an essential imaging technique available for all clinical centers, hospitals or laboratories.

Best known for imaging, ultrasound can also be used as a therapeutic tool. Without impact on tissues when used for imaging, ultrasound can be focused to deliver more energy in a smaller volume. When focused, ultrasound can deliver enough energy to trigger bioeffects and so become therapeutic. The action mechanisms of ultrasound on tissues can be sorted in three main groups: the shock waves, the energy deposition inducing tissue heating and the cavitation mechanisms (Kießling et al., 2012). The various therapeutic approaches associated with each mechanism of action will be described and cavitation mechanisms will be investigated in more details in the paragraph 1.1.4.

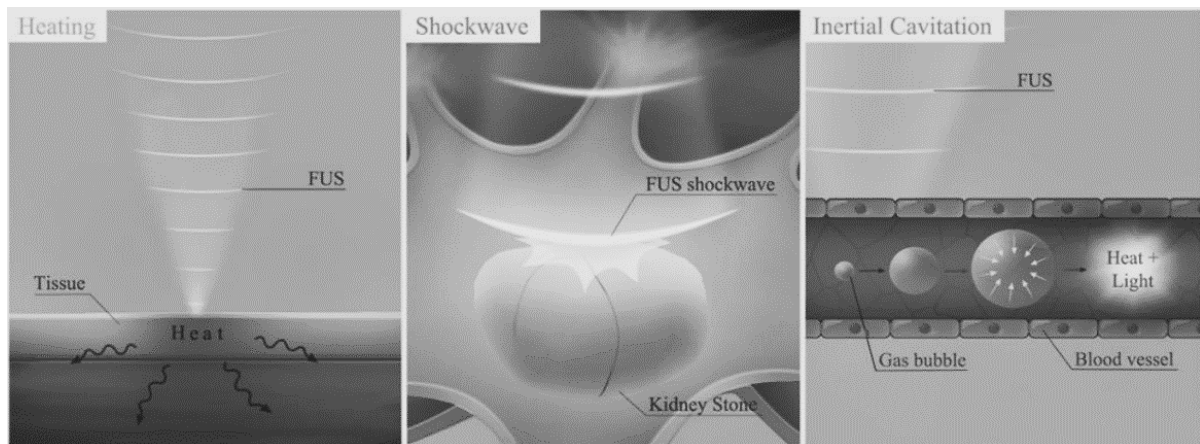


Figure 1-1: Mechanisms of action of ultrasound on tissues (from O'Reilly & Hynynen 2016)

Shockwave therapy uses high pressures (tens of MPa) and short pulses (few microseconds) to deliver shockwaves at the target (Cleveland and McAteer, 2007). The shockwave results in a strong mechanical stress on the target tissues. Until the 1980's, the treatment of kidney stones relied on open surgery and so was invasive. Ultrasound brought a revolutionary tool with extracorporeal shock wave lithotripsy (ESWL). In this non-invasive technique, the ultrasound transducer is coupled to the skin through ultrasonic gel and ultrasound are generated outside of the body (Bhojani and Lingeman, 2013). The shockwaves impacting the kidney stones lead to their mechanical destruction. At lower intensity, shockwave therapy is also used for tissue healing (Watson, 2008). By increasing the activity of cells, ultrasound start a pro-inflammatory response in the early repair phase. It has been shown to work on bone healing, scars and the vibrational movements have been shown to be able of improving the circulation and help break down adhesions between the muscles and their sheaths.

Ultrasound, when they are absorbed by tissues, lead to heating, mainly where they are focused. The degree of heating depends on the absorption coefficient of the tissue, the frequency of the ultrasound and the duration of the ultrasound pulse. The greater they are the higher is the heating. Focused ultrasound are capable of heating really local and small areas (millimeter-sized). Temperature rises of 10-15°C are enough to thermally ablate cells, typically cancer cells. Currently used to ablate cancer cells in the liver (Al-Bataineh et al., 2012) or the prostate (Pauly et al., 2006) using catheter-mounted ultrasound transducers, thermal ablation in the brain is more challenging. The Exablate Neuro (Insightec, Israel) can focus ultrasound behind the skull, thanks to dephasings based on the skull shape, and make use of thermal ablation in the brain (Elias et al., 2016). This protocol is now FDA approved for the treatment of essential tremor by ablation of the VIM nuclei in the thalamus. In Europe, the Exablate 4000 (Insightec, Israel) is also approved for the treatment of neuropathic pain and Parkinson disease. Several research teams are demonstrating the feasibility of thermal ablation of brain tumors thanks to High Intensity Focused Ultrasound (HIFU) (Coluccia et al., 2014; Macdonell et al., 2018). Hopefully, these could be the future technology to reach surgically inaccessible tumors. HIFU induced hyperthermia was also tried as a boost for radiotherapy of brain tumors (Guthkelch et al., 1991). This technique was limited to a phase I study but could now be pushed forward thank to the advance of MR-guided HIFU.

Ultrasound can be combined with microbubbles injected in the blood to make use of a phenomenon called cavitation. Ultrasound propagate through the tissue and encounter the microbubbles which

expand at low pressure and contract at high pressure. If the resulting size oscillation is stable, the cavitation is called “stable”. The oscillations produce micro-streams around the bubbles, the speed of the liquid is proportional to the amplitude of the ultrasound. If the acoustic pressure is increased, microbubbles can implode. This collapse can create liquid-jets and shockwaves, those violent phenomena concentrate the energy of the ultrasound and can break down membranes of nearby cells. This effect is called “inertial cavitation”. Inertial cavitation can for instance be used to clear artery or vein occlusions with a catheter approach (Crouch et al., 2008). In the brain, inertial cavitation is investigated as a promising tool for strokes (Ilyas et al., 2018). With MR guidance, HIFU could be transcranially focused in the brain to destroy clots. Cavitation is also used to enhance drug delivery. Drug delivery is enhanced by affecting either the drug carrier, which are drug-loaded microbubbles, or the cells surrounding the microbubbles. Cavitation can fragment the shell of microbubbles, made of liposomes or micelles, and trigger the release of their content, genes, proteins or drugs, in the targeted tissue (Pitt et al., 2004). Cavitation can also form temporary pores in the cell membrane surrounding the microbubbles, this phenomenon is called sonoporation (Pan et al., 2004). Cavitation is a very interesting tool but inertial cavitation has to be handled with care because it can damage the cells surrounding the microbubbles.

### 1.1.2. The blood-brain barrier

In the body, blood vessels are permeable to allow the transport of molecules from the blood to the organs. The brain is one special organ regarding molecular transport. Indeed, the blood vessels supplying the brain are a far less permeable structure. This barrier, limiting the diffusion of molecules to the brain, is called the blood-brain barrier (BBB). The BBB is made of endothelial cells, astrocyte end-feet and pericytes. An illustration of its structure is given on Figure 1-2. The endothelial cells, which forms the wall of the blood vessels, are, together with the tight junctions, the barrier itself whereas astrocytes are not thought to play directly a barrier role but they are key to ensure the maintenance of the tight junctions and provides a cellular link between the blood vasculature and the neurons (Ballabh et al., 2004). Pericytes seems to play an important role in the inhibition of properties normally associated with permeable vessels such as transcytosis (Davson et al., 2015).

This diffusion barrier plays a crucial role in maintaining the hemostasis of the brain (Engelhardt, 2003). The brain has a high energy consumption rate, 20% of the whole energy consumption of the body for only 2% of its mass. To properly function, the brains needs a precise oxygen delivery and metabolites supply, in particular glucose (Attwell et al., 2010), in the one hand and a protection from potential neurotoxic molecules and pathogens (Winkler et al., 2014) and waste disposal in the other hand. The BBB provides those functions by being highly impermeable to big molecules and allowing small molecules – metabolites, amino acids, hormones, vitamins etc. – to cross the BBB via transcellular mechanisms (Zhao et al., 2015). As illustrated on Figure 1-2, these transcellular transport of small molecules can be passive for lipophilic molecules or active, through transport proteins, for molecules such as glucose or amino acids (Abbott et al., 2010).

To summarize, brain endothelial cells differ significantly from non-brain endothelial cells by the presence of intercellular tight junctions, the low level of transcytosis and paracellular diffusion, a strong metabolic activity and the polarized expression of membrane receptors, and transporters

which are responsible for the active transport of nutrients to the brain or the efflux of potentially toxic compounds from the brain to the blood vessels. Only drugs with a molecular weight smaller than 400 Da can naturally cross the BBB (Pardridge, 2005). This is the reason why huge efforts are done to overcome this barrier.

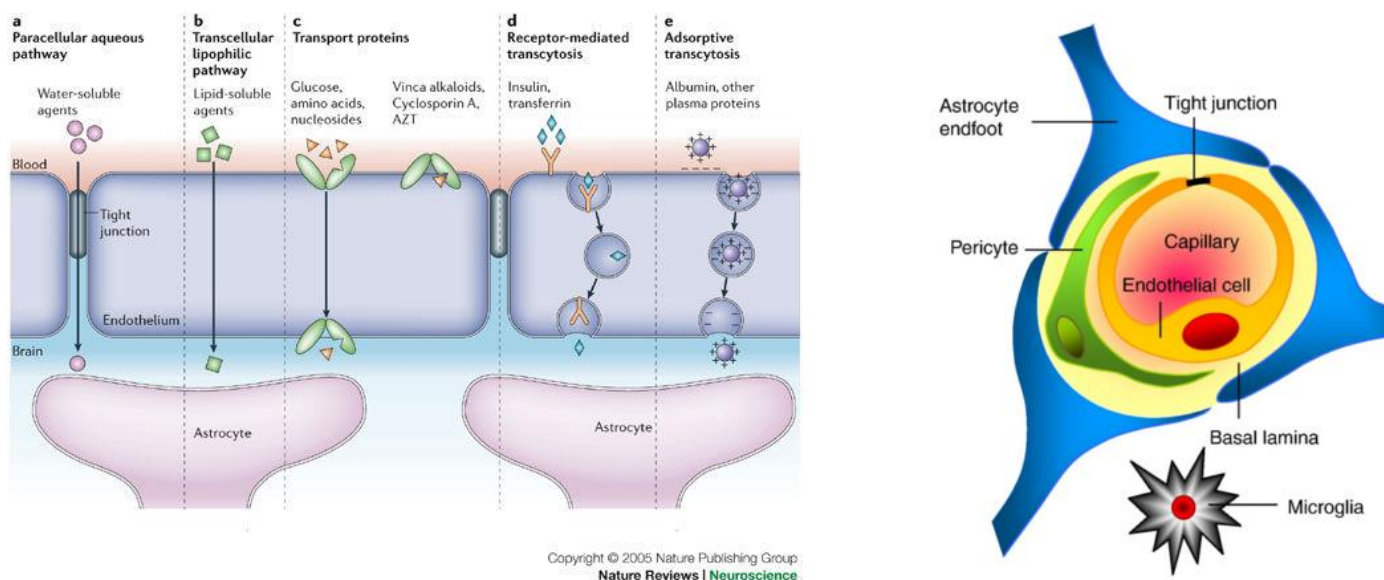


Figure 1-2:

*On the left: Pathways across the blood–brain barrier (from Abbott et al. 2006). On the right: together with the endothelial cells, pericytes, glial cells (especially astrocytes), and the basal lamina are indirectly involved in the establishment and maintenance of the BBB (from Abbott et al. 2010).*

A malfunctioning BBB has been associated with meningitis, epilepsy (Oby and Janigro, 2006), multiple sclerosis (Waubant, 2006), ischemia (Busto and Ginsberg, 1996), tumors (Weiss et al., 2009) or neurodegenerative disorders such as Alzheimer’s disease (Zenaro et al., 2016). The BBB is essential to the brain, but becomes a limit to deliver therapeutic molecules to the brain. Usually nanometer sized or larger, they are too big to naturally cross the BBB.

### 1.1.3. Improving drug delivery to the brain

Improving the delivery of therapeutic molecules to the brain allows to decrease the whole injected dose given to the patient in order to decrease peripheral toxicity. We already saw that only small lipophilic molecules can diffuse through the BBB (molecular weight under 400-500 Da) which disqualifies most therapeutic molecules. To overcome the BBB, one idea consists in the use of receptor-mediated endocytosis by conjugation of therapeutic molecules to ligands, such as antibodies and peptides, against receptors that are expressed on the surface of endothelial cells of the BBB allowing the drug to be transported into the brain. So far those receptors includes insulin receptors, transferrin receptors, LDL receptors and their related proteins, but more are being looked for (Gabathuler, 2010). The main drawback of this approach is the long and expensive design of each new compound. Moreover, modifications to the drug structure often result in the (at least partial) loss of

the drug's biological activity. More recently several nano-carriers, which can be loaded with a drug, have been engineered such as liposome, micelles, carbon nano-tubes, dendrimers or gold nanoparticles (Figure 1-3). Those nano-carriers can be loaded with drugs and, as before, can be conjugated to ligands to target receptors of the BBB, acting like Trojan Horses. Moreover, loading the drug in a carrier protects the drugs and thus helps to further increase the concentration of the drugs to the target region. Of those nano-carriers, liposomes seem to be the most promising ones due to their capability to incorporate both hydrophilic and hydrophobic drugs, their low toxicity and because ligands can easily be attached to their surface to target biomarkers such as amyloid plaques in Alzheimer's disease (Agrawal et al., 2017; Spuch and Navarro, 2011; Vieira and Gamarra, 2016). For more efficacy of the drug, its release can be triggered by degrading the shell of the carrier. For example lipid shells can be degraded by a pH change, by thiolysis or by heating (Kumari et al., 2014). Moreover, the diffusion of the drug in the brain parenchyma must be efficient. However, cytotoxicity generated by nanoparticles or their degradation products remains a major problem in drug development (Upadhyay, 2014).

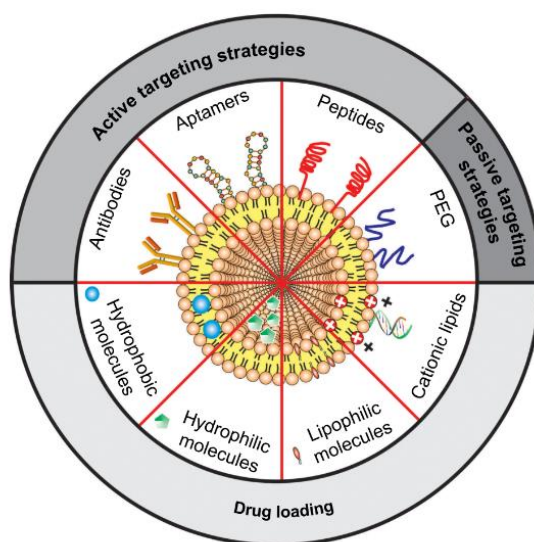


Figure 1-3: Schematic representation of the main liposomal drugs and targeting agents that improve liposome affinity and selectivity for brain delivery (from Vieira & Gamarra 2016)

For drugs that do not naturally cross the BBB, two techniques have been developed to overcome this impermeability: direct injections (Krewson et al., 1995), which can be intracranial directly in the brain tissue, intracranial in the ventricles or trans-nasal, and chemical disruption of the BBB, with hyperosmotic solutions such as mannitol (Guillaume et al., 2010). In direct injections, the compound is delivered directly on site within the brain. Although direct injections showed therapeutic benefits in the treatment of brain tumors (Brem and Gabikian, 2001), it presents the clear disadvantage of being invasive, with a risk of infection, and neurosurgery is mandatory, making it really not suitable for repeated interventions. The drug release is also challenging to control as it is highly concentrated at the delivering site and the concentration decreases exponentially around this site (Voges et al., 2003), thus resulting in a non-homogeneous drug availability in the tissue. In the second method, the injection of hyperosmotic solutions causes the shrinkage of endothelial cells and the transient opening of the tight junctions (Rapoport, 1970) allowing drugs to pass through the BBB. Studies showed benefits of this method, especially in oncology (Hall et al., 2006). With mannitol the BBB remains open

for 2 to 3 hours (Chi et al., 1996). But this method does not allow to choose the delivery site, since the hyperosmotic solution is injected in the blood flow and thus disrupts the BBB in the whole brain. The surgery is relatively serious because it requires general anesthesia and because the injection is intra-arterial and in order to target specific regions of the brain, researchers have used transient flow arrest, which causes a risk of strokes. So, once again, this technique can be considered invasive. Moreover some patients experienced hypotension or bradycardia (Bellavance et al., 2008). So although those techniques have shown their potential in clinical trials, they remains relatively invasive, difficult for the patients and not suitable for repeated treatments.

#### 1.1.4. Ultrasound to increase the drug delivery to the brain

Ultrasound can be focused deep in the body, such ultrasound are called FUS for Focused Ultrasound, and can trigger bioeffects: hyperthermia or cavitation. As we saw, cavitation can enhance drug delivery using cavitation of microbubbles to permeate locally and temporarily the endothelial walls of the blood vessels in the brain we speak about FUS-induced BBB disruption.

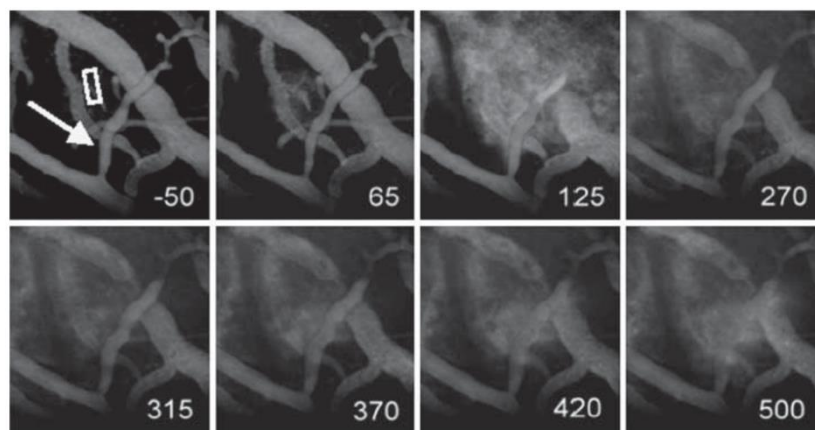


Figure 1-4: two photon microscopy to follow the leakage of a dye from a blood vessel after FUS-induced BBB opening. Numbers are the time in second after the sonication (Cho et al., 2011)

First, it has to be said that the mechanisms ruling ultrasound-induced BBB opening are still unclear but several hypothesis prevail. Stable cavitation is thought to be the required regime of cavitation for BBB opening. Inertial cavitation even has to be avoided. It has often been associated with damages such as edema and extravasation of red blood cells suggesting hemorrhages. We will discuss in more details those effects and how to avoid them in paragraph 1.1.6 on safety. Micro-streams and direct contact generated by the stable cavitation mechanically stress the endothelial cells of the BBB (Krizanac-Bengez et al., 2004). The mechanical stress depends on the amplitude and frequency of the ultrasound, and also on the size of the microbubbles compared to the size of the blood vessels. The parameters affecting the efficacy of the BBB opening will be addressed in the paragraph 1.1.5. This mechanical stress generates cellular changes at the BBB. FUS have been shown to enhance at least 4 ways of molecular passage across the BBB: transcytosis using cellular vesicles, endocytosis, paracellular passage through widened tight junctions, and through the cytoplasmic channels in the

endothelium (Sheikov et al., 2004). The dominant way of passage is probably paracellular with the endothelial cells contracting under the stress and loosening the tight junctions between them (Sheikov et al., 2008). More recently, two photon microscopy has been used to characterize the BBB opening with a high temporal resolution (Cho et al., 2011), authors described two kinds of leakage, slow and fast. The fast one, reaching its maximum during the ultrasound application, corresponding to the paracellular way through the tight junctions and the slow one, reaching its maximum few minutes after the ultrasound application, corresponding to the transcellular way.

FUS-induced BBB opening for drug delivery has three main advantages. First, this technique is non-invasive. There is no need for surgery because ultrasound are shot from outside the body and the microbubbles are intravenously injected. The fact that this technique does not imply major surgery, and thus is relatively free from associated risks, makes FUS suitable for repeated treatments. Secondly, FUS can be MR-guided. Before the sonications, it is possible to visualize the focal spot of the ultrasound beam in the brain or to geometrically estimate it by visualizing the ultrasound probe and the brain on the same image. At the focus, the acoustic pressure is maximum. With an ultrasound beam properly calibrated, the cavitation will only take place at this location. The delivery site can be chosen by visualizing the focal spot using Acoustic Radiation Force Imaging sequences (Dervishi et al., 2013; Larrat et al., 2010a), thermometry (Kim, 2015) or with geometrical extrapolations by looking at the transducer surface. After BBB opening, MR-contrast agent that do not naturally cross the BBB can be intravenously injected. On  $T_1$ -weighted images, the contrast of the MR images will be enhanced only at the site of the BBB opening (Magnin et al., 2015). It is also possible to acquire  $T_2$ - and  $T_2^*$ -weighted images to assess the safety of the procedure. Indeed,  $T_2$  images have hypersignals if edema are present (Sun et al., 2017) and  $T_2^*$  images have hyposignals in case of hemorrhages (Aoki et al., 2014). Finally, FUS-induced BBB opening is transient, lasting for few hours (Marty et al., 2012a) and going back to a complete functionality of the BBB with no long term effects. FUS-induced BBB opening is currently used for drug or genes delivery (Al-Bataineh et al., 2012; Burgess et al., 2016; Huang et al., 2018) but also shows exciting results as a therapy by itself for Alzheimer's disease (Burgess et al., 2014; Leinenga and Götz, 2015) as detailed in the Chapter 5.

#### 1.1.5. Optimum experimental parameters

The intensity of the BBB opening is measured through the extravasation of molecular probes from the blood vessels to the brain. More intense (or stronger) BBB opening leads to more extravagated molecular probes (for the same injected dose). Those probe molecules can be: optically visible dyes like Evan's Blue, where cutting the brain after an exsanguinous perfusion is enough to see the extravasation site, fluorescent dyes like the dextrans, observable under microscopy, MR-contrast agent leading to an increase of contrast on the MR images or radiotracers imaged in Positron Emission Tomography (PET) or Single Positron Emission computed Tomography (SPECT). The optimum acoustic parameters are the ones giving the stronger openings while remaining safe. So far, the vast majority of the pre-clinical research to optimize those parameters was done on small animal models, mainly rabbits, rats and mice. They demonstrate that several experimental parameters are essential.

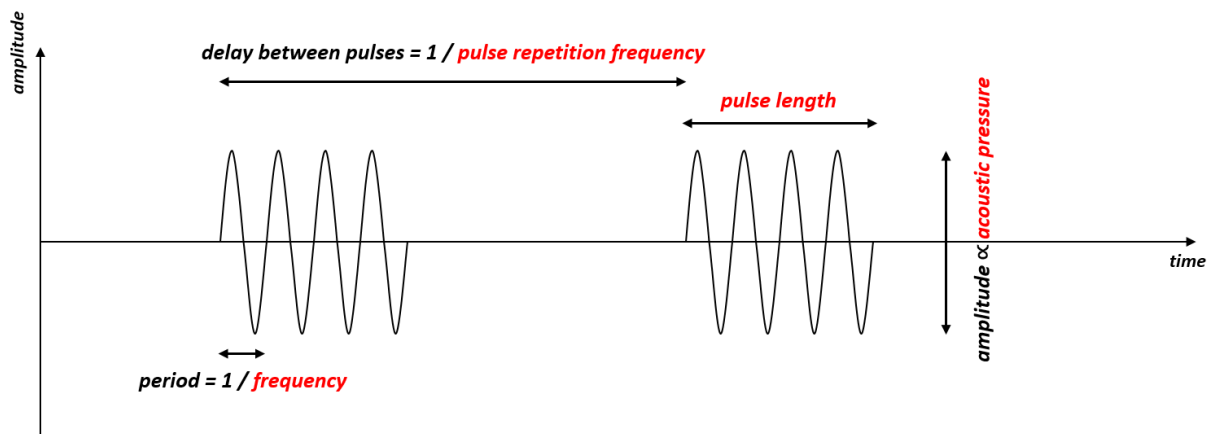


Figure 1-5: Illustration of an ultrasound shot made of two short pulses.

The impact of the critical experimental parameters are going to be detailed below. The parameters related to ultrasound are presented on Figure 1-5: the frequency of the ultrasound wave ( $f$ ), the pulse length, the pulse repetition frequency ( $PRF$ ), the acoustic pressure, which is proportional to the input voltage transmitted to the transducer, and the total sonication time.

### Frequency

High frequencies are not suitable for clinical experiment as the thick, heterogeneous and curved human skull generates more attenuation and more aberration with increasing frequencies. For this reason, the frequency range suitable for clinical trials through skulls seems to be between 0.2 and 1.5 MHz but in rodents efficient BBB openings have been obtained from 28 kHz to 8 MHz.

### Acoustic pressure

Several studies showed that higher acoustic pressures lead to stronger opening but that this relationship seems to saturate at high pressure (Hynynen et al., 2005). Numerous studies report the existence of an acoustic efficacy threshold for the minimal peak negative pressure (PNP) inducing some disruption (Aryal et al., 2014; Baseri et al., 2010; McDannold et al., 2006). But this threshold seems to depend on the frequency. *McDannold's* team proposed to link this threshold to the mechanical index. This index is the ratio between the acoustic pressure and the square root of the frequency. They found that the different pairs frequency/pressure threshold give a constant mechanical index between 0.4 and 0.5 (McDannold et al., 2008), meaning that the higher the frequency the higher the acoustic pressure needed.

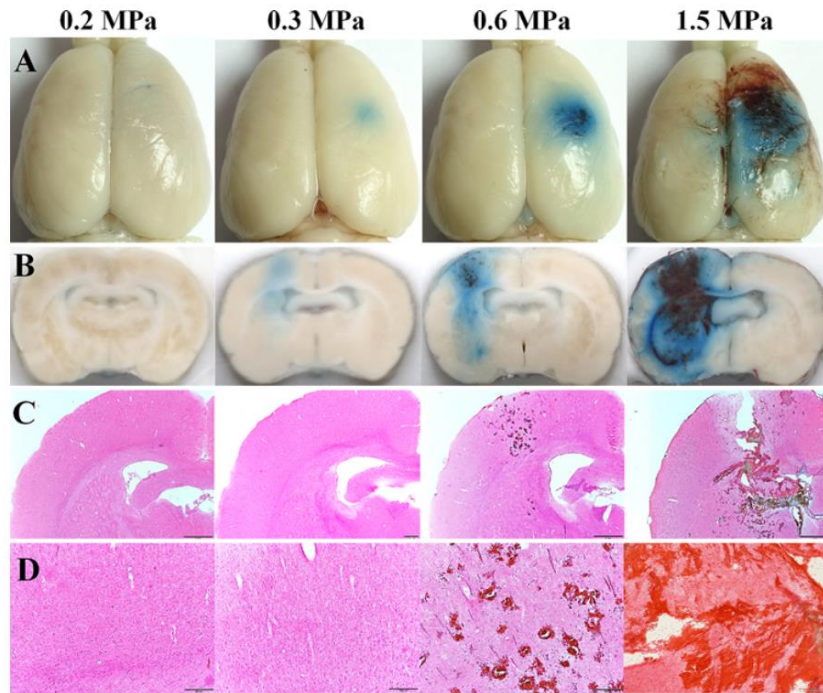


Figure 1-6: Evan's Blue extravasation (A and B) shows an acoustic pressure threshold, around 0.3 MPa, for FUS-induced BBB opening. Histology (C and D) already shows damages at 0.6 MPa. At this frequency (515 kHz) the window for an efficient and safe BBB opening is somewhere between 0.3 and 0.6 MPa (Shin et al., 2018)

#### Pulse duration

Pulse durations from a few  $\mu\text{s}$  to 100 ms have been tested. Increase of the pulse duration seems to increase the intensity of the opening with no real benefit above 10 ms. Short pulses, under 3  $\mu\text{s}$ , are appreciated for their capacity to reduce standing waves in the skull cavity (Choi et al., 2011).

#### Pulse repetition frequency and total sonication time

The effect of the pulse repetition frequency (PRF) is less clear as studies showed a better opening with higher repetition rate (O'Reilly et al., 2011; Shin et al., 2018) and others do not observe any dependency (Mcdannold et al., 2008). Finally total longer sonication time increase the intensity of the opening (Shin et al., 2018) but sonication time longer than the lifetime of microbubbles in the blood (few minutes) are useless and can lead to damages (Yang et al., 2011).

We just saw that the BBB opening is impacted by many acoustic parameters. So, performing the expected BBB opening requires to carefully characterize the ultrasound setup and also requires to precisely dose the ultrasound energy deposited *in situ*. Dosing the energy deposition can be achieved before the sonication for example by measuring the passage of the ultrasound beam through the skull or imaging the ultrasound beam *in situ* with acoustic radiation force imaging (these techniques will be detailed in Chapter 2) or during the sonication with passive cavitation detection (see the next paragraph on safety). But this variety of acoustic parameters represents an advantage compared with other techniques. Indeed, it makes FUS-induced BBB opening tunable, in terms of spatial extend,

## Chapter 1

intensity or duration. In addition to the acoustic parameters, two other experimental parameters can impact BBB opening: the microbubbles and the anesthesia.

Table 1-1: Reported effects of the experimental parameters on BBB disruption via FUS and microbubbles (Aryal et al., 2014)

Parameter	Effect on BBB disruption
Pressure amplitude	Increase in BBB disruption magnitude as pressure amplitude increases; saturation at some point [82–84]; vascular damage produced at high pressure amplitudes.
Ultrasound frequency	Decrease in BBB disruption threshold as frequency decreases; some evidence of improved safety for lower frequencies [85].
Burst length	For burst lengths less than 10 ms, BBB disruption threshold increases and BBB disruption magnitude decreases as burst length is reduced [86,90–92]; little or no increase in disruption magnitude for longer bursts [77,81,90].
Pulse repetition frequency	BBB disruption magnitude increases as repetition frequency increases up to a point [90]. Other works have observed no effect on BBB disruption magnitude [86].
Ultrasound contrast agent dose	Magnitude of BBB disruption increases with dose [83,90,94,188]; other experiments have reported no effect [86].
Sonication duration	Longer durations [84] or repeated sonication [96,97] increase magnitude of BBB disruption; damage reported with excessive sonication [84,97].
Microbubble diameter	Threshold for BBB disruption lower for larger microbubbles; disruption magnitude increased with larger microbubbles [87–89].
Ultrasound contrast agent	Similar outcomes reported for Optison® and Definity® microbubbles [189]. Sonovue® microbubbles and research agents are also commonly used.

### Microbubbles

Microbubbles are usually made of an innocuous heavy gas (perfluorocarbon or sulfur hexafluoride) encapsulated in a shell (Martin and Dayton, 2014). The shell is made of lipids, proteins, or polymers and its role is to protect the gas in its inside. Used gases are heavy (heavier than air) in order to increase their lifetime in the blood and thus increase their availability. Indeed, heavier gas take longer time to diffuse through the shell which prevents dissolution in the blood. Their sizes range approximately from 1 to 5  $\mu\text{m}$ . This diameter is smaller than brain capillaries, which prevents them from obstructing these vessels. The microbubbles I used during my PhD are Sonovue from Bracco (Schneider, 1999). Their mean diameter is 2.5  $\mu\text{m}$  and their lifetime in the body is approximately 5 minutes long (data acquired in rabbit).

Microbubbles size and dose seems to have an important impact on BBB opening as larger doses lead to stronger openings (Yang et al., 2008) (Shin et al., 2018) (Choi et al., 2010). At last, it can be noticed that microbubbles injection rate does not seem to affect the intensity of the opening (O'Reilly et al., 2011) but attention must be paid to the diameter of the syringe used to inject the microbubbles as small syringes can destroy the microbubbles (Talu et al., 2009).

### Anesthesia

At last, the physiological state of the animals has an impact on the BBB opening, mainly temperature and anesthesia since they both affect perfusion, vasoconstriction and microbubble clearance rate from blood, three parameters that modify the efficacy of BBB opening. Two anesthesia protocols are commonly used: gas anesthesia with isoflurane mixed with oxygen (and sometime air) or chemical anesthesia with ketamine/xylazine intraperitoneally injected. *McDannold's* team showed that, for identical acoustic parameters, the quantity of extravagated probe molecules was greater with ketamine/xylazine than with isoflurane (McDannold et al., 2012a). Indeed, isoflurane is a well-known vasodilator and it is possible that microbubbles cavitating in larger blood vessels apply less mechanical stress on the endothelial cells as they are further from them (especially capillaries which are

considered as being responsible for the major part of BBB leakage after ultrasound). This also results in lower acoustic pressure efficacy threshold when using ketamine/xylazine than when using isoflurane. When using isoflurane anesthesia, the percentage of oxygen in the carrier gas mixture also matters. It has been showed that BBB openings were stronger when isoflurane was mixed with air than when it was mixed with oxygen (Annold et al., 2017). Indeed, a faster clearance of microbubbles from the blood with higher amount of oxygen was observed. Those results prove that comparisons between groups using different anesthesia conditions must be done really carefully and that experimental conditions among animals in a group study needs to be highly reproducible.

Even if the main parameter characterizing the BBB opening is the quantity of extravagated probe molecules, it can be interesting to look at the duration of the opening. In their first experiment, *Hynynen's* team observed that the BBB was closed 48h after opening (Hynynen et al., 2001). With a better temporal sampling, they observed that the BBB could close back as early as 6 hours after sonication. It is important to remember that the closure is a dynamic and progressive mechanism and that at one given time after the opening, the BBB can be closed to big molecules but open to smaller ones. As a consequence, the apparent duration of the increased vascular permeability can depend on the molecular probe used to quantify it. Marty et al. showed that, with identical BBB openings, the BBB was already closed at 2 hours for big molecules (around 60 nm hydrodynamic diameter) and that small molecules (around 1 nm) could cross the BBB for more than 10 hours (Marty et al., 2012a). BBB closure time seems to depend as well on the acoustic pressure used with opening lasting few hours more for higher pressure (Samiotaki and Konofagou, 2013). This influence need to be studied more in details.

#### 1.1.6. Safety

The safety of FUS-induced BBB opening has been extensively investigated to help transfer this technique to the clinic. We will review in this paragraph the main studies. For given conditions, the pressure must be sufficient to trigger the stable oscillation of the microbubbles and thus a permeabilisation of the blood vessels, but a too high pressure might cause inertial cavitation with the associated damaging effects, such as edema or hemorrhages. These two thresholds, the efficacy threshold and the safety threshold, involved the existence of safety window.

The effects of BBB opening on tissues were first investigated on rodents. This investigation starts by looking at radiologically visible tissue lesions or reactions such as edema on  $T_2$  and diffusion images or hemorrhages on  $T_2^*$  images. In most studies, histopathology was done after one sonication (Baseri et al., 2010; Hynynen et al., 2005). The main reported deleterious effect is extravasation of few red blood cells or small petechial hemorrhages. Groups usually report damages for their higher pressure conditions and they associate it with inertial cavitation (McDannold et al., 2006). Repeated BBB opening sessions, once a week for 6 weeks, on rats show no or limited tissue damages (Kobus et al., 2015). Authors found small damages like micro-hemorrhages or scars and neuronal-necrosis for their higher pressure conditions. Finally, no effect on behavior or locomotion were observed on mice up to 6 months after BBB opening (Olumoladea et al., 2017).

The best proofs of the safety of the technique were more recently brought with studies on non-human primates. The reference study for assessing the safety of the BBB opening was done by *McDannold's* team (McDannold et al., 2012b). They identified a clear safety window for the acoustic pressure in which BBB opening could be performed without tissue damages. Histological results showed no effect on neurons or on white matter fibers. They only reported hemosiderin deposits in the meninges and hemorrhagic tissue in ventricles when the focal spot of the ultrasound was intersecting those tissues. Moreover, animals recovered from each ultrasound session without behavior deficit. Repeated sessions of BBB opening in non-human primates did not show negative long term physiological or neurological effects either (Downs et al., 2015).

Real-time monitoring is now commonly achieved using passive cavitation detectors (Arvanitis et al., 2012; O'Reilly and Hynynen, 2012). One or several small ultrasonic transducers, often placed at the center of the emission transducer, are used in reception mode to record and analyze the diverging pressure waves emitted by the oscillating microbubbles during FUS-induced BBB disruption. The spectral content allows to tell stable cavitation, emitting harmonics of the emission frequency, from inertial cavitation, emitting a broadband signal. Our group designed a real time feed-back controller for rodents and primates which increases the acoustic pressure for each pulse until internal cavitation appears (Kamimura et al., 2018), thus allowing to perform FUS-induced BBB opening without inertial cavitation, that is to say safely. The role of real-time monitoring is crucial for this technique as it is now moving to clinical trials.

Recently, more subtle tissue reactions were investigated. In particular, the effect of FUS-induced neuro-inflammation was studied. In an extensive study *Kovacs et al.* showed that sterile inflammatory responses to ultrasound with elevations in pro-inflammatory, anti-inflammatory, trophic factors, activated astrocytes and microglia (Kovacs et al., 2016). Another study reported activated microglia after FUS-induced BBB opening in an Alzheimer's disease mouse model. The authors suggested that this activation is the mechanism responsible for the amyloid plaque clearance they observed (Leinenga and Götz, 2015). It is not clear if this inflammation is caused by the entry of endogenous compounds in the brain through an open BBB or if it is a direct mechanical effect due to the cavitation forces but *Kovacs et al.* advocates for the second hypothesis.

The effects of BBB opening are numerous and depend on the experimental parameters previously listed. But FUS-induced BBB opening is a potential therapeutic tool and so what matters is the cost to benefit ratio. It can be anticipated that this technique will first be approved for brain tumors or neurodegenerative diseases where current treatment options are limited and the benefits are high. For these applications, the existing set of radiology, histopathology and behavior data acquired in non-human primates gives sufficient evidence for a clinical transfer. This is why FUS-induced BBB opening is already undergoing few clinical trials in France (Carpentier et al., 2016) and in Canada (Huang et al. 2016). Nevertheless, FUS-induced BBB opening triggers mechanisms in the brain which are not completely understood and need further investigations.

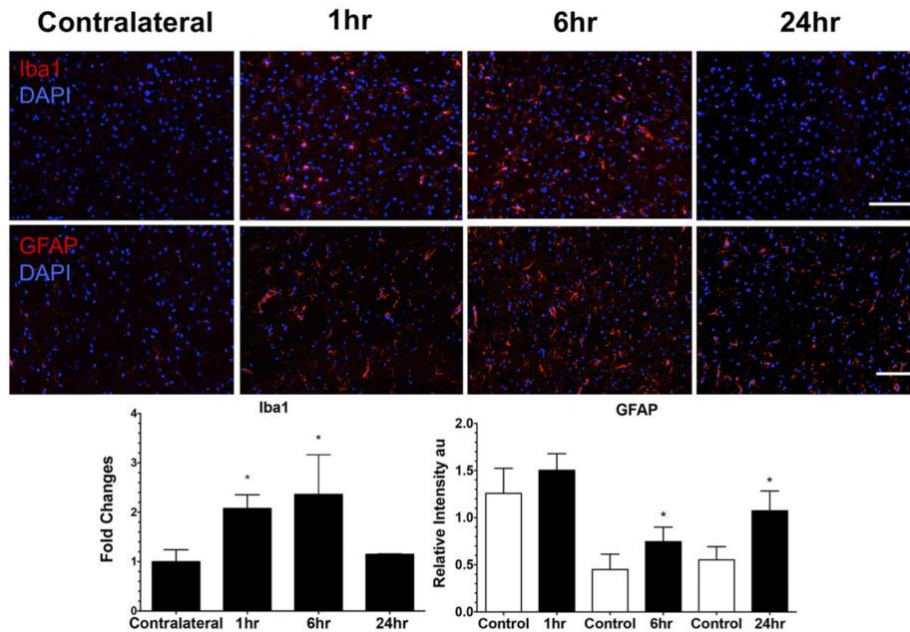


Figure 1-7: the first line shows microglia (Iba1) and nuclei (DAPI) in a sonicated region several hours after FUS-induced BBB opening and a control region (contralateral) and the second line shows astrocytes (GFAP) and nuclei. Microglia and astrocytes are both overexpressed after FUS-induced BBB opening compare to the contralateral region (Kovacs *et al.*, 2016)

### 1.1.7. Protocol for blood-brain barrier opening

Here, I briefly describe the BBB opening protocol I used during my PhD (Figure 1-8). I will firstly describe the full BBB opening protocol under MR-guidance and then adaptations of this protocols without MR guidance. The protocol under MR guidance was exclusively for rats as the MR coil is only suitable for them. The used anesthesia was always isoflurane in a mixture of air and oxygen. I used about 3% of isoflurane to get the animals asleep and this percentage was decreased to 1.5-2% once the animal was in the scanner. Animals had to be shaved to ensure a good coupling between the head and the water balloon of the transducer. We used an electrical razor and a depilatory cream. Then, a catheter was placed in a tail vein to inject the microbubbles and the contrast agent later on. To continue, the animals was placed in the MR bed, the head inside a specific coil which allows to position the transducer in its center. A temperature probe and a breathing probe were installed to monitor vitals parameters. Then, the bed was put inside the MR scanner. Before BBB opening, pre-scans can be acquired for positioning the ultrasound beam (MR ARFI) or for reference images. For BBB opening, a bolus of microbubbles was injected via the catheter in the tail vein, usually 200  $\mu$ L for a rat, and ultrasound were shot. Finally, to validate or quantify the BBB opening, a contrast agent was injected via the catheter and MR images were acquired with a set of parameters tuned to detect the contrast agent.

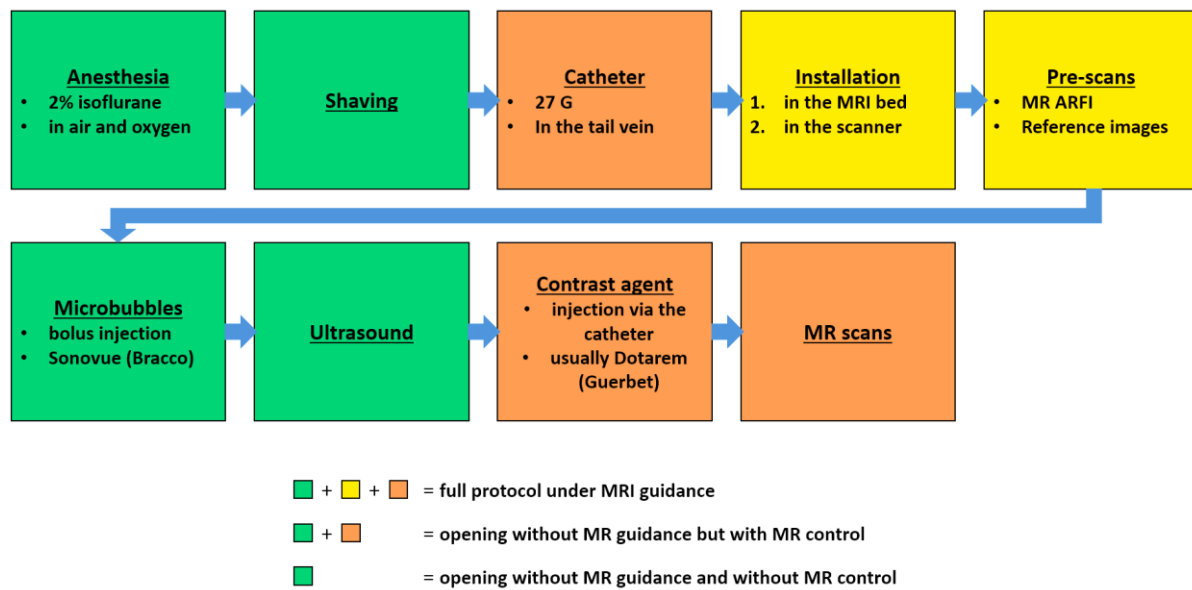


Figure 1-8: BBB opening protocols.

I used two other kinds of protocols without MR guidance. The first kind was without MR guidance but with a control after the BBB opening (protocol green and orange on Figure 1-8). The sonications were performed outside of the scanner and after contrast agent injection animals were placed in the scanner to validate the opening. In this protocol, BBB openings cannot be quantified due to the absence of references images, the description of the opening can only be quantitative. This protocol was used in particular for optimization of the BBB opening without MR guidance. Indeed, I performed repeated sessions of BBB openings on many animals for several weeks (see Chapter 5) and doing it without guidance and control (protocol green on Figure 1-8) is a huge gain of time. When using mice, microbubbles injection and contrast agent injection were always retro-orbital. More details on the protocols will be given when used in the next chapters. The last protocol was without MR guidance and without control, it was only used for the repeated sessions of FUS-induced BBB opening in Chapter 5.

## 1.2. Alzheimer's disease

### 1.2.1. Epidemiology of Alzheimer's disease

44 million people worldwide have Alzheimer's disease (AD) and with aging of the population this number is expected to double by 2050 (Hebert et al., 2013). AD is the first cause of dementia (around 70% of the cases). Doctor Alois Alzheimer first described the symptoms of the disease in his patient August Deter in 1906. For a long time AD was wrongly considered as a natural effect of aging and not as a specific disease, thus explaining the limited resources governments have provided to its understanding, unlike other diseases such as cancer. It is only since the 2000s' that governments launched ambitious research funding plans.

The Organization for Economic Cooperation and Development (OECD) evaluates the cost of an AD patient at 20 000€ a year (Hebert et al., 2013) but other studies put the figure up to 90 000€ (Huang et coll., 1998). Due to the aging of the population, the Office parlementaire d'évaluation des politiques de santé (Opeps) anticipates a cost of 1 to 1.5 % of the PIB in 2040 for France. Wilkinson (Wilkinson, 2005) considers that in UK the cost of AD exceeds those of cardiac disease, cerebrovascular accidents and cancers while the budget on AD research is only 10% the budget for cardiac disease research and 3% the budget for cancer research. The cost of an AD patient is relatively high due to the loss of autonomy and socio-medical help needed to face it.

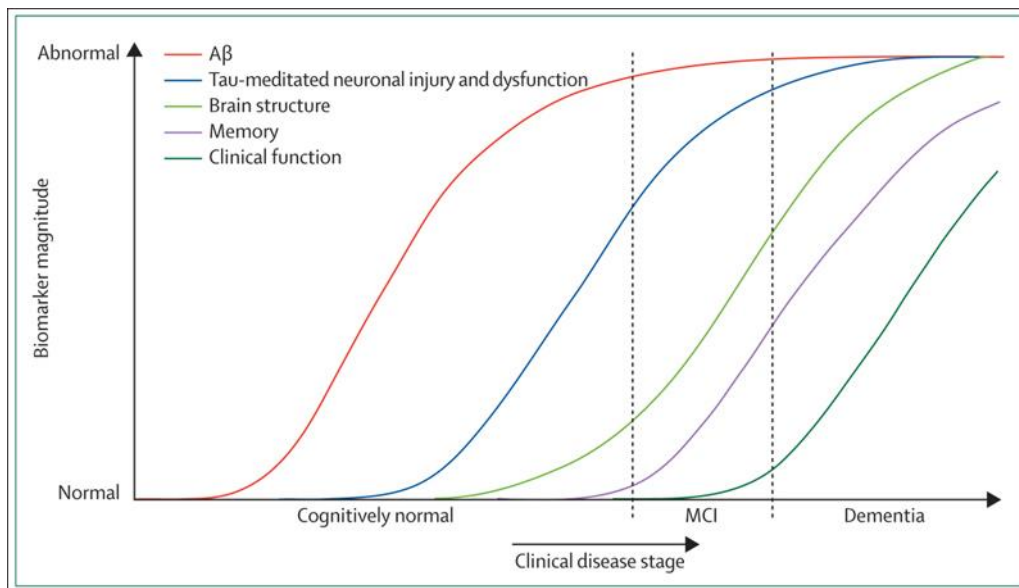


Figure 1-9: Change in the biomarkers of AD over time. A $\beta$  accumulation is the first biomarker of the disease, appearing years before cognitive decline (Aisen et al., 2017)

AD is a neurodegenerative disease and is characterized by an alteration of the cognitive capacities. The only way to have an indisputable diagnosis of the disease is through postmortem analysis. Indeed, histopathology can reveal the presence of amyloid plaques and neurofibrillary tangles which are the hallmarks of the disease (NIA, 1997). Fortunately, physicians have developed ways to identify Alzheimer's patients during their lifetime in order to analyze and prevent the progression of the symptoms. The clinical diagnosis is done in two steps. Firstly, dementia is diagnosed. Dementia is defined as a memory deficit associated with one cognitive function - language, praxis, gnosis... - strong enough to lead to a loss of autonomy. Then, various criteria allows to diagnose AD, the McKhann criteria (McKhann et al., 1984) are the most used. They are based on the progressivity of the disease and the absence of other cerebral diseases. McKhann criteria have a good sensibility, around 80%, but a low specificity, around 70%, when compared to postmortem analysis. The term Mild Cognitive Impairment (MCI) is used to define the early stages of the disease, when the amnesic syndrome is non-disabling but progressive. At autopsy, 80% of the patient who received MCI diagnosis happened to have AD (JC et al., 2001). The goal of this classification is to better anticipate the evolution of the pathology. Those mental status tests conducted by interviewing patients should be combined with brain imaging and CSF analysis (Waldemar et al., 2007). Brain imaging, mainly done with PET and MRI, is

used more to rule out other possible causes of dementia, such as tumors, subdural hematomas, cerebrovascular disease, than to confirm AD. The current role and the possible future contribution of neuroimaging will be discussed later on. Low concentrations of A $\beta$  and high concentration of tau hyperphosphorylated in the CSF have been associated with AD with a good specificity and a good sensitivity, both about 70% (Mattsson et al., 2009). But these CSF analyzes strongly need to be standardized. Many new biomarkers are being studied. The potential of this technique is enormous as a single CSF sampling could allow to diagnose AD. Biomarkers in the blood are also being looked for.

Detecting the disease as early as possible is key because, as illustrated on Figure 1-9, dementia is the last step of the disease. A $\beta$  accumulation or tauopathy can start decades before the clinical symptoms. Early detection would allow a better therapeutic management.

### 1.2.2. Physiopathology of AD and the amyloid cascade hypothesis

Neuropathologically, AD is characterized by two hallmark features: amyloid plaques and neurofibrillary tangles. A $\beta$  peptide is naturally produced in the brain and comes from the APP protein (for Amyloid Precursor Protein (Soderberg, 1987)). The role of APP is not well understood but seems vital as APP knockout mice are not viable (Von Koch et al., 1997). Normally, APP is cleaved mostly within the plasma membrane by  $\alpha$ -secretase releasing a soluble fragment: A $\beta$ <sub>1-40</sub>. In AD, APP is firstly cleaved by  $\beta$ -secretase releasing APP $\beta$ . APP $\beta$  is then cleaved by  $\gamma$ -secretase releasing an insoluble fragment: A $\beta$ <sub>1-42</sub>. Insoluble A $\beta$ <sub>1-42</sub> aggregates into  $\beta$ -sheets and precipitate to form amyloid plaques (Soderberg, 1987). It is also thought to trigger neurofibrillary tangles, even if the mechanism remains unknown. Amyloid plaques are either diffuse (immature) or neuritic (senile). The relationship between dementia and diffuse plaques is not strong since diffuse plaques can be found in non-AD patients (Buldyrev et al., 2000). Neuritic plaques (5-200 $\mu$ m) are made of an insoluble amyloid  $\beta$  core (Soderberg, 1987) mainly A $\beta$ <sub>42</sub>, surrounded by neuritic elements (dystrophic axons and dendrites) which are a reaction to this insoluble core and contain pathological bundles of tau proteins. The evolution of amyloid deposition was defined in 3 steps. Firstly, deposition in the basal neocortex, especially in the temporal areas. Secondly, in the hippocampus and thirdly in all the cortical regions (Braak and Braak, 1997). A $\beta$  peptide can also accumulate around blood vessel. In this case, it is called amyloid angiopathy.

The second hallmark of AD is neurofibrillary tangles, also called tau tangles. They are not made of neurofilaments, as it was first thought, but of a normal protein, the tau protein. Tau is a cytoskeletal protein which function is to stabilize microtubules (Gustke et al., 1992). In AD, tau is abnormally phosphorylated (hyper-phosphorylated) and loses its physiological role. This impairs microtubules binding, then neurons cannot maintain dendrites and axons which may lead to synaptic loss and neuronal death. Indeed, neuronal death is huge where neurofibrillary tangles are heavily present (Grignon et al., 1998). It is still unclear whether neurofibrillary tangles or neuronal death correlate better with dementia (Takashima, 2009) but amyloid plaques deposition clearly does not correlate with dementia (Mesulam, 1999). The symptoms of AD related to neurofibrillary tangles can be referred to as tauopathy.

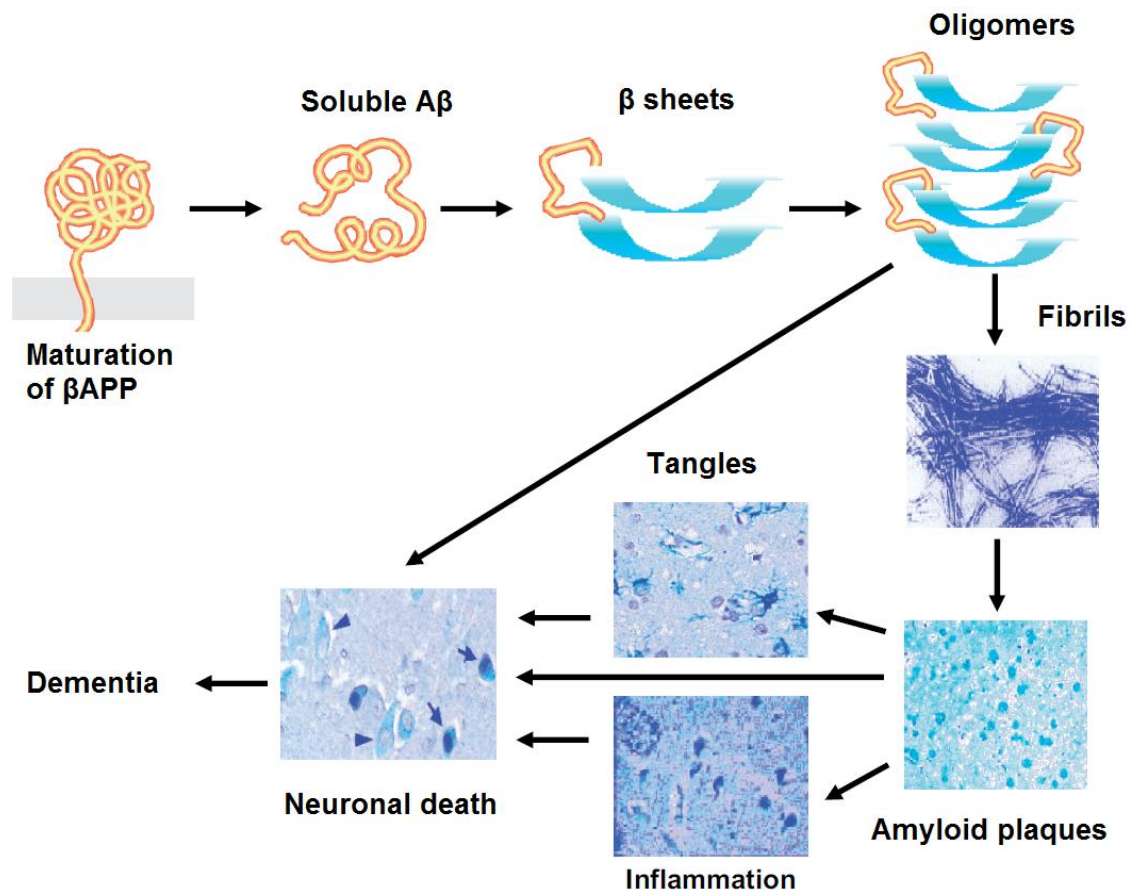


Figure 1-10: Amyloid cascade hypothesis ((Inserm), 2007)

For the past 25 years, the main scientific framework to explain the mechanisms underlying AD is the amyloid cascade hypothesis. It gives to amyloidosis a central role in the progression of the disease. In this hypothesis, illustrated on Figure 1-10, the accumulation of A $\beta$  peptides triggers amyloid plaque formation, neurotoxicity and clinical symptoms of AD. The sequence of events is the following: i) accumulation of A $\beta$  peptides ii) oligomers formation iii) diffuse deposit of amyloid in the brain iv) subtle effects of A $\beta$  oligomers on synapses v) activation of astrocytes and microglia vi) progressive synaptic and neuritic injury vii) altered neuronal ionic homeostasis viii) altered kinase/phosphatase activates leading to neurofibrillary tangles ix) spreading of neuronal dysfunction and neuronal death, and finally dementia (Hardy and Selkoe, 2002). The amyloid cascade hypothesis is strongly supported by the discovery of the PS1 and PS2 genes. In one hand, mutations on these genes cause AD in genetic forms of the disease and in the other hand, they enhance the processing of APP to form A $\beta$  through a direct effect on  $\gamma$ -secretase. Experiments on transgenic mice suggest that APP is at the source of the cascade. For instance, mutations of only the tau protein do not cause AD (Hardy et al., 1998). Those results suggest that cerebral A $\beta$  accumulation is the primary factor in AD and that the rest of the disease process, including tau tangle formation, results from an imbalance between A $\beta$  production and A $\beta$  clearance.

However, to date, this amyloid cascade hypothesis is not a consensus. The main concern with this hypothesis is the poor correlation between amyloid plaques and the degree of cognitive impairment. And some people, even with huge amyloid load, do not present dementia (Katzman et al., 1988).

Another concern is that in other pathologies the amyloid load is important but no neurofibrillary tangles are present (Levy et al., 1990). Finally, transgenic mice with amyloid plaques do not exhibit strong neuronal loss (Irizarry et al., 1997). Alone, this hypothesis fails to explain some observations on AD. This is why other hypotheses have emerged giving a more important role of neurofibrillary tangles.

The tau hypothesis states that excessive or abnormal phosphorylation of tau results in the transformation of normal tau into hyperphosphorylated tau and neurofibrillary tangles. Hyperphosphorylated tau disassembles the microtubules, which interferes with axonal transport and lead to cell death (Iqbal and Grundke-Iqbal, 2005). Another hypothesis is a cardiovascular origin of AD. Capillaries in the brain are altered with aging and lesions could trigger the production of amyloid plaques through microglia (De la Torre and Mussivan, 1993). Recently, the viral hypothesis came back on stage with a study showing that active herpes infections in the brain may accelerate amyloid deposition and the progression of Alzheimer's disease (Eimer et al., 2018). Finally, multiple other hypotheses have been put forward including, oxidative stress, dysfunctional calcium homeostasis, hormones, inflammation, and cell cycle dysregulation with the resultant neurotransmitter dysfunctions and cognitive decline (Mohandas et al., 2009).

### 1.2.3. A difficult therapy

Two main families of drug exist on the market for Alzheimer's disease, Cholinesterase inhibitors (Donepezil, Galantamine, Rivastigmine) and antagonists for NMDA (N-methyl-D-aspartate) receptors. Acting on neuronal death or signal transmission, those treatments do not cure nor stop the disease but they seem to improve the symptoms for some patients (Scarpini et al., 2003). Undergoing research is mainly focused on A $\beta$ , as illustrated on Figure 1-11, only one drug in phase III acts on tau tangles. Those approaches are based on the amyloid cascade hypothesis: clearing amyloid aggregates or slowing down the aggregation should be beneficial. They aim to decrease the quantity of A $\beta$  peptides in the brain, acting on  $\beta$ - or  $\gamma$ -secretase or with antibodies against A $\beta$ , and so stop the cascade from the beginning. Some results are promising. For example patient treated with solanezumab showed a reduction in the rate of progression of the disease (Siemers et al., 2016). But recently results from a phase III trial on mid stage AD failed to give similar results. In fact, so far all phase III trials are not conclusive. A list of these failed trial is given on Table 1-2. These failures are another argument against the amyloid cascade hypothesis and big pharmaceutical companies have lost billions of dollars running these programs since the 90's.

In 2018, the French government chose to stop refunding drugs for Alzheimer's disease claiming that the therapeutic benefit were too small. The conclusion reached by many regarding those failed trials is that the interventions were too late but could have been successful if started earlier. Those trials might have been started too late (Cedernaes et al., 2014; Van Dyck, 2018), when A $\beta$  concentration was already plateaued and the disease already driven by tau pathology (T. Hyman et al., 1993). There is also a debate on the criteria of inclusion of patients participating to these trials: until the early 2000's, this was based on cognitive scores and resulted in pooling patients at different stages of the disease if not even patients suffering from other dementia. As seen on Figure 1-9, A $\beta$  accumulation starts years before the other symptoms. Drug evaluation is hard for such a slow evolution disease, the beneficial outcome being assessed years after trial start.

Table 1-2: Trials of anti- A $\beta$  antibodies for Alzheimer's disease (from Van Dyck 2018)

Drug	Publication	Phase	Sample	Participants	Age, Years	Dose	Duration, Weeks	Efficacy	ARIA-E	Biomarkers
Bapineuzumab	Salloway <i>et al.</i> , 2009 (15)	2	234	Mild-moderate AD	50–85	0.15, 0.5, 1, 2 mg/kg IV every 3 months	78	Failed primary end points	17%, retrospective analysis	No effect on CSF A $\beta$ 42, tau, or p-tau
Bapineuzumab	Rinne <i>et al.</i> , 2010 (19)	2	28	Mild-moderate AD	50–80	0.5, 1, 2 mg/kg IV every 3 months	78		Retrospective analysis combined with Salloway, 2009	↓ Cortical <sup>11</sup> C-PIB compared with baseline and placebo
Bapineuzumab	Salloway <i>et al.</i> , 2014 (21)	3	2204	Mild-moderate AD	50–88	0.5, 1, 2 mg/kg IV every 3 months	78	Failed primary end points	15.3% of APOE $\epsilon$ 4 carriers, 4.2%, 9.4%, and 14.2% of three dose groups in noncarriers	↓ Cortical <sup>11</sup> C-PIB and ↓ CSF p-tau in APOE $\epsilon$ 4+
Solanezumab	Farlow <i>et al.</i> , 2012 (27)	2	52	Mild-moderate AD	>50	100, 400, 1600 mg/month IV	52		No cases	↑ A $\beta$ 40 and ↑ A $\beta$ 42 in CSF
Solanezumab	Doody <i>et al.</i> , 2014 (28)	3	2052	Mild-moderate AD	>55	400 mg IV every month	78	Failed primary end points; ↓ decline in mild AD subgroup	0.9% solanezumab vs. 0.4% placebo	No effect on brain A $\beta$ (PET); ↑ A $\beta$ 40 and ↑ A $\beta$ 42 in CSF
Solanezumab	Completed	3	2129	Mild AD, A $\beta$ +	55–90	400 mg IV every month	78	Failed primary end point		No effect on brain A $\beta$ or tau (PET)
Gantenerumab	Ostrowitzki <i>et al.</i> , 2012 (34)	1	18	Mild-moderate AD	50–90	60, 200 mg IV every 4 weeks	24		2/6 participants on 200-mg dose	↓ Cortical <sup>11</sup> C-PIB compared with baseline
Gantenerumab	Ongoing	2/3	799	Prodromal AD, A $\beta$ +	50–85	105 or 225 mg SC every 4 weeks	104	Nonsignificant benefit in rapid progressors, post hoc		
Crenezumab	Cummings <i>et al.</i> , in press (38)	2	431	Mild-moderate AD	50–80	300 mg SC every 2 weeks, 15 mg/kg IV every 4 weeks	68	Failed primary end points	1 case, APOE $\epsilon$ 4 homozygote	↑ CSF A $\beta$ 42
Crenezumab	Completed	2	91	Mild-moderate AD	50–80	300 mg SC every 2 weeks, 15 mg/kg IV every 4 weeks	68	Failed primary end points		No effect on brain A $\beta$ (PET); ↑ A $\beta$ in CSF
Crenezumab	Ongoing	3		Mild-prodromal AD, A $\beta$ +	50–85		100			
BAN2401	Ongoing	2		Mild-prodromal AD, A $\beta$ +	50–90	2.5, 5, 10 mg/kg IV every 2 weeks, 5, 10 mg/kg IV every 4 weeks	78			
Ponezumab	Landen <i>et al.</i> , 2013 (44)	1		Mild-moderate AD	>50	10 mg/kg IV	52	Failed primary end points	No cases	↑ CSF A $\beta$ 42
Aducanumab	Sevigny <i>et al.</i> , 2016 (50)	1	165	Mild-prodromal AD, A $\beta$ +	50–90	1, 3, 6, 10 mg/kg IV every 4 weeks	54	Exploratory; ↓ decline in CDR (10 mg/kg) and MMSE (3, 10 mg/kg)	3%, 6%, 37%, 41% of four dose groups	↓ Cortical [ <sup>18</sup> F]-florbetapir
Aducanumab	Ongoing	3		Mild-prodromal AD, A $\beta$ +	50–85		78			

AD, Alzheimer's disease; A $\beta$ +, positive for amyloid- $\beta$  biomarker (PET or CSF); APOE  $\epsilon$ 4+, positive for APOE  $\epsilon$ 4; ARIA-E, amyloid-related imaging abnormalities–edema; CDR, Clinical Dementia Rating; CSF, cerebrospinal fluid; IV, intravenous; MMSE, Mini-Mental State Examination; PET, positron emission tomography; p-tau, phosphorylated tau; <sup>11</sup>C-PIB, [<sup>11</sup>C]-Pittsburgh compound B; SC, subcutaneous.

### Imaging for earlier diagnosis of AD

Medical imaging can help detecting AD patient earlier and more specifically in order to select them for early clinical trials. The two tools for *in vivo* imaging of the brain are Magnetic Resonance Imaging (MRI) and Positron Emission Tomography (PET).

PET offers molecular imaging through specific ligands. The most famous one in the Pittsburgh compound (PIB) which targets A $\beta$  (Klunk *et al.*, 2004). PIB allows detecting amyloid plaques and so estimating the A $\beta$  concentration in the brain but correlation between cerebral amyloid levels and cognitive deficit remains weak (Nelson P. T. *et al.*, 2013). With PET, very recent results show that microglial activation, which is a biomarker of AD, can be imaged (Hamelin *et al.*, 2018). An increase in activated microglia results in higher expression of the 18-kD translocator protein (TSPO) to whom DPA binds. Neuronal loss can be assessed with MR-spectroscopy. The decrease of the concentration in N-acetylaspartate (NAA) in the temporal and parietal lobes progress with the disease and was correlated with cognitive deficit (Frederick *et al.*, 1997; T. Hyman *et al.*, 1993).

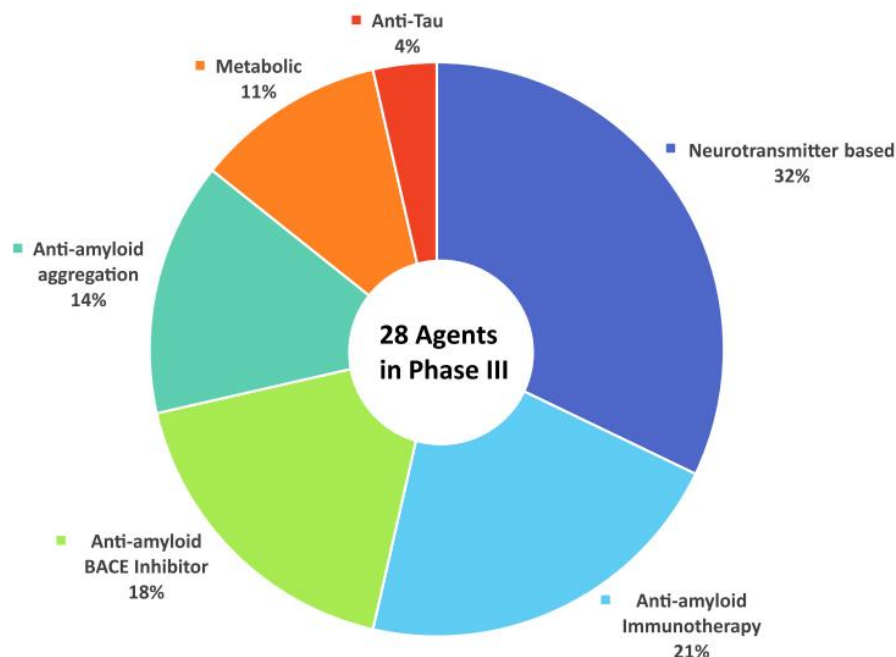


Figure 1-11: Mechanisms of action of agents in phase III (from Cummings et al. 2017).

With fluorodeoxyglucose, PET can measure glucose metabolism. A reduction of glucose metabolism in bilateral temporal parietal regions and in the posterior cingulate cortex has been described as a biomarker for Alzheimer's disease. This imaging method has been approved in the USA for diagnostic purposes and sensitivity and specificity of 86% for diagnosis of Alzheimer's disease have been reported, although there were wide variations between studies (Patwardhan et al., 2004). Finally, brain perfusion is also an interesting biomarker of AD, which can be evaluated both with PET and with MRI. AD patients have a hypo-perfusion of several regions such as parieto-temporal cortex, hippocampus or thalamus (Johnson et al., 1998). Perfusion data truly improve the diagnosis of AD and perfusion could even be an early biomarker of AD appearing before cognitive decline (Johnson et al., 2001).

With MRI, AD is mainly characterized by a decrease of the hippocampal volume (Jack et al., 1992). Brain atrophy is global in AD (Jack et al., 1992) but is first detectable in the hippocampus. One idea is that cortical/grey matter thickness is more relevant than hippocampal volumetry (Knopman et al., 2016) as age-dependent head size changes must be taken into account for volumetry. Others techniques including ventricular volumetry, diffusion tensor imaging, resting state functional MRI can be used. They all rely on the progressive decline in cerebral anatomy and functionality.

#### 1.2.4. Animal models to study AD

Some animals present natural lesions similar to AD. Aged dogs can develop diffuse plaques in the cortex and amyloid angiopathy could affect one third of all aged dogs (Cummings et al., 1993). Cats and sheeps present amyloid plaques but not neurofibrillary tangles (Nelson et al., 1994). Finally, it is probably monkeys which have the pathology the closest to the human one with senile plaques in the

cortex (Struble et al., 1985). But these species are not commonly used to study AD because they are species hard to deal with. Indeed, they need a lot of room to breed, their lifespan is long and they develop the disease only when old. Moreover, they naturally develop the disease, meaning that the majority of the bred animals will not develop the lesions (or develop lesion of different intensity) and cannot be included in the studies.

Fortunately, the discovery on the genes affecting amyloidosis and that are absent in familial forms of AD allowed geneticists to develop rodent models of the disease, especially mice models. A full description of the existing models can be found on the reference website [www.alzforum.org](http://www.alzforum.org) with to date 153 different models referenced in the database. The first models had only one mutation, most of the time on the APP gene. Those mutations lead to an overexpression of the A $\beta$  peptides and to the deposition of amyloid plaques in the brain. The nature of the plaques, their number, their density and the age at which the deposition starts depend on the mutations and so varies between models. APP23 and CRND8 are two widely used models. APP23 have a lot of amyloid angiopathy in capillaries in addition to amyloid plaques in brain parenchyma (Calhoun et al., 1999). CRND8 has two mutations on the APP gene, resulting in a more aggressive model with amyloid plaques as soon as 3 months old (Watzlawik et al., 2006), compared to 9-12 months for most of the other models. Then, other models with double mutation were introduced, with mice mutated on the PS1 or more rarely PS2 and crossing with APP mice, those models are the so called APP/PS1 models expressing a lot of amyloid plaques.

More recently, mice that exhibit neurofibrillary tangles and amyloid plaques have been produced by combining mutations on the APP coding gene with mutant forms of tau. Those models in addition to amyloid plaques deposition, develop neurofibrillary tangles. The most widely used model is certainly the 3xTg (Oddo et al., 2003). These mice exhibit amyloid plaques at 6 months and tau tangles at 12 months. They also show synaptic dysfunction and cognitive impairment prior to tau tangles. Even if more complete than the amyloid only models, the question still remains: is this Alzheimer's disease? Indeed, the plaque development is almost certainly driven by the APP and PS1 mutations and the tangle-like pathology is driven by the tau mutations (Lalonde et al., 2013), whereas in human these two hallmarks of AD can be triggered with a single mutation on the APP coding gene.

The mice that I used in my PhD and that we breed at NeuroSpin are APP<sup>swe</sup>/PS1<sup>dE9</sup> mice provided by the team of Aloise Mabondzo in CEA Saclay. Erwan Selingue, technician in our team, is responsible for the breeding. Genotyping of the animals is externalized. Those mice begin to develop A $\beta$  deposits by six months of age, with abundant plaques in the hippocampus and cortex by nine months (Jankowsky et al., 2004). The number of GFAP-positive cells progressively increases with age, with extensive staining throughout the cortex by 15 months (Kamphuis et al., 2012). Between 8 and 10 months, modest neuronal loss was observed adjacent to plaques relative to more distal areas (Jackson et al., 2016). Tau tangles and neuronal loss are not typical in these animals. Regarding behavior, spatial learning is comparable to non-transgenic mice at 7 months of age, but impaired by 12 months as measured by performance in the Morris water maze (Volianskis et al., 2010). In the next chapters, this model will simply be referred to as the APP/PS1 model but this is somewhat imprecise.

## Chapter 1

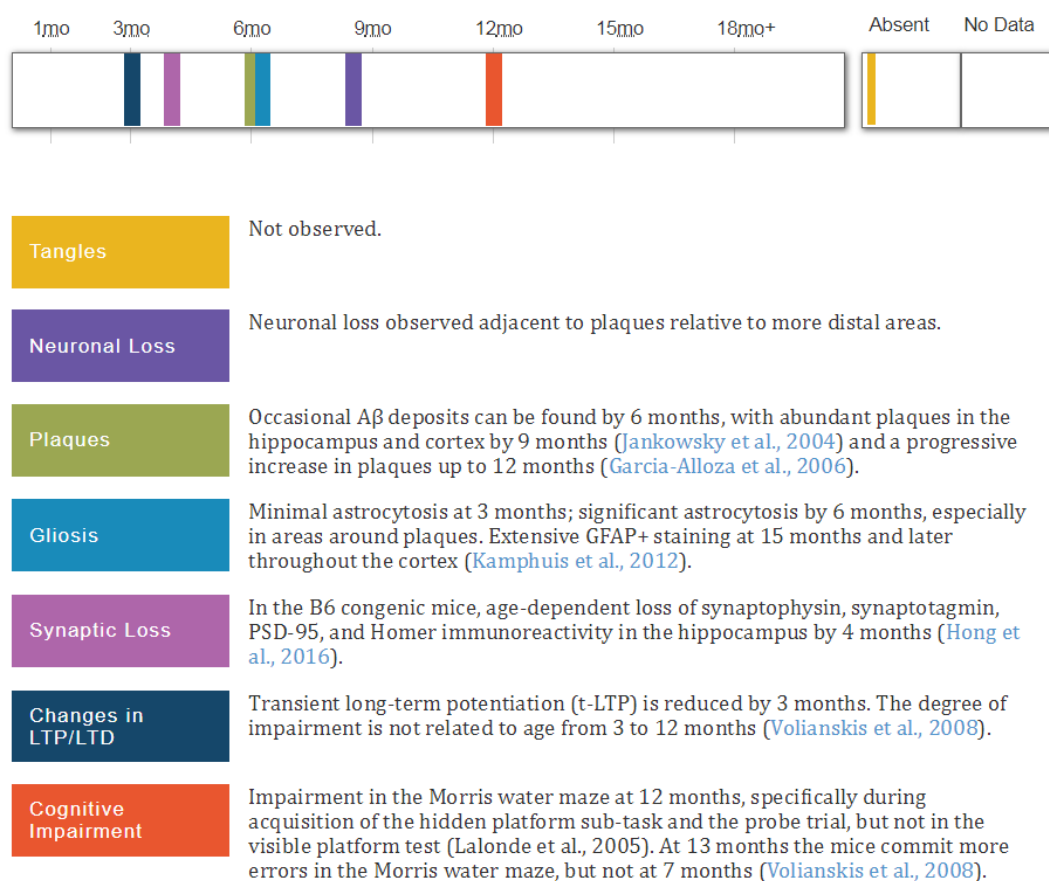


Figure 1-12: Phenotype characterization of the APPswe/PS1dE9 mouse from [www.alzforum.org](http://www.alzforum.org)

I also used during my PhD an APP/PS1 rat model (Cohen et al., 2013) provided by the team of Hervé Boutin in Manchester: the TgF344-AD model. This model has the huge advantage to manifest age-dependent cerebral amyloidosis that precedes tauopathy, gliosis, apoptotic loss of neurons in the cerebral cortex and hippocampus, and cognitive disturbance. The spectrum of symptoms in this model is much closer to the human AD, especially because it expresses both amyloid plaques, which is common in rodent models, and tauopathy with neurofibrillary tangles which is rare in transgenic rodent models, especially in APP/PS1 models.

Those models never fully depict AD and have to be selected for their specificity regarding the working hypothesis of the study. Rodent models differ from human AD on several points but fit it on others, the review by Duyckaerts et al. summarized this well (Duyckaerts et al., 2007). Briefly, rodent models do not show particular brain atrophy (Delatour et al., 2006) unlike AD patient. Most of the time they do not show neither neurofibrillary tangles and neuronal loss is debatable (C. Irizarry et al., 1997). But they do show a lot of amyloid plaques (Blanchard et al., 2003), sometimes even surrounded by dystrophic neurites. They present angiopathy (Garcia-Alloza et al., 2006), as soon as 6 months for some APP/PS1 models. As AD patient, those rodents present neuro-inflammation (Matsuoka et al., 2001). Finally, during behavior tests, they exhibit learning impairment, memory impairment and high levels of stress (Webster et al., 2014) which are typical of the human pathology.

### 1.2.5. Ethics of animal research

Animal research is now performed under the supervision of ethical committees. Every new project must be submitted to the referent ethical committee of the organization. The committee issues an opinion and the final word is given by the competent ministry, which usually follows the opinion of the ethical committee. The project can be started only with a favorable opinion. In France, the GIRCOR is an association of researchers promoting the development of ethical committees. They are a reference authority which publishes guidelines for better projects approval.

Projects are evaluated according to the rule of the 3Rs: Replacement, Reduction and Refinement. Replacement suggests to avoid using animals. The replacement techniques include *in vitro* and *in silico* studies. Reduction suggests to use the strict minimum of animals per study. This includes to build a smart plan of experiment and the use of good statistical models. Refinement suggests to enhance animal welfare by reducing their pain or their stress for example by using non-invasive techniques.

The experiments presented in this manuscript were performed in C57BL/6 mice, nude mice, Sprague-Dawley rats and Fisher rats. They have all been approved by our local ethical committee and validated by the French Ministry of Research. All the experiments were performed under the supervision of a person having the animal experimentation certificate of level 1, which I passed in 2016.

## 1.3. Magnetic Resonance Imaging

### 1.3.1. A brief history of MRI

MRI is an imaging technique that allows to non-invasively obtain 2D and 3D images of the body. MRI scanners use strong magnetic fields, magnetic gradients, and radiofrequency waves to generate images of the organs in the body. MRI relies on the Nuclear Magnetic Resonance (NMR) phenomenon, theorized by Rabi in 1937 and experimentally demonstrated in 1946 by Felix Bloch and Edwards Mills Purcell. In 1950, spin echoes and free induction decay were first detected by Erwin Hahn and in 1952 Herman Carr produced a one-dimensional NMR spectrum. Paul Lauterbur expanded on Carr's technique and developed a way to generate the first MRI images, in 2D and 3D, using gradients. In 1973, Lauterbur published the first nuclear magnetic resonance image. In the late 1970s, Peter Mansfield developed the echo-planar imaging technique that would lead to scans taking seconds rather than hours and produce clearer images than Lauterbur had. In the 80s, the first full body scanners were built and with the implication of industries such as General Electric, the technique has much improved (stronger and more homogeneous magnetic fields, better coil design for better RF penetration, slower magnetic field drifts, more linear gradients), also helped by the progresses in informatics and electronics, to become commercially available. Reflecting the fundamental importance and applicability of MRI in medicine Paul Lauterbur and Peter Mansfield received in 2003 the Nobel Prize "for their discoveries concerning magnetic resonance imaging". More globally, the discovery of NMR was a great source of Nobel Prizes. Indeed, Isidor Isaac Rabi received the Nobel Prize in 1944 "for his resonance method for recording the magnetic properties of atomic nuclei" and Felix Bloch and Edwards Mills Purcell in 1952 "for their development of new methods for nuclear magnetic precision measurements and discoveries in connection therewith".

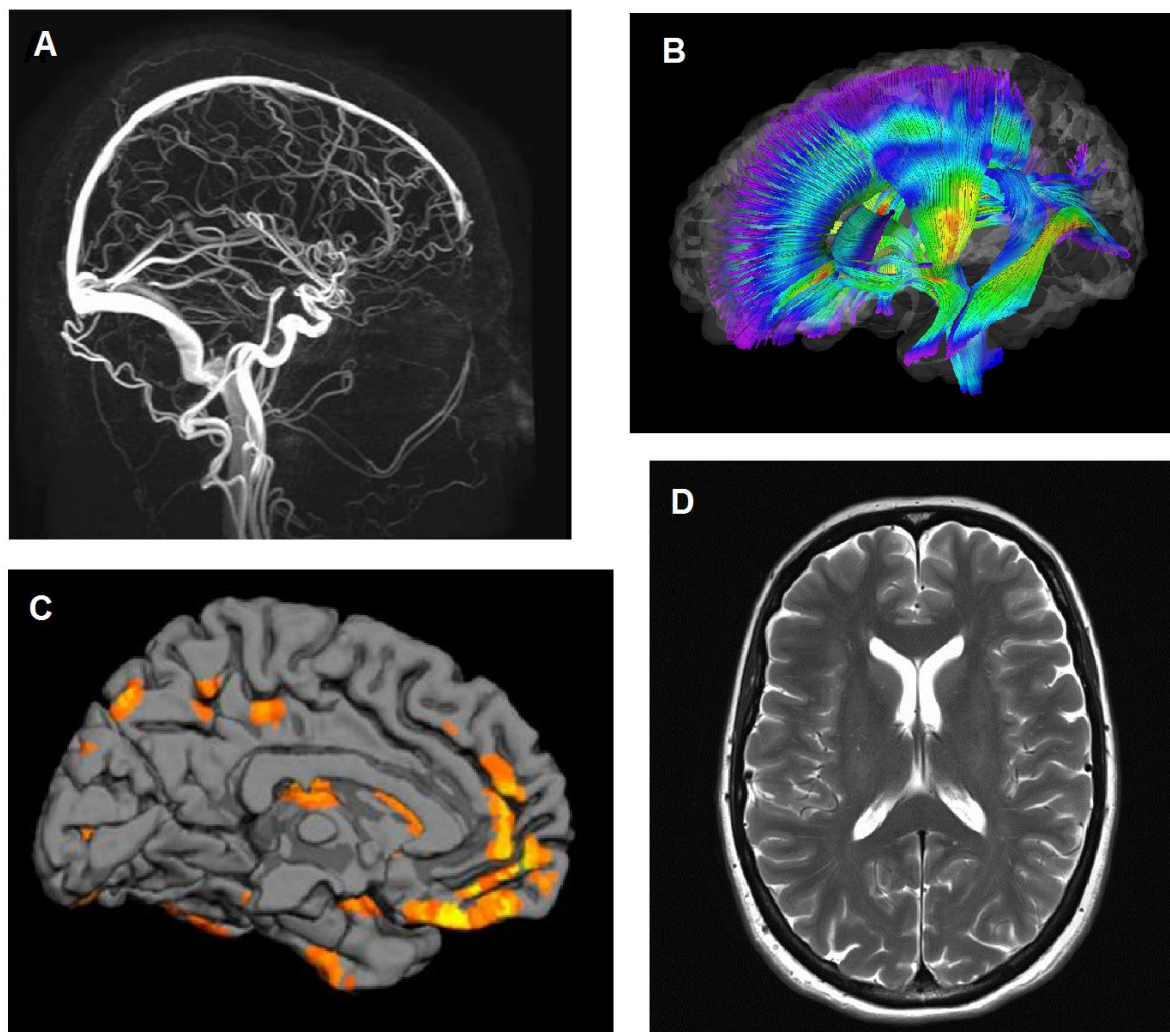


*Figure 1-13: Four kinds of imaging accessible with MRI. A – Angiography to see the blood vessels. B – Tractography to see the connections between brain areas. C – BOLD imaging to see the activation of the brain. D – Anatomical imaging to see the structure of the brain.*

Since 1980, MRI has proven to be a highly valuable imaging tool. It is now the gold standard for soft tissue imaging (brain, ligaments, muscles, etc.). As an example, the number of MRI units in France is 12.6 per million inhabitants, almost as much as the 16.6 CT scanners although the number of exams is only 105 for 1000 patients compared to 197 exams for CT. Indeed, MRI remains an expensive tool. In the US, an MR scan of the brain has an average cost of \$500. More than 25 000 MRI units are estimated worldwide (OECD, 2017). In the United States, there are approximately 11 500 clinical MR scanners. Between 60% and 75% operate at 1.5 Tesla, less than 25% below 1.5 Tesla, around 10% at 3.0 Tesla.

MRI can give a lot of information by playing with the acquisition parameters, such as structural information on the tissues ( $T_1$ - and  $T_2$ -weighted images), information on the connectivity (diffusion images) and also functional information (BOLD sequences). Examples are given on Figure 1-13.

MRI is not straightforward to explain as it goes from quantum mechanism to space encoding with field gradients and image formation. Many books and online courses do it pretty well (Brown et al., 2014; McRobbie et al., 2006). In order to keep the presentation clear, this chapter will be limited to introducing the basic principles of MRI, sufficiently to present the specific sequences I used in my PhD.

### 1.3.2. Basic principles of MRI

The NMR is a physical phenomenon in which a nucleus in a magnetic field absorbs and re-emits electromagnetic radiation, the phenomenon can only occur in nuclei with a non-null spin. The hydrogen nuclei (H, often called “proton” in MRI) has a spin of  $\frac{1}{2}$  and is abundantly present in the body. Indeed the body is made of 70-80% of water molecules, which contain two hydrogens. Hydrogen is by far the most used nuclei in MRI and all the sequences present in my thesis are based on proton imaging.

Without external magnetic field, magnetic moments  $\vec{\mu}$  (proportional to the spin) of the hydrogen nucleus are randomly aligned. Placed in a constant magnetic field  $\vec{B}_0$ , the spins will align with the magnetic field and take quantized values, this part is called the polarization. For hydrogen, the spins can have two possible states: parallel and antiparallel states. The number of spins is slightly superior in the state of lower energy, the parallel state, thus their vector sum in a volume results in a macroscopic magnetization  $\vec{M}$  aligned with  $\vec{B}_0$ . This equilibrium of the spins can be disturbed with radio-frequency (RF) pulse (absorption of the electromagnetic radiation), this part is called the excitation on the spins. Only RF pulses at the Larmor frequency, the precession frequency of the spins, can put the spins out of alignment, this frequency is also known as the resonance frequency.

$$f_0 = \gamma \cdot B_0 / 2\pi \quad (1.1)$$

Then the spins go back to their equilibrium emitting a RF signal (re-emission of the electromagnetic radiation). This phenomenon, called relaxation, is not instantaneous and is described by the Bloch equations. The relaxation has two components:

- The spin-lattice relaxation responsible for the return to equilibrium of the parallel magnetization  $M_z$  collinear to the  $\vec{B}_0$  field. This redistribution of the population of spins on the two energy levels happens with a time constant  $T_1$  of hundreds of milliseconds to few seconds:

$$M_z(t) = M_0(0) \cdot (1 - e^{-t/T_1}) \quad (1.2)$$

But this component of the magnetization cannot be directly detected because it is collinear and much smaller than the permanent  $\vec{B}_0$  field.

- The spin-spin relaxation responsible for the decrease of the transverse magnetization  $M_{XY}$  perpendicular to the  $\vec{B}_0$  field. This loss of angular coherence of the spins in their precession around  $\vec{B}_0$  happens with a time constant  $T_2$  of few milliseconds to tens of milliseconds:

$$M_{XY}(t) = M_{XY}(0) \cdot e^{-t/T_2} \quad (1.3)$$

It is this component of the magnetization, perpendicular to the  $\vec{B}_0$  field that is detected by the receive RF antenna. Moreover, local variations of the  $\vec{B}_0$  field (inherent to imperfections of the magnet or to the presence of high contrasts of susceptibility in the field of view) make the spins lose their coherence even faster with a time constant  $T_2^* < T_2$ . But these local variation are not random, there are spatially located. This is why they can be corrected with spin-echo sequences (Hahn, 1950).

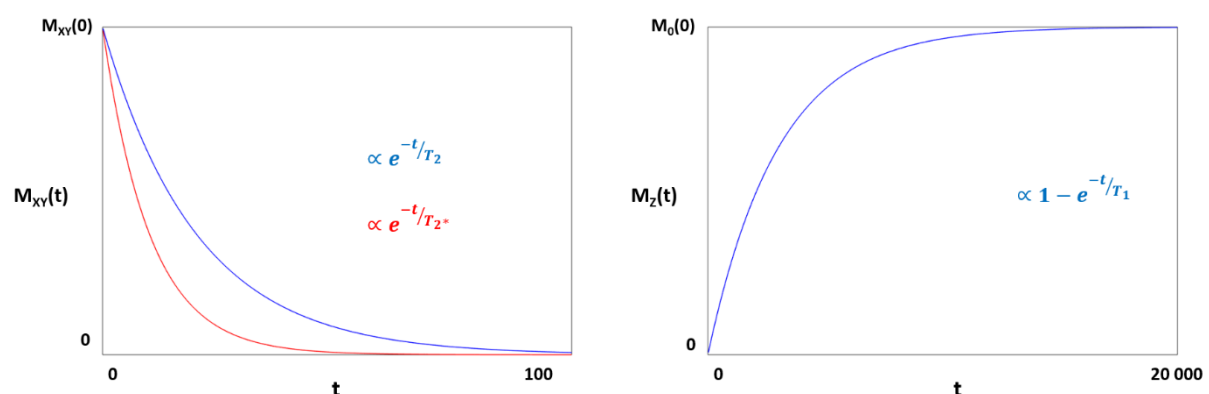


Figure 1-14: On the left: decrease of the longitudinal magnetization due to the spin-spin relaxation.  $T_2^*$  relaxation is faster than  $T_2$  relaxation. On the right: return to equilibrium of the longitudinal magnetization.  $T_1$  relaxation is much longer than  $T_2$  and  $T_2^*$  relaxation.

Typical values:  $T_2 = 20$ ,  $T_2^* = 10$  and  $T_1 = 2000$  s.

$T_1$ ,  $T_2$ ,  $T_2^*$  and proton density are characteristic of each tissue in the body. It is possible to make the MR signal dependent on  $T_1$ ,  $T_2$ ,  $T_2^*$  and proton density. For example, in a  $T_1$  image, different tissues will be differentiable if they have different  $T_1$  with no other contrast coming from  $T_2$ , in this case we speak of  $T_1$ -weighted images. To weight images in  $T_1$ ,  $T_2$  or  $T_2^*$ , two time constants can be tuned in the imaging sequence:

- the echo time (TE) corresponding to the delay between the excitation RF pulse and the signal recording;
- the repetition time (TR) corresponding to the delay between two consecutive pulse sequences.

In short,  $T_1$  weighting is obtained with TE much shorter than  $T_2$  and TR in the same order as  $T_1$  whereas  $T_2$  weighting is obtained with TE in the same order as  $T_2$  and TR much longer than  $T_1$ .

Without going into much details, a classical way to overcome the fast decay of the  $M_{XY}$  magnetization in order to make MR images is to create echoes. The first method is the "spin-echo": after the

excitation RF pulse, a so called refocusing  $180^\circ$  pulse allows refocusing of spins whose coherence have been lost by constant field distortions and inhomogeneities. The sequence is described in details in Figure 1-15. This sequence does not depend on the local variations of the  $\vec{B}_0$  field, they are canceled out by the  $180^\circ$  RF pulse, so the decrease of the signal has a time constant  $T_2$ .

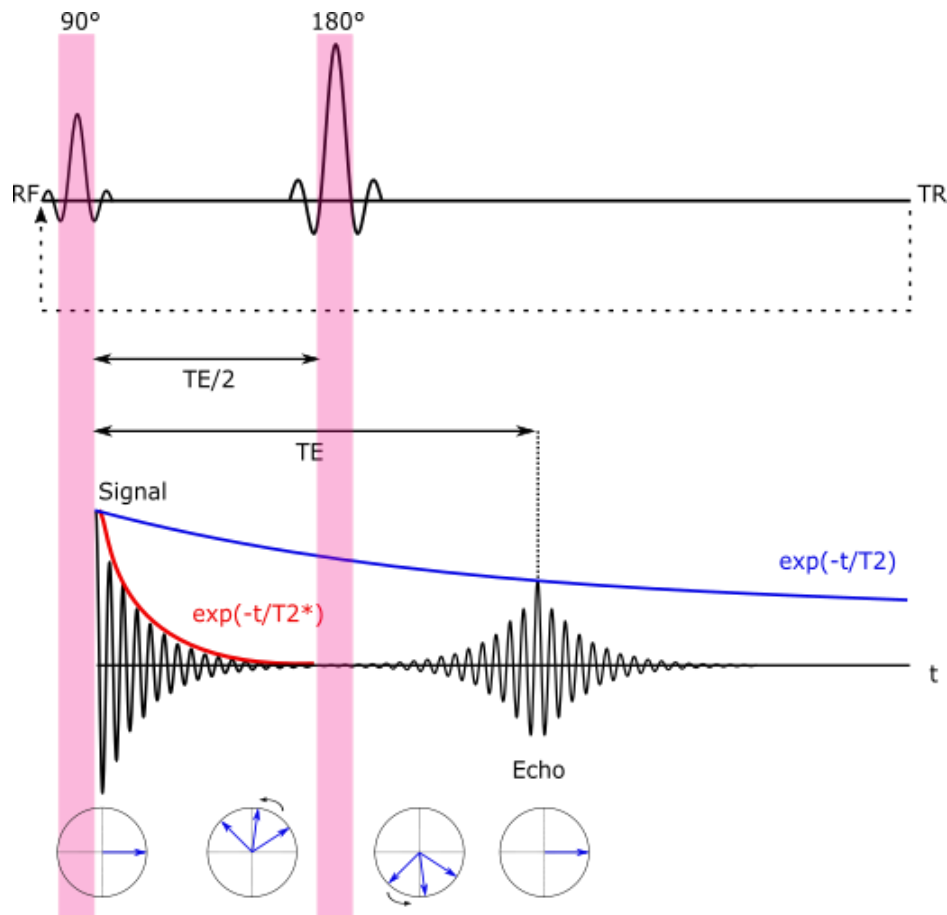


Figure 1-15: Diagram of a spin-echo sequence: i) a  $90^\circ$  RF excitation pulse tilts the longitudinal magnetization to the transversal plan ii) spins diphase with the time constant  $T_2^*$  due to the inhomogeneity of the magnetic field iii) a  $180^\circ$  excitation pulse inverse the transversal magnetization iv) spins rephase and form an spin-echo at the time TE. Courtesy of Remi Magnin (from Magnin, 2016).

The second one is the “gradient-echo” where, after the RF pulse, a gradient is played. First, the negative lobe of the gradient causes a phase dispersion of the precessing spins. Then, this gradient is reversed and the spins refocus and form a so called “gradient echo”. The sequence is detailed on Figure 1-16. This sequence is sensible to the local variations of the  $\vec{B}_0$  field, so the decrease of the signal has a time constant  $T_2^*$ .

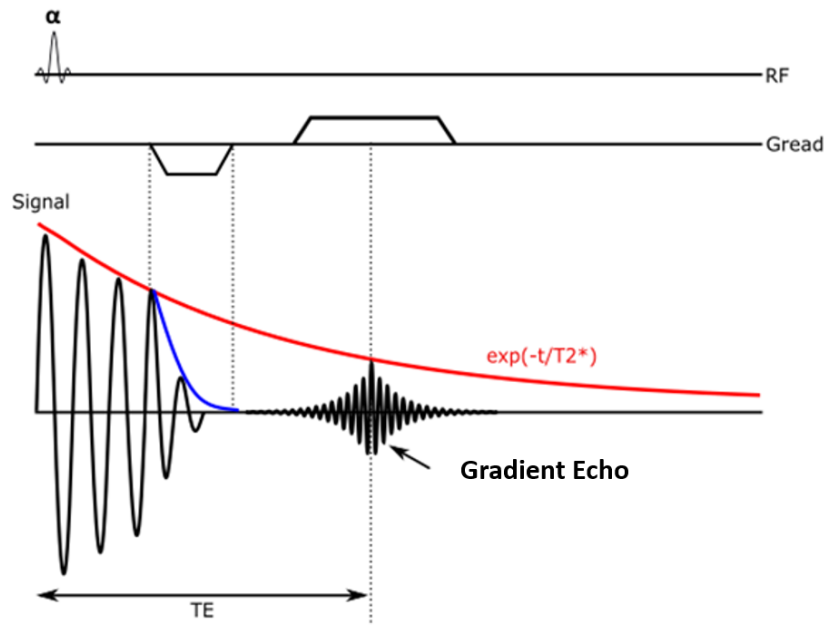


Figure 1-16: Diagram of a gradient-echo sequence: i) an RF excitation pulse of an angle  $\alpha$  tilts a part of the longitudinal magnetization to the transversal plan ii) a first gradient on the read axis speed up the dephasing of the spins iii) a gradient with an inverse polarity rephase the spins to form a gradient echo. Courtesy of Remi Magnin (from Magnin, 2016).

Finally, in order to obtain an image from the RMN signal, space must be encoded in the signal. To do so, three magnetic field gradients are located inside the MR scanner. They can change the  $\vec{B}_0$  field in a controlled way so that its intensity depends on space and so the Larmor frequency of the protons depends on their positions. In a classic 2D sequence the first gradient is used for the so called “Slice selection” and the two others gradients are used for the “Phase encoding” and the “Frequency encoding”. In MRI, the acquisition of the image is done in the frequency domain, also called  $k$ -scape. At each TR, when the echo is being recorded, on line of the  $k$ -space is filled. Between TR, the encoding gradient allows to move from one line of the  $k$ -space to another. When  $k$ -space is full the data are mathematically processed with an inverse Fourier transforms to produce the final image. I will not detail space encoding in this manuscript but I will explain the sequences I used and why they are interesting.

### 1.3.3. Anatomical images

Anatomical images certainly are the most common MR images. They allow to distinguish different tissues based on their  $T_1$ ,  $T_2$ ,  $T_2^*$  and proton density. A structural change of a tissue will affect the local magnetic environment of proton spins and therefore modify its relaxation times and thus it will give this tissue a different signal than surrounding tissues on the MR images. For example, MR imaging is an instrument of choice for brain tumor detection (Deike-Hofmann et al., 2018; Durmo et al., 2018; Suh et al., 2016). In tumors, the free water content is higher than in healthy brain tissue (Kiricuta Jr. and Simplaceanu, 1975). In free water  $T_2$  is longer than in tissue where water is restricted (Paul et al., 1998). So, tumors have a longer  $T_2$  than healthy brain tissue. The spins in the tumors will keep their

coherence for a longer time after excitation and thus give more signal than the normal brain tissue resulting in contrast on  $T_2$ -weighted MR image: the tumor is brighter than healthy brain tissues (Figure 1-17 A). This is also true for edema where water content is high. In my PhD, I routinely used a  $T_2$ -weighted RARE sequence (Rapid Acquisition with Refocusing Echoes) to look for edema after BBB opening or to follow tumor growth in rats.

#### Rapid Acquisition with Refocusing Echoes sequence

The RARE or turbo spin-echo sequence was originally described in 1986 (Hennig et al., 1986). If used with short TE and long TR, the image is mainly  $T_2$ -weighted. After the excitation pulse, not only one refocusing  $180^\circ$  pulse is played (like in a classic spin-echo) but several ones to speed up the acquisition.

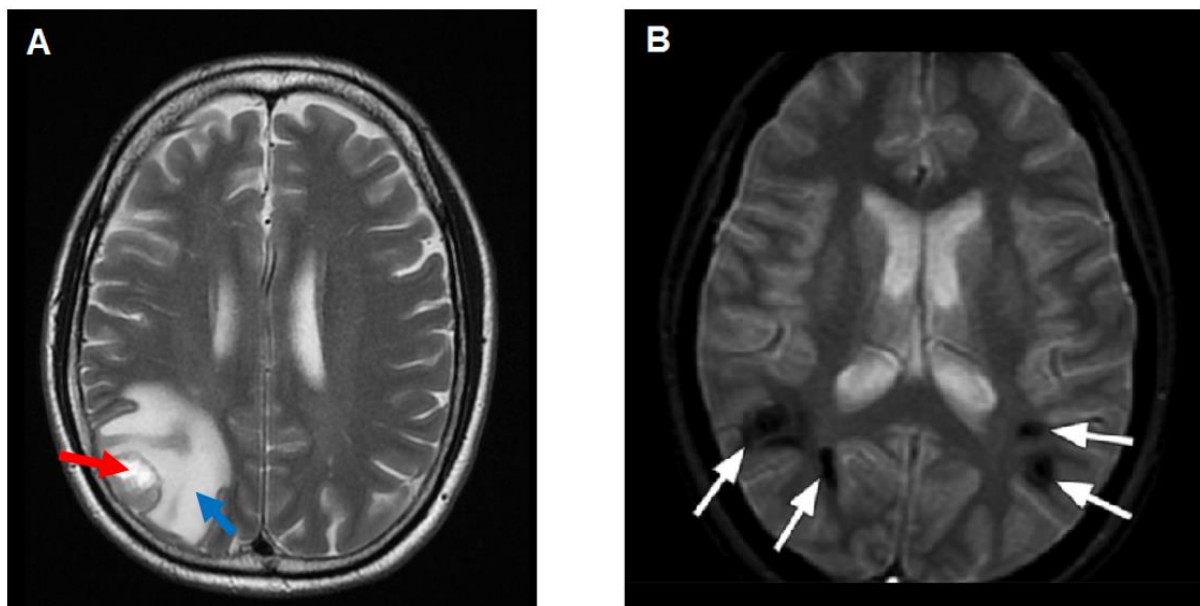


Figure 1-17: A – A tumor (red arrow) and the edema around it (blue arrow), both have an increased contrast on this  $T_2$  image. B – Hemorrhages (white arrows) decrease the signal on this  $T_2^*$  image.

This number is called RARE factor or Echo Train Length (ETL). A gradient of phase encoding is also applied between each  $180^\circ$  pulse to change the line of acquisition in the Fourier domain of the image. With a RARE factor of 2, two lines of k-space can be acquired instead of one for a standard spin-echo, dividing the total acquisition time by 2. TR can also be lengthened (because there is no need for one TR per k-space line) allowing more time for recovery of longitudinal magnetization and so improve SNR (and give more flexibility on the obtained contrast). The drawback of a high RARE factor is an overall decrease of the signal-to-noise ratio (SNR) and contrast-to-noise ratio (CNR) because the later echoes of the echo train are weaker. Over the years, RARE has mostly replaced the conventional spin-echo pulse sequence, which was the most common sequence used in clinical imaging (Walker and Fram, 2010).

### Multi Gradient Echoes sequence

The same gradient reversal process used to create a single gradient-echo can be repeated to produce two or more additional gradient echoes after a single excitation RF-pulse, those kind of sequences are called Multi Gradient Echoes (MGE). Gradient echo based, the echo does not compensate small field inhomogeneities, so the images are mainly  $T_2^*$ -weighted. After the first refocusing gradient, a gradient re-diphases the spin and another refocuses them to form another echo. The process may be repeated, but because of  $T_2^*$  decay, the maximum usable number of echoes is limited. The sequence gives several images at different echo time. On later echoes, the SNR is decreased and the field inhomogeneities are important but the contrast between tissues can be more interesting as we will see later.

$T_2^*$  weighted sequences such as Gradient Echo and Multi Gradient Echoes are really useful for detecting thrombosis (Crassard and Bousser, 2006; Selim et al., 2002), hemorrhage (Tosaka et al., 2007) or iron overload in organs (Ibrahim et al., 2016). The common point of those lesions is that they all heavily loaded with iron, either directly or indirectly with blood which contains iron. Iron is a ferromagnetic element and immersed in the magnetic field of the MR scanner it creates small local inhomogeneities in the magnetic field. Those inhomogeneities cause faster  $T_2^*$  relaxation, leading to signal intensity loss on GRE and MGE images (Chavhan et al., 2009).

#### **1.3.4. Imaging contrast agents**

We already explained that MRI is a powerful tool to assess drug delivery to the brain, in particular after FUS-induced BBB opening. The standard protocol used in our studies to assess the efficacy of the BBB opening is to inject a MR contrast agent which does not naturally cross the BBB. Dotarem (Guerbet, France) was mainly used for this purpose, it is one of the MR contrast agents already FDA or CE clinically approved. This contrast agent is gadolinium based. Because of its unique electronic structure (7 unpaired electrons in the 4f shell), the Gadolinium is strongly paramagnetic (Coey et al., 1999). A dipolar interaction between its unpaired electrons and the spins of hydrogens facilitates the relaxation of those spins (Weinmann et al., 1983). This shortens  $T_1$  (and  $T_2$  but mainly  $T_1$ ) values of nearby protons in tissues where Gadolinium accumulates making them bright on  $T_1$ -weighted images that is to say in our case where the BBB is open. It has to be noticed that due to its toxicity, the gadolinium ion  $Gd^{3+}$  has to be chelated (Laufer, 1987).

### $T_1$ -weighted images

The  $T_1$ -weighted images used in my PhD are Multi Slices Multi Echoes (MSME) sequences. We used spin echoes with short TR to be sensitive to  $T_1$  and multislice acceleration method to reduce acquisition time by acquiring several 2D slices in parallel during every TR. As one can see on Figure 1-18, the contrast is enhanced where the BBB is open. But this contrast enhancement is only qualitative, it is the effect of Gadolinium on the water protons that is visible on the image, not the

exact concentration in Gadolinium.  $T_1$  contrast enhancement is not linearly dose dependent since it saturates for large gadolinium concentrations. However, it is possible to get quantitative information, which is really helpful to compare efficacy of BBB openings. Indeed, acquiring  $T_1$  parametric maps, where the physical value in seconds of  $T_1$  is known in each voxel, allows to come back to the Gadolinium concentration thanks to the following relationship:

Quantitative relaxometry requires longer acquisition times than simple  $T_1$ -weighted images typically 12 minutes versus 2 minutes for the same field of view and resolution.

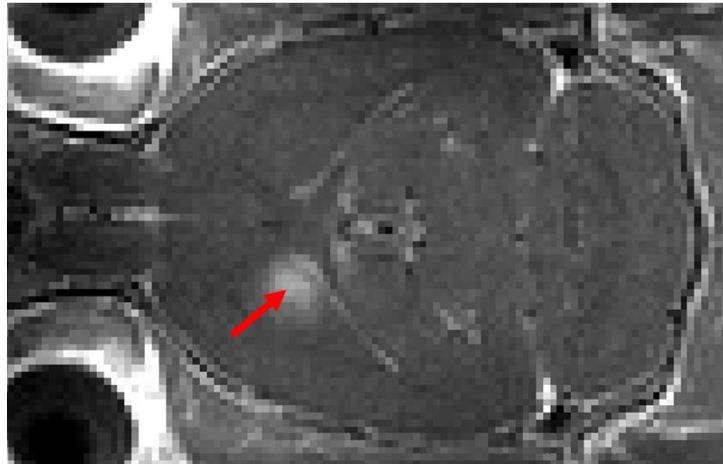


*Figure 1-18:  $T_1$ -weighted image after FUS-induced BBB opening and injection of a contrast agent. Performed in rats, this BBB opening experiment was done under MR guidance in order to precisely opening the BBB in the striatum. The region where the BBB is opening is indicated with a red arrow, its size is approximately 1 mm in diameter which is the size of the focal spot of the ultrasound.*

### $T_1$ maps

During his PhD in our laboratory, Benjamin Marty (Marty et al., 2012a) implemented a FISP (Fast Imaging with Steady State in Precession) sequence capable of measuring  $T_1$  in each voxel of the image. This sequence was first introduced by Deichmann (Deichmann and Haase, 1992). It is based on the inversion-recovery where the longitudinal magnetization  $M_z$  is flipped upside-down with a  $180^\circ$  pulse and the return to equilibrium is sampled with a  $90^\circ$  pulse which transfers the  $M_z$  magnetization to a  $M_{xy}$  magnetization to measure it. In the Deichmann sequence the sampling is accelerated by using flip angles lower than  $90^\circ$  (typically 5 to  $10^\circ$ ), allowing the sample the whole return to equilibrium in one TR instead of several. For a more complete description of this technique, the reader can refer to the PhD thesis of Benjamin Marty (Marty, 2012).

Once  $T_1$  maps are acquired is possible to retrieve Gadolinium concentration maps. Indeed,  $T_1$  can be described as one diamagnetic term  $T_{1\text{ dia}}$  corresponding to the  $T_1$  of the tissue and one paramagnetic term  $T_{1\text{ para}}$  corresponding to the  $T_1$  of the contrast agent (Bloembergen et al., 1948; Solomon, 1955). Those terms are linked together by the following equation:

$$\frac{1}{T_1} = \frac{1}{T_{1 \text{ dia}}} + \frac{1}{T_{1 \text{ para}}} \quad (1.4)$$

And  $T_{1 \text{ para}}$  has been shown to be proportional to the concentration in contrast agent (Swift and Connick, 1962), Gadolinium in our case [Gd]. The proportional coefficient  $r$  is called relaxivity:

$$\frac{1}{T_{1 \text{ para}}} = r \cdot [\text{Gd}] \quad (1.5)$$

With those two equations and knowing the relaxivity of Gadolinium (we will see in Chapter 3 how to measure the relaxivity of a contrast agent), it is possible to calculate the concentration of Gadolinium present into the brain. To do so, a first  $T_1$  map is acquired before injection of Gadolinium, this map informs on the  $T_{1 \text{ dia}}$  of the tissue. A second  $T_1$  map is acquired after injection and informs on the effective  $T_1$  from which  $T_{1 \text{ para}}$  and then the CA concentration are calculated.

### 1.3.5. Imaging the ultrasound beam

We just saw how MRI can help validate and quantify FUS-induced BBB opening. But MRI can also help chose the spatial location of the BBB opening. Indeed, thanks to a specific sequence called MR Acoustic Radiation Force Imaging (MR ARFI), it is possible to encode in phase MR images the tissue displacement at the ultrasound focus generated by the acoustic radiation force.

The acoustic radiation force is a movement transfer between the ultrasound beam and the tissue they are propagating in (Torr, 1984). This transfer happens at interphases between tissues or when the tissue is absorbing the energy, which is the case of brain tissue. This force is proportional to the acoustic intensity. In our case, only at the focal spot the displacement is sufficient to be measured. This displacement is typically on the order of a few microns. ARFI was initially used in ultrasound imaging to measure viscoelastic properties of tissues (Bercoff et al., 2004a). The first MR image of a tissue displacement induced by a propagating external shear wave goes back to 1995 (Muthupillai et al., 1995), but the idea to image displacements induced by focused ultrasound was introduced only in 2008 (Mcdannold and Maier, 2008) and applied *in vivo* in 2010 (Larrat et al., 2010a) in rats brain.

At focus, the radiation force induced by the ultrasound displaces the tissue along the propagation axis of the beam. This displacement is encoded by the addition of Motion Sensitizing Gradients (MSG) oriented along the Slice selection axis and synchronized with the ultrasound shots. The tissue pushed away from its usual location undergoes a slightly higher magnetic field, so the phase of its spins increases. When those spins come back to their initial location, they have a different phase than the nearby spins that did not move. This is seen as a hypo- or hyper-signal on the phase image (depending on the polarity of the MSG). For a more complete description of this technique, the reader can refer to the PhD thesis of Benoit Larrat (Larrat, 2010).

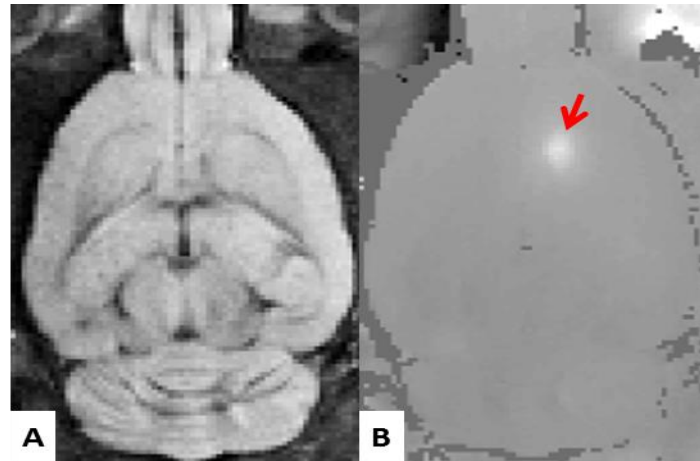


Figure 1-19: A – Magnitude image. B – Corresponding phase image after unwrapping, the red arrows shows the position of the focal spot of the ultrasound where the tissue has been pushed by the radiation force and has accumulated a greater phase.

### 1.3.6. Presentation of the preclinical MR scanner of NeuroSpin

Three preclinical scanner are present at NeuroSpin, a 7 Telsa, an 11.7 Telsa and a 17 Tesla. They are all Bruker (Germany) systems. I used only the 7 T (Figure 1-20) and the 11.7 T (Figure 1-21) scanners during my PhD.

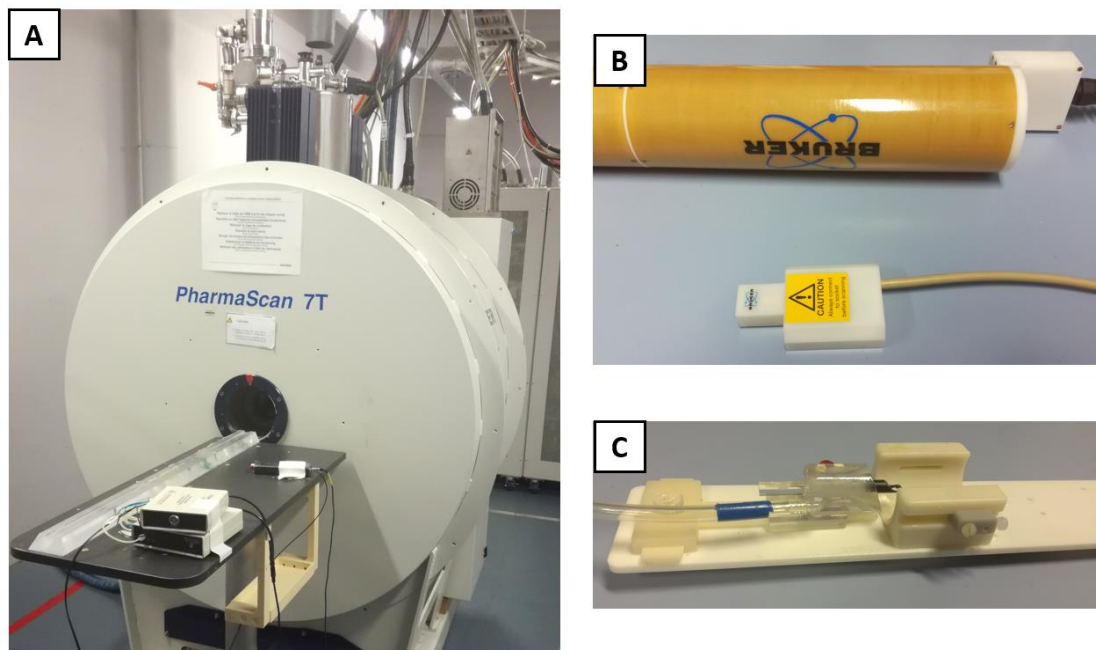
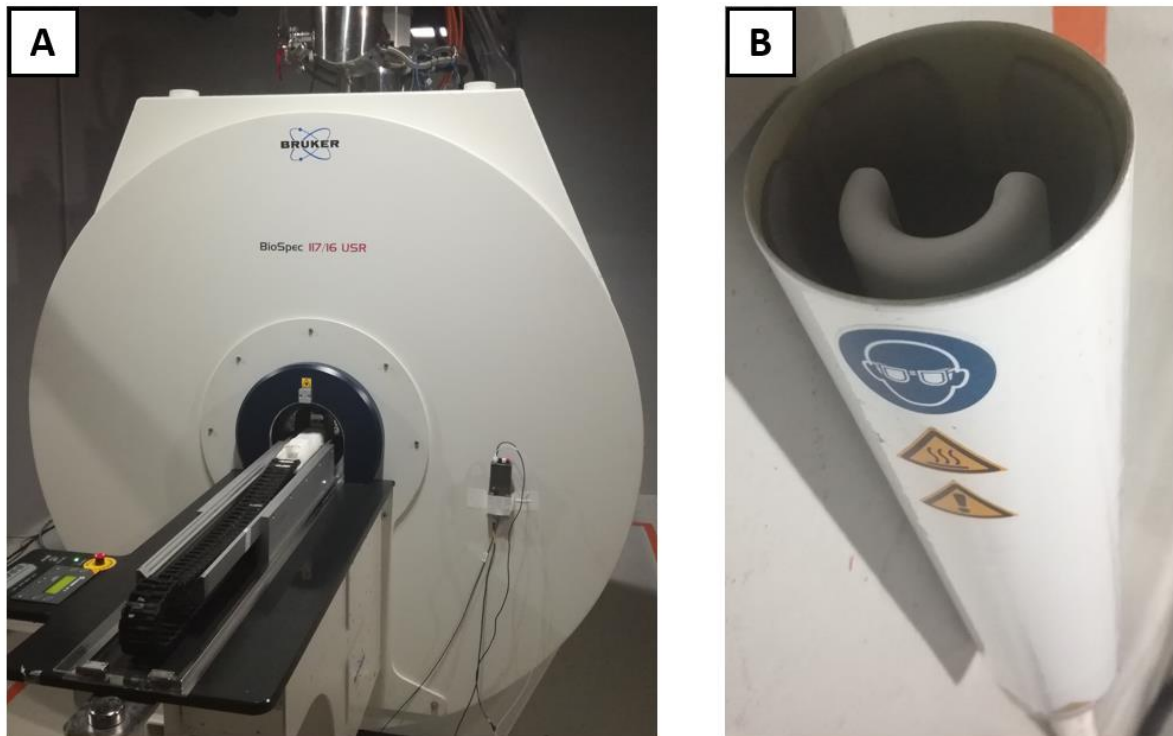


Figure 1-20: A – 7 Tesla scanner. B –Volume transmit and receive antenna. C – Homemade coil for MR-guided BBB opening.



*Figure 1-21: A – 11.7 T scanner. B – Cryo-probe.*

The gradients of the 7 T scanner have an intensity of 840 mT/m and an inside diameter of 9 cm. This scanner can be equipped with an ultrasound setup for MG-guided FUS-induced BBB opening. This ultrasound setup will be described in detail in the next chapter.

The gradients of the 11.7 T scanner have an intensity of 740 mT/m and an inside diameter of 8.9 cm. This scanner is equipped of a cryo-probe, a cooled down antenna with a reduced electronic noise. This antenna provides a much higher signal-to-noise ratio than room temperature antenna. I extensively used this scanner for ex vivo imaging of mouse brains (see Chapter 4).

## 1.4. Conclusion

In this chapter, I introduced the context of the PhD and the techniques I used: ultrasound and MRI. I reminded that the blood-brain barrier was a limit to deliver drugs to the brain and that ultrasound-induced blood-brain barrier opening was a solution to overcome this limit.

I gave background knowledges on Alzheimer's disease and on the animal models used to study it. A significant part of my PhD was dedicated to the study of those animal models. More detailed introductions will be given on Chapter 4 and Chapter 5 regarding the imaging of Alzheimer's disease and the promising therapy based on ultrasound.

I also introduced MRI and specifically how it could be used to image contrast agent, to assess lesions and to guide and quantify ultrasound induced blood-brain barrier opening.



**CHAPTER 2. METHODOLOGICAL ADVANCEMENTS ON ULTRASOUND-INDUCED BBB OPENING.. 37**

<b>2.1. Acoustic field calibration .....</b>	<b>37</b>
2.1.1. <i>Transducer calibration .....</i>	37
a) <i>Transducers to emit ultrasound .....</i>	37
b) <i>Setup for calibration.....</i>	38
c) <i>Single element transducer.....</i>	40
d) <i>Multi element transducer.....</i>	40
2.1.2. <i>Transmission through rat skulls .....</i>	42
a) <i>Context and methods.....</i>	42
a) <i>Transmission factor decreases with frequency and body mass .....</i>	45
b) <i>Correlation with skull thickness .....</i>	46
c) <i>Spatial variation of the transmission factor.....</i>	47
d) <i>The different components of the insertion loss: aberration, attenuation and impedance mismatch.....</i>	47
e) <i>Other transmission factor measurements .....</i>	48
2.1.3. <i>In vivo estimation of the transmission factor with MR-ARFI.....</i>	49
a) <i>MR-ARFI mapping .....</i>	49
b) <i>Simulation of the viscoelastic response of the brain.....</i>	51
c) <i>Acoustic transmission mapping .....</i>	52
<b>2.2. Control of the position of the focal spot .....</b>	<b>54</b>
2.2.1. <i>MR-guided displacement of the transducer.....</i>	54
a) <i>Thermoguide.....</i>	54
b) <i>MR-guided global BBB opening in rats .....</i>	55
2.2.2. <i>Motorized trajectories outside the MR scanner.....</i>	57
a) <i>Motorized positioning system.....</i>	57
b) <i>Validation and safety of a global BBB opening protocol in mice .....</i>	58
2.2.3. <i>Mapping of a rat skull with a transducer in pulse-echo mode.....</i>	60
<b>2.3. Influence of the acoustic pressure on BBB opening .....</b>	<b>61</b>
2.3.1. <i>An acoustic pressure threshold .....</i>	61
a) <i>Co-registration of MR-ARFI and concentration maps.....</i>	62
b) <i>Estimation of the acoustic pressure threshold.....</i>	63
c) <i>Different acoustic pressures in an unique BBB opening experiment .....</i>	64
2.3.2. <i>Higher pressures open the BBB longer.....</i>	66
a) <i>Square trajectory.....</i>	66
b) <i>Opening and follow-up of the permeabilisation .....</i>	67
c) <i>Estimation of a closing time constant depending on the pressure .....</i>	68
<b>2.4. Conclusion .....</b>	<b>70</b>

## Chapter 2. Methodological advancements on ultrasound-induced BBB opening

In this chapter, I will present the developments I made in order to open the blood-brain barrier of rodents in a safe and reproducible manner over small or extended brain regions. As explained in the introduction chapter, accurate ultrasound dose is key to ensure reproducible and controlled results. The first section is dedicated to simulation and calibration of the ultrasound transducers that will be used *in vivo*, I present my efforts to measure the transmission factor of the ultrasound beam through rat skulls in order to properly calibrate the beam *in vivo*. In the second section, a new 3-axis motorized system is experimentally validated to control spatial targeting of FUS and perform spatially extended BBB openings. The last section studies the effect of acoustic pressure, one of the most important acoustic parameters mentioned in the introduction on the intensity and duration of the BBB opening.

### 2.1. Acoustic field calibration

MR-guided FUS-induced BBB opening implies to make various systems work together. So my PhD started by ensuring a good knowledge of the acoustic field distribution in rodent brains.

#### 2.1.1. Transducer calibration

##### a) Transducers to emit ultrasound

Piezoelectric transducers convert electrical power to acoustic power and vice versa. They are made of a piezoelectric materials which change size and shape when a voltage is applied to them. Under alternative current, their shape oscillates and an acoustic wave is emitted at their surface at the frequency of the electrical signal. I only used piezocomposite transducers in my PhD. Our transducers are MR compatible, meaning that not only they have no ferromagnetic parts inside but they also do not affect the magnetic field when they are placed in the MR scanner. Our transducers were previously designed by B Larrat and were manufactured by Imasonic (Voray-sur-l'Ognon, France). In order to be geometrically focused, the transducers are spherically shaped. Concave transducers are very efficient in concentrating much of their energy in a highly localized focal zone, making them particularly used in therapy. They are characterized by their active diameter  $D$  and focal length  $F$  (the more concave the transducer the shorter the focal length). Those 2 parameters set the size of the focal spot, the full width at half maximum along the axis of the transducer ( $l_{axial}$ ) and on the perpendicular plane ( $l_{per}$ ) are often approximated by (Cobbold, 2007):

$$l_{per} = \lambda \cdot F/D \quad (2.1)$$

$$l_{axial} = 7 \cdot \lambda \cdot (F/D)^2 \quad (2.2)$$

with  $\lambda$  the wavelength.

The central frequency of most of our transducers for rodents is 1.5 MHz. Indeed, it is a good compromise between the size of the focal spot and the ability of the ultrasound to cross the skull. Those transducers are equipped with an inflow and an outflow pipe to fill in a latex membrane, attached to the transducer, with degassed water. This water compartment allows a good coupling between the transducer and the head of the animals since ultrasound does not propagate in the air. The transducers were connected, through the inflow and outflow pipes, to degassing systems furnished by Image Guided Therapy (IGT)(Pessac, France). These degassing systems are made of two pumps, one to circulate the water and one to extract dissolved gas, and a filter. The used water was always deionized water.

### b) Setup for calibration

In order to know the acoustic pressure delivered during the experiments, it is mandatory to precisely calibrate the ultrasound transducers in a water tank prior to in vivo experiments. These measurements were repeated on a regular basis over the course of my PhD since properties of transducers and electronic parts can fluctuate with time. In these calibrations, we are interested in the spatial distribution of the acoustic pressure field and the peak negative pressure at the focus as a function of transmitted electrical power. This transmitted power will depend on:

- Impedance matching : consumed electrical power is the difference between transmitted electrical power and reflected electrical power which is null in case of a 50 ohms transducer circuit;
- Mecano-electrical conversion: the conversion rate of electrical power to acoustic power.

Both parameters depend on frequency. Here, I will only present calibration curves at the central frequency of the transducer but relevant frequencies close to it were also acquired.

The transducers were driven by a generator and amplifier (Image Guided Therapy, Pessac, France). We had two systems at our disposal. One is portable and self-sufficient. It is equipped with a touchscreen which allows to parameter the shape of the ultrasound pulse and also to control the 3-axis motorized system that will be presented later on. It can be used only for the single element transducer. This portable electronic system is called “benchtop” electronic. The other electronic that drives the single element transducer is located close to the 7 Telsa MR scanner, together with a degassing system and the electronic to control the motors inside the scanner. This electronic has to be piloted from the control room with the Thermoguide software. This electronic system is called “integrated” electronic. Finally, a last electronic system drives the multi-element transducer. This electronic is also located with the degassing system and the “integrated” electronic and driven by the Thermoguide software which allows to steer. It was always used with an impedance adaptation.

In the IGT user interface, the power transmitted to the transducer is expressed in percentage of the maximum voltage or maximum power that the amplifier electronic board can provide (typically 15W/channel for the single element or for the multi-element). The calibration curves given below are expressed in percent of the maximum voltage amplitude. The conversion of this percentage into watts depends on the generator used but also on the impedance of the whole transducer circuit which in

turn depends on the impedance of the transducer, the cable length and the addition or not of an end cable matching circuit. The exact configuration will be given for each experiment.

For the calibrations, the transducers were mounted on a fixed holder and immersed in a tank filled with deionized and degassed water (Figure 2-1). A calibrated hydrophone (HGL-0200, preamplifier AH-2020, Onda Corporation, Sunnyvale, USA) was used to measure the acoustic pressures. Its active surface at the tip is a disk of 200  $\mu\text{m}$  diameter. The hydrophone was mounted either on a micrometric three axis manual positioning stage or a three axis motorized positioning stage and placed in front of the transducer. For measurements, the standard pulses were 10 periods long with 0.1 second of pause between two pulses, rising and falling two periods at the beginning and at the end of the burst, when harmonic content could affect our measurement, were excluded from analysis. The signal acquired by the hydrophone was directed to an oscilloscope (WaveRunner 44Xi, LeCroy, Chestnut Ridge, New York, USA) or a Picoscope (3204A, St Noets, UK). The signal was averaged fifty times and the peak to peak voltage was measured on screen and converted into acoustic pressure thanks to the calibration data provided by the hydrophone manufacturer.

In general, we did not map the whole pressure field. We solely acquired the acoustic pressure as a function of electrical power after finding the center of the focal spot. Then we measured the full width half maximum (FWHM) of the focal spot and compared it with simulations.

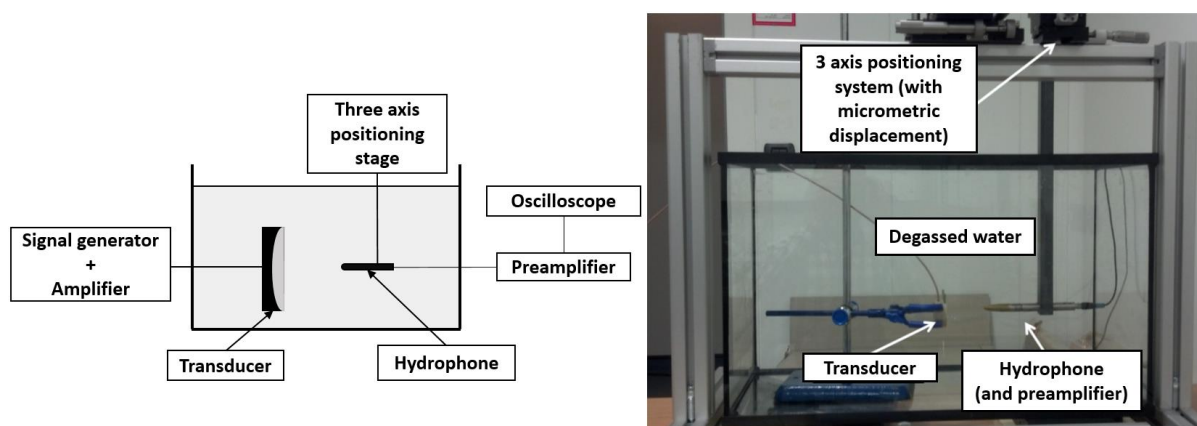


Figure 2-1: Diagram and picture of the setup for the water tank experiments

The acoustic pressure fields generated by our transducers were also simulated in 3D. My simulations were run under Matlab (Mathworks, Natick, USA) with Field II library (Jensen, 1996; Jensen and Svendsen, 1992), but I would now recommend in the future to use k-Wave (E Treeby and Cox, 2010) which runs simulations faster and allows to simulate the passage of the ultrasound through layers (like skulls). The goal of these simulations was to compare the field distribution measured in vitro with the theoretical ones. The calibrations in water tank were done with the help of Benjamin Fella. The acoustic pressure given in this manuscript is always the peak-negative-pressure (PNP).

c) Single element transducer

The first transducer I used is a concave single element transducer with a central frequency of 1.5 MHz, diameter of 25 mm and focal depth of 20 mm. This transducer is used without specific impedance matching since the real part of the natural impedance of the circuit is close from 50 ohms. The full width at half maximum of this transducer is  $1.2 \times 1.2 \times 5.8 \text{ mm}^3$  at 1.5 MHz. As described by the equations 2.1 and 2.2, the size of the focal spot depends on the frequency, it enlarges at low frequency and shrinks at high frequency. Its size becomes  $1.5 \times 1.5 \times 8.1 \text{ mm}^3$  at 1 MHz and  $0.9 \times 0.9 \times 4.5 \text{ mm}^3$  at 2 MHz. The calibration curves of the transducer are given in Figure 2-2. The size of the focal spot matches well with the simulations.

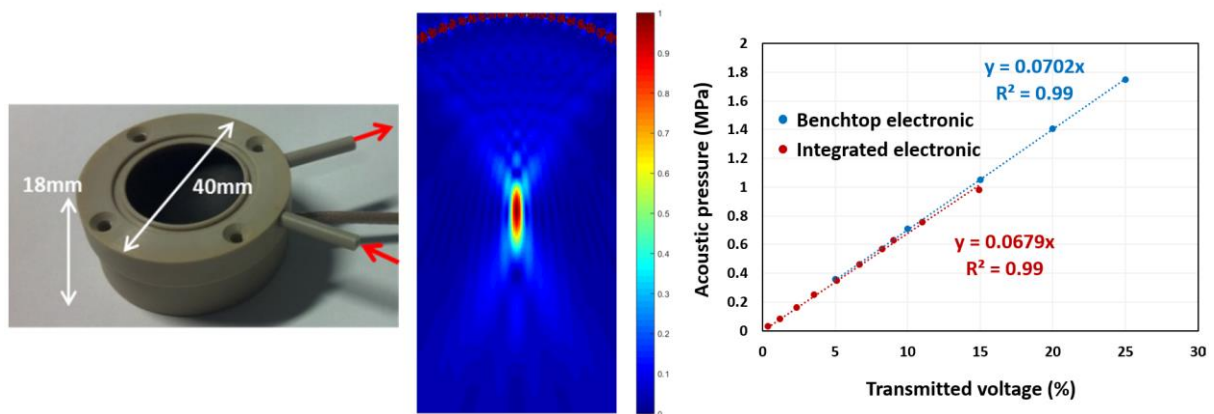


Figure 2-2: Picture of the single element transducer with its simulated normalized pressure field and the calibration curve with the two possible generators to drive it.

d) Multi element transducer

The second transducer I used is a concave multiple elements transducer array made of 8 annular concentric rings of equal surfaces, with a central frequency of 1.5 MHz, a diameter of 25 mm and focal depth of 20 mm giving an F/D number of 0.8. The 8 elements allow to steer (change the distance between the transducer and the focal spot) by applying time delays to the electrical pulses exciting the eight elements.

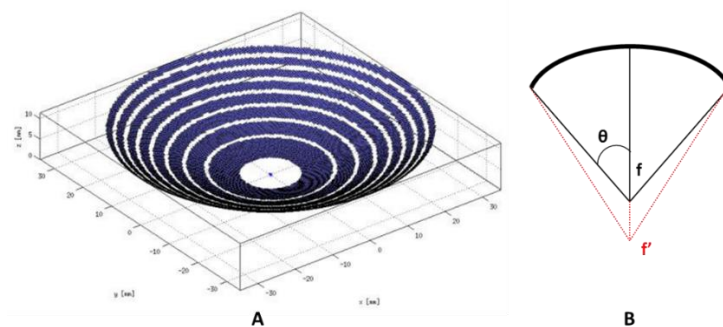


Figure 2-3: A – Simulation of the surface of an 8-element annular array transducer. B – Diagram of the electronic steering in depth of this transducer.

The calibration curve is given on Figure 2-4. Steering is often expressed as a change in the ratio  $F/D$  where  $F$  changes from  $F$  to  $F'$  with steering and the diameter  $D$  stays constant.

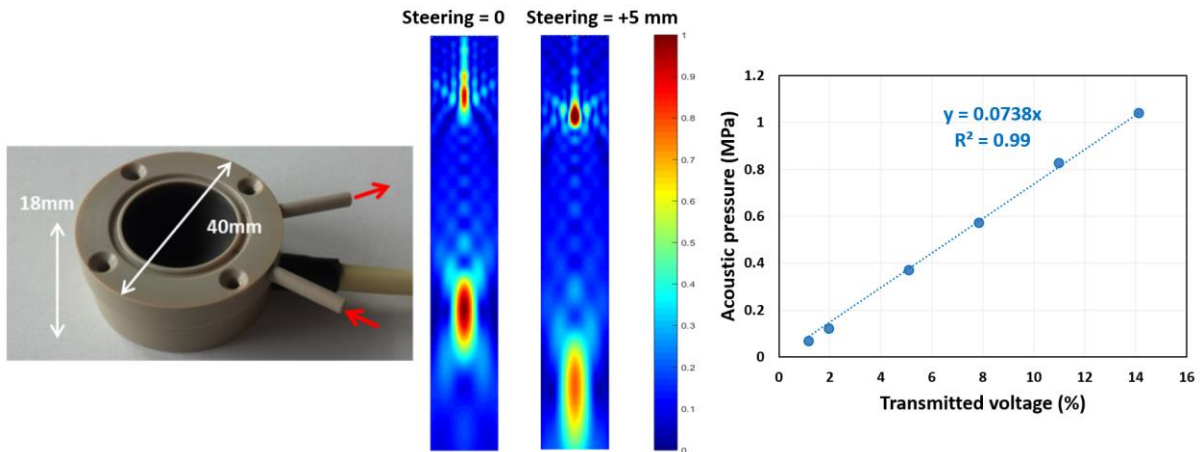


Figure 2-4: Picture of the 8-elements transducer, simulated normalized pressure fields without and with steering and the corresponding calibration curve with no steering.

As shown on Figure 2-5, steering away from the transducer ( $F/D > 0.8$ ) causes a spreading of the focal spot and a decrease of the maximum pressure (for a given transmitted power and at a given frequency). On contrary, steering toward the transducer ( $F/D < 0.8$ ) causes the focal spot to contract and the maximum pressure to increase.

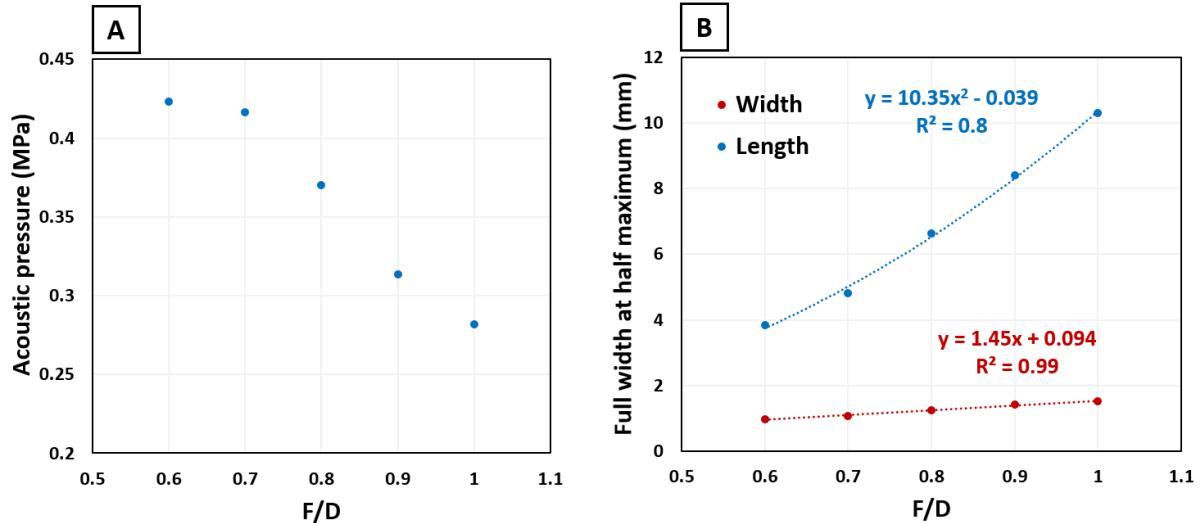


Figure 2-5: A – Pressure at the center of the focal spot as a function of steering. B – Full width at half maximum of the focal spot as a function of steering.

This steering enables to change the depth of focusing in a medium. It can also be used to adapt the shape of the focal spot. A negative steering can be selected to get a smaller focal spot and the pressure increase can be compensated by a decrease of the electrical power transmitted to the transducer.

I verified in the water tank that the steering set on the Thermoguide software provided by Image Guided Therapy corresponds exactly to the displacement of the focal spot, both with positive and negative steering.

Simulations with Field II gave the good width of the focal spot and the good relative acoustic pressure change with the steering but failed to predict the length of the focal spot. The experimental length was under estimated by approximately 15%. This can be due to a wrong simulation of the surface of the transducer, especially of the thin gaps between the rings of piezo-material, or to a wrong delay law between the individual rings (I do not know the law used by Thermoguide).

### 2.1.2. Transmission through rat skulls

As already mentioned, ensuring a good knowledge of the acoustic pressure *in vivo* is key. The beam is strongly attenuated by the skull bone. Unfortunately very little data are available about the transmission factor through rat skulls in our range of frequencies. The work presented in this section lead to a publication (Gerstenmayer et al., 2018).

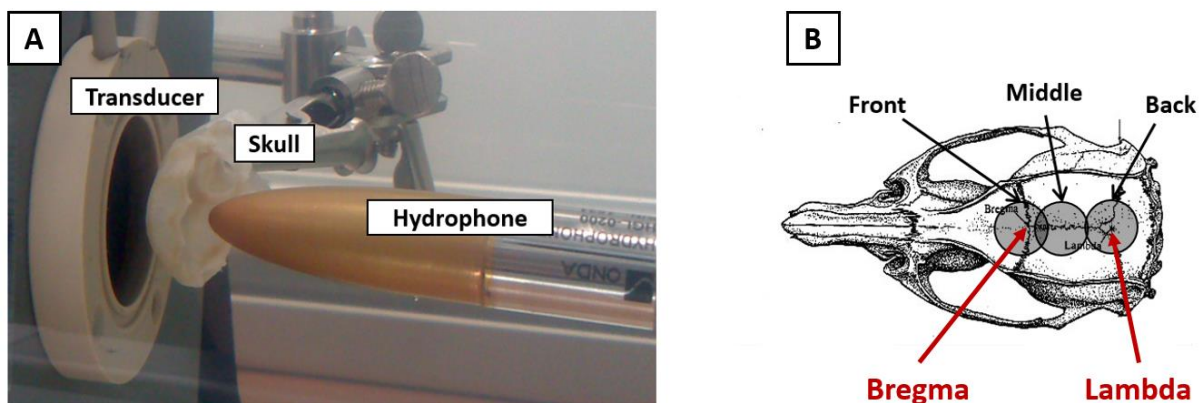


Figure 2-6: A – Set up for the measurements of the acoustic transmission in a water tank filed with deionized and degassed water. B – Surfaces of intersection of the ultrasound beam on the skull for the three different positions, for illustration purposes.

#### a) Context and methods

Knowing the peak negative pressure (PNP) through the rodent skull is not useful only in the context of my work. Indeed, for all *in vivo* transcranial applications, knowing the peak negative pressure (PNP) at the focus as precisely as possible is key to ensure both efficiency and safety of the procedures such as thermal ablation (Dervishi et al., 2013), neurostimulation (Deffieux et al., 2013), photoacoustic imaging (Lavaud et al., 2017) or passive cavitation detection (Arvanitis et al., 2016), and of course FUS-induced BBB opening. To tune up the PNP *in situ*, the first step is to calibrate the ultrasound transducer in a water tank as done in paragraph 2.1. A second and influential step is to correct for ultrasound insertion loss through the skull. The insertion loss results from the addition of several physical

phenomena induced by the presence of bone and contributing to decrease the PNP at focus: aberration (distortion and shift of the focal spot), reflections, absorption and scattering. Many new FUS developments are first performed in rodents. Due to its larger size than mouse, rat is a widely used animal model (Magnin et al., 2015; Mead et al., 2017; Yuan et al., 2016). Unfortunately, only one previous study reports on the transmission factor through rat skulls (O'Reilly et al. 2012). Here, I investigate a larger range of body mass (90 to 520g) and a different rat strain named Sprague Dawley.

### Acoustic setup

For this study I used the single element transducer driven by the Benchtop and the hydrophone. The transducer and the hydrophone were mounted on a fixed holder in the tank filled with deionized water (Figure 2-6). For all measurements, the pulses were 10 periods long with a 0.1-second of pause between two pulses. Two periods at the beginning and at the end of each pulse were excluded in order to ensure a purely monochromatic measurement. The electrical power was set to obtain 0.8 MPa PNP at focus in free water (at 1.5 MHz). The signal acquired by the hydrophone was directed to an oscilloscope (WaveRunner 44Xi, LeCroy, Chestnut Ridge, NY, USA), and the signal was an average of 50 measurements. The peak-to-peak voltage was measured on screen and converted into acoustic pressure thanks to the calibration data provided by the hydrophone manufacturer.

### Skulls

Thirteen skulls were excised from Sprague-Dawley male rats with a body mass ranging from 90 to 520 grams. After removing as much tissue as possible, the skulls were boiled in a solution of water and sodium bicarbonate and then preserved in phosphate-buffered saline with azide. Skulls were never dry stored. The skulls, mounted on a micrometric three-axis positioning stage, were placed in the water tank. The water was degassed for 15 min prior to any measurement. The degassing system was provided by Image Guided Therapy. They were placed so that the focal spot of the ultrasound beam was approximately 5 mm under the skull, in order to mimic a realistic in vivo experiment with this transducer. The skulls were visually oriented with a normal incidence. The whole cone of the ultrasound beam intersected the skull for all measurements. The distance between the transducer center and skull surface was kept constant for all measurements ( $16 \pm 1$  mm), which made the beam cross the skull over a circular surface of  $6 \pm 1$  mm in diameter.

### Transmission measurements

For all acoustic measurements through skulls, the hydrophone was moved on the three axes to find the maximum pressure. It is to be noted that this location was never found to be farther than 0.1 mm from its location without the skull, which means that aberration is negligible. The transmission factor was then defined as the ratio:

$$\tau = P_{skull}/P_{free} \quad (2.3)$$

where  $P_{skull}$  is the acoustic pressure at the focus through the skull and  $P_{free}$  the acoustic pressure at focus in free water. The voltage in output of the hydrophone was proportional to the acoustic pressure, and the transmission factor was directly calculated by obtaining the ratio of the voltages.

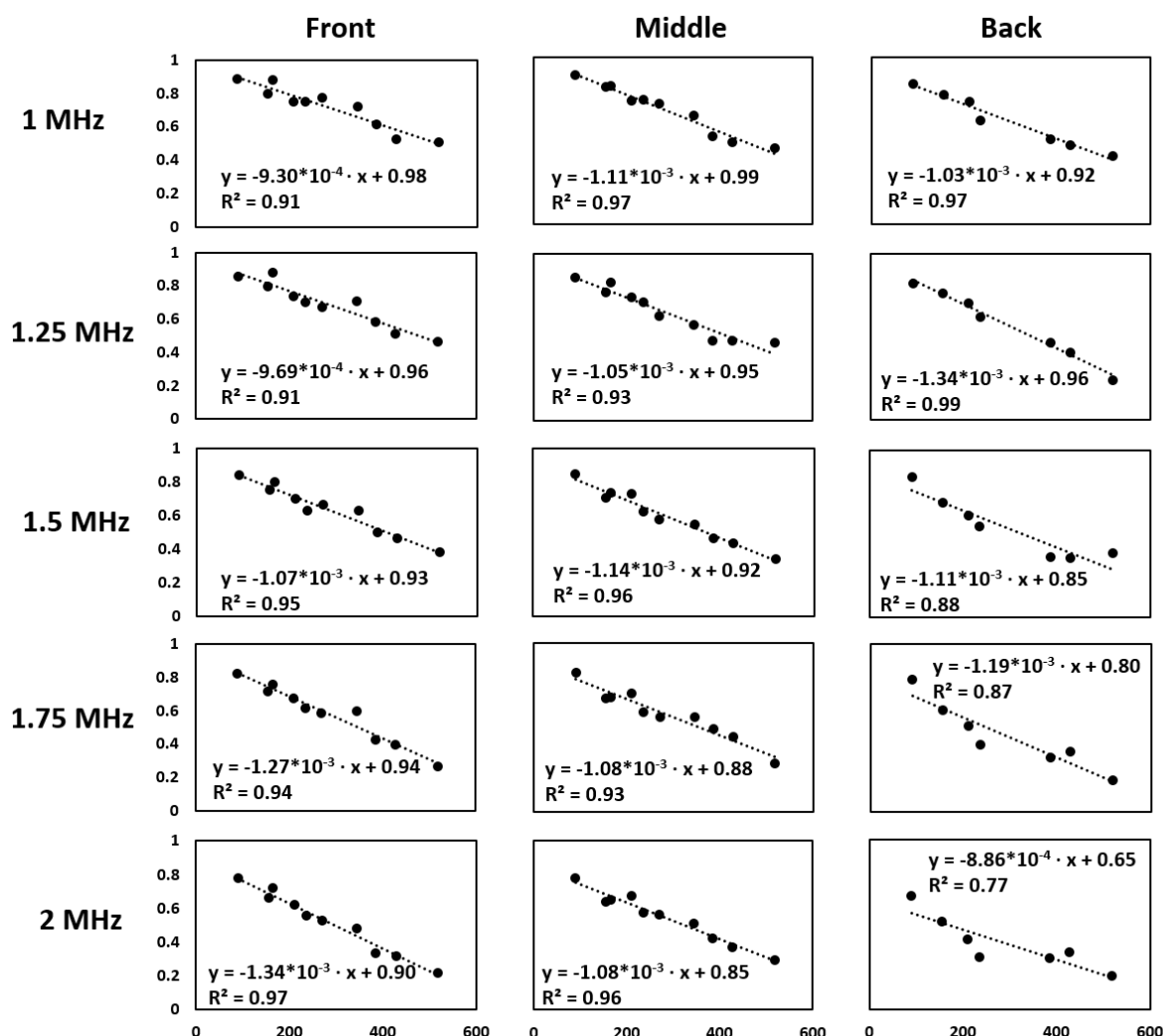


Figure 2-7: Transmission factor as a function of the body mass (g) for the five frequencies (1, 1.25, 1.5, 1.75 and 2 MHz) and the three positions (front, middle, back). A linear regression and its equation are given for each graph.

In the first experiment, three transmission measurements were done on 10 skulls at three different positions along the interhemispheric line: front, middle, and back, as shown in Figure 2-6. The front position corresponds to the striatum, often used in diffusion experiments after ultrasound-induced the blood-brain barrier opening (Magnin et al., 2015) or to implant tumors for ultrasound treatments (Sun et al., 2017). The middle position corresponds to the hippocampus, a common target in studies on Alzheimer's disease models (Burgess et al. 2014). The back position corresponds to the cerebellum, an interesting region often used as a reference. Three skulls were missing the back part (behind lambda), lost during the extraction of the skull. Five frequencies were studied (1 MHz, 1.25 MHz, 1.5 MHz, 1.75 MHz, 2 MHz). After the transmission measurements, the skulls were carefully cut at the three positions (front, middle, and back) to measure their thicknesses with a caliper. Two

measurements were done and averaged per position, one on each hemisphere. Unfortunately, one skull could not be measured in thickness and two others could not be measured at the back position. This results in thickness measurements for nine, nine, and four skulls at the front, middle, and back positions, respectively.

In a second experiment, the transmission factors of the left hemisphere of three additional skulls were mapped by translating the skulls millimeter by millimeter in a plane perpendicular to the axis of the transducer. These measurements were done at 1.5 MHz only. The scanning range was 7 mm in the left-right direction and 12 to 15 mm in the antero-posterior direction.

a) Transmission factor decreases with frequency and body mass

Figure 2-7 shows that the transmission factor decreases linearly with the body mass of the rats, at each frequency and at each position (front, middle, and back), the equations of the linear regressions and  $R^2$  values are displayed.

Based on this observation of linear dependency of the transmission on body mass and frequency, a bilinear regression of the data was performed at each position, following the equation:

$$\tau = a + b \cdot mass + c \cdot frequency \quad (2.4)$$

The value and 95% confidence intervals of  $a$ ,  $b$ , and  $c$  are given in Table 2-1.

*Table 2-1 Bilinear analysis of the transmission factor  $\tau$  as a function of the body mass of the animals (in grams) and the frequency (in MHz). Values of the parameters of the model and their confidence interval at 95%*

$\tau = a + b \cdot mass(g) + c \cdot frequency (MHz)$	<b>Position</b>		
	<b>Front</b>	<b>Middle</b>	<b>Back</b>
<b>a</b>	$1.238 \pm 0.058$	$1.134 \pm 0.046$	$1.195 \pm 0.094$
<b>b (x1000)</b>	$-1.107 \pm 0.088$	$-1.092 \pm 0.073$	$-1.166 \pm 0.135$
<b>c</b>	$-0.1989 \pm 0.0336$	$-0.1425 \pm 0.0264$	$-0.2318 \pm 0.0557$
<b><math>R^2</math></b>	<b>0.94</b>	<b>0.96</b>	<b>0.92</b>

As shown in Figure 2-8, when averaging on the three positions and body mass, the transmission factors decrease linearly ( $R^2 = 0.99$ ) with the frequency.

The spreading of the focal spot was measured on a 280-g rat for the middle position. The width of the focal spot behind the skull was 1.55, 1.24, and 0.95 mm at 1, 1.5, and 2 MHz, compared with 1.46,

1.23, and 0.91 mm without the skull. The length of the focal spot behind the skull was 8.28, 5.73, and 4.95 mm at 1, 1.5, and 2 MHz, compared with 8.15, 5.85, and 4.53 mm without the skull.

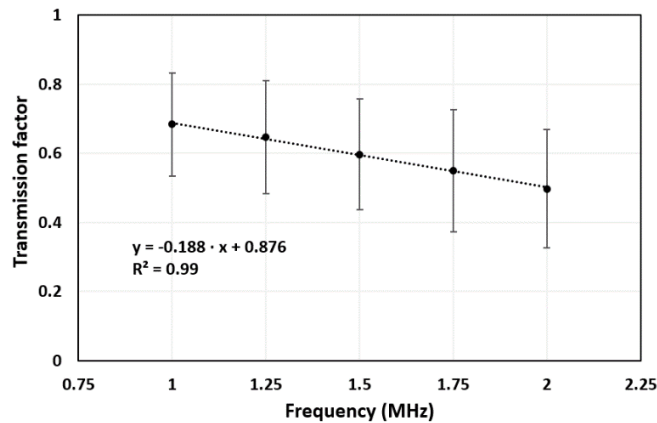


Figure 2-8: Transmission factor as a function of the frequency (MHz). For each frequency, an averaged (the mean±s.d. are displayed) transmission factor on all the skulls and all the three positions is calculated.

b) Correlation with skull thickness

After cutting the skulls, the measurements of their thicknesses with a caliper are shown in the plot of Figure 2-9 A. It appears that the skull thickness, at each position, is proportional to the body mass. The skull thicknesses at the front and middle positions are very alike in both their absolute value and in their dependency on body mass, unlike the thickness at the back, which is higher and increases faster with increasing body mass.

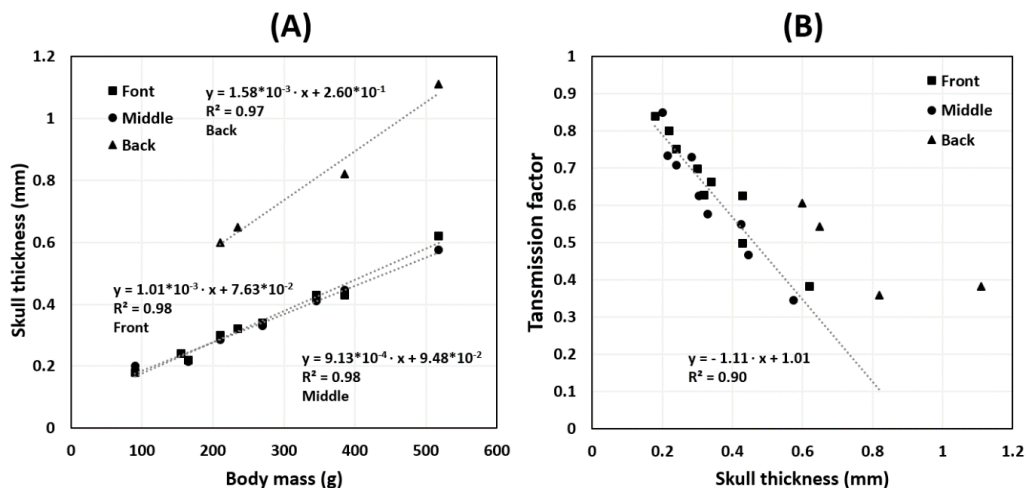


Figure 2-9: A – The skull thickness at the three positions as a function of the body mass of the animals. Linear regressions and their equations are shown for each position. B – Transmission factor as a function of the skull thickness for all the skulls and all the positions, at 1.5 MHz. A linear regression for the “front” and “middle” position and its equation is shown.

Figure 2-9 B shows the transmission factor as a function of skull thickness for 1.5 MHz and its linear regression for the front and middle position. The linear regression includes only those two positions because measurements at the back seem to follow a different law. On the linear regression, it can be seen that the transmission factor tends to be 1 when the skull thickness tends to be 0, as expected.

c) Spatial variation of the transmission factor

As shown in Figure 2-10, the transmission factor also strongly depends on the intersected region of skull. In accordance with the above data displayed in Figure 2-7, the overall transmission factor is higher for the 180-g and 240-g skulls than for the 320-g skull. When moving left-right from the central suture to the sides of the skull, the transmission factor decreases fast from 68%, 64%, and 59% to 43%, 41%, and 30% for the 180-g, 240-g, and 320-g skulls, respectively. This lateral decrease is hypothesized to come mainly from the beam incidence angle that becomes less orthogonal to the skull surface, increasing reflection and so insertion loss, rather than from skull thickness variations. The transmission factor also decreases continuously when moving toward the back of the skull, such as in previous measurements done at three discrete positions. The transmission factor decreases from 68%, 64%, and 59% to 48%, 49%, and 38%, respectively, for the three measured skulls when moving toward the back of the skulls.

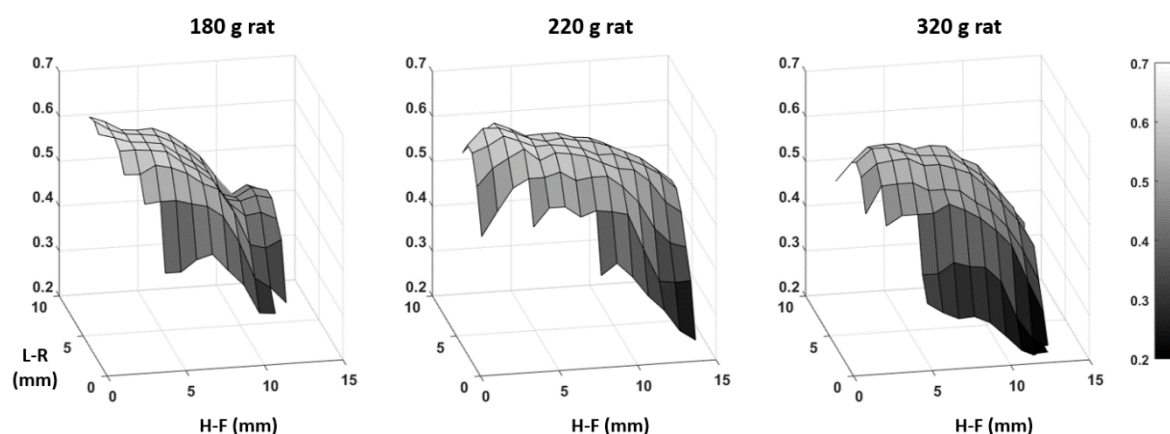


Figure 2-10: Transmission factor at 1.5 MHz as a function of the position of the skull between the transducer and the hydrophone. From the left to the right of each surface the skulls are mapped in the antero-posterior direction, starting from the “front” position. From the top to the bottom of each surface the skulls are mapped in the Left-Right direction, starting from the middle suture.

d) The different components of the insertion loss: aberration, attenuation and impedance mismatch

Skull aberration could explain part of the insertion loss as it can spread the focal spot behind the skull. No direct measurement of the phase was done. Nevertheless, few measurements suggest that aberration was not a main component of the insertion loss. As already mentioned, the location of the maximum pressure behind the skull was never found to be farther than 0.1 mm away from its location

without the skull and, the spreading of the focal spot behind the skull was small. Thus, both the displacement and the spreading of the focal spot remained very limited. This agrees with the finding reported by *O'Reilly et al.*. Indeed, they measured a severe phase change at only 2.53 MHz and not up to 2 MHz and for “thicker animal skulls.” In their study, the skull thicknesses ranged from 0.5 to 1 mm, whereas the thicknesses in our study were always less than 0.5 mm for the front and middle positions. However, this may explain why at 2 MHz and for the back position, where the wavelength is closer to skull thickness (the shorter wavelength used was 1.45 mm at 2 MHz, with a speed of sound of 2900 m/s in bones, as reported by Fry et al. in 1978, and the thicker skull portion is 1.06 mm at the back position), the correlation between body mass and transmission factor is the poorest ( $R^2 = 0.77$ ). In this case, aberration might be non-negligible and deteriorate the relationship between body mass and transmission factor.

Attenuation and reflections are the two main components of the insertion loss, the aberrations being negligible. Given the reported attenuation values for bone,  $\alpha = 6.9$  dB/cm/MHz (Culjat et al., 2010), we calculated skull insertion losses due to attenuation for all our specimens at 1.5 MHz following the equation (Cobbold, 2007):

$$P = P_0 e^{-\alpha x} \quad (2.5)$$

where  $P_0$  is the acoustic pressure before the skull,  $P$  the acoustic pressure after the skull, and  $x$  the thickness of the skull. For all skull thicknesses, the part of insertion loss that can be attributed to attenuation remains low, between 10% and 20%. The remaining part of the measured insertion loss (80% to 90%) is expected to come from the impedance mismatch at the water-skull interface.

#### e) Other transmission factor measurements

Less extensively, I also measured in the same way the acoustic transmission factors through old C57BL/6 mice and one-year old adult Fisher rats. I did these complementary measurements because these strains and ages were the one I will use in the work reported in Chapter 5. The materials and methods use for those calibrations are the same as the ones used in the previous paragraphs. For mice, the transmission factors were between 75 and 80 % at the center of the skulls for several individuals ( $n=4$ ) at 1.5MHz. For rats, the transmissions factors were around 40 % at the center of the skull and decreased to 30 % on the lateral side and to 25 % on the back.

This study demonstrates a strong dependency of the acoustic transmission of rat skulls upon body mass, position, and frequency in the frequency range of 1 to 2 MHz. These data are particularly useful for therapeutic applications of transcranial ultrasound. Indeed, an accurate knowledge of PNP is critical for most of these applications. For instance, it was proved by several groups that efficient and safe blood-brain barrier opening could be obtained in rats using only a narrow range of *in situ* focal pressure, typically 0.3 to 0.5 MPa at 1.5 MHz (Kobus et al., 2015). Below this range, no opening is observed since circulating microbubbles do not cavitate strongly enough, whereas above this range, inertial cavitation can be detected, resulting in permanent damage.

Such a data set will help calibrate the ultrasound beam *in vivo* at first order. However, several experimental variables that cannot always be precisely controlled *in vivo* could strongly affect this

calibration. Mainly, one should care about acoustic coupling (bubble trapping), beam incidence angle at the skull surface, and multiple reflections in the whole skull cavity. To confirm the true *in situ* acoustic pressure and, if needed, to adjust it further, one should also rely on indirect *in situ* measurements during the *in vivo* intervention. For instance, under MRI guidance, acoustic radiation force imaging (Larrat et al. 2010) can be used as an independent measurement of the acoustic intensity right before the intervention. Then, during FUS therapy, other indirect monitoring techniques, such as MR thermometry (Larrat et al. 2010) and passive cavitation detection (Arvanitis et al., 2016) can be used in a feedback loop to adjust acoustic power on the fly.

### 2.1.3. *In vivo* estimation of the transmission factor with MR-ARFI

Estimating the transmission factor from *ex vivo* measurement is already helpful, but measuring it *in vivo* would be even more convenient. Indeed, it would allow to sonicate the tissue with an *in situ* controlled pressure. The MR-ARFI sequence introduced in Chapter 1 is sensitive to the displacement of the tissue induced by the radiation force which is itself proportional to the intensity of the ultrasound that is to say to the square of the pressure. In this study, I tried to develop a pipeline to estimate the transmission factor from an *in vivo* MR-ARFI image. The idea is to simulate the MR-ARFI signal from the simulated pressure field of the transducer and the local viscoelastic properties of the brain and to compare it to the experimental *in vivo* MR-ARFI signal. The difference between the simulated MR-ARFI signal and the experimental MR-ARFI signal is hypothesized to come from the transmission of the ultrasound through the rats' skull, thus giving an estimation of this transmission factor (see figure 2-21). These MR-ARFI acquisition were performed with the help of Benjamin Fellah.

#### a) MR-ARFI mapping

Two Fisher rats (males, 250 grams) were head shaved, anesthetized with isoflurane (2%) in a mixture of air and oxygen (50% ratio) and placed on the bed in the MR scanner. The 8-elements transducer, mounted on our 2 axis MR compatible motor stages, was placed over the head of the animals. The transducer was moved on a 7 mm x 5 mm grid with steps of 1 mm over the left hemispheres, as shown on Figure 2-12 F. MR-ARFI images were acquired for each position of the transducer with the following parameters : 4 ms pulses synchronized on the second lobe of each MSG (frequency 125 Hz, duration 4 ms), frequency of 1.5 MHz, matrix size 128x128x5, resolution 0.25x0.25x2 mm, strength of the encoding gradients 80 % of maximum strength (the maximum strength of the gradients is 740 MT/m), electrical voltage transmitted at 100 % of the maximum amplitude for the 8 channels. MR-ARFI images without ultrasound were also acquired for each location to serve as reference images. Figure 2-11 shows three typical MR-ARFI images in a horizontal brain slice (red arrows point the focal spot of the ultrasound beam) for three different positions of the transducer.

The pipeline to properly calculate the phase of each MR-ARFI image is explained on Figure 2-12. A mask of the brain is computed from the magnitude image (A). Both MR-ARFI phase images with ultrasound ON and OFF are masked. The OFF image is subtracted from the ON image (B). The focal spot is segmented out (C). The remaining spatial fluctuations of phase are fitted with a 2D polynomial

fit of the 5<sup>th</sup> order with a Matlab function (D). Finally, this best fit is subtracted from the image (B) which gives an estimation of the acoustic intensity weighted image (E).

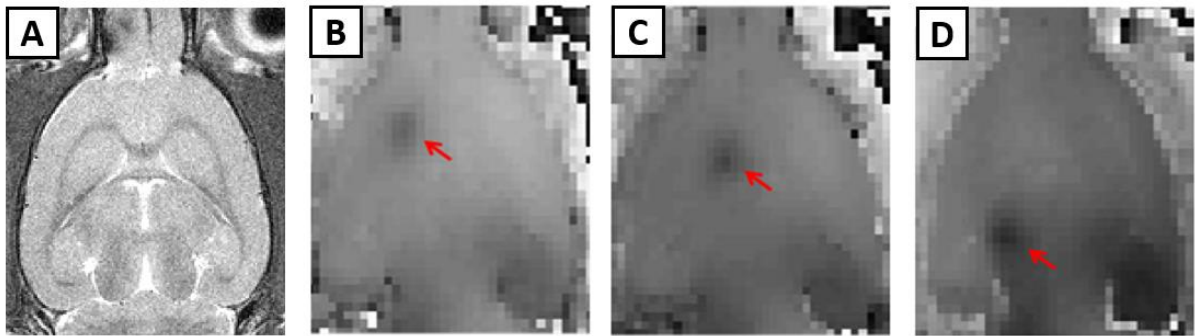


Figure 2-11: A –  $T_2$ -weighted image. B,C and D - Three MR-ARFI images (phase images) on for different position of the transducer. Red arrows point to the focal spot of the ultrasound beam.

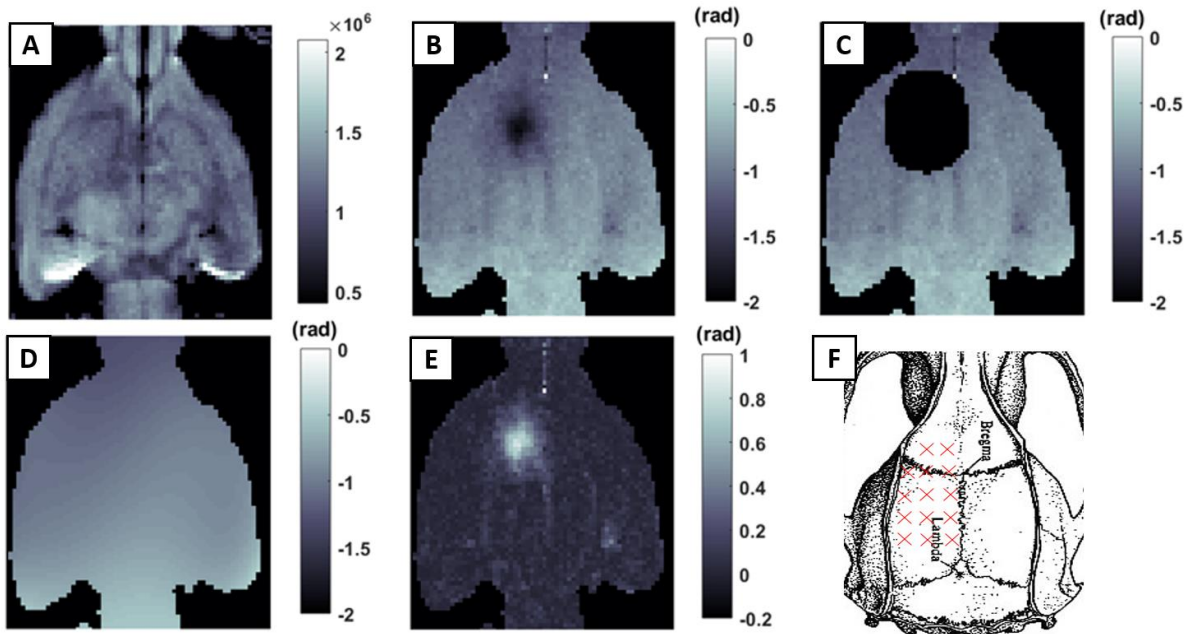


Figure 2-12: Pipeline for the phase processing: mask on the magnitude image (A), subtraction of the reference phase (B), segmentation out of the focal spot (C), fitting of the background variation (D) and subtraction of those variation (E). F – Representation of the grid on which the transducer was moved.

This pipeline gives a robust way to clear MR-ARFI images from background variations of the phase and so to be able to quantitatively compare the different ARFI spots. The same post-processing pipeline will also be used in the paragraph 2.3.1 of this Chapter.

b) Simulation of the viscoelastic response of the brain

The experimental phase obtained with the MR-ARFI mapping was compared to a simulated phase in order to estimate the transmission factor through the skull. First, the normalized pressure field of the transducer was simulated with Field II as already explained. This pressure map was made quantitative by multiplying it by the focal pressure measured in the water tank. Then, the ultrasound radiation force is computed from the equation given on Figure 2-14 (Bercoff et al., 2004b; Sarvazyan et al., 1998). This force is proportional to the square of the pressure. Here, we introduce the transmission factor through the skull  $\tau$ . It is first set at 100 % which is a perfect transmission. For each animal, a  $T_2$ -weighted anatomical image was acquired before the ARFI mapping. This image was aligned on an atlas with the Statistical Parametric Mapping (SPM, <https://www.fil.ion.ucl.ac.uk/spm/>) software to segment the cerebro-spinal fluid (CSF), the gray matter and the white matter. The displacement of tissue induced by the radiation force depends on the shear wave speed ( $v_{shear}$ ) of this tissue at the frequencies of mechanical excitation of the tissue (in our case given by the Fourier transform of a 4ms long square pulse so typically around 250 Hz). Indeed, the same MR-ARFI signal at focus can be induced by different sets of parameters (pressure, shear wave speed) as illustrated on Figure 2-13. White matter, which is stiffer than gray matter, has a higher shear wave speed than gray matter (Larrat et al., 2007). Thus, the same radiation force induces a higher displacement in the softer gray matter (and so a stronger MR-ARFI signal) than in the harder gray matter. The chosen values of  $v_{shear}$  are the following: gray matter 3 m/s, white matter 5m/s, CSF 0.5 m/s (Mace et al., 2011).

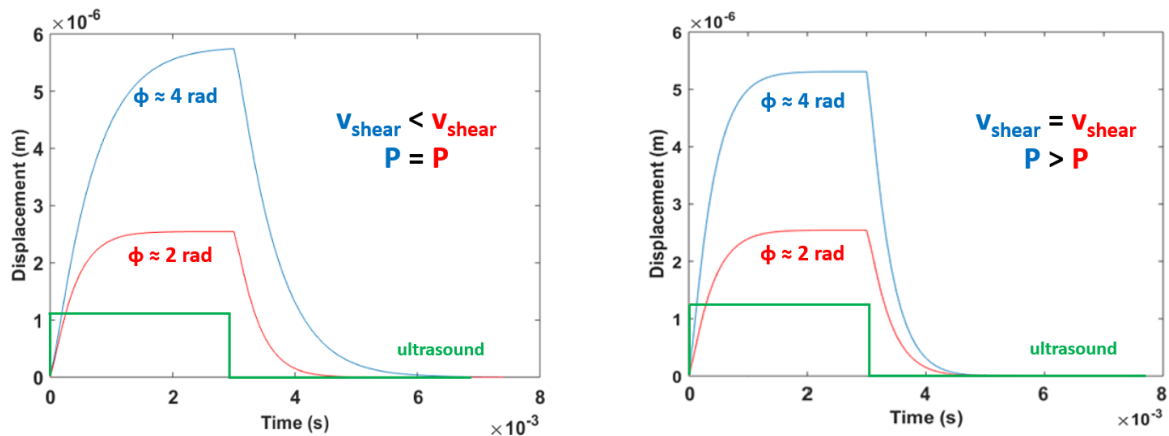


Figure 2-13: The displacement of the tissue depends on the pressure but also on the shear wave speed of the tissue. The same displacement can be reached for different values or the pair pressure/shear wave speed.

For the three brain compartments, the speed of sound was chosen constant at 1540 m/s. The tissue displacement at focus is simulated from the viscoelastic Green's function as a solution of the system of equations published in *J Bercoff* paper and PhD manuscript (Bercoff et al., 2004b). Once the displacement  $\vec{u}$  is simulated, the phase of the ARFI image  $\phi_{simu}$  is simulated according to the equation on Figure 2-14. This phase depends on the shape and strength of the motion encoding gradients of the MR sequence.  $\phi_{simu}$  is compared to the experimental phase  $\phi_{exp}$ . If the simulated phase is higher

than the experimental one, this means that the ultrasound push is overestimated and thus the transmission factor underestimated. The value of the transmission factor is iteratively tuned (decreased with steps of 0.01) until the simulated phase becomes just smaller than the experimental phase.

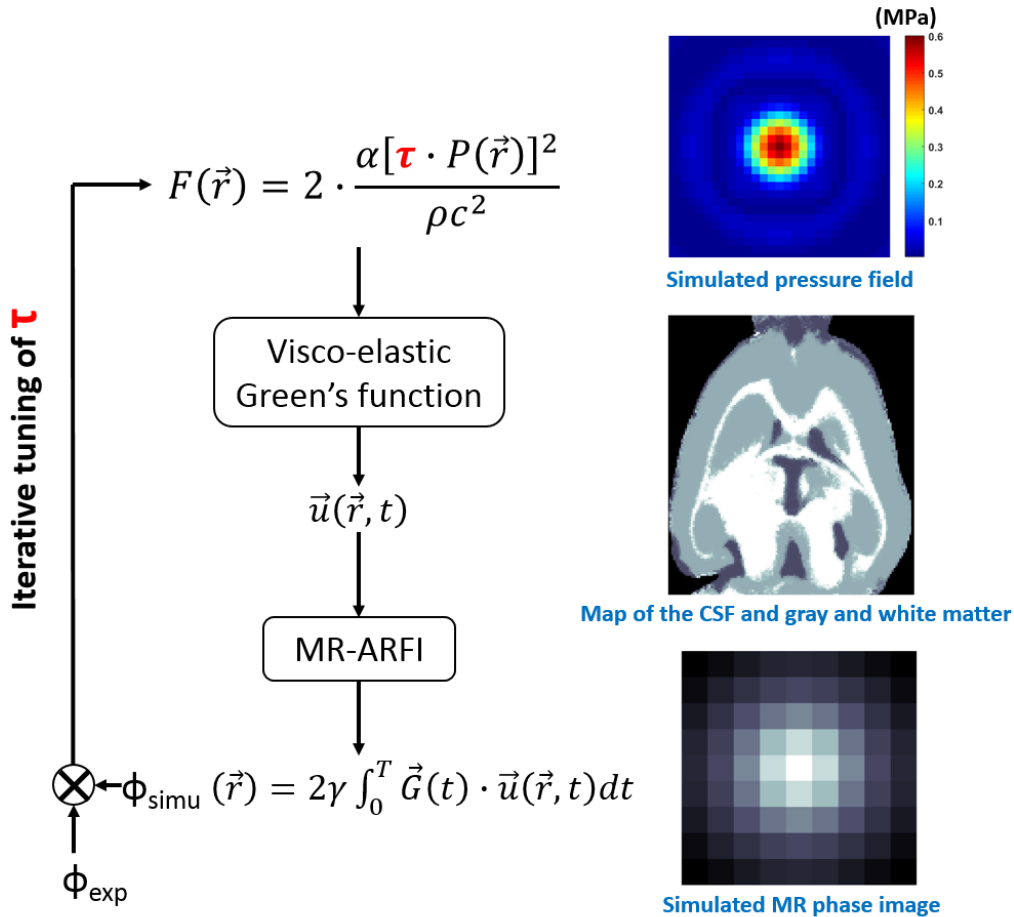


Figure 2-14: Loop for the iterative tuning of the transmission factor  $\tau$ . The tissue displacement  $\vec{u}$  is simulated from the acoustic pressure (estimation with the calibration) through the radiation force  $F$  and the Green's functions. A map of CSF, gray and white matter is given in input for the simulation of the displacement. Then the encoding by the gradients is simulated to give a simulated phase  $\phi_{simu}$  which is compared to the experimental phase  $\phi_{exp}$ .

c) Acoustic transmission mapping

For each position of the transducer, the pipeline described on Figure 2-12 is applied to the MR-ARFI signal and an estimation of the transmission factor is computed from the viscoelastic response of the brain. The Figure 2-15 B shows an example of the transmission map obtained from the MR-ARFI mapping. After MR-ARFI mapping the rats were sacrificed and the acoustic transmission factors were measured in a water tank (C) as described in the paragraph a). This gold standard technique gives us our reference measurement for  $\tau$ . Qualitatively, the spatial distribution of the MR-ARFI based transmission map is similar to the one measured in vitro, decreasing on the sides and toward the front

of the head. The range of the grid of the MR-ARFI mapping was not sufficient to measure the decrease on the back. The transmission estimated with MR-ARFI is in the same order of magnitude as the transmission measured in water tank but is far less precise. Indeed, this technique suffers from several limitations.

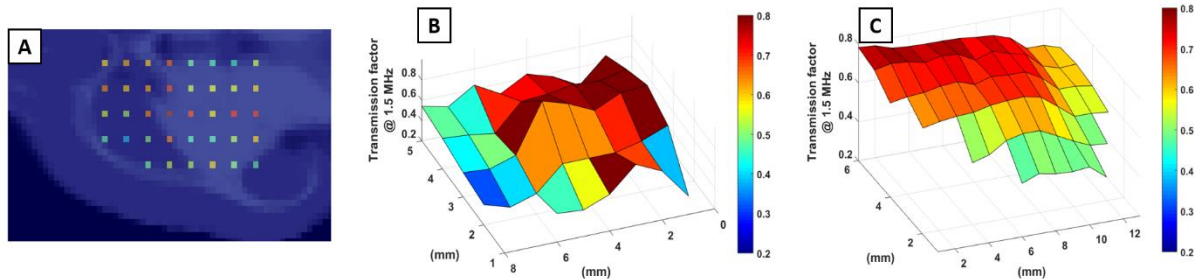


Figure 2-15: A – Overlay of the maximum phase of the MR-ARFI image on the CSF, gray/white matter segmentation. B – Transmission map obtained from the MR-ARFI mapping. C – Transmission map obtained from the water tank measurements.

First, experimental conditions such as the coupling between the transducer and the head, the tune and match of the MRI coil, the shim of the MR scanner (affecting the signal to noise ratio of the MR-ARFI phase), the blood pressure of the animal, can change during the experiment which lasted quite long, typically more than one hour. The head of the animal may be not perfectly aligned with the transducer and so incidence angle can change when moving the transducer.

The second limitation comes from the simulation of the viscoelastic response. Indeed, the simulation of the displacement strongly depends on the value chosen for the shear wave speed but values vary a lot in the literature, especially depending on the shear wave frequency. Moreover, the segmentation based on the  $T_2$ -weighted image is not really clean and it is difficult to take into account the fact that the region of the focal spot never fully contains one kind of tissue but partly contains gray and white matter.

It is to be noted that only the phase signals at focus were compared in this iterative algorithm, not the shape of the simulated/experimental MR-ARFI. In the future, this could improve the technique by allowing the joint fit of multiple unknowns such as  $\tau$  and  $v_{\text{shear}}$ .

To summarize, the experimental part is working and it was the opportunity to develop a useful pipeline for MR-ARFI phase correction. Iterative simulation based determination of the transmission factor seems to be a reasonable approach. Unfortunately, MR-ARFI simulation turned out to be quite challenging, especially because the brain is made of structures with really different viscoelastic properties. During my PhD, this method was not pushed forward after this first investigational work since *ex vivo* measurements of transmission factors were sufficient to conduct my *in vivo* experiments.

## 2.2. Control of the position of the focal spot

### 2.2.1. MR-guided displacement of the transducer

#### a) Thermoguide

Our MR compatible transducers are made for performing MR-guided focused ultrasound experiments in rodents. Our experimental MR compatible setup was designed, built and validated by B. Larrat and R. Magnin during his PhD in collaboration with Image Guided Therapy (IGT). The latest version of this system is described in (Magnin et al., 2015). Briefly, it is made of an MRI bed with stereotaxic frame to place the animal under anesthesia in the MR scanner. The respiration rate and body temperature are monitored continuously. A heated air flow maintains the animal temperature during scans. A catheter is inserted in the tail vein to be able to inject microbubbles and contrast agents from outside the magnet. The head of the animal is placed in a RF coil equipped with a matching circuit that leaves space for shooting ultrasound in the animal through the MR coil. To be able to precisely position the ultrasound focal spot in the rodent's brain in 3D, the transducer holder can be moved mechanically in the xy plane by motors. In addition, axial electronic steering along z axis can be achieved when using the annular array transducer.

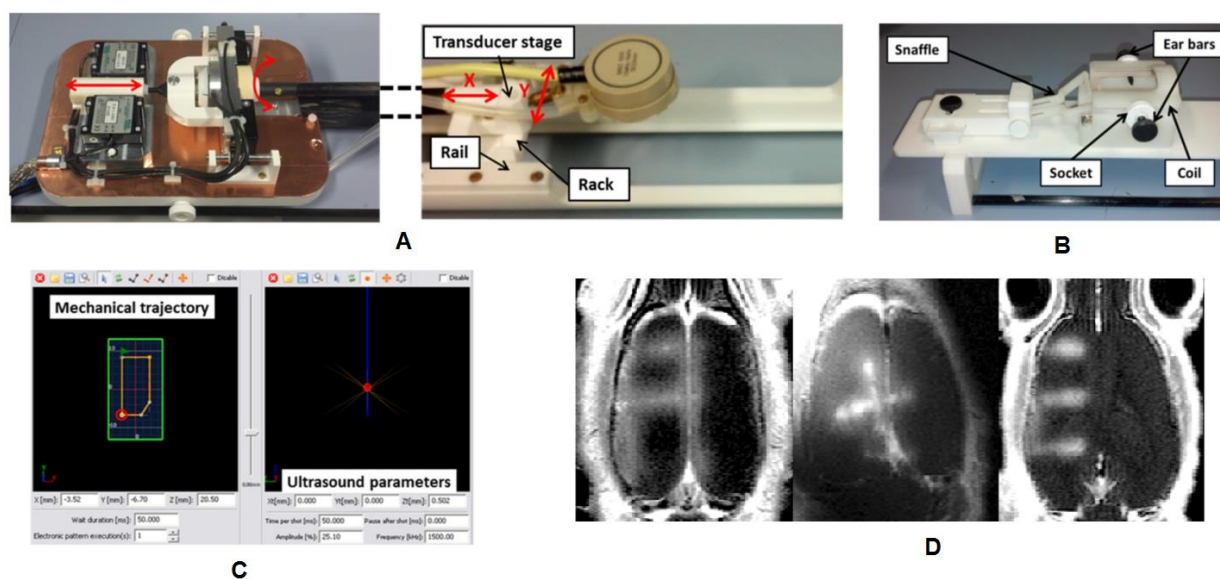


Figure 2-16: A – Motors and transducer holder to move the transducer inside the MR scanner. B – Coil and stereotaxic to maintain the head of the animal. C – Screenshot of the Thermoguide software, on the left the window to design trajectories and on the right, the window to set the ultrasound parameters. D – Examples of BBB opening along arbitrary trajectories (letters A, X and E).

The motors and the ultrasound emission are driven by the Thermoguide IGT software. This software allows to move the transducer, set the acoustic parameters (frequency, acoustic pressure, duty cycle, pause between shots, number of shots, steering distance,...) and even define complex acoustic trajectories. Trajectories can either alternate a displacement of the transducer with ultrasound shots

at fixed locations or ultrasound shots during this displacement. Figure 2-16, adapted from *Magnin et al.*, shows the setup with the piezoelectric motors and the transducer (A) that can be moved in the xy plan over the coil (B). On image D, the BBB was opened along arbitrary trajectories programmed in three different rats by moving the transducer and shooting the ultrasound at the same time.

### b) MR-guided global BBB opening in rats

In this paragraph, I tried to pursue the work of Rémi Magnin to use the above described setup in order to perform a global BBB opening (i.e. opening a large volume of the brain) under MRI guidance with the highest degree of reproducibility, safety and homogeneity within the brain. We will see what our degrees of freedom are and what the limits are.

As we saw in the introduction Chapter, MR-ARFI allows to visualize the ultrasound beam in the brain. In a classic protocol, once the initial location of the ultrasound beam in the brain is known, it is possible to move it remotely from the ultrasound console thank to the motors. Last, we acquire a second MR-ARFI to confirm the new position. This way, we can chose very precisely the position where the mechanical trajectory will start.

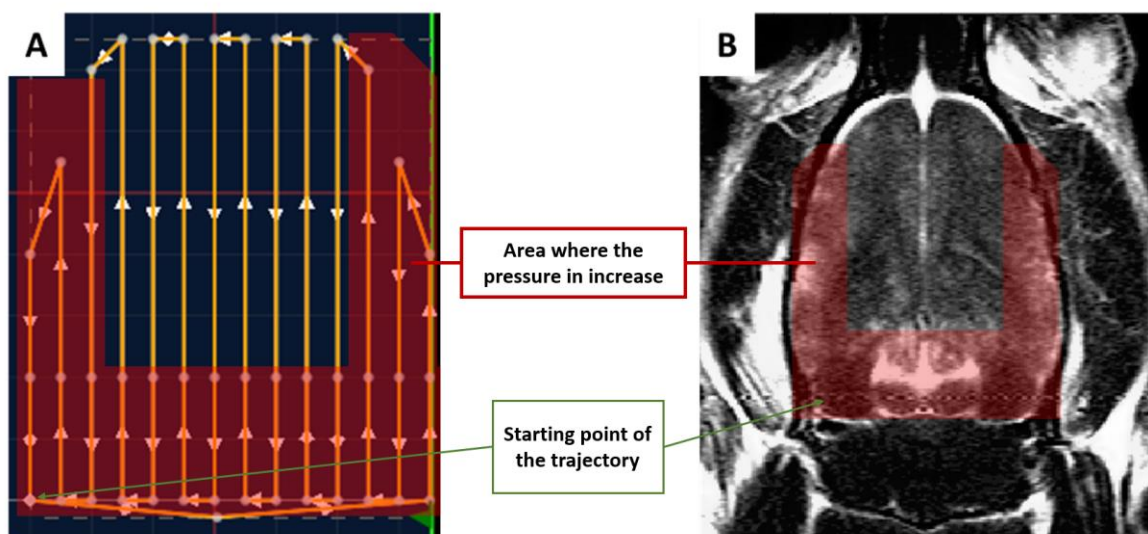


*Figure 2-17: A – Weighted trajectory, which take into account variations of transmission factor through the skull, for a global opening of the BBB. B –  $T_1$ -weighted image showing a global contrast enhancement in the brain after the gadolinium injection.*

The trajectories chosen to cover the whole brain are parallel lines distant of 1 mm (about the full width half maximum of the focal spot) as illustrated on Figure 2-17 A. As seen in the paragraph 2.1.2, the acoustic transmission factor through a skull depends on the position of the ultrasound beam in the brain. In temporal regions, the incidence angle is higher than in the center of the brain, causing more reflections and so a decrease of the acoustic transmission factor. To balance this effect, we designed a trajectory where ultrasound are shot with a higher pressure on the lateral lines. They are also shot with a higher pressure toward the back of the skull due to its higher thickness which also decreases the acoustic transmission factor. The beam intensity on the trajectory of Figure 2-17 is tuned to

sonicate at 0.6 MPa PNP in the brain. In order to have a sonication as homogenous as possible, ultrasound are shot only along the segments in the antero-posterior direction. After injection of a bolus of 200  $\mu$ L Sonovue microbubbles, this trajectory is played 30 times for a total duration of 6 min. The opening is followed by an intravenous injection of Dotarem. The  $T_1$ -weighted image (Figure 2-17 B) shows a global contrast enhancement in the brain when compared to the cerebellum, which was not sonicated.

This technique suffers from some limitations which lead to a lack of reproducibility between animals. One important factor is the coupling between the transducer and the brain. During the sonication, the displacement of the transducer air bubbles can be trapped between the skin and the latex membrane, even if a lot of care was given in coupling them well with acoustic gel at the beginning of the experiment. Another factor is the position of the head of the animal in the stereotaxic frame. If the head is tilted (front-back or left-right or both) some parts of the skulls will receive the ultrasound with a normal incidence ( $0^\circ$  incidence angle) and others with a high incidence angle, leading to spatial variability in the transmission factor that are not accounting for in the trajectory. Finally, an important problem is the lifetime of the microbubbles in blood. This lifetime is not well known in rodents but under this kind of sonications it is expected to be short (around one minute) (Kamimura et al., 2018). If it is so, the first repetitions of the trajectory are the only ones that matter. There is a tradeoff between the spatial extent of the trajectory, the density of sonicated lines and the sonication time of each region of the brain (effective duty cycle). This depends also on the performances of the motors that are currently limited to a maximum speed of 1cm/s. For trajectories with more segments, each segment is played fewer times and it can happen that the opening is not homogeneous but stronger where the trajectory starts. To prevent this, I tried to infuse the microbubbles during the first 30 seconds of the opening. Figure 2-18 shows two examples of the same trajectory on two different rats. The first received a bolus injection and the second an infusion of the microbubbles. The contrast enhancement on the  $T_1$ -weighted is stronger when microbubbles are infused but this remains hard to do in practice since Sonovue microbubbles have a poor stability.

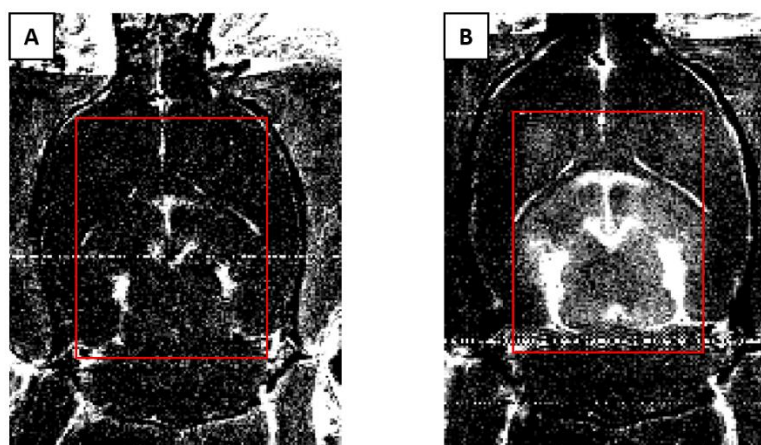


Figure 2-18: A – Example of a global BBB opening with a bolus injection. B – Example of a global BBB opening with infusion of the microbubbles

Nevertheless, this technique is very innovative as, to our knowledge, only McDannold's group performed global opening in rats quite recently (Mcdannold et al., 2018). To do so, they used the costly clinical ExAblate Neuro (InSightec, Haifa, Israel) setup. Our setup is specifically designed for rats and can fit in preclinical high magnetic field scanners, which makes it more relevant for this application. And even if this protocol is difficult, being aware of the critical steps allows to carefully install the animals and so to have reach sufficient reproducibility.

## 2.2.2. Motorized trajectories outside the MR scanner

### a) Motorized positioning system

The motivation to develop a global BBB opening trajectory that is not MR-guided is to highly reduce the time needed to open the BBB per animal and thus to allow treat large cohorts in reasonable times (as in the protocols in Chapter 5).

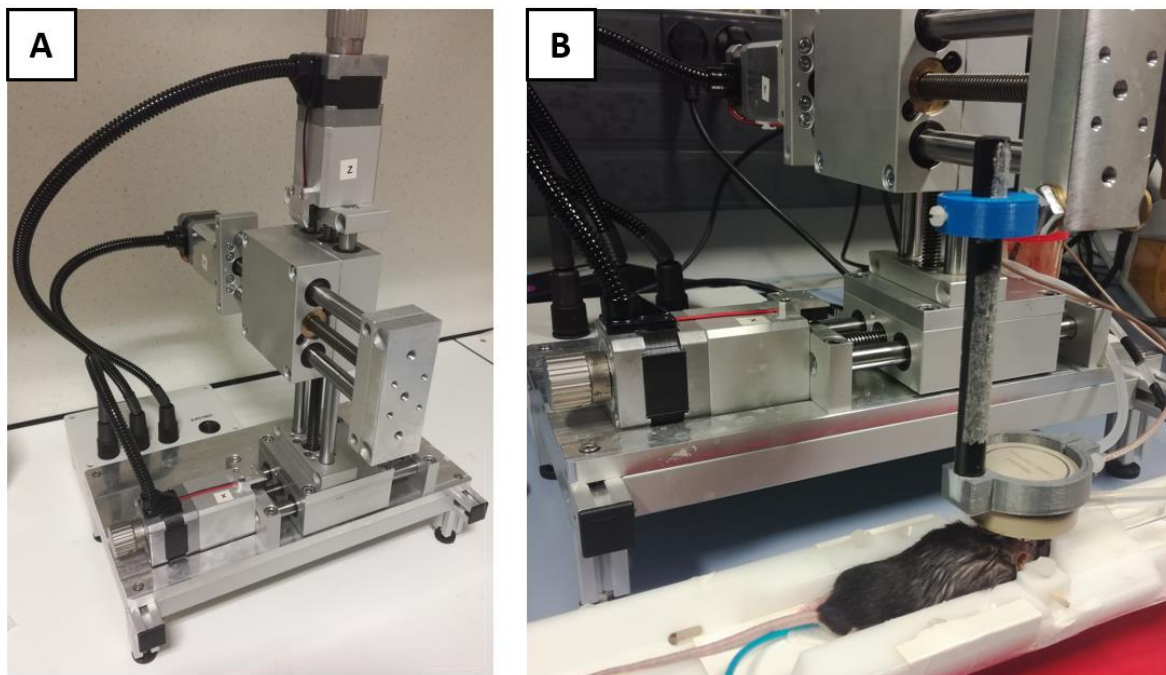


Figure 2-19: A – The motorized positioning system. B – In vivo use of the motorized system. A single element transducer is mounted on the system for global BBB opening on mice.

The system on Figure 2-19 A is a 3-axis positioning stage where each axis is motorized. The motors are driven by an Arduino system with a USB connection which can be driven either from Python or Matlab with a dedicated DLL or directly from the graphical interface of the Benchtop IGT generator. Both methods allow to move the stage and to program mechanical trajectories which can be repeated any number of times. In my PhD, this system was sometimes used for transducer calibration instead of the manual stage already introduced for skull transmission measurements. In this case, the stage is placed in front of a small dedicated water tank that includes a transducer holder and the hydrophone is mounted on the stage to scan the field. This 3D stage was also used to move a transducer on top of animal heads for *in vivo* experiments. In this case, the transducer is mounted on the stage thank to a

homemade 3D printed holder as illustrated on Figure 1-19 B. The stage is placed in front of the animal bed.

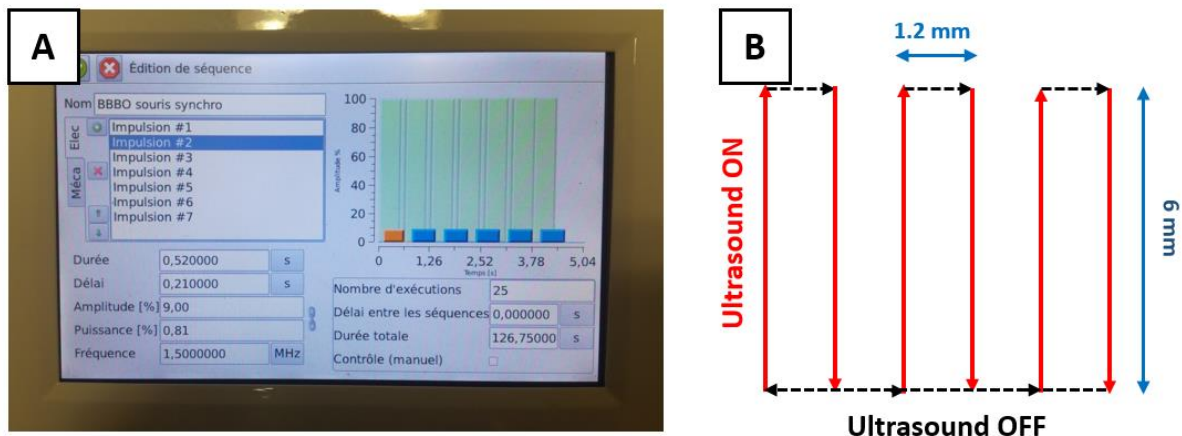


Figure 2-20: A – Control screen of the Benchtop. Ultrasound pulses (acoustic pressure, frequency, duty cycle) and mechanical displacements can be parameters. B – Schematic representation of the trajectory for the global BB opening on mice. Ultrasound are shot (continuous waves) along the vertical lines and turned off when the transducer changes line.

#### b) Validation and safety of a global BBB opening protocol in mice

A trajectory was designed in order to achieve global opening in mice. The single element transducer was mounted on the motorized positioning stage moved over the head of the animals while shooting the ultrasound to sonicate a large volume of the brain. A first approach was to control on one side the motorized stage from a Python script running on a computer and on the other side, separately, the transducer from the graphical interface of the benchtop generator. The trajectory is shown on Figure 2-20 B. The limit of this approach is that displacements and ultrasound shots are asynchronous. Indeed, ultrasound are shot all along the trajectory, leading to overshooting at locations where the transducer stops to change direction or on the way back to the start of the trajectory. The second and current approach is to control everything from the graphical interface of the benchtop generator. This was not feasible at first but with its latest upgrade from IGT, it became possible to control both ultrasound emissions and the stage displacement. As shown on Figure 2-20 A, displacements can be programmed during sonications. As seen previously, Thermoguide and the MR-compatible generator handles well the time synchrony between displacements and shots. On contrary with the benchtop system, they are still not well synchronized one with the other: the mechanical and electronic trajectories start at the same time, but small timing errors accumulate during the execution of the trajectory resulting in a growing time shift. I had to manually adjust the delays between the shots so that ultrasound are only shot during the long displacements (in red). To do so, I visualized the sonication in a water tank with an acoustic fountain setup. The trajectory was chosen to be  $6 \times 6 \text{ mm}^2$  large to give each point of the volume a sufficient sonication time during the lifetime of the microbubbles.

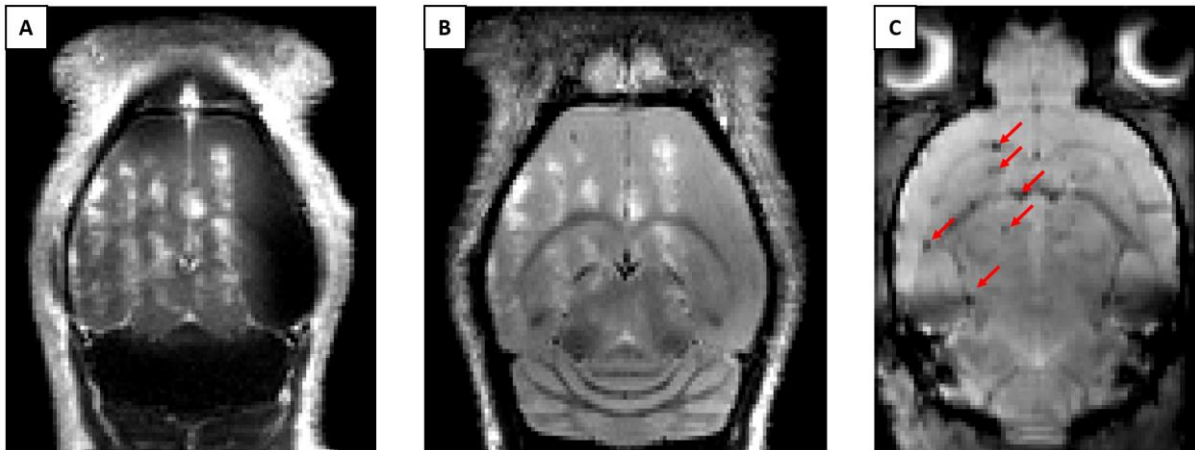


Figure 2-21: Example of a global BBB opening on mice done with an acoustic pressure that is too high. On the  $T_1$ -weighted (A), huge leakages of Dotarem are present on the segments of the trajectory. One day later, edema are visible on the  $T_2$  image (B) and probably small hemorrhages on the  $T_2^*$  image (C).

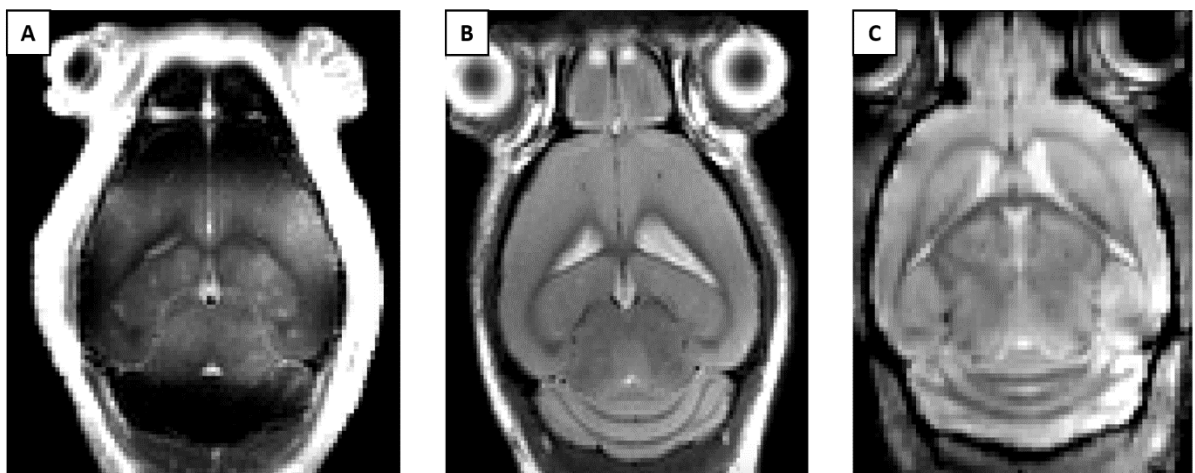


Figure 2-22: Example of a safe global BBB opening on mice. On the  $T_1$ -weighted (A) no intense leakages of Dotarem are present on the segments of the trajectory. The day after no edema and no hemorrhages are visible on the  $T_2$  image (B) and  $T_2^*$  image (C).

In order to optimize the acoustic parameters for global BBB opening, the following protocol was used. Mice were anesthetized, shaved and placed in a stereotaxic frame. The transducer was placed at the top of the head, at the center of the skull between bregma and lambda (see Figure 2-6 A for the position of bregma and lambda), this position is the center of the 6x6 mm<sup>2</sup> trajectory. The transducer was moved by 3 mm in the X and Y directions because the trajectory starts in a corner of the 6x6 square. Then, mice were injected with 50  $\mu$ L of microbubbles in the retro-orbitary sinus and the trajectory started. After sonication, mice were injected with an MR contrast agent (Dotarem) and placed in the MR scanner.  $T_1$ -weighted images were acquired to visualize the extent of the BBB opening. The day after, mice were scanned again.  $T_2$  and  $T_2^*$  images were acquired to look for edema and hemorrhages.

Figure 2-21 is an example of acoustic pressure that was too high and caused a huge leakage of Dotarem along the lines of the trajectory (A). One day later, edema is clearly visible on the  $T_2$  image (B) and correlates very well with the huge leakages of the previous day. Hemorrhages seems also visible on  $T_2^*$  images (C). This experiment was performed in a young nude mice. The PNP was set to 0.65 MPa in free water. The Figure 2-22 shows an example of a safe BBB opening experiment. The contrast enhancement on the  $T_1$ -weighted is homogenous (A) and no edema nor hemorrhages are visible on the  $T_2$  (B) and  $T_2^*$  (C) weighted images after 24 hours. This experiment was performed in an old C57BL/6 mice, the PNP was estimated set to 0.65 MPa in free water. This difference in the intensities of the BBB opening could be explained by a stronger attenuation of the skull of the old mouse.

This development was really important in my PhD project because I will use this protocol intensively in chapters 3, 4 and 5. I also did the same development for rats, adjusting mainly the mechanical trajectory to the rat anatomy and the PNP.

### 2.2.3. Mapping of a rat skull with a transducer in pulse-echo mode

In order to automatically position the transducer at the center of the skull for non MR-guided BBB opening protocols, I tried to develop a way to use the acoustic echo of the skull surface to map its curvature. I tried several set up of transducers. For example emitting the ultrasound with a 650 kHz transducer and receiving the echoes with a small transducer, designed for passive cavitation detection, in its center. I finally used only the small transducer designed for passive cavitation detection for emitting and receiving ultrasound shots. This 2 mm diameter transducer is a flat piston with a central frequency of 4.5 MHz. It was used in pulse-echo mode, mounted on the motorized positioning system, and driven with a transmit/receive pulser (US-wave, Lecoecur, Chuelles, France) and a Matlab code to drive the motors and to process data. The transducer was connected to the US-wave which emitted a sinusoidal apodized pulse (2 MHz, 5 periods) and receives the echoes. The setup is shown on Figure 2-23 A and E, the rat skull lies on an absorbing layer to avoid echoes from the glass container. The transducer was moved on a  $2 \times 5 \text{ cm}^2$  grid with steps of 1 mm. At each location 50 pulse-echoes were acquired and averaged. The signal processing to detect the maximum of the echo was the following:

- 1) The signal is filtered with a bandpass filter centered around the frequency of the pulse
- 2) The signal undergoes a Hilbert transform to detect the envelope of the sinusoidal pulse
- 3) The signal is filtered with a low pass filter to smooth out the envelope
- 4) The maximum is looked for and the time of flight is calculated. If the maximum is lower than a given threshold it is not considered as an echo

The filters are designed with the Matlab Filter Design & Analysis toolbox, they are both Equiripple filters. Their Bode's diagram are shown on Figure 2-23 B. An example on the signal processing to detect the maximum of the echo is shown on Figure 2-23 C. For each position of the transducer, the distance between the transducer and the skull is computed from the time of flight. Figure 2-23 D shows the distance between the skull and the bottom of the container (equal to the distance from transducer to bottom minus the distance from transducer to skull). The front part of the skull, toward the teeth,

where the skull is thinner can be clearly told from back part, toward the cerebellum, where the skull is thicker.

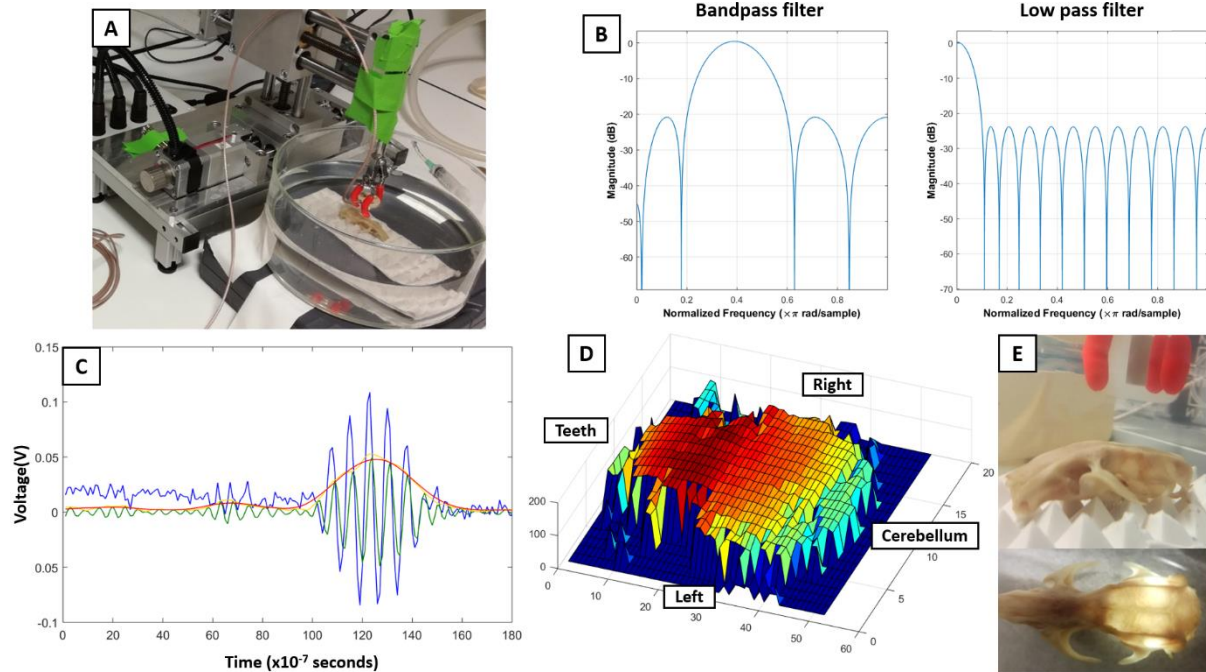


Figure 2-23: A – Experimental setup. B – Bode diagrams of the bandpass and low pass filter used for echo detection. C – Signal processing of an echo: in blue the experimental signal, in green the signal after the bandpass filter, in orange the Hilbert transform of the filtered signal and finally in red the Hilbert transform after the low pass filter. D – Surface showing the distance between the skull and the bottom of the water tank for each position of the transducer. E – Pictures of the skull lying on the absorbing layer.

The technique is promising but I did not have time to pursue its implementation as an automatic positioner. The main remaining challenge is the long scan time (around one hour) that was required and the limited benefit in term of precision of such an automatic positioning technique compared to a visual positioning by an experienced user.

### 2.3. Influence of the acoustic pressure on BBB opening

Now that we have a proper calibration of the ultrasonic beam within the rodent skull, we can focus on the influence of the pressure on the intensity and the duration of the BBB opening.

#### 2.3.1. An acoustic pressure threshold

As already explained in the introduction Chapter, the existence of an acoustic pressure threshold is already well known but the value of this threshold slightly depends on other parameters such as the frequency, anesthesia and composition of the microbubbles. So firstly, it was important to determine

this pressure threshold in our conditions Secondly, it was the opportunity to develop new technics to investigate this threshold.

a) Co-registration of MR-ARFI and concentration maps

In this paragraph, I show how I co-registered MR-ARFI images and concentration maps in order to correlate, voxel to voxel, the acoustic pressure used for BBB opening (derivated from the MR-ARFI images) and the concentration of contrast agent that extravagate to the brain.

Male Sprague Dawley rats (between 250 and 300 grams) were used in this study. The rats were headshaved, anesthetized with 2% isoflurane in a mixture of air and oxygen, a catheter was placed in the tail vein and the rat was placed on the bed in the 7 Tesla MR scanner. The 8-element transducer was positioned over the head of the animal. A first MR-ARFI image was acquired to localize the focal spot, the transducer was moved in order to focus in the striatum. A second MR-ARFI image was acquired (pulses of 4 ms, frequency 1.5 MHz, matrix size 128x128, 5 slices, resolution 0.25x0.25x2 mm, strength of the encoding gradients 80 %, electrical power transmitted 100 % of the amplifier amplitude) and the corresponding reference MR-ARFI image as well. A first  $T_1$  map (TR1 = 5 ms, TE = 2.5 ms, 6 segments, 60 inversion times (from 64 to 5800 ms), flip angle = 5°, resolution 0.25x0.25x1 mm, matrix size 128x102x14, repetition time between segments TR2 = 9 s, total acquisition time was 12.5 minutes) was acquired as a reference. The size of the field of view and the position of both MR-ARFI and  $T_1$  maps were fixed the same so that each voxel of the MR-ARFI corresponds exactly to two voxels of the  $T_1$  map (same in plane resolution, double slice thickness for MR-ARFI)

Then, we proceeded with BBB opening: 200  $\mu$ L of microbubbles (SonoVue, Bracco) were injected via the catheter and immediately after ultrasound were shot (0.6 MPa *in situ*, 1.5 MHz, 3% duty cycle, repetition frequency 10 Hz, for 2 min). Right after sonications, 250  $\mu$ L of Dotarem were injected via the catheter and a second  $T_1$  map was acquired to quantify the BBB opening. On the one hand, thanks to equations 1.4 and 1.5 in the Chapter 1, a concentration map can be computed from the  $T_1$  maps (Figure 2-24 B), and on the other hand, a pressure map can be calculated from the MR-ARFI signal. MR-ARFI phase images were post-processed in the same way as previously introduced in this chapter. Indeed, as demonstrated by *Larrat et al.* (Larrat et al., 2010a), the MR-ARFI signal induced by tissue displacement is proportional to the square of the acoustic pressure. So with  $\varphi$ , the phase obtained with the pipeline presented on the Figure 2-12,  $\varphi_{max}$ , the maximum phase of the image and  $P$ , the acoustic pressure we have:

$$P = A \cdot \sqrt{\varphi / \varphi_{max}} \quad (2.6)$$

With  $A$  a proportionality coefficient.  $A$  can be estimated from the calibration of the transducer and from the previous *in vitro* measurements of the acoustic transmission factor through the skull. Here, the peak negative pressure was set in order to have 0.6 MPa at focus, so  $A = 0.6$  MPa. With this equation, an estimated pressure map was computed from the phase image (Figure 2-24 A).

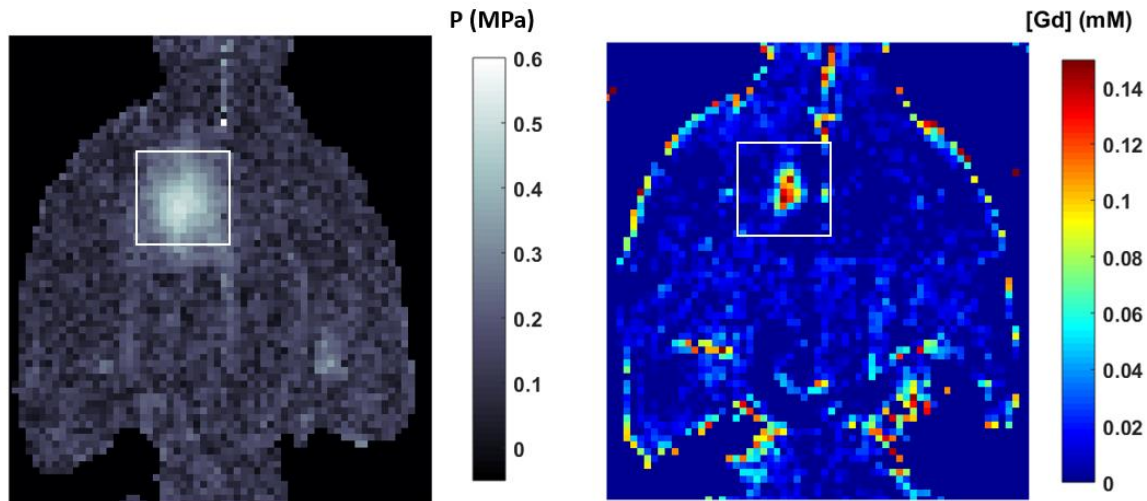


Figure 2-24: A – Pressure map computed from the phase of the ARFI image with the equation (2.6).  
 B – Concentration map computed from  $T_1$  maps before and just after injection of Dotarem.

#### b) Estimation of the acoustic pressure threshold

As already explained, pressure maps and concentration maps were co-registered. The slice with the maximum concentration of gadolinium was selected as well as the corresponding ARFI slice. Images were slightly realigned (1 or 2 pixels) so that the maximum pressure corresponds to the maximum concentration. Then, voxels were correlated one by one between pressure and concentration maps. The gadolinium concentration of each voxel is displayed as a function of the acoustic pressure this voxel received during the BBB opening (Figure 2-25 A). Two tendencies can be observed. First, between 0 and 0.4 MPa, the concentration seems to stay around 0 (negative values are due to the noise on the  $T_1$  maps). Second, between 0.4 and 0.6 MPa, the concentration seems to rise linearly with pressure.

This tendency is even clearer when the voxels are grouped in bins of pressure. On Figure 2-25 B, voxels are grouped in 13 pressure intervals. Each cluster is placed at the mean pressure and mean concentration of the cluster and error bars represent the standard deviation of each cluster. The number of voxels per cluster is given above the error bar. With this display, it is clear that the concentration remains at 0 until about 0.42 MPa and then increases linearly with the pressure. On the four last bins (with concentration above 0), a linear regression of the concentration as a function of the pressure was applied. The intersection of this linear regression with the abscissa axis is taken as the acoustic pressure threshold for BBB opening. This study was done on 6 rats with the same conditions and the acoustic pressure found for our setup at 1.5 MHz is  $0.42 \pm 0.05$  MPa (mean  $\pm$  s.d). The mean value of the linear slopes is  $0.47 \pm 0.1$  mM/MPa (mean  $\pm$  s.d).

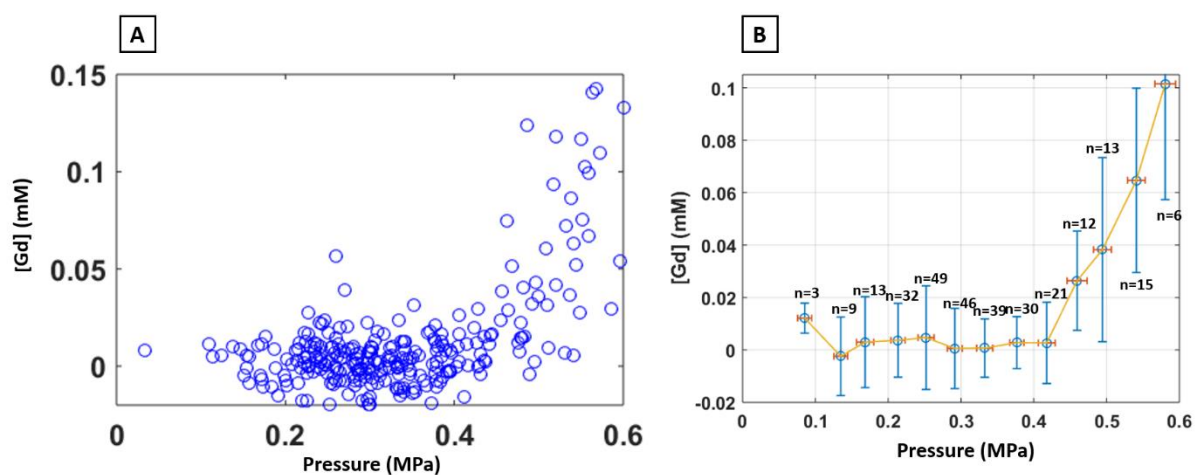


Figure 2-25: A – Correlation voxel to voxel between the concentration and the pressure map. B – Same representation than (A) but gather in 13 pressure intervals.

The small variability between the 6 rats (the standard deviation on the threshold value is only 50 kPa) makes us think that this technique is robust. This first experiment gives us, with a new technique, an estimate of the acoustic pressure threshold for our setup. Thanks to MR-ARFI and the motorized system, the openings were always performed in the striatum. This reduces the variability between the different experiments.

### c) Different acoustic pressures in an unique BBB opening experiment

A second experiment was designed in order to estimate the acoustic pressure threshold. On one Sprague Dawley rat, the BBB opening was performed along a square trajectory. The transducer was placed at the corner of a square trajectory symmetrically located in the striatum thanks to an MR-ARFI image. The mechanical trajectory of the beam was a 5 mm wide square. On Figure 2-26 A, the trajectory is shown overlaid on a  $T_2$ -weighted anatomical image. With Thermoguide and the motors, the transducer was moved at 1 cm/s and ultrasound were shot continuously (duty cycle 100 %) at 0.25, 0.35, 0.45 and 0.55 MPa respectively on the four sides of the square. It is to be noted that since the transducer is moving during sonications, the local acoustic duty cycle is not 100%. It can be estimated by assuming that microbubbles are cavitating if they are located inside half or less of the focal spot. Given the size of the focal spot, the speed of the motors and the repetition time of the whole trajectory (2s), this duty cycle is below 5% that is to say of the same order as the single spot experiments reported above (3%), with longer equivalent pulse duration though which could make a difference.

After microbubbles injection (200  $\mu$ L), this trajectory was played 60 times.  $T_1$  maps were acquired before and after the BBB opening and the injection of Dotarem (250  $\mu$ L) to compute a concentration map as shown on Figure 2-26 B.

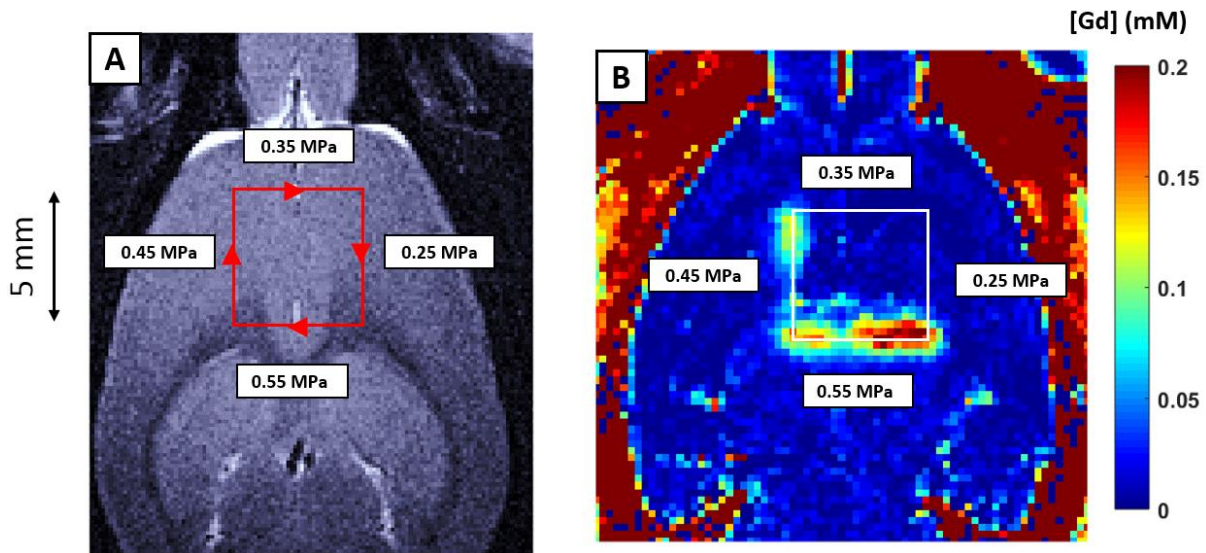


Figure 2-26: A – Representation, on a  $T_2$ -weighted image, of the trajectory of the transducer over the head of the animal and so of the focal spot in the brain. The pressure used on each segment of the trajectory for BBB opening is indicated. B – Concentration map after the BBB opening.

On the concentration map, gadolinium penetrated into the brain on the sides that were sonicated at 0.45 and 0.55 MPa but not on the side sonicated at 0.25 and 0.35 MPa. Here, the threshold effect is clearly seen, the BBB is not open at 0.35 MPa and on the same condition it is open at 0.45 MPa. The threshold is between those values, which is consistent with the previous experiments. As expected, the 0.55 MPa segment presents more BBB opening than the 0.45 MPa one.

One has to keep in mind that this is only a preliminary study done on one animal and the kind of sonication, especially the equivalent pulse duration and to a lesser extent the duty cycle, differs from the previous experiments. Nevertheless, we exhibit a great tool to investigate the BBB opening pressure threshold. Indeed, with this method, different conditions are tested on the same animal, so it overcomes the matter of comparing different animals (with different skull shape and thicknesses, different positioning in the MR scanner, different body physiological states). The animal is its own control. However, it assumes that brain vasculature (vessel density and size distribution) at our scale of observation can be considered sufficiently close in the four segments of sonication so that to be able to compare BBB leakage at the four positions. Nevertheless, differences in concentration within a line can be explained by small differences in the vascularization of the structures (gray matter, white matter, ventricles). In the future, we will repeat this experiment narrowing the pressures around the threshold, for example 0.35, 0.38, 0.42, 0.45 MPa, to estimate more precisely the threshold.

Here, I demonstrated that i) the opening threshold lies between 0.35 and 0.45 MPa at 1.5 MHz as referenced in the literature ii) MR-ARFI can predict the spatial extent of the BBB disruption iii) the amount of contrast agent delivered increases linearly with pressure above the opening threshold iv) the same opening threshold can be found with two different techniques. The acoustic pressure threshold might depend on the speed of the displacement of the ultrasound beam, which was always fixed at 1 cm/s in all experiments. Slower displacements result in a longer sonication time per location. But longer pulse durations have not been associated with stronger openings above 10 ms (see the paragraph on the acoustic parameters 1.1.5).

As a conclusion, in this paragraph 2.3.1, I brought the experimental evidence of the opening threshold and I presented two techniques to estimate its value. Furthermore, I demonstrated a linear dependency of the amount of delivered CA as a function of PNP. This is in accordance with the work of McDannold in 2008 showing that the mechanical index was ruling the efficacy of BBB opening. This means that if properly calibrated in situ, the intensity of the ultrasound beam can be finely tuned to reach the desired vascular permeability depending on the application.

### 2.3.2. Higher pressures open the BBB longer

A parameter far less studied in the literature is how long the BBB remains open after sonication and how this duration depends on the acoustic pressure used for the opening. Here, I present two experiments aimed at measuring this duration: the first one using the previously described square trajectory experiment and the second one based on localized disruptions of the BBB. Dotarem is a small molecule (1.5 nm of hydrodynamic diameter) which can probe BBB opening for a long time.

#### a) Square trajectory

The rat that underwent the BBB opening along the square trajectory was re-injected with Dotarem at 4 hours and 24 hours after sonication. For each re-injection, the rat was anesthetized, a catheter was placed in its tail vein and it was installed in the MR scanner. At each time point, a  $T_1$  reference map was acquired (same parameters as in the paragraph 2.3.1.c), then 250  $\mu$ L of Dotarem were injected and a second  $T_1$  map was acquired. From our experience, Dotarem is cleared from the brain after 2 hours, in the sense that it does not give contrast on the MR images anymore. Even if some Dotarem was left in the brain after 4 hours it would not affect the concentration map because a reference map was acquired just before injection of Dotarem. Figure 2-27 shows the three concentration maps at  $T_0$  (A), 4 hours (B) and 24 hours (C).

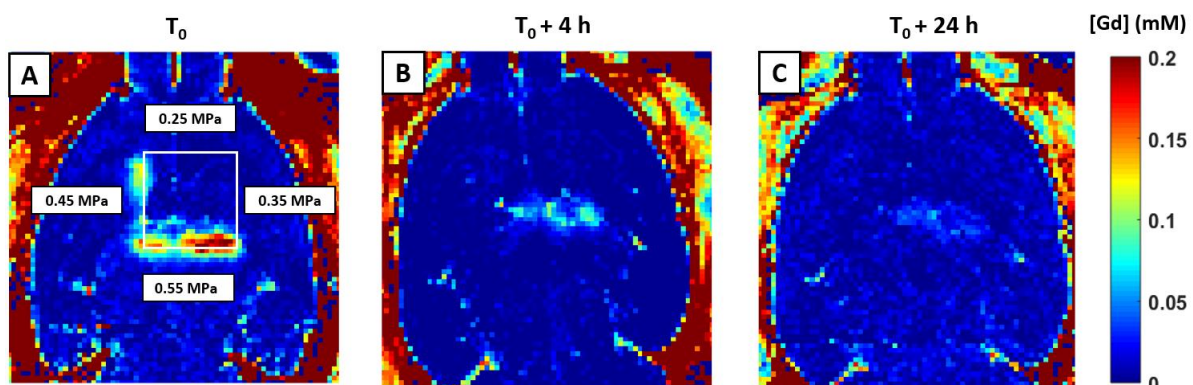


Figure 2-27: Concentration maps right after (A), 4 (B) and 24 (C) hours after the BBB opening along the square trajectory with the 4 different acoustic pressures.

At 4 hours, we detected Gadolinium leakage, meaning that the BBB permeability was still increased, only on the segment of the brain which was opened at 0.55 MPa. At 24 hours only a very weak leakage was observed on the 0.55 MPa side. Those results suggest that the acoustic pressure used for BBB opening affects not only the intensity of the BBB opening (as described in the Introduction chapter) but also the duration of the BBB opening in a joint way. Therefore, for a given drug, one can tune the duration for which the BBB stays open.

This experiment brings a clear confirmation that higher pressures open the BBB over a longer period. However, the time sampling was relatively poor (0, 4 and 24 hours), the number of pressure conditions were limited (only 0.45 and 0.55 MPa) and this experiment was performed in only one animal. To study this dependency in more details, I designed a second set of experiments.

b) Opening and follow-up of the permeabilisation

4 Sprague Dawley male rats (300 to 350 grams) were used. The BBB openings were done with the single-element transducer, with fixed beam and with the following parameters: 3 % duty cycle, 10 Hz of pulse repetition frequency, frequency of 1.5 MHz. Two rats were done at an estimated in situ PNP of 0.65 MPa and two at 0.55 MPa. The protocol is described on Figure 2-28. For each time point ( $T_0$ , H+3, H+6 and H+24), 250  $\mu$ L of contrast agent (Dotarem) were injected via the catheter in the tail vein. BBB opening were always performed in the right striatum. Rats woke up between each session.

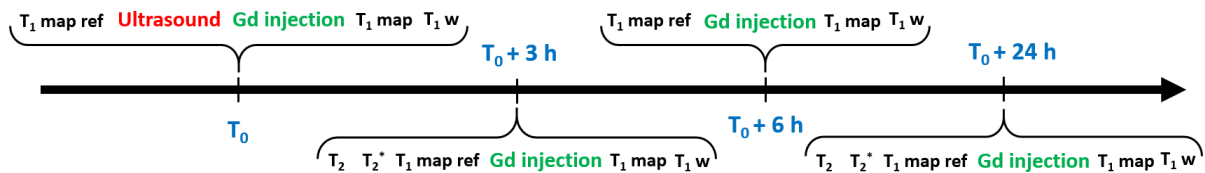
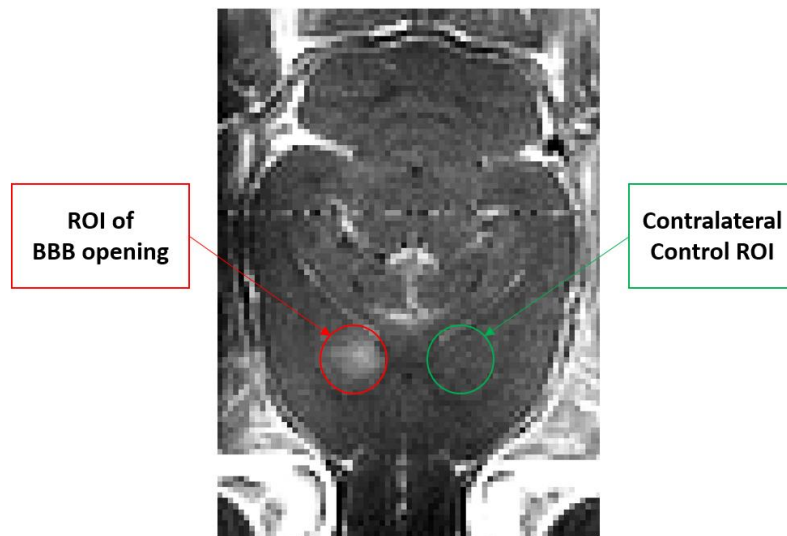


Figure 2-28: Protocol for the follow-up the BBB permeability.  $T_1$  map to assess the extravasation of Dotarem,  $T_2$  to assess edema and  $T_2^*$  to assess hemorrhages.



*Figure 2-29:  $T_1$ -weighted image after BBB opening and injection of contrast agent (first time point) and the ROIs to calculate contrast enhancements.*

$T_2$ - and  $T_2^*$ -weighted images were used to check for edema and hemorrhages.  $T_2$ - and  $T_2^*$ -weighted images were reconstructed and no damages (edema or hemorrhages) were found. So far, I only had time to analyze the  $T_1$ -weighted images but I the analysis of the  $T_1$  maps would probably give similar results.

The status of the BBB open, i.e. how much open the BBB is, was estimated through the extravasation of contrast agent. Contrast enhancements were calculated after every contrast agent injection. An example of the ROIs used to calculate contrast enhancement is given on Figure 2-29. These contrast enhancement, expressed in percent, were used to compare the status of the BBB opening. Leakages of contrast agent overserved at H+3 and H+6 are probably not due to hemorrhages as non were observed on  $T_2^*$  images.

c) Estimation of a closing time constant depending on the pressure

Figure 2-30 illustrates the status of the BBB for each time point by plotting the contrast enhancement as a function of time (after BBB opening). For each time point, the contrast enhancement of the two rats of the same group were averaged, data are showed as mean $\pm$ s.d. At 24 hours, the contrast enhancement was at zero, meaning that the BBB opening was closed for the two pressures. For the first three time point, the contrast enhancement was always higher for 0.65 MPa than for 0.55 MPa.

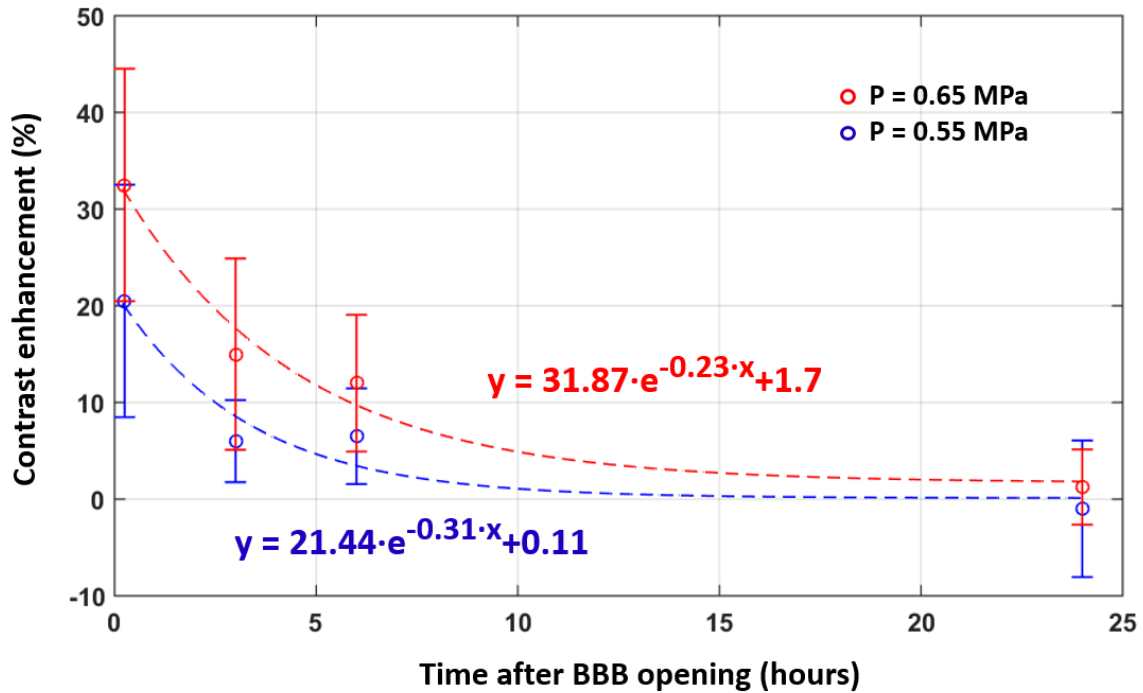


Figure 2-30: BBB closure. Contrast enhancement as a function of time after BBB opening. New injection of contrast agent for each time point.

The BBB closure time was fitted with a mono-exponential. This model represents a simple, damped, elastic model assuming an exponential decay of individual gap sizes. This first order model has already been used in Marty et al. (Marty et al., 2012a). According to this model, the decay of contrast enhancement was slower for 0.65 MPa than for 0.55 MPa.

Two main conclusions can be drawn from these results:

- BBB opening lasts longer when the acoustic pressure used during sonication is higher. Indeed, the mono-exponential fits exhibit a time constant of 4.3 hours for 0.65 MPa and of 3.2 hours for 0.55 MPa. This means a closure 35% slower for 0.65 MPa compared with 0.55 MPa. The sensitivity of the contrast enhancement computing can be estimated to 3 to 4% when comparing contralateral ROIs with no BBB opening. With a threshold at 4%, the BBB closure time can be estimated at 5.7 hours for 0.55 MPa and 11.5 hours for 0.65 MPa. So, BBB opening lasts around twice longer for 0.65 MPa than for 0.55 MPa.
- BBB opening is stronger, the leakage of the contrast agent is important, when the acoustic pressure is higher. Here, using 0.65 MPa leads to an opening 60% stronger than using 0.55 MPa. This was already observed in the previous experiments (2.3.1) where a dependency of 0.47 mM/MPa was found. According to the results of this previous experiment, using 0.65 MPa leads to an opening 77% stronger than using 0.55 MPa, which is in relatively good agreements with the present results.

As, a conclusion, I showed with this experiment that BBB openings is stronger when the acoustic pressure is higher. This characteristic of FUS-induced BBB opening is well known and was already

described in the introduction chapter. Moreover, I also showed that BBB opening lasts longer when the when the acoustic pressure is higher.

## 2.4. Conclusion

In this Chapter, I presented technological developments of our ultrasound setups, characterization of transmission of the ultrasound through the skull and *in vivo* studies on blood-brain barrier opening. These studies were fundamental in my PhD project because the obtained results will be used in many protocols to deliver drugs or nanoparticles (Chapter 3 and 4) and to evaluate BBB opening as a potential therapy for Alzheimer's disease (Chapter 5). Moreover, in this Chapter, I developed new techniques to investigate the acoustic pressure threshold for BBB opening and I investigated a poorly known relationship, the one between pressure and duration of opening.



**Chapter 3. PHYSICAL AND FUNCTIONAL PROPERTIES OF THE BRAIN AFTER ULTRASOUND-INDUCED BBB OPENING 73**

<b>3.1. Tortuosity of the brain .....</b>	<b>73</b>
3.1.1. <i>Free diffusion of contrast agent.....</i>	<i>74</i>
3.1.2. <i>In vivo restricted diffusion.....</i>	<i>76</i>
<b>3.2. Activity of the efflux pumps .....</b>	<b>78</b>
3.2.1. <i>Reminders on Positron Emission Tomography and efflux pumps.....</i>	<i>79</i>
3.2.2. <i>Protocol to follow erlotinib extravasation .....</i>	<i>80</i>
a) <i>Chemicals and radiochemicals.....</i>	<i>80</i>
b) <i>The ultrasound protocol.....</i>	<i>80</i>
c) <i><sup>11</sup>C-erlotinib PET study.....</i>	<i>82</i>
d) <i><sup>11</sup>C-N-desmethyl-loperamide PET study.....</i>	<i>83</i>
e) <i>Image analysis.....</i>	<i>83</i>
3.2.3. <i>FUS-induced BBB opening did not increase the brain exposure to <sup>11</sup>C-erlotinib and <sup>11</sup>C-N-desmethyl-loperamide .....</i>	<i>83</i>
3.2.4. <i>Not only size matter .....</i>	<i>87</i>
<b>3.3. Increased delivery of therapeutic compounds with ultrasound.....</b>	<b>88</b>
3.3.1. <i>Delivery of gold nanoparticles followed by MRI .....</i>	<i>88</i>
a) <i>BBB opening.....</i>	<i>89</i>
b) <i>Correlation between MRI and ICPMS.....</i>	<i>90</i>
3.3.2. <i>Delivery of an anti-cancer antibody followed by PET imaging.....</i>	<i>91</i>
a) <i>BBB opening.....</i>	<i>91</i>
b) <i>PET imaging .....</i>	<i>92</i>
<b>3.4. FUS-induced blood-tumor barrier opening.....</b>	<b>93</b>
3.4.1. <i>Symmetrical double implantation of tumors in rats' brains. ....</i>	<i>93</i>
3.4.2. <i>Ultrasound-induced opening of the blood-tumor barrier .....</i>	<i>94</i>
3.4.3. <i>An increased permeability after FUS-induced BTB opening.....</i>	<i>95</i>
<b>3.5. Conclusion.....</b>	<b>97</b>

## Chapter 3. Physical and functional properties of the brain after ultrasound-induced BBB opening

In this chapter I will describe four independent studies where ultrasound induced BBB opening was used to investigate the properties of the brain or to increase the delivery of various compounds. I will begin with the study of the tortuosity of the brain. We will see how fast different MRI contrast agents diffuse to the brain after BBB opening. I will continue with the study of the efflux pumps at the BBB. This “functional” barrier actively transfers some molecules back to the blood vasculature. We will see if opening the BBB with ultrasound is sufficient to counteract this mechanism. In the last two sections, I will present results of increased drug delivery in the context of cancer therapy, first with a therapeutic antibody in healthy brain tissue and second with a radiosensitizing agent in brain tumors.

### 3.1. Tortuosity of the brain

Here, we will see how, after FUS-induced BBB opening, the diffusion of contrast agents can be followed by MRI with  $T_1$  maps and how we can extract an intrinsic property of the brain from these measurements: the tortuosity. Tortuosity is a measure of hindrance of cellular obstructions. This work was a project led by Allegra Conti, a postdoctoral fellow in our team and by Remi Magnin, a former PhD student.

As we saw in the previous chapter, ultrasound provides a reliable way to locally deliver drugs or contrast agent to the brain. After BBB opening and MR-contrast agent injection, the diffusion of the contrast agent in the brain can then be followed over time with  $T_1$  images. The *in vivo* Apparent Diffusion Coefficient (ADC) which is hindered by the brain tissue can be compared to the free diffusion ( $D_{free}$ ) in an extremely light agar-agar gel. From these two coefficients, the tortuosity  $\lambda$  of the brain (Nicholson, 2001) can be calculated according to the following formula:

$$\lambda = \sqrt{\frac{D_{free}}{ADC}} \quad (3.6)$$

Few years ago, during Benjamin Marty’s PhD, our team tried to estimate this tortuosity after direct intracranial injection in rat brains (Marty et al., 2012a). The found values for the tortuosity were between 3.2 and 4. These values were too high compared with the literature. The gold standard technique, the TMA<sup>+</sup> method, measuring the diffusion of tetramethylammonium cations with electrodes in the brain (Endocrine et al., 1998), gives values of tortuosity around 1.6. These results might be explained by the invasive way to deliver the contrast agent. Indeed, direct injection causes structural modifications such as inflammation to the brain tissue which can artificially increase the diffusion of the contrast agent and lead to an overestimation of the ADC and of the tortuosity. We will

show how drug delivery with FUS-induced BBB opening leads to a correct estimation of the tortuosity, suggesting that this method is non deleterious.

### 3.1.1. Free diffusion of contrast agent

In order to estimate the tortuosity, the first step is to properly characterize the contrast agents used in terms of relaxivity (the capacity of the contrast agent to change the  $T_1$  and  $T_2$  relaxation times of the surrounding water molecules) and of free diffusion.

We will use only paramagnetic contrast agents in this study. They mainly shorten  $T_1$ . As a consequence we will focus on  $r_1$  relaxivity measurements. The relaxivity  $r_1$  was measured with phantoms containing several tubes filled with the contrast agent at different concentrations (Figure 3-1 A, B and C). With the  $T_1$  map sequence, the  $T_1$  is measured in each tubes and its inverse is plotted as a function of the concentration (Figure 3-1 D). The slope of this straight line is the relaxivity, expressed in  $s^{-1}mM^{-1}$ . The values of the relaxivity  $r$  for the different contrast agents are given on Table 3-1.

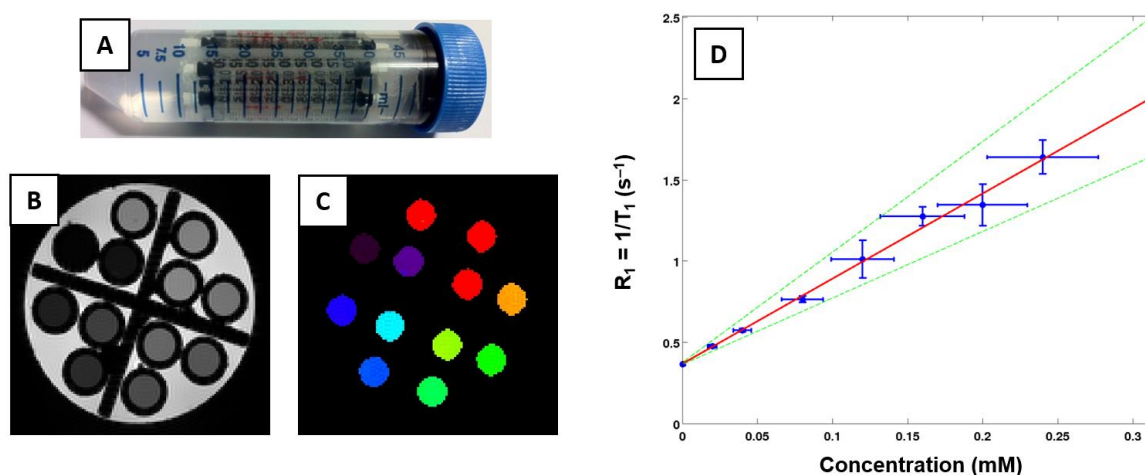


Figure 3-1: A – Phantom containing tubes filled with contrast agent in different concentration. B – Axial view of a  $T_2$  map of a phantom. C – Segmentation of tubes. D – The inverse of the relaxation time as a function of the concentration in contrast agent.

Then, the free diffusion coefficients of the contrast agents were measured. To do so, a column of contrast agent was deposited in a 0.3 % (in weight) agar-agar gel. Figure 3-2 shows the tube filled with the gel and the syringe containing the contrast agent. As the syringe was pulled up with the stereotaxic apparatus, the contrast agent was slowly flushed in the gel. This tube was then sealed and put inside the 7 Tesla scanner and warmed up to 37°C.  $T_1$  maps were acquired for one hour to follow the diffusion of the contrast agent in the gel as shown on the first row of Figure 3-3 A.

The concentration maps shown on Figure 3-3 are perpendicular to the Z axis, along which the contrast agent has been deposited. The slice thickness of the concentration map (0.5 mm) was really small compared to the 2 centimeters of the contrast agent column. So it is a reasonable hypothesis to say

that we were looking at a 2D diffusion process in the perpendicular plane ( $XY$ ) when the slice was chosen in the middle of the contrast agent column. Indeed, there was no concentration gradient in the  $Z$  direction as there was an equal quantity of contrast agent above and below.

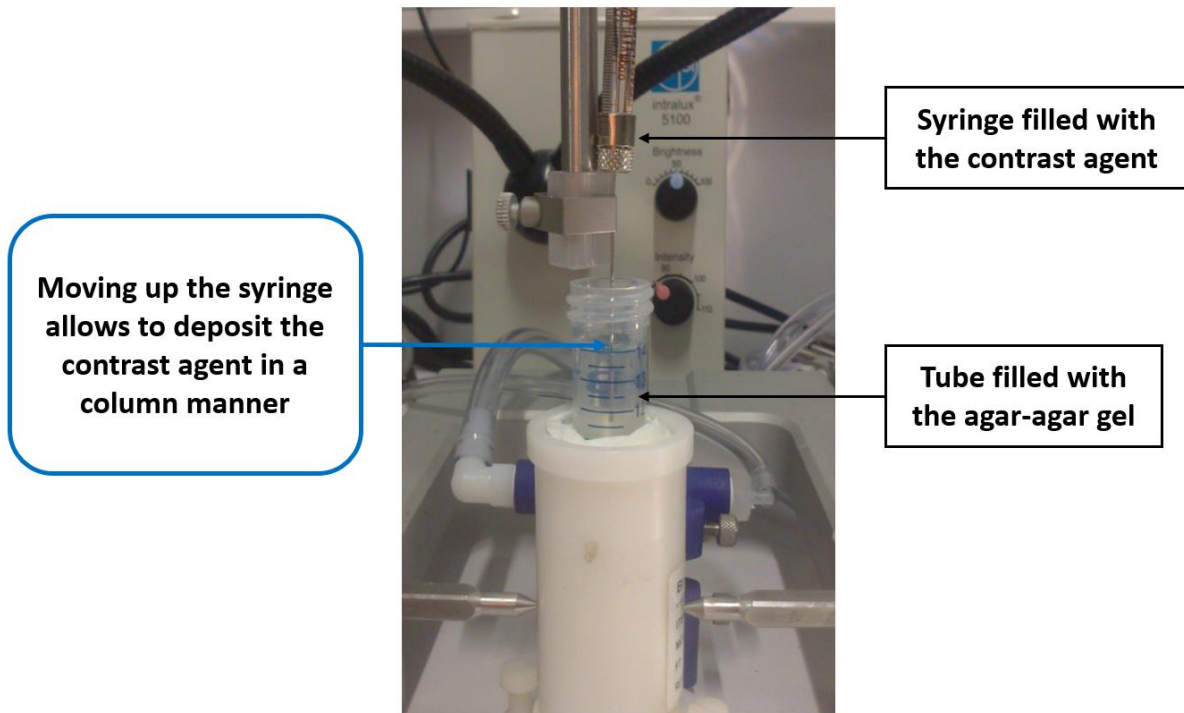


Figure 3-2: Contrast agent being deposited in the agar-agar gel. The tube and the syringe are held by a stereotaxic frame so that the contrast agent is precisely deposited in a column at the center of the tube.

The second row of Figure 3-3 B shows the data processing of the concentration maps. For each time point, a 2D normal distribution was fitted on the distribution of contrast agent. The results of this fit are two width of the normal distribution  $\sigma_x$  and  $\sigma_y$  along the two main directions of the ellipse found by the fit.

The square of the widths ( $\sigma_x^2$  and  $\sigma_y^2$ ) are plotted as a function of time, time zero being the injection time. Indeed, according to the *Fick's law* describing random diffusion, the square of the widths increases linearly with time. The *Fick's law* is given here:

$$\sigma^2 = 2 \cdot D \cdot t \quad (3.1)$$

From the slope of the graph on Figure 3-3 we can extract two diffusion coefficients  $D_{free\ x}$  and  $D_{free\ y}$  along the two main directions. The global free diffusion coefficient  $D_{free}$  is taken as the mean of  $D_{free\ x}$  and  $D_{free\ y}$ . The values of  $D_{free}$  for the different contrast agents are given in Table 3-1.

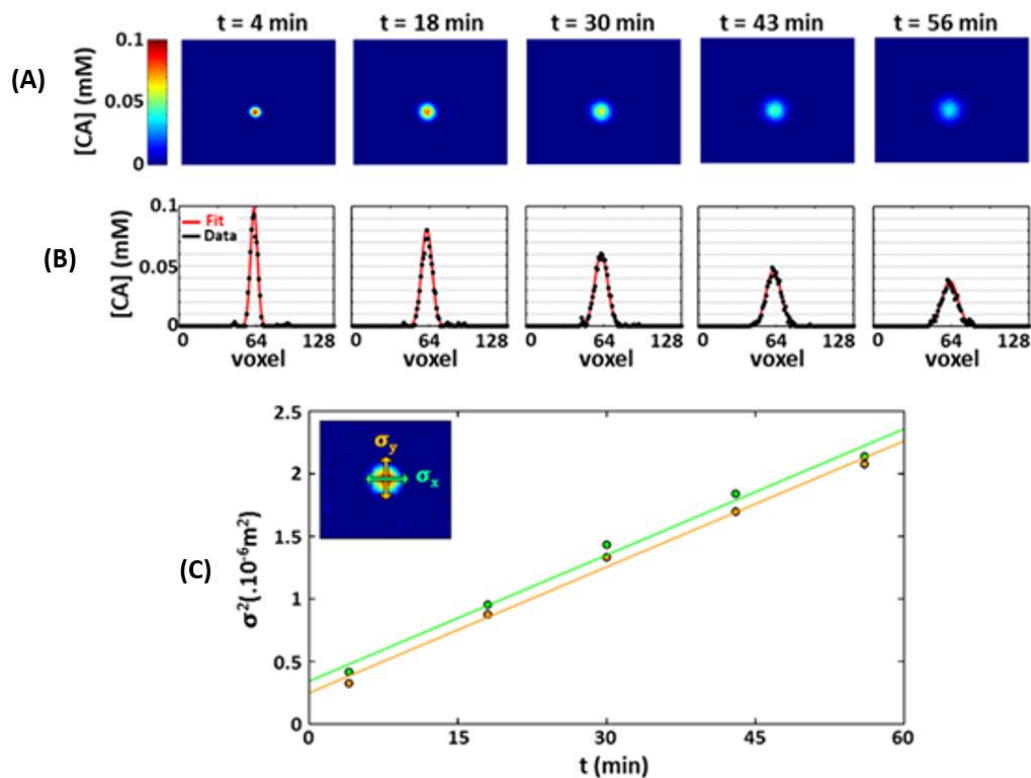


Figure 3-3: The first row (A) shows the axial view of the concentration maps over time. The second row (B) shows the profile going through the center (black dots) and the normal law fit of the experimental data (red line) over time. The third row (C) shows the square of the widths of the normal law fits as a function of time.

### 3.1.2. In vivo restricted diffusion

Now that the free diffusion  $D_{free}$  of the contrast agents has been characterized, the *in vivo* apparent diffusion ADC will allow to estimate the tortuosity of the brain (Equation 3.1). To do so, punctual FUS-induced BBB opening was performed in males Sprague Dewlay rats, followed by i.v. contrast agent injection and diffusion monitoring with  $T_1$  maps.

Rats were anesthetized and head shaved. A catheter was placed in the tail vein and they were installed on the bed in the MR scanner. The single element transducer was positioned over the head on the animals. A first MR-ARFI was acquired to localize the focal spot, the transducer is moved in order to have the focal spot in the striatum. A first  $T_1$  map (TR1 = 5 ms, TE = 2.5 ms, 6 segments, 60 inversion times (from 64 to 5800 ms), flip angle =  $5^\circ$ , resolution  $0.25 \times 0.25 \times 1$  mm, matrix size  $128 \times 102 \times 14$ , repetition time between segments TR2 = 9 s, total acquisition time was 12.5 minutes) was acquired as a reference. For BBB opening, 200  $\mu\text{L}$  of microbubbles, were injected via the catheter and immediately after ultrasound were shot (1.4 MPa in free water, 1.5 MHz, 3% duty cycle, repetition frequency 10 Hz, for 1 min). Then, 250  $\mu\text{L}$  of contrast agent are injected via the catheter.  $T_1$  maps are acquired in a repeated way for around one hour.

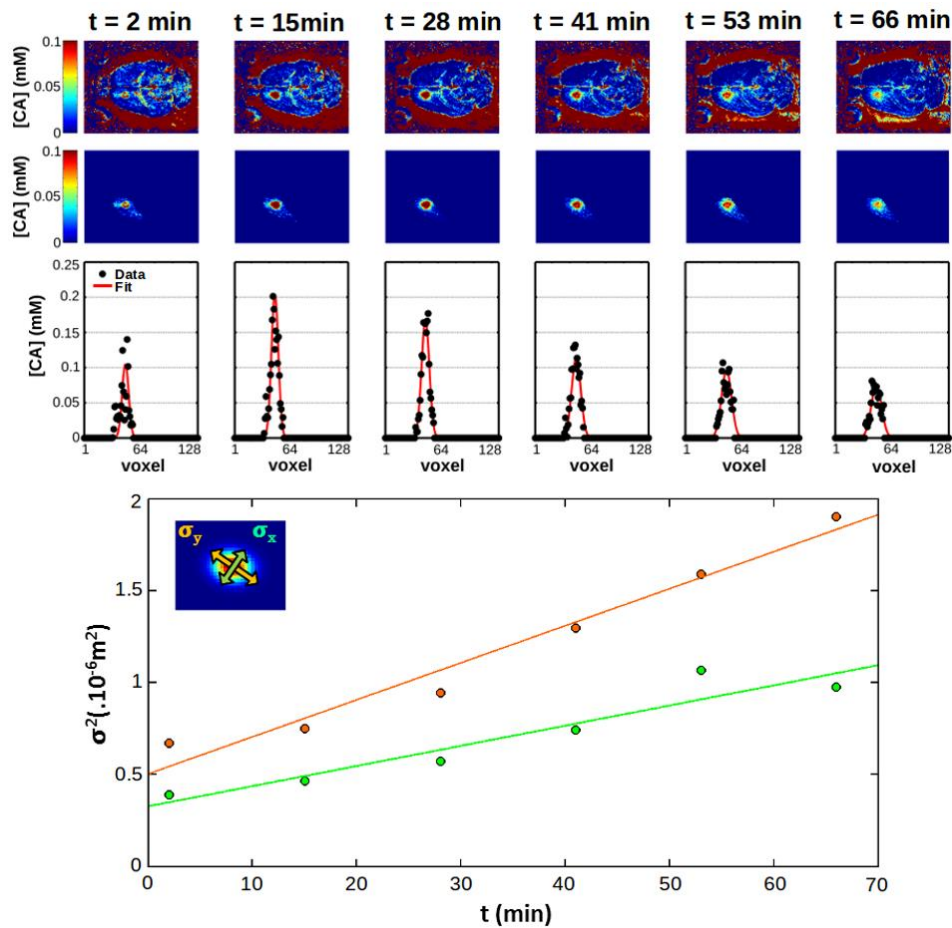


Figure 3-4: The first row shows the axial view of the concentration maps over time. The second row shows manual segmentation of the BBB opening site. The third row shows the profile passing through the center (black dots) and the normal law fit of the experimental data (red line) over time. The fourth row shows the square of the widths of the normal law fits as a function of time.

The analysis, described on Figure 3-3, was similar to the analysis of the *in vitro* data. The only difference was an additional segmentation step (second row on Figure 3-3) to mask out the brain and only apply the normal distribution function fit to the sonicated region. The widths of the normal distribution were interpreted according to the *Fick's law* and ADC was taken as the mean of  $ADC_x$  and  $ADC_y$ .

Table 3-1: characteristics of the different contrast agent studied

MRI Contrast Agent	Number of animals	$r_1$ ( $s^{-1}mM^{-1}$ )	$D_{free}$ ( $10^{-10} m^2/s$ )	$D_H$ S-E (nm)	$D_H$ DLS (nm)	ADC ( $10^{-10} m^2/s$ )	Tortuosity
Dotarem	3	4.7	4.5	1.5	1.6	1.6	<b>1.7</b>
Gadovist	3	5.5	3.9	1.7	1.8	1.5	<b>1.6</b>
MultiHance	3	6.9	2.8	2.3	2.3	1.1	<b>1.6</b>
AguIX	2	8	0.11	5.8	3.5	0.6	<b>1.5</b>

The values of ADC for the different contrast agents are given in Table 3-1. From the Stokes-Einstein equation:

$$d_H = \frac{kT}{3\pi\eta D_{free}} \quad (3.2)$$

where  $k$  is the Boltzmann's constant,  $T$  the temperature and  $\eta$  the viscosity. The hydrodynamic diameter  $d_h$  of the different molecules can be estimated. Values are given in Table 3-1 in the  $d_h$  S-E column. The hydrodynamic diameters were also measured by Diffuse Light Scattering (DLS) (thanks to Nicolas Tsapis, institut Gallien, Chatenay Malabry, France). The results are given in Table 3-1 in the  $d_h$  DLS column.

These results show that *i*) the hydrodynamic diameters between *in vitro* diffusion and Dynamic Light Scattering are coherent (except for AguIX), which validates our *in vitro* protocol *ii*) the diffusion coefficients ( $D_{free}$  and ADC) of the particles decrease as their size increases, which was expected *iii*) the found tortuosity values are in good agreement with the literature. The fact that the tortuosity of the brain is not affected by the ultrasound delivery method, unlike the intracranial injection method (Marty et al., 2012b), means that our drug delivery method does not induce any tissue modification that would restrain bio-availability. This result is one more argument in favor of the safety and efficacy of FUS-induced BBB opening as a way to deliver drugs to the brain.

### 3.2. Activity of the Efflux pumps

The objective of this collaboration between our team and the team of Nicolas Tournier in the Service Hospitalier Frédéric Joliot (SHFJ, CEA, Orsay, France) was to investigate the effects of FUS-induced BBB opening on the delivery of erlotinib, an efficient anti-cancer drug outside the brain. In the brain, efflux pumps were shown to restrict the permeation of most tyrosine kinase inhibitors, such as erlotinib, through the intact blood-brain barrier (Kort et al., 2015a). This considerably limits the clinical

perspectives of molecularly targeted therapies against brain malignancies. Here, we investigated “physical” BBB opening obtained using focused ultrasound as a strategy to improve the brain delivery of erlotinib in rats.

In this study, I was responsible for the ultrasound part. Radiotracer labeling and PET imaging were done by our partners at SHFJ: Sébastien Goutal, Sylvain Auvity, Fabien Caillé, Irène Buvat, and Nicolas Tournier. The reconstruction and analysis of the PET images was done by Sébastien Goutal.

### 3.2.1. Reminders on Positron Emission Tomography and efflux pumps

The concept of emission and transmission tomography was introduced by David E. Kuhl, Luke Chapman and Roy Edwards in the late 1950s. Positron Emission Tomography (PET) is an imaging modality that makes use of radioactive compounds injected in the body. The system detects pairs of gamma rays emitted indirectly by the radioactive tracer. The radioactive tracer naturally emits positrons which will annihilates with electrons resulting in two 511 keV gamma photons being emitted at 180 degrees to each other. They are detected by the gamma-cameras placed around the subject. Hence, it is possible to localize their source along a straight line of coincidence. The tracer is a short-life isotope such as carbon 11, oxygen 15 or fluorine 18, attached to a molecule of interest that binds to receptors or accumulates into specific organs. Due to the short half-lives of most positron-emitting radioisotopes, the radiotracers have traditionally been produced using a cyclotron in close proximity to the PET imaging facility. This is the case in Orsay Hospital where radiotracers are produced on site.

As we saw, the BBB, resulting from tight junctions between the endothelial cells, is the main limitation to deliver drugs to the brain. Despite dramatic advances in understanding the molecular basis of carcinogenesis, the development of targeted cancer therapy against the Central Nervous System (CNS) malignancies is hampered by the low brain permeation of most tyrosine kinase inhibitors (TKIs) (Ballard et al., 2016). Efflux pumps are proteins overexpressed at the endothelial cell membranes that pump certain molecules like TKIs from the brain parenchyma back to the blood circulation (Durmus et al., 2015; Kort et al., 2015b). Inadequate brain exposure to erlotinib is assumed to account for the high rate of metastatic progression within the CNS during or after systemic benefit in patients who have non-small cell lung cancer with activating mutation of the *EGFR* gene (Camidge et al., 2014). Improving the delivery of small TKI molecules such as erlotinib to the tumor and brain regions surrounding the tumor is often proposed as a putative strategy to limit the progression of CNS lesions through molecularly targeted therapy (Agarwal et al., 2011; How et al., 2017).

Here, we hypothesized that FUS-induced BBB opening may be sufficient to overwhelm and overcome the ABCB1/ABCG2-mediated efflux of erlotinib at the BBB, thus providing an alternative strategy to locally improve erlotinib delivery to the brain (van Tellingen et al., 2015). To that end, the brain kinetics of the ABCB1/ABCG2 substrate erlotinib was investigated using <sup>11</sup>C-erlotinib PET imaging in the context of FUS-induced BBB opening and/or efflux transporter inhibition in rats. The impact of BBB disruption on ABCB1 function was specifically assessed using <sup>11</sup>C-*N*-desmethyl-loperamide PET imaging.

### 3.2.2. Protocol to follow erlotinib extravasation

#### a) Chemicals and radiochemicals

Pharmacological inhibition of ABCB1 and ABCG2 was obtained using elacridar. Elacridar hydrochloride and 6-*O*-desmethyl erlotinib (OSI-420) were purchased from Syncom BV (Netherlands). Elacridar for i.v injection ( $10 \text{ mg}\cdot\text{mL}^{-1}$ ) was formulated using a co-solvent strategy resulting in a final tetrahydrofuran concentration of 4% (v/v) in sterile aqueous D-glucose solution at 2.5% (w/v) (Goutal et al., 2018). ABCB1-specific inhibition was achieved using tariquidar. Tariquidar was purchased from Eras Labo (France). Evans Blue (EB) was obtained from Sigma-Aldrich, France. Four grams of EB were dissolved in 10 mL sterile aqueous NaCl 0.9% (w/v). All solutions were extemporaneously prepared the day of animal experiments.

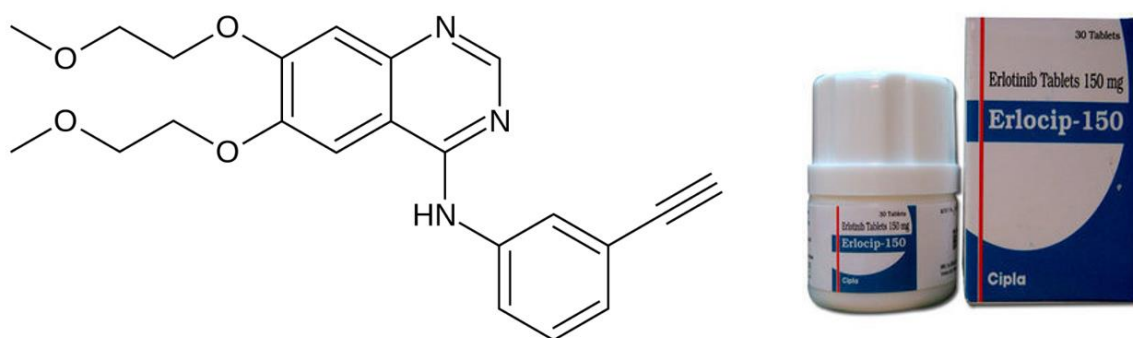


Figure 3-5: Topological representation of the erlotinib molecule and the commercial compound.

$^{11}\text{C}$ -Erlotinib was synthesized by  $^{11}\text{C}$ -methylation of OSI-420 following a previously described procedure (Bahce et al., 2013).  $^{11}\text{C}$ -erlotinib was formulated in 0.9% aqueous saline with 10% ethanol (v/v) at an approximate concentration of 50 MBq/mL for intravenous (i.v.) injection into animals. Radiochemical purity of  $^{11}\text{C}$ -erlotinib was greater than 98% and specific activity at the end of synthesis was 140 - 300 GBq/ $\mu\text{mol}$ .

#### b) The ultrasound protocol

A protocol using FUS was developed to induce a large and controlled 'line' shaped BBB opening in rats in one brain hemisphere. The ultrasound set up was made of a single element concave transducer (diameter of 25 mm, focal depth 20 mm, Imasonic, France) with a central frequency at 1.5 MHz. The transducer was calibrated in water tank, using a 200- $\mu\text{m}$  calibrated hydrophone (HGL-0200, preamplifier AH-2020, Onda Corporation, USA) mounted on a micrometric 3D positioning stage.

Rats were installed in prone position on a dedicated bed into a stereotactic frame. The transducer holder was fixed on a rail allowing reproducible antero-posterior displacement over a line scanning the head of the animals in order to specifically sonicate the left hemisphere. The transducer was

coupled to the shaved head of the animals with a latex balloon filled with deionized and degassed water. Acoustic gel was applied to the skin in order to ensure efficient coupling with the balloon. A 200  $\mu\text{L}$  bolus of commercially available microbubbles (Sonovue<sup>®</sup>, Bracco, Italy) was injected i.v.. Ultrasound sonication started immediately after microbubbles injection, with continuous waves set at an estimated peak negative acoustic pressure of 0.6 MPa in situ at focus. Animal weight was accounted for in this estimation according to the results in Chapter 2. The transducer, continuously shooting the ultrasound wave, was repeatedly moved back and forth above the left hemisphere with 2s repetition cycles during 5 minutes.

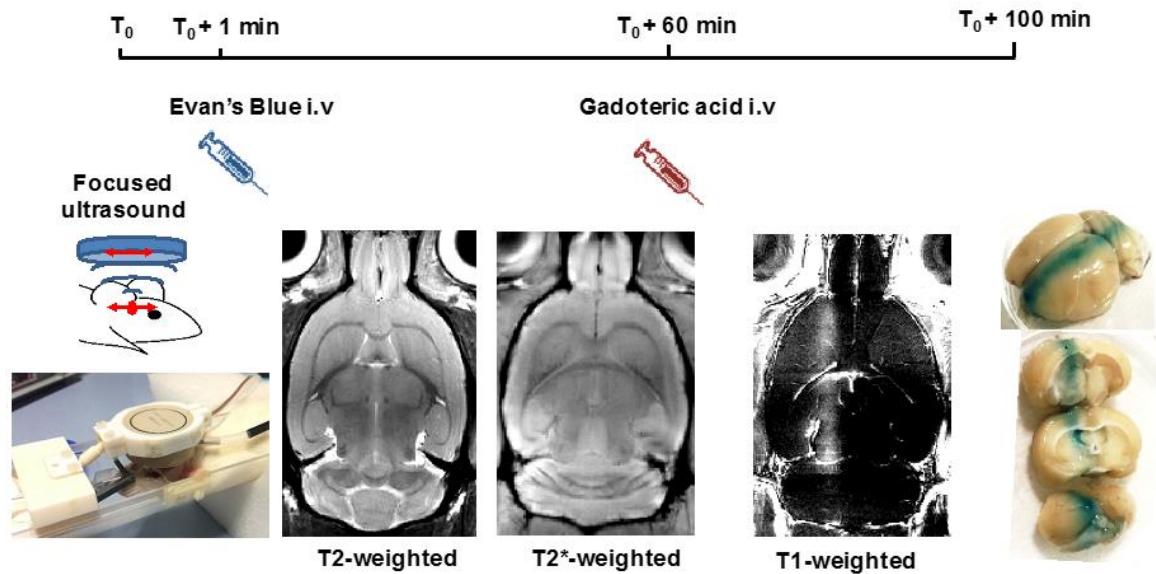


Figure 3-6: Sonications are targeted along a line in the antero-posterior direction located inside the left hemisphere. Evan's Blue is injected immediately after FUS in order to evidence BBB opening and an MRI contrast agent is injected one hour after FUS and its leakage into the parenchyma is imaged for 40 minutes with  $T_1$ -weighted images.  $T_2$  and  $T_2^*$  images do not show any tissue damage following ultrasound.

In preliminary experiments, the efficacy and tolerance of the FUS-induced BBB opening protocol was validated using magnetic resonance imaging (MRI) with a gadolinium chelate as a contrast agent (Dotarem<sup>®</sup> 0,5 mmol/mL, Guerbet, France).

Two rats were injected with EB immediately after the FUS protocol and 2 other rats underwent the same EB injection after a sham ultrasound sonication. Right after the EB injection, MRI images were acquired for all 4 animals using a 7T small animal MRI scanner (Bruker, Germany).  $T_2$ -weighted and  $T_2^*$ -weighted acquisitions were performed to assess the absence of both edema and hemorrhage. One hour after FUS, animals were i.v. injected with 200  $\mu\text{L}$  Dotarem. Animals were then MRI scanned again in order to visualize and localize the hemispheric BBB opening and assess whether BBB was still disrupted 60 min after FUS. A  $T_1$ -weighted sequence was used to detect the signal enhancement due to gadolinium chelate delivered into brain tissues. Signal enhancement due to BBB leakage was quantified by calculating the left/right ratio of the signals in brain hemispheres.

T<sub>2</sub>-weighted and T<sub>2</sub>\*-weighted images confirmed the absence of FUS-induced tissue damages, such as edema or hemorrhages. Subsequent T<sub>1</sub>-weighted MR images showed that the BBB was still permeable to Dotarem, at least an hour after FUS. Images highlighted a large stripe from the front of the brain to the cerebellum on a width of ~2mm which matches with the width of the ultrasound focal spot (Figure 3-6). The left-to-right hemisphere signal ratio was 2.3 and 1.7 for the two rats. The volume of interest (VOI) corresponding to the disrupted BBB covered 41 to 44 % of the volume of the left hemisphere (volume measured on the slice displayed on Figure 3-6).

c) <sup>11</sup>C-erlotinib PET study

Twenty rats were randomly split into four groups of five individuals (Figure 3-7). Animals of the “baseline” group were used as a reference to determine the brain kinetics of erlotinib in case of intact physical and functional BBB. Animals of the “ELA” group received the ABCB1/ABCG2 inhibition protocol using i.v. elacridar 10 mg/kg (Tournier et al., 2017). Animals of the “FUS” group underwent the FUS-induced BBB opening in the left hemisphere. Animals of the “FUS+ELA” group had both the hemispheric FUS-induced BBB opening and the ABCB1/ABCG2 inhibition protocol.

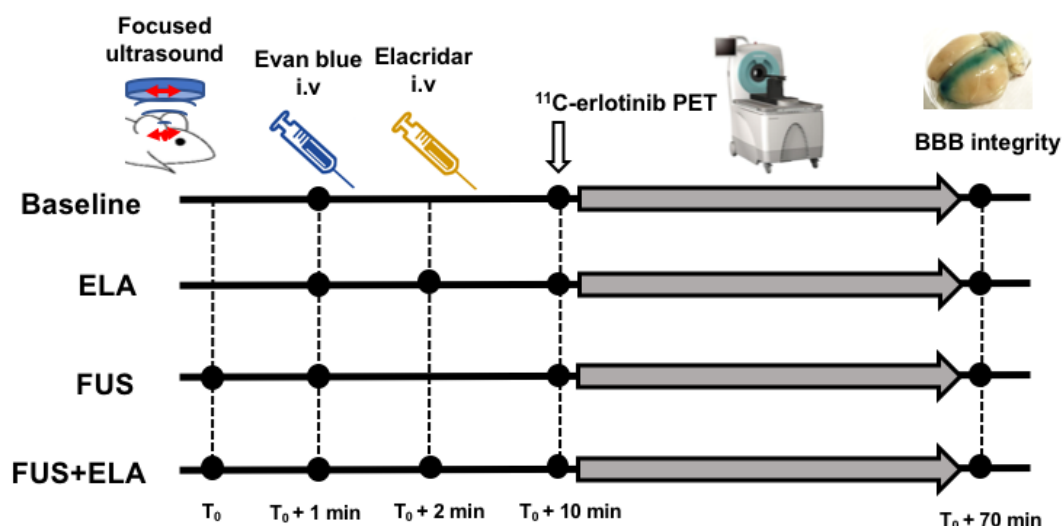


Figure 3-7: Animals were scanned either at baseline with intact blood-brain barrier (BBB), during focused ultrasound (FUS) induced BBB disruption, ABCB1/ABCG2 inhibition (ELA) or both the FUS-induced BBB disruption and ABCB1/ABCG2 inhibition (FUS+ELA).

All animals received EB injection as a BBB integrity marker followed by <sup>11</sup>C-erlotinib injection as soon as possible (typically 1 min) after ultrasound exposure. BBB integrity was assessed at the end of the PET acquisition, 60 min after <sup>11</sup>C-erlotinib injection, using the EB extravasation test as shows on the right of Figure 3-6.

All groups received an equivalent dose of <sup>11</sup>C-erlotinib which was i.v. injected, followed by 60 min brain PET dynamic acquisitions. PET scans were performed under isoflurane anesthesia using an

Inveon<sup>®</sup> microPET system (Siemens, Germany). Images were reconstructed with the FORE+OSEM2D algorithm including normalization, attenuation, scatter and random corrections.

Four additional rats have been used to investigate a putative delayed impact of FUS on BBB integrity and the brain kinetics of <sup>11</sup>C-erlotinib (FUS+48h group). First, animals underwent the FUS-induced BBB disruption protocol followed by gadoterate-enhanced T1-weighted MRI (but not EB) to check BBB disruption, 60 min after FUS. Forty-eight hours after FUS, anesthesia was re-induced and animals were i.v injected by EB prior to <sup>11</sup>C-erlotinib PET imaging (30 min scan). The EB extravasation test was performed at the end of PET acquisition to check BBB integrity 48h after FUS.

#### d) <sup>11</sup>C-N-desmethyl-loperamide PET study

The impact of BBB disruption on ABCB1 function at the BBB was addressed using our FUS protocol and <sup>11</sup>C-N-desmethyl-loperamide as an ABCB1-specific PET probe (Kannan et al., 2010). Three animals underwent FUS followed by EB injection. Ten min after FUS, <sup>11</sup>C-N-desmethyl-loperamide was i.v injected ( $39.7 \pm 3.3$  MBq) followed by 30 min PET acquisition. EB extravasation test was assessed at the end of PET acquisition. Tariquidar (8 mg/kg i.v) was used as positive control for ABCB1 inhibition in two additional animals, as previously described (Pottier et al., 2016).

#### e) Image analysis

Image analysis was performed using PMOD<sup>®</sup> software (version 3.8, PMOD Technologies Ltd, Switzerland). Summed PET images from 0 to 30 min were co-registered to a T<sub>2</sub>-weighted MR template built in PMOD software where a volume of interest (VOI) in the expected sonicated area of the left hemisphere has been drawn according to the MRI images obtained during preliminary experiments. The left hemisphere region was mirrored to the right hemisphere to obtain a reference VOI with intact BBB. Corresponding time-activity curves (TACs) in each VOI were generated with time frame duration of 0.25 min; 0.5 min x 2; 0.75 min; 1 min x 4; 1.5 min; 2 min x 4; 2.5 min; 3 min x 3; 3.5 min; 4 min x 2; 4.5 min and 5 min x 4. TACs were generated in these regions to describe the local kinetics of <sup>11</sup>C-erlotinib, expressed as the percentage of injected dose per volume (%ID.mL<sup>-3</sup>) *versus* time. T<sub>max</sub> was defined as the time at which the maximum of the TAC curve (C<sub>max</sub>) occurred and was used to characterize the TACs. The effect of elacridar was shown to be rapidly reversible (Tournier et al., 2017). Therefore, erlotinib exposure to each VOI was estimated as the area under the TAC (AUC) of radioactivity from 5 to 30 min in the region with disrupted (AUC<sub>left</sub>) and intact (AUC<sub>right</sub>) BBB.

### 3.2.3. **FUS-induced BBB opening did not increase the brain exposure to <sup>11</sup>C-erlotinib and <sup>11</sup>C-N-desmethyl-loperamide**

In baseline condition, the brain concentration of <sup>11</sup>C-erlotinib was low and consistent with previous <sup>11</sup>C-erlotinib time-activity curves (TACs) in the brain of mice (Traxl et al., 2015), nonhuman primates

(Tournier et al., 2017) and humans (Weber et al., 2011). ABCB1/ABCG2 inhibition using elacridar resulted in a significant 2-fold increase in the brain maximal concentration compared with baseline in both hemispheres ( $p < 0.05$ ; Figure 3-10). Twenty minutes post injection, the brain concentration of  $^{11}\text{C}$ -erlotinib was still significantly higher in animals who received elacridar. This difference was no longer significant after 30 min scanning, thus showing the reversibility of the ABCB1/ABCG2 inhibition effect of elacridar (Tournier et al., 2017). The brain exposure to erlotinib was therefore calculated from 5 to 30 min and was significantly higher in the ELA group ( $\text{AUC}_{\text{left}} = 2.18 \pm 0.49 \text{ \%ID}\cdot\text{cm}^{-3}\cdot\text{min}$ ) compared to the baseline group ( $\text{AUC}_{\text{left}} = 1.36 \pm 0.50 \text{ \% ID}\cdot\text{cm}^{-3}\cdot\text{min}$ ;  $p < 0.001$ ) (Figure 3-10). Neither  $C_{\text{max}}$  nor  $T_{\text{max}}$  were significantly different between the left and right brain hemispheres of animals of the four groups ( $p > 0.05$ ).

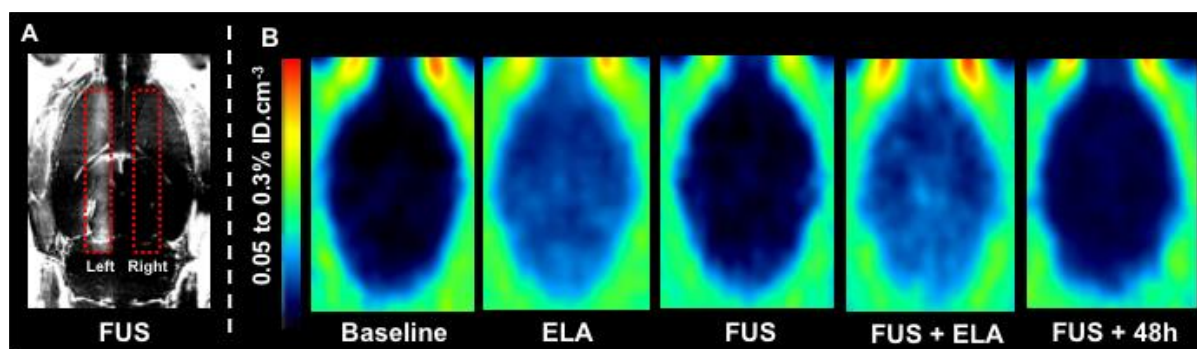


Figure 3-8: A – The contrast enhanced  $T_1$ -weighted MR image used to localize the FUS-induced BBB opening and delineate the region-of-interest drawn on the left and the right hemisphere. B – Co-registered summed (0 to 30 min) PET images obtained at baseline with intact blood-brain barrier (BBB), during focused ultrasound (FUS) induced BBB opening, ABCB1/ABCG2 inhibition (ELA), both the FUS-induced BBB opening and ABCB1/ABCG2 inhibition (FUS+ELA) and 48h after FUS (FUS+48h). Images were corrected for injected doses and expressed as % of injected dose per volume ( $\text{\%ID}\cdot\text{cm}^{-3}$ ).

Hemispheric BBB opening performed in the FUS group did not measurably impact  $C_{\text{max}}$  nor  $T_{\text{max}}$  compared with baseline (Figure 3-10,  $p > 0.05$ ). As illustrated on Figure 3-9, the brain kinetics of  $^{11}\text{C}$ -erlotinib in the FUS+ELA group were similar to those obtained in the ELA group. Erlotinib exposure to the left hemisphere in the FUS+ELA group was significantly higher than baseline ( $p < 0.001$ ) and FUS ( $p < 0.001$ ) but was not different from that measured in the ELA group ( $p > 0.05$ ).

Animals scanned 48h after FUS showed similar brain kinetics than baseline and FUS rats. Consistently,  $\text{AUC}_{\text{left}}$  measured in animals of the FUS+48h group was not significantly different than baseline and FUS ( $p > 0.05$ ) (Figure 3-10).

In all tested conditions,  $\text{AUC}_{\text{left}}$  was not significantly different from  $\text{AUC}_{\text{right}}$ , thus showing the lack of difference in the brain exposure to erlotinib between the left and the right hemisphere, regardless of the presence of FUS-induced BBB opening or ABCB1/ABCG2 inhibition (Figure 3-10,  $p > 0.05$ ).

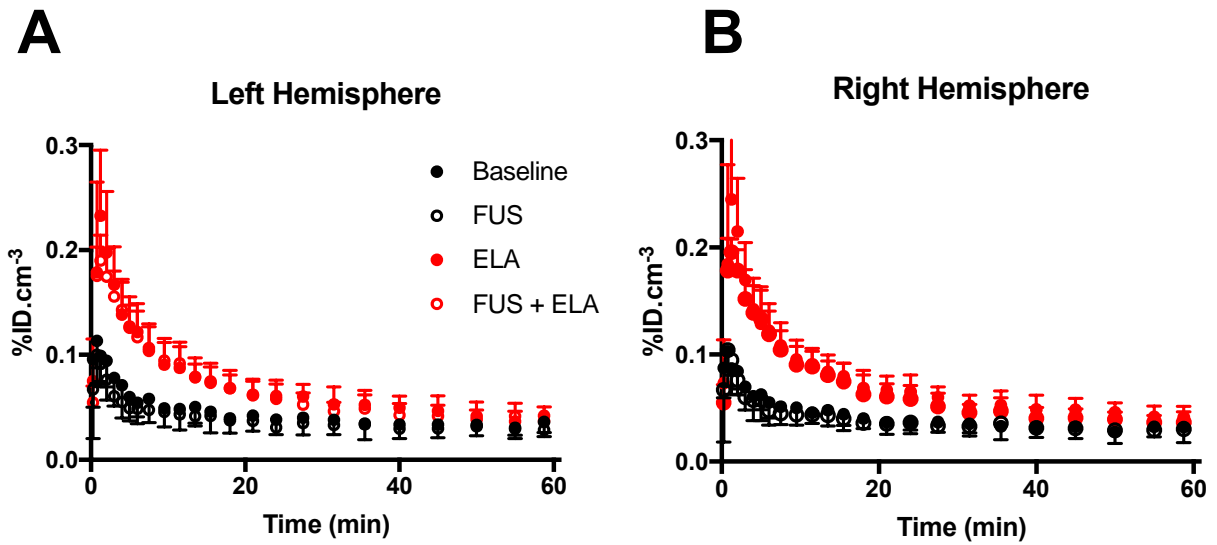


Figure 3-9: Erlotinib brain kinetics assessed using  $^{11}\text{C}$ -erlotinib PET imaging in rats. Kinetic data obtained in volumes of interest drawn in the left (A) and the right (B) hemispheres were assessed for 60 min. PET acquisitions were performed for the four groups: Baseline, FUS, ELA and FUS+ELA. PET data were corrected for injected doses and expressed as % of injected dose (%I.D) versus time (min). Data are showed as mean  $\pm$  s.d.

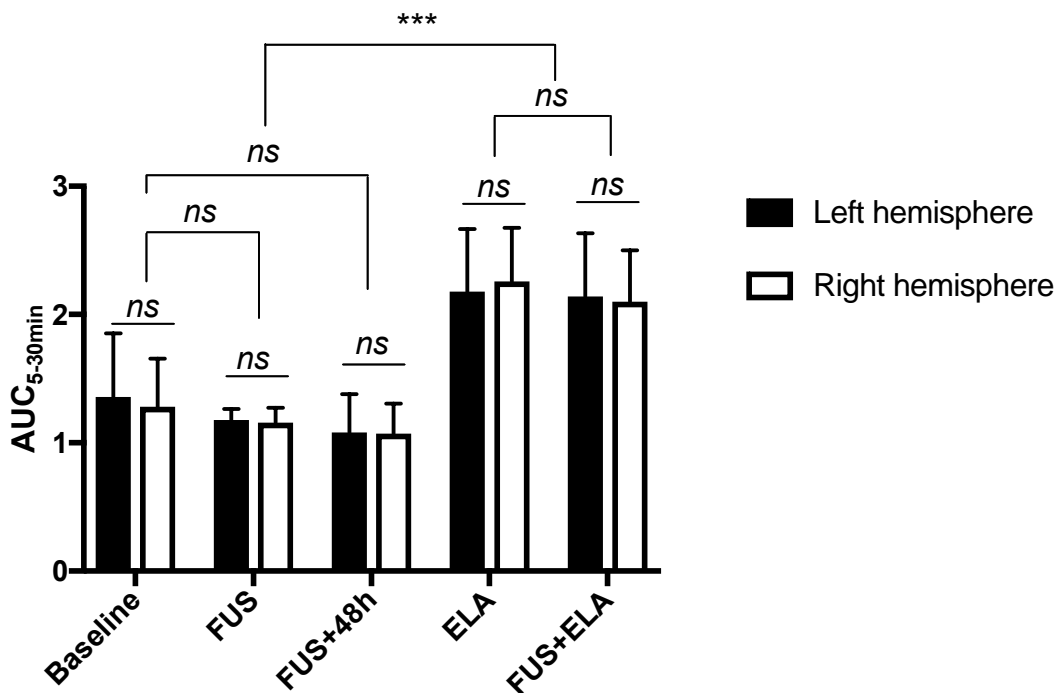


Figure 3-10:  $^{11}\text{C}$ -erlotinib exposure to the brain in the presence of focused ultrasound FUS-induced BBB opening and/or ABCB1/ABCG2 inhibition. Areas under the time-activity curve from 5 to 30 min were calculated in volumes of interest drawn in each brain hemisphere. Data are showed as mean  $\pm$  s.d.

The brain distribution of the ABCB1-specific PET probe  $^{11}\text{C-N-desmethyl-loperamide}$  was low and consistent with previously reported PET data in rats (Farwell et al., 2013). FUS did not increase the brain exposure to the left hemisphere compared with the right hemisphere (paired  $t$ -test,  $p > 0.05$ ). ABCB1 inhibition using tariquidar substantially increased the brain uptake of  $^{11}\text{C-N-desmethyl-loperamide}$ . In the right (intact) hemisphere,  $\text{AUC}_{\text{right}}$  was 3.2 and 3.9-fold higher in tariquidar-treated animals compared with FUS animals (Figure 3-11).

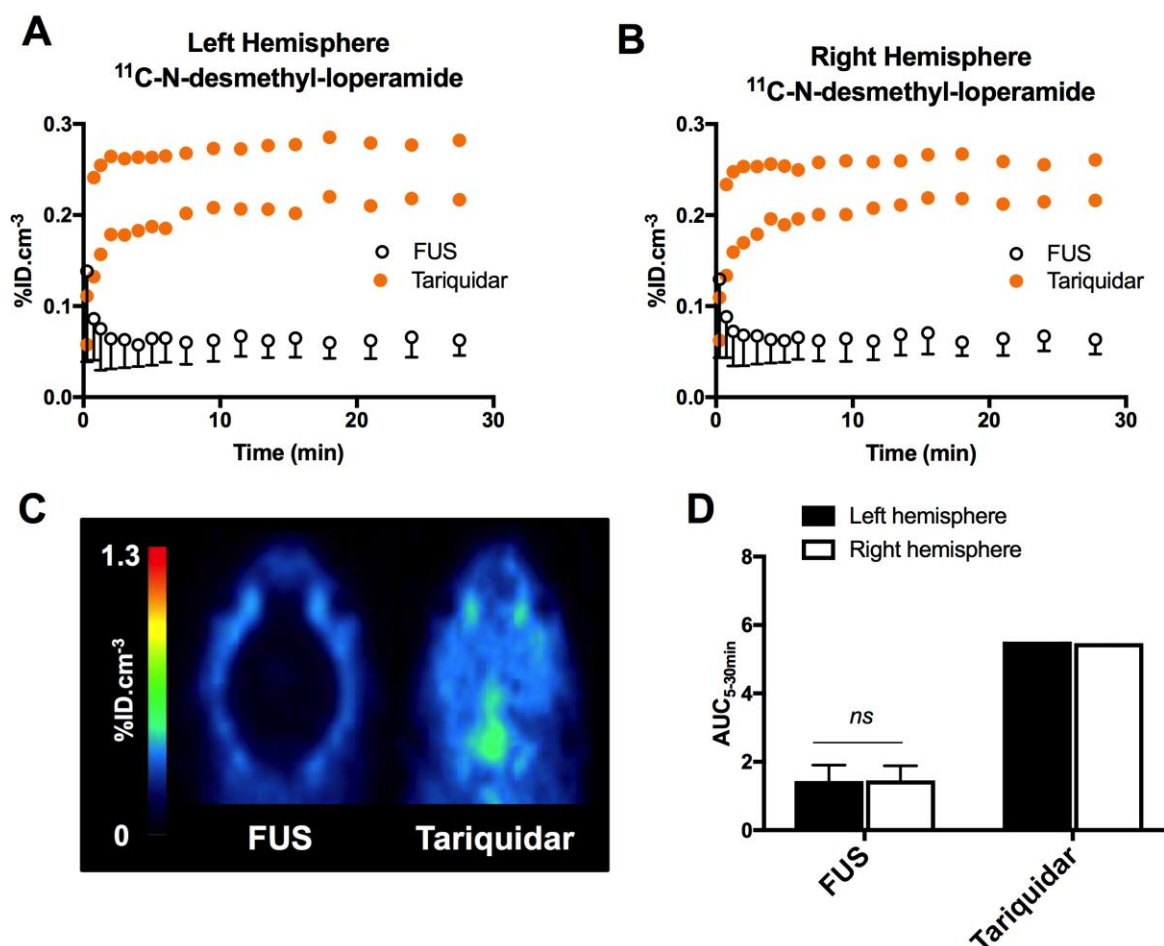


Figure 3-11: The brain kinetics of  $^{11}\text{C-N-desmethyl-loperamide}$  in the left (A) and right (B) are shown during FUS-induced BBB disruption of the left hemisphere (FUS) and after ABCB1 inhibition using tariquidar (8 mg/kg, i.v) as a positive control. Corresponding summed PET images are reported in C.  $^{11}\text{C-N-desmethyl-loperamide}$  exposure to each hemisphere ( $\text{AUC}_{5-30\text{min}}$ ) are reported in D. Data are mean  $\pm$  S.D for the FUS condition ( $n=3$ ) and mean or individual values for the tariquidar condition ( $n=2$ ).

To summarize, we used  $^{11}\text{C-erlotinib}$  PET imaging in rats during FUS-induced BBB disruption and/or pharmacological inhibition of efflux transporters. FUS-induced BBB disruption did not improve the brain exposure to  $^{11}\text{C-erlotinib}$  while ABCB1/ABCG2 inhibition did. A similar result was obtained using the ABCB1-specific PET probe  $^{11}\text{C-N-desmethyl-loperamide}$ . Using this alternative PET probe, we

showed that lack of effect of FUS on erlotinib brain kinetics may not restrict to dual ABCB1/ABCG2 substrates but may also concern ABCB1 substrate.

Table 3-2: <sup>11</sup>C-erlotinib PET study data

Condition	n	Animal weight (g)	Injected dose <sup>11</sup> C-erlotinib (MBq)	T <sub>max</sub> (min)		C <sub>max</sub> (%ID.cm <sup>-3</sup> )		EB extravasion	
				Left	Right	Left	Right	Left	Right
Baseline	5	302±22	42±9	0.75 ± 0.00	0.75 ± 0.00	0.11 ± 0.04	0.10 ± 0.03	0	0
FUS	5	281±14	45±6	0.85 ± 0.22	0.85 ± 0.22	0.11 ± 0.01	0.11 ± 0.01	+	0
ELA	5	267±15	41±5	1.15 ± 0.22	1.15 ± 0.22	0.23 ± 0.06	0.25 ± 0.07	0	0
FUS+ELA	5	289±18	50±7	1.15 ± 0.22	1.15 ± 0.22	0.19 ± 0.03	0.20 ± 0.01	+	0
FUS+48h	4	303±8	53±6	0.75 ± 0.00	0.75 ± 0.00	0.13 ± 0.05	0.13 ± 0.04	0	0

### 3.2.4. Not only size matter

So far, criteria of selection of therapeutic compounds and objects to be delivered through FUS-induced BBB opening is based on their size and molecular weight, thus only taking into account their interaction with the “physical” barrier component of the BBB (Wang et al. 2017; Marty et al. 2012). The molecular weight of erlotinib (MW = 393.4 g/mol) is lower than gadoteric acid (MW = 558.64 g/mol). Our study highlights for the first time the limited impact of FUS-induced BBB opening on the brain exposure to compounds for which BBB permeation is predominantly governed by interaction with the “functional” efflux component of the BBB. In other words, the carrier-mediated efflux has to be taken into account as a new criterion for the selection of drug candidates to be delivered through FUS-aided BBB opening.

Several experimental conditions were used to confirm this unexpected result. In particular, we observed that tested elacridar dose similarly increased the brain delivery of erlotinib regardless of BBB integrity. This ensured that the presence of EB in the brain parenchyma, allowed by BBB opening, did not impede <sup>11</sup>C-erlotinib binding to the brain. Moreover, this indicates that *i)* ABCB1/ABCG2-transport ability persists during physical BBB opening and *ii)* the response to ABCB1/ABCG2 inhibition is similar in the presence and the absence of local BBB opening.

Several studies suggested that FUS may not restrict to the “physical” disruption, but might also impact BBB physiology (McMahon et al., 2017). Using similar conditions than ours, Cho and colleagues reported a decrease in ABCB1 expression at the BBB of the sonicated area, 24h after FUS (Cho et al., 2016). Aryal et al., confirmed this observation and showed that the effect was maximum 48h post FUS (~50% decrease) (Aryal et al., 2017). These studies suggest a connection between the regulation

of the “physical” and the “functional” components of the BBB *in vivo*. In our study, the brain exposure to <sup>11</sup>C-erlotinib measured 48h after FUS did not differ from the Baseline and the FUS group. It has however been demonstrated that a 50% decrease in ABCB1 expression at the BBB may not be sufficient to enhance the brain uptake of avid ABCB1 substrates (Wanek et al., 2015). A dramatic decrease in efflux transporter expression, approaching complete depletion or inhibition may thus be necessary to enhance the brain delivery of erlotinib *in vivo* (Verheijen et al., 2017). Moreover, ABCG2 may functionally compensate any decline in ABCB1 as shown in ABCB1-deficient mice (Kodaira et al., 2010; Traxl et al., 2015). The putative long-term impact of FUS on the kinetics of ABCB1 and ABCG2 expression at the BBB remain to be assessed to conclude on the relevance of acute or repeated FUS as a strategy to enhance the brain delivery of their respective or shared substrates.

Interestingly, we showed that FUS did not further enhance the brain exposure to erlotinib in the situation of partial ABCB1/ABCG2 inhibition. Residual efflux was thus sufficient to counteract physically induced BBB permeation, assuming a partial ABCB1/ABCG2 inhibition in the ELA condition. The absence of additional or synergistic effect between ABCB1/ABCG2 inhibition and BBB opening confirms that ABC-transporter function is the rate-limiting factor for erlotinib brain delivery, thus highlighting the predominance of the “functional” component barrier rather than the “physical” component in controlling the brain penetration of this compound. Therefore, FUS-induced BBB opening is not a relevant strategy to transiently overcome ABC-transporter efflux at the BBB so as to improve the brain delivery of erlotinib and/or to locally potentiate the brain exposure, even in the presence of ABCB1/ABCG2 inhibition.

Our results show that a large and controlled FUS-induced BBB opening did not translate into changes in the brain kinetics of erlotinib. This result highlights the distinction between the “physical” and the “functional” components of the BBB in terms of neuropharmacokinetics. Altogether, these results suggest that drug exposure to the tumor does not solely depend on the “physical” integrity of the BBB and is difficult to predict, especially when interaction with transporters of the BBB is suspected.

### **3.3. Increased delivery of therapeutic compounds with ultrasound**

In this paragraph, I will describe two protocols in which FUS-induced BBB opening was used to increase the delivery to the brain of intravenously injected compounds. Firstly, a co-injection of gadolinium and gold nanoparticles. Secondly, injection of an antibody radiolabelled for PET.

#### **3.3.1. Delivery of gold nanoparticles followed by MRI**

The aim of this study was to deliver gold nanoparticles to the brain. This study was part of the project GRAVITY founded by the French cancer research plan. In addition to NeuroSpin, this project associates four teams in Marseille: physics synthesizing the nanoparticles (LP3), an acoustic lab (LMA), a wave physics lab (Fresnel institute), a neuropharmacology lab (CRO2). These gold nanoparticles are proposed as photothermal agents that can deliver heat to tumors under laser at their peak of absorption. The goal of the project is to deliver them to brain tumors to treat them.

a) BBB opening

The FUS-induced BBB openings were performed as described in Chapter 2: with the 3 axis motorized system, the benchtop RF electronic and the single element transducer. Eight one-year old C57Bl6 mice were used for this study. Mice were anesthetized with 2% isoflurane in a mixture of air and oxygen. They were shaved and placed in an MRI bed for imaging later on. 100  $\mu$ L of microbubbles were injected in the retro-orbital sinus and ultrasound started immediately after. The ultrasound parameters for the opening are the following: 0.9 MPa *in situ*, continuous waves, transducer moving at 10 mm/s, width of the trajectory 5x6 mm<sup>2</sup>, total sonication time of 2 minutes. This acoustic pressure was quite high because at that time we overestimated the attenuation of the skull. Then, gold nanoparticles and 100  $\mu$ L of Dotarem were i.v. injected in the tail vein and animals were put in the 7T scanner. T<sub>1</sub>-weighted images (Multi Slice Multi Echoes, TE 5 ms, TR 300 ms, resolution 0.15x0.15x0.4 mm<sup>3</sup>, matrix size 128x128x20, 8 averages, total acquisition time 5 minutes) were acquired to validate the BBB opening and the extravasation of Dotarem.

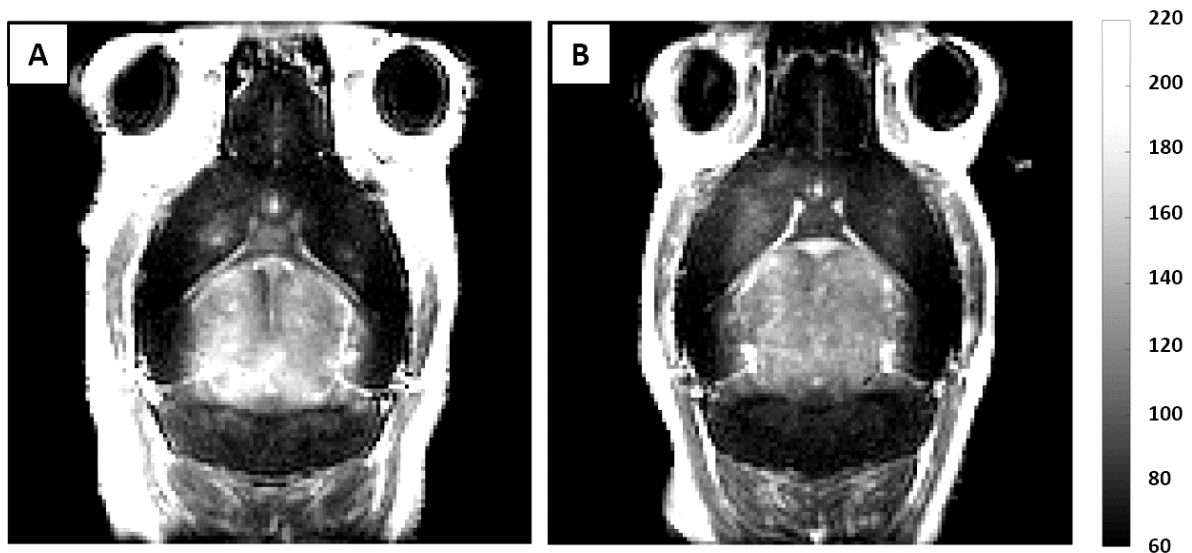


Figure 3-12: T<sub>1</sub>-weighted images after global BBB opening and injection of gadolinium for two different mice.

Figure 3-12 shows two T<sub>1</sub>-weighted images (with the same grey scale) on two different mice. As it can be seen on this figure, the same acoustic parameters can lead to quite different intensity of contrast enhancement. For example, the extravasation of gadolinium was stronger at the back (near cerebellum) for mouse 3 (Figure 3-12 A) than for mouse 4 (Figure 3-12 B). But the extravasation was more homogenous in the striatum for mouse 4 than for mouse 3. These differences might come from the inter-individual differences in terms of skull shape or thickness and/or from the positioning of the transducer on the head on the animals which is sometimes a little bit tilted. These variations of position slightly change the pressure field in the skull cavity and therefore the strength of BBB opening.

Mice were sacrificed one hour after ultrasound with an exsanguino-perfusion protocol and the brains were extracted in order to quantify the amount of gold and gadolinium. This quantification was done

with Inductively Coupled Plasma-Mass Spectrometry (ICP-MS) by collaborators in Marseille Florian Correard and Florence Chaspoul.

b) Correlation between MRI and ICPMS

Figure 3-13 shows the correlation between the quantity of gold or gadolinium and the intensity of the contrast enhancement of  $T_1$ -weighted images. The  $T_1$ -weighted intensity is measured as the mean voxel intensity in the brain. The brain was manually segmented with a Matlab code and only the 6 central slices were used for quantification.

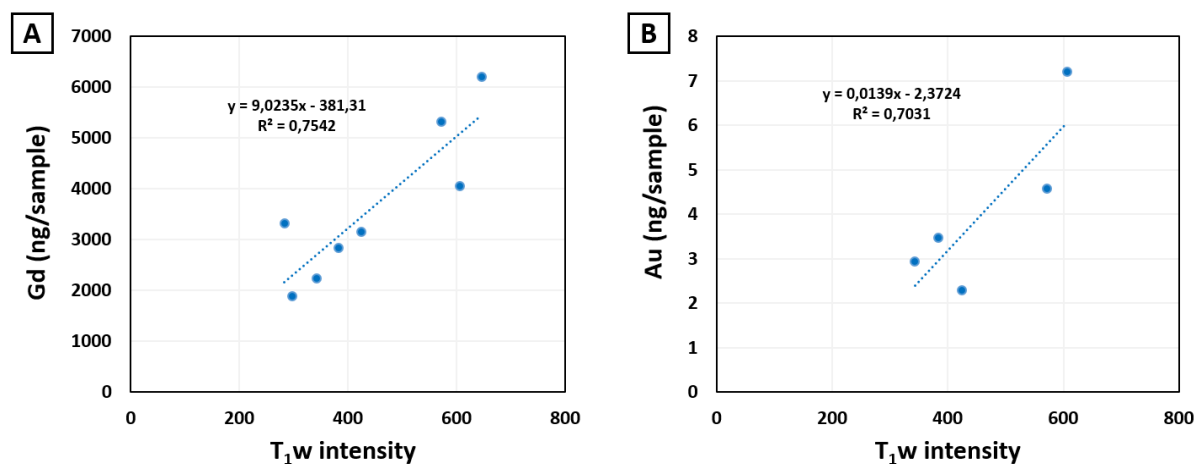


Figure 3-13: A – Correlation between the intensity of the  $T_1$ -weighted image and the mass of Gadolinium in the brain (normalized by the mass of the brain). A – Correlation between the intensity of the  $T_1$ -weighted image and the mass of Gold in the brain (normalized by the mass of the brain).

Interestingly, the mass of gadolinium in the brain correlates well with the intensity of the  $T_1$ -weighted images. The linear regression between the two has a  $R^2$  of 0.75.  $T_1$ -weighted images are not quantitative, unlike  $T_1$  maps, they cannot inform on the quantity of gadolinium in the brain. Indeed, the effect of gadolinium on the signal is indirect: gadolinium impacts the relaxation time of the surrounding water molecules which will, in return, weight the signal on the image. But despite being qualitative the relationship between the quantity of gadolinium and the intensity of the  $T_1$ -weighted image seems proportional, meaning that  $T_1$ -weighted images acquired with the same setup and the same parameters can be used to compare the relative efficiency of the BBB opening between different animals.

Gold nanoparticles were actually found in the brain (Figure 3-13 B) and quantity of Gold in the brain seems to be roughly proportional to the intensity of the  $T_1$ -weighted image as well ( $R^2=0.7$ ). The quantification of gold nanoparticles in the brain with ICP-MS failed in three mice, this results in only five animals on Figure 3-13 B. These results suggest two things *i*) that Gold nanoparticles did extravagate to the brain after BBB opening, which is promising regarding therapy *ii*) that MRI, with  $T_1$ -weighted images, could be used as a good predicting tool.

### 3.3.2. Delivery of an anti-cancer antibody followed by PET imaging

This preliminary study is a collaboration with the team of Charles Truillet in SHFJ, Orsay. The objective of the project is to deliver a therapeutic monoclonal antibody into the brain (Cetuximab, anti-EGFR). The receptor for epidermal growth factor (EGFR) is a prime target for cancer therapy across a broad variety of tumors types, especially in glioblastoma where the EGFR is overexpressed. However due to the problematic of penetrability of blood brain barrier, the potential of anti-EGFR therapy has been unfulfilled. FUS-induced BBB opening should be a promising method to overcome this problem. In this project, the passage of this antibody after BBB opening was studied with PET imaging. To do so, this antibody was labeled with  $^{89}\text{Zr}$ , a long half-life isotope ( $t_{1/2}=3.3$  days). The radioactive compound will be referred to as  $^{89}\text{Zr}$ -mAb. Radiolabeling was done in Orsay. The long half-life of  $^{89}\text{Zr}$  allows to perform several imaging session after one single injection in order to longitudinally follow the biodistribution of the compound. In this section I will only present how FUS-induced BBB opening can improve the delivery of this antibody to the brain. PET imaging and image analysis were done by Charles Truillet.

#### a) BBB opening

The protocol for this experiment is the following. Mice were anesthetized with isoflurane 2% and oxygen. A catheter was placed in the tail vein for injection of microbubbles (50  $\mu\text{L}$ ) and of the radioactive compound. The opening was done with a single element transducer, driven by the “benchtop” portable electronic and moved over the brain by the 3-axis motorized positioning system. After opening, mice were placed in the PET scanner and the radiotracer injected for imaging. Mice were imaged for 1 hour. PET scans were also acquired at 1h, 24h, 48h, 72h and 7 days after opening.

It was the only time in my PhD when I worked on nude mice. On the first day of this study, the mortality after BBB opening and injection of the radiotracer was surprisingly high. Similar acoustic protocol on other mouse strains did not lead to such mortality. Our hypothesis was that ultrasound were shot with an excessive acoustic pressure for nude mice and caused lesions leading to death. So, I performed in nude mice the same optimization of the pressure than the one presented in the Chapter 2 paragraph 2.2.2. After BBB opening, an MR contrast agent was injected and MR images were acquired to validate the BBB opening. 24 hours after ultrasound, mice were imaged once again to assess damages. It appears that an acoustic pressure leading to an opening without damages in C57BL/6 mice, could lead to an opening with damages on nude mice. This might be due to a thinner skull on nude mice than on C57BL/6 mice but we did not perform *ex vivo* measurements to verify it. Within few trials, I was able to perform safe BBB openings on nude mice. In the end, I used an acoustic pressure corresponding to 0.47 MPa in free water, whereas I used an acoustic pressure corresponding to 0.62 MPa in free water in my other protocols in black mice (Chapter 5).

5 mice underwent FUS-induced BBB opening and 5 mice were used as controls without BBB opening.

b) PET imaging

Figure 3-14 shows PET images at 24 hours. These images correspond to the second PET scan session. They are shown because the background noise is lower than immediately after injection. Two mice are presented. On the left (A, B and C), is a control mice which did not undergo BBB opening. On the right (D, E and F), is a mice which underwent BBB opening. The concentration of  $^{89}\text{Zr}$ -mAb in the brain of the ultrasound-treated mice (indicated with orange arrows) is clearly higher than in the brain of the control mice.

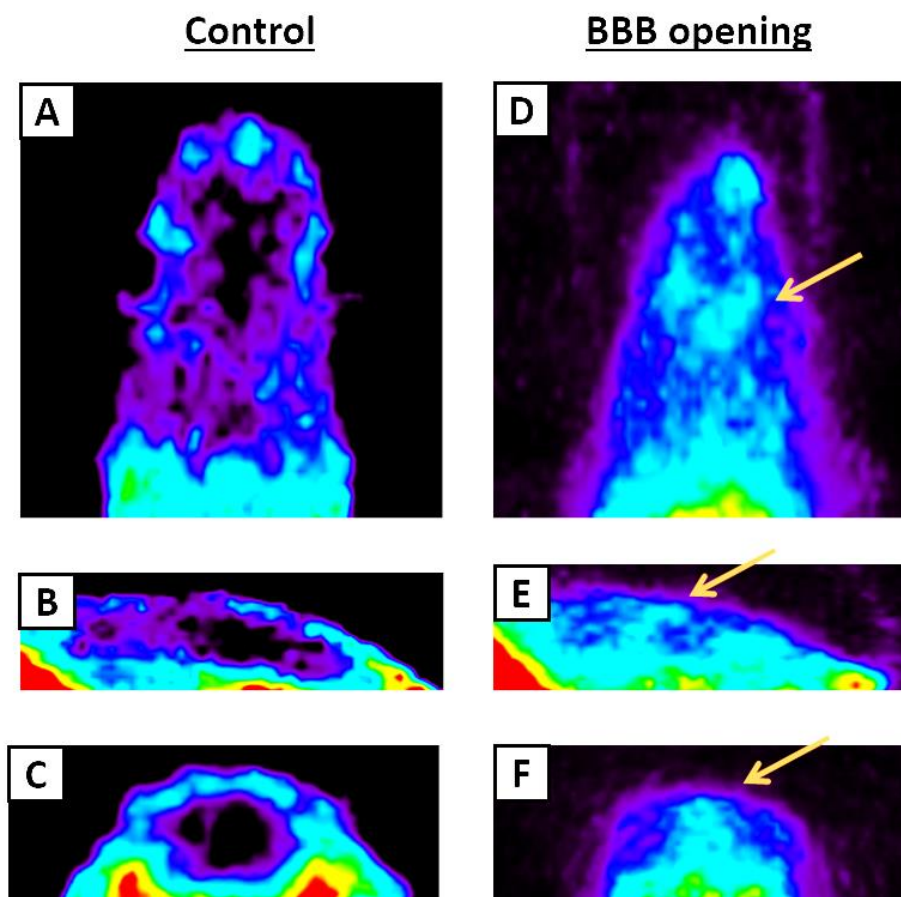


Figure 3-14: PET images. Signal is given by the presence of  $^{89}\text{Zr}$ -mAb in the tissues. A, B and C – Horizontal, sagittal and coronal view of a control mouse with no signal in the brain. D, E and F – Horizontal, sagittal and coronal view of a mouse with BBB opening and with signal in the brain (the brain is indicated with the orange arrow).

Figure 3-15 shows the activity of  $^{89}\text{Zr}$ -mAb. Figure 3-15 A shows its activity in the brain during the first scan, directly after injection. Figure 3-15 B shows the activity of  $^{89}\text{Zr}$ -mAb in the brain for the 10 mice for each imaging session. At 4 hours, the activity is 100% higher in the group with BBB opening when compared with the control group.

As a conclusion, FUS-induced BBB opening was successful in significantly increasing the delivery of  $^{89}\text{Zr}$ -mAb to the brain of nude mice. This work required some optimization of ultrasound parameters but BBB opening could finally be performed safely.

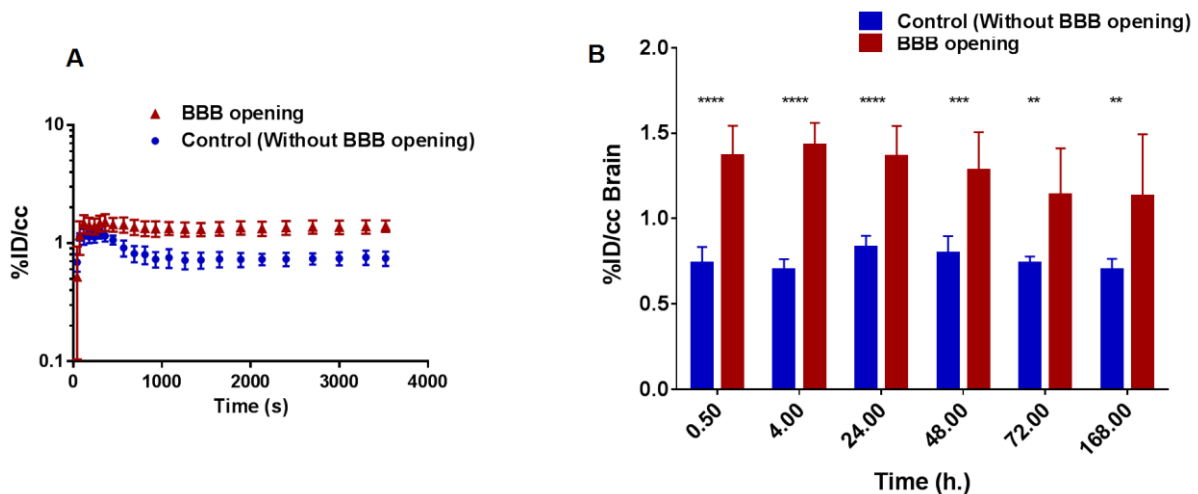


Figure 3-15: A –  $^{89}\text{Zr}$ -mAb activity in the brain as a function of time. B –  $^{89}\text{Zr}$ -mAb activity for each imaging session. %DC = percentage of the injected dose.

### 3.4. FUS-induced Blood-Tumor Barrier opening

Brain tumor therapy is limited by the Blood-Tumor Barrier (BTB) which is an altered and a leakier version of the BBB. The vascular properties of the BTB are heterogeneous among brain tumors and they also spatially vary inside one given tumor. Low intensity Focused-Ultrasound in conjunction with microbubbles has proven efficient in opening the BTB (Shang et al., 2011). Proper studies of the influence of the acoustic parameters on the amount of delivered nanoparticles are not available so far. Although my PhD was not focused on brain tumor therapy, I participated to a protocol run by Allegra Conti, a postdoctoral fellow in our team. In order to enhance the delivery of a contrast agent in brain tumors, we compared two acoustic strategies: a *single spot sonication* and *8-point sonication* covering a larger area but with lower duty cycle. The efficacy of the two methods is compared on the basis of absolute concentrations of delivered MR-contrast agents (MR-CA) and on their rates of uptake/clearance in the tumors.

#### 3.4.1. Symmetrical double implantation of tumors in rats' brains.

8 Fisher rats (6 months old females) were used in this experiment. They were injected, by Françoise Geffroy, senior technician in our team, in charge of cell culture and histology, with the same amount of tumor cells in both left and right striatum in order to be able to compare on the same animal CA leakage with and without ultrasound. During surgery, animals were anesthetized with ketamine/xylazine and maintained in a stereotactic frame under careful monitoring of respiration rate and temperature. An analgesic drug was given to the animals after the surgery. The injected cancer cells are 9L gliosarcoma, 100 000 cells were injected per location. Cancerous cells were injected at two

symmetrical locations, 3 mm on the left and 3 mm on the right of the bregma and at a depth of 4 mm under the skull. The skulls were pierced with a drill and sealed with wax after the injection. Tumor growth was followed by MRI (7 Telsa Bruker) with T<sub>2</sub>-weighted images (RARE sequence). Figure 3-16 shows the evolution of the tumor size as evaluated by 3D manual segmentation of the T<sub>2</sub> images before BTB opening.

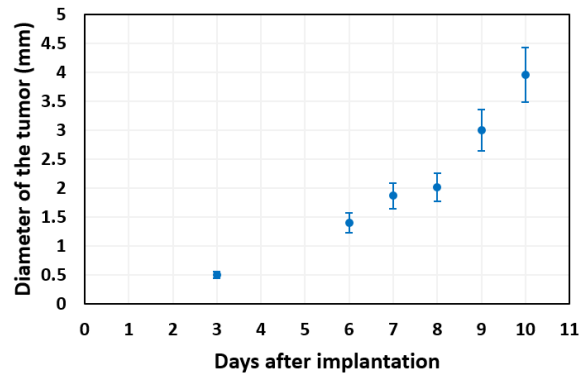


Figure 3-16: Follow-up of the 9L tumor size.

At Day 9, the tumors are already 3 mm large which is enough to perform the experiment.

#### 3.4.2. Ultrasound-induced opening of the blood-tumor barrier

Two strategies were tested to sonicate the tumors. For both of them the 8-element transducer was used. All the ultrasound parameters and the displacements of the transducer are controlled with the Thermoguide software and the motors presented in the paragraph 2.2.1. The first strategy was a “single spot” sonication (Figure 3-17 A) in which the transducer is not moving. The ultrasound parameters are the following: 1.5 MHz, 3ms shots every 100 ms, 1.2 MPa of acoustic pressure *in situ*, 2 minutes of sonication, 1.5 mm steering away from the transducer. Thanks to MR-ARFI, the focal spot can be placed at the center of the tumor before BTB opening.

In order to open the BTB over a larger volume, a second strategy was used. Indeed, the tumors were typically 3-4 mm wide and the focal in the XY plane is only 1.2 mm large. In this “8-point sonication” strategy (Figure 3-17 B), the transducer is moved on a square with 1 mm edges. Two depth of steering are alternated, at 3 mm distance one from the other. The ultrasound parameters are the following: 1.5 MHz, 3 ms shots per points, 1.2 MPa of acoustic pressure *in situ* and 2 minutes total sonication time. At each corner of the square a first shot of 3 ms is done with 1.5 mm of steering and a second shot at 3 ms at 4.5 mm of steering away from the transducer, this second shot is 4 ms after the first one (minimum delay between two shots with a change of steering). One “8-point sonication” trajectory lasts approximately 150 ms long, this results in a slightly shorter duty cycle per points of 2% instead of 3% for the first strategy but this is balanced by the fact that the focal spots are partly overlapping.

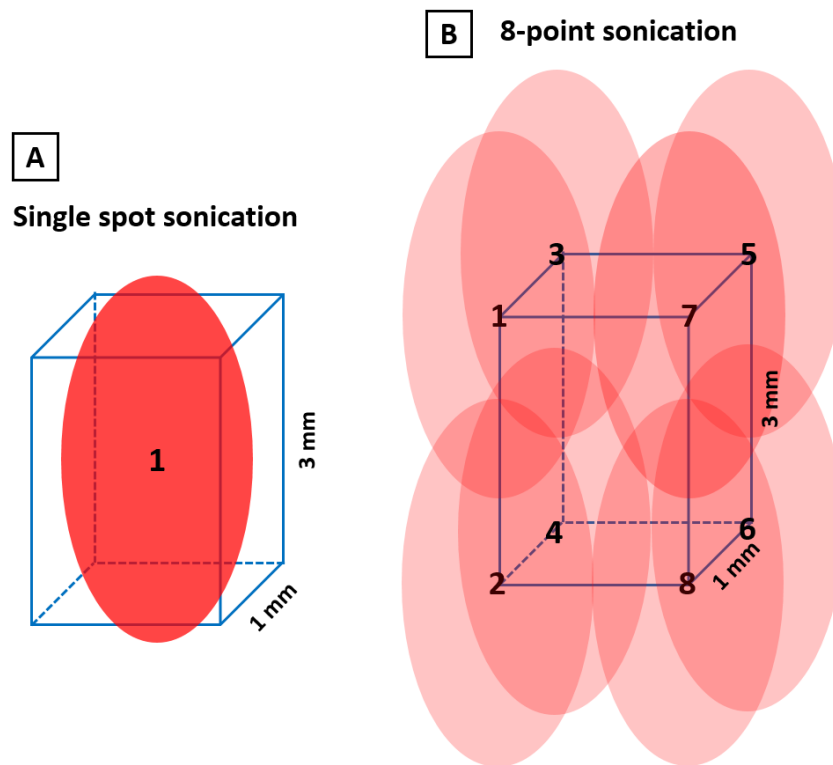


Figure 3-17: Schematic representation of the two strategies for the sonication of the tumors. The red ovals represent the focal spot of the ultrasound beam. On the right, the single spot opening. On the left, the 8-point sonication, on each corner, two 3 ms pulses are shot with two different steerings, then the transducer moved to another corner. The numbers are the order of the shots.

The protocol for the FUS-induced BTB opening is the same protocol as the one described in the paragraphs 2.2.1, 2.3.1 and 2.3.2 of the previous Chapter. Animals were headshaved, anesthetized, a catheter was placed in the tail vein and rats were placed on the bed in the MR scanner. The 8-elements transducer was positioned over the head of the animals. A MR-ARFI was acquired to localize the focal spot, the transducer is moved in order to have the focal spot in the tumor. A first  $T_1$  map was acquired as a reference. Then, 200  $\mu\text{L}$  of microbubbles, were injected via the catheter. Ultrasound started right after bolus injection of the microbubbles. Three animals underwent the “single spot” protocol and five underwent the “8-point sonication” protocol. Then, 250  $\mu\text{L}$  of Dotarem were injected via the catheter and a second  $T_1$  map was acquired to quantify BTB opening.

### 3.4.3. An increased permeability after FUS-induced BTB opening

Figure 3-18 is an example of a *single spot* opening in a tumor. The concentration maps show that the concentration in contrast agent is higher in the sonicated tumor (right tumor) than in the control tumor both at 6 and 19 min after injection of the contrast agent (approximately 20% higher).

Figure 3-19 shows the concentrations in contrast agent over time for the 8 animals as averaged over the whole tumor after manual segmentation on the  $T_2$  images. The mean concentration in the

sonicated tumor is always greater or equal to the concentration in the control tumor. The evolution of the concentrations for the 3 rats that underwent single spot sonication is very much alike, with a maximum concentration in the sonicated tumor around 0.07-0.08 mM rapidly reached followed by a slow decrease. The concentration in the sonicated tumor is always higher (but not necessarily significantly higher) than in the control tumor. The *8-point sonication* gives more variable results: on two rats, it resulted in higher concentrations in the sonicated tumor with a faster washout than for the *single spot strategy*; on the three other rats, the concentrations in the sonicated tumor are not higher than in the control tumor.

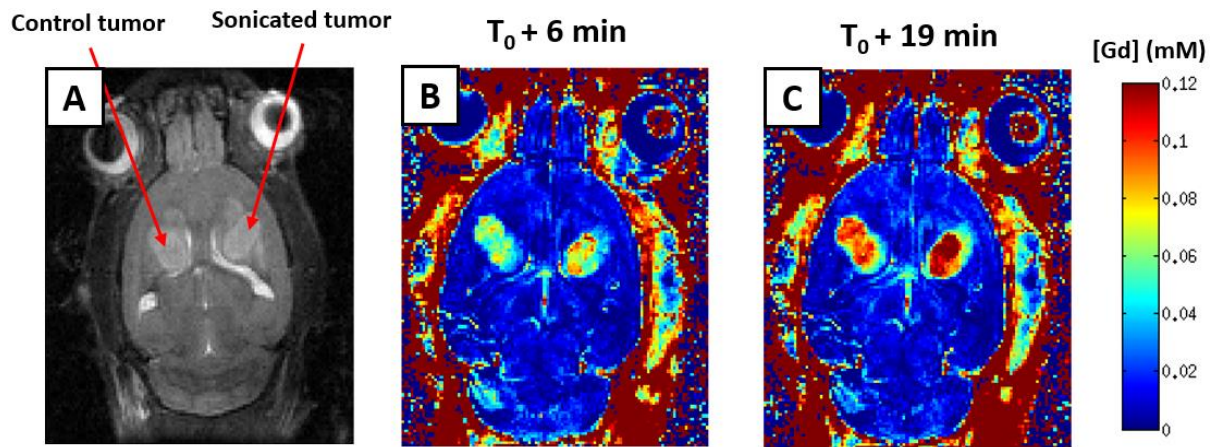


Figure 3-18: Example of a single spot BTB opening. A –  $T_2$ -weighted image to visualize the tumors. B – Concentration map 6 minutes after BTB opening and the injection of the contrast agent. C - Concentration map 19 minutes after BTB opening and the injection of the contrast agent.

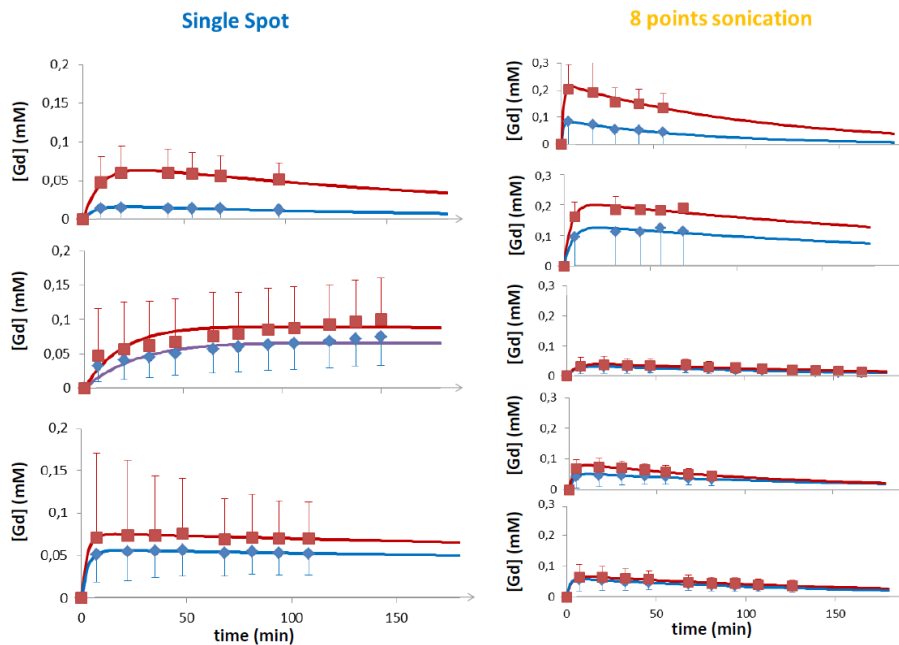


Figure 3-19: Evolution of the concentration in contrast agent in the tumors over time, for the 8 rats. In red the concentration in the sonicated tumor and in blue the concentration in the control tumor. Time 0 correspond to the injection of the contrast agent.

At this stage, it is not clear what strategy is the most efficient to deliver drugs in tumors with FUS-induced BTB opening. This study is still on-going to further compare the strategies. Still, these first results confirmed that, even if at the basal state the BTB of 9L tumors is more leaky than the BBB of surrounding tissues, drug (or contrast agent) leakage to the tumor can be further increased thanks to focused ultrasound.

### 3.5. Conclusion

In this chapter, I firstly presented the study of the diffusion of several contrast agents after BBB opening. The found tortuosity was in good accordance with the literature unlike with direct intracranial injections. So, we concluded that FUS-induced BBB opening is a way to deliver drugs to the brains that does not alter diffusion properties in the parenchyma that is to say does not restrain bio-availability. Then, I studied the delivery of erlotinib after FUS-induced BBB opening. It appeared that opening the “physical barrier” (i.e. loosening the tight junctions) with ultrasound was not enough to counter the activity of the efflux pumps. In the next section, I proved that FUS-induced BBB opening was successful in increasing the delivery of gold nanoparticles, as assessed by ICP-MS, and a therapeutic antibody, as assessed by PET imaging. Finally, I showed that even if the blood-tumor barrier is already more leaky than the blood-brain barrier, it can be further permeated thanks to ultrasound.

<b>CHAPTER 4. IMAGING OF ALZHEIMER'S DISEASE .....</b>	<b>99</b>
<b>4.1. A new functionalized contrast agent: AgulX-Peg-PIB.....</b>	<b>99</b>
4.1.1. Characterization of AgulX.....	100
4.1.2. Delivery of AgulX-Peg-PIB in the brain of APP/PS1 mice .....	102
a) Context .....	102
b) Ultrasound protocol for AgulX-Peg-PIB delivery .....	103
c) MR imaging .....	103
4.1.3. Validation of the targeting with histology.....	104
<b>4.2. Ex vivo imaging of Alzheimer's disease.....</b>	<b>106</b>
4.2.2. Automatic plaque detection .....	107
a) Optimization of sum of the echoes.....	108
b) Cortex segmentation.....	109
c) Detection of the hyposignals.....	110
4.2.3. Amyloid plaque load quantification .....	111
a) On mice .....	111
b) On rats.....	112
4.2.4. In vivo imaging .....	113
4.2.5. An efficient method to quantify amyloid load.....	115
<b>4.3. Imaging AD with X-ray phase-contrast at the ESRF .....</b>	<b>115</b>
4.3.1. Phase-contrast imaging.....	116
4.3.2. AgulX delivery.....	116
4.3.3. Imaging of Alzheimer's mouse brains.....	118
4.3.4. Correlation with MRI .....	120
<b>4.4. Imaging Alzheimer's disease with histology .....</b>	<b>121</b>
4.4.1. Amyloid plaques imaging .....	121
a) Imaging of A $\beta$ deposits: Thioflavin-S.....	121
b) Imaging of iron deposits: Perls' .....	122
c) Correlation between iron and amyloid plaques .....	123
4.4.2. Other stains related to Alzheimer's disease .....	125
a) Tau protein imaging.....	125
b) Neuroinflammation imaging.....	125
<b>4.5. Conclusion.....</b>	<b>126</b>

## Chapter 4. Imaging of Alzheimer's disease

The development of an imaging technology capable of visualizing and quantifying A $\beta$  plaques in animal models is critically important for translational, preclinical and clinical research. In this Chapter, I aim to image one characteristic of AD: the amyloid plaques. I will present different methods, *in vivo* or *ex vivo*, with or without contrast agents, with MRI, histology or phase contrast imaging. In the first section, I will present a new contrast agent that can be grafted to target amyloid plaques. Delivered with FUS-induced BBB opening to the brain of mice modeling AD, its binding to amyloid plaques was assessed with histology. In the second section, the development of a pipeline for amyloid plaques detection of amyloid plaques on APP/PS1 mice will be presented. This pipeline goes from MR imaging of *ex vivo* mouse heads to automatic quantification with a homemade software. The third section will introduce X-ray phase contrast imaging and how it can be used for amyloid plaques detection. The last section will be focused on brain staining.

### 4.1. A new functionalized contrast agent: AgulX-Peg-PIB

AgulX are a new efficient type of gadolinium-based theranostic molecules (drug and contrast agent), which has recently been developed for MRI-guided radiotherapy. These new particles consist of a polysiloxane network surrounded by a number of gadolinium chelates, usually 10. They approximate formula is  $Gd_{10}Si_{40}C_{200}N_{50}O_{150}H_x$  and their size inferior to 5 nm for a mass of 10 kDa. They were developed by the team of Francois Lux and Olivier Tillement from Institut Lumière Matière in Lyon (France).

It has been shown that the relaxivity of AgulX can be 2 to 3 time superior to Dotarem (Sancey et al., 2014) which makes them a good MR-contrast agent. The toxicity and elimination of the compound has also been extensively studied (Sanden et al., 2015). AgulX are eliminated via the urinary route in a two-step process involving rapid elimination of biodegraded and smaller particles and slower elimination of larger particles. The effect of AgulX on renal function was limited to the vacuolation of the proximal tubules cells; this phenomenon was moderate, transient, and did not affect renal function itself. It turned out that AgulX eliminated well from the organism, which is a prerequisite for the clinical development of such agents.

Pre-clinical studies have also demonstrated the impact of such particles on different heterotopic and orthotopic tumors (Francis et al., 2009). We have at our disposal three kinds of AgulX provided by our partners in Lyon: naked AgulX, Peg grafted AgulX (AgulX-Peg) to increase its bio-stability and AgulX grafted with Peg and Pittsburg compound (AgulX-Peg-PIB) to target amyloid plaques of Alzheimer's disease (Plissonneau et al., 2016).

In this section, I will firstly characterize the relaxivity and diffusivity of the different AgulX and secondly, I will present a study in which we delivered those nanoparticles in the brain of Alzheimer's mice.

### 4.1.1. Characterization of AgulX

The three AgulX were characterized in terms of relaxivity and diffusion. Indeed, their relaxivity has never been studied at high field. Figure 4-1 shows the relaxivity of the AgulX at 7 T. They were measured in phantoms which are tubes filled with the compound dissolved in an agar-agar gel. The protocol was identical to the one presented in Chapter 3. The found relaxivity were  $5.3 \text{ s}^{-1}\text{mM}^{-1}$  for the naked AgulX, 8 for the AgulX-Peg and 9.4 for the AgulX-Peg-PIB.

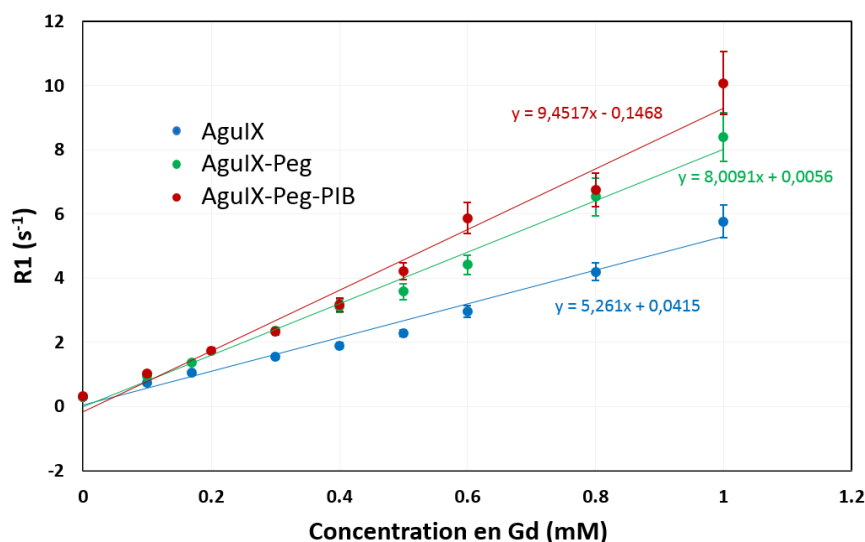


Figure 4-1: The inverse of the relaxation time as a function of the concentration in contrast agent, for the three kinds of AgulX at 7 Tesla.

Figure 4-1 shows that the relaxivity increases with the size of the AgulX, the grafted AgulX being bigger than naked AgulX. Those results are in accordance with the BBP model of Bloembergen, Purcell Pound (Bloembergen et al., 1948). Indeed, as described in this model, the bigger the molecules the higher the relaxivity. This model explains that big molecules rotate more slowly and therefore the interactions between one gadolinium and the surrounding water molecules are longer. Those longer interactions make the spin-lattice interaction more efficient which means that bigger molecules shorten more the  $T_1$  of surrounding water molecules (so they have a higher relaxivity).

The stability of the relaxivity was also studied over time. The phantom was left up to 6 hours in the MR scanner and warmed up at  $37^\circ\text{C}$ . Figure 4-2 shows the relaxivity of AgulX-Peg and AgulX-Peg-PIB over time (for 4 and 6 hours respectively). The relaxivity of AgulX-Peg and AgulX-Peg-PIB appeared to be really stable over time (around 8 and 9.4 respectively). This result is important regarding the diffusion experiments. Indeed, it means that the diffusion protocols relying on  $T_1$  maps remain valid because the relaxivity does not change over time.

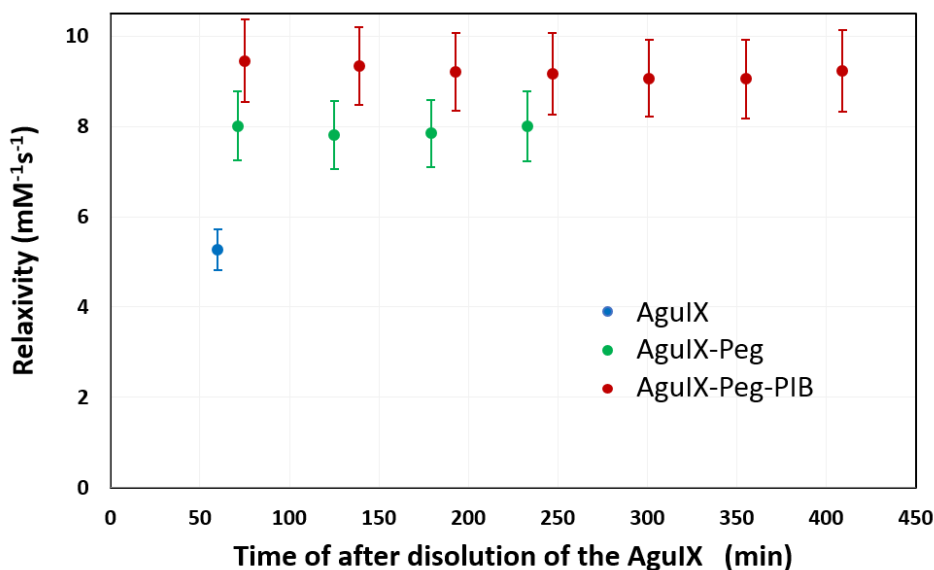


Figure 4-2: Evolution of the relaxivity over time, for the three kinds of AgulX.

The *in vitro* diffusion was measured with the same protocol as in Chapter 3. The diffusion of the three kind of AgulX is displayed on Figure 4-3 as well as the square of the normal distribution's width over time.

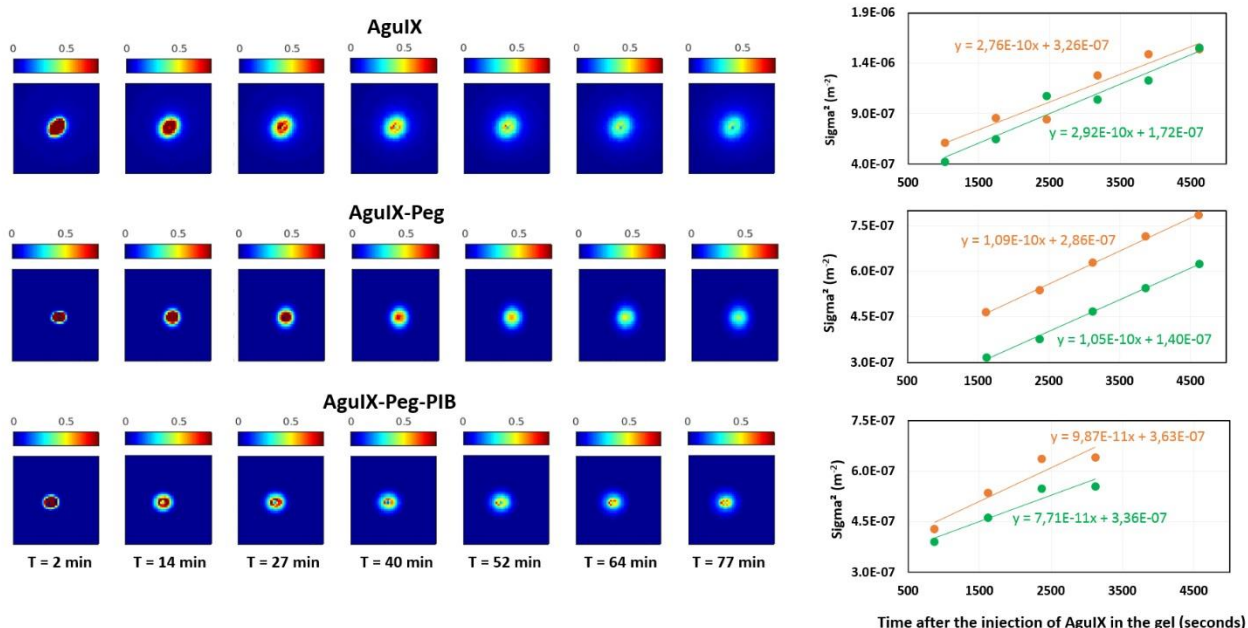


Figure 4-3: On the left the diffusion of the three kinds of AgulX. Axial view of the concentration maps over time. On the right the square of the widths of the normal law fits as a function of time.

The free diffusion coefficient  $D_{free}$  were  $2.84 \cdot 10^{-10}$  m<sup>2</sup>/s for the naked AgulX,  $1.07 \cdot 10^{-10}$  m<sup>2</sup>/s for the AgulX-Peg and  $0.88 \cdot 10^{-10}$  m<sup>2</sup>/s for the AgulX-Peg-PIB. As predicted by the Stokes-Einstein equation, larger molecules diffuse more slowly, so have a smaller diffusion coefficient. Only the diffusion in rat brains of the naked AgulX was studied, the results were presented in Chapter 3.

So, with a high relaxivity, AgulX can be efficient contrast agents. But their low diffusion coefficient, around one fourth of the diffusion of Dotarem, might prevent them to diffuse efficiently into brain tissues.

#### 4.1.2. Delivery of AgulX-Peg-PIB in the brain of APP/PS1 mice

In this study our objective was to get AgulX-Peg-PIB in the brain of APP/PS1 mice, thanks to FUS-induced BBB opening, and to study their binding to amyloid plaques later on with histology. This study was done in collaboration with Jonathan Pansieri and Christel Marquette from the laboratory of Chimie et Biologie des Métaux of CEA Grenoble.

##### a) Context

*In-vivo* imaging of amyloid plaques remains a challenge. The current technique to assess amyloid load in patients is PET and radio-tracers grafted with PIB (Klunk et al., 2004). PET allows to quantify amyloid, however, its low spatial resolution does not allow to visualize single amyloid plaques. MRI is currently investigated as a unique tool to achieve single plaque imaging. The iron core of amyloid plaques induces a susceptibility effect on  $T_2^*$  MR images. In mice, this effect allows direct single plaque imaging (Jack Jr et al., 2005) but with the low SNR on *in vivo* images, amyloid plaques imaging remains a challenge. One challenge is to tell amyloid plaques from blood vessels which also contain iron. Hence the need to develop targeted magnetic nanoparticles (MNPs) to strengthen this effect. Such MNPs have been developed like USPIO-PEG-A $\beta$ 1-42 (Wadghiri et al., 2013) or PUT-Gd-A $\beta$  (Poduslo et al., 2002). Both compounds allow *in-vivo* detection of amyloid plaques. For USPIO-PEG-A $\beta$ 1-42, authors reported hypo-signals similar to compound targeted amyloid in WT mice, emphasizing the difficulty to tell marked amyloid plaques from blood vessel on  $T_2^*$  images. To avoid confusion with blood vessels, contrast agent affecting  $T_1$  relaxation might come in useful, as blood vessels do not have strong contrast on  $T_1$ -weighted images. PUT-Gd-A $\beta$  enhances the contrast of amyloid plaques on  $T_1$ -weighted images with a low, but significant, contrast between plaques and tissue. In both cases those compounds rely on their natural crossing of the BBB, which is moderate and constrain to use large dose of product. Their efficacy could therefore be increased using ultrasound-induced BBB opening, or the quantity injected could be decreased for the same efficacy. Our experience is the first attempt, to our knowledge, to target amyloid plaques *in vivo* with PIB grafted MNPs after ultrasound induced BBB opening to increase their delivery.

Our MNPs also affect the  $T_1$  relaxation time and could allow single plaque imaging on  $T_1w$  images. Unfortunately, due to the small quantity of AgulX-Peg-PIB at our disposal, we only had few tries to tune a lot of parameters such as ultrasound parameters, quantity of MNPs injected, the delay between MNPs injection and imaging or the TE/TR and resolution of the  $T_1$ -weighted MR images. Aware of the number of tries required to tune those parameters in order to achieve single plaques imaging, our main focus was to get AgulX-Peg-PIB to the brain, thanks to ultrasound and study their binding to amyloid plaques later on with histology.

b) Ultrasound protocol for AgulX-Peg-PIB delivery

Mice were anesthetized with Isoflurane (3% in an air-oxygen mix, 1L/min) and their head were shaved to ensure a good coupling with the latex balloon. 100 $\mu$ L of microbubbles (diameter 2-8  $\mu$ m, Sonovue, Bracco) were retro-orbitary injected. Ultrasound were immediately applied with two different protocols. In the first protocol the focal spot of the ultrasound was fixed and ultrasound were pulsed (3% duty cycle), thus opening a 1x1x5 mm<sup>3</sup> volume in the brain (corresponding to the size of the focal spot of the ultrasounds). One mouse underwent this protocol. In the second protocol, the transducer was moved over the head of the mice so the focal spot covered a large volume of the brain with continuous ultrasounds (100% duty cycle), as described in (Magnin et al., 2015). Three mice underwent this protocol. In both cases, the estimated peak negative pressure in the brain was 0.6 MPa and the frequency 1.5 MHz. After the opening, the MNPS were intravenously injected and mice were moved in the MR scanner (11.7 Tesla, Bruker, Germany) equipped with a cryo-probe. Temperature and breathing frequency were monitored.  $T_1$ -weighted images (MSME, 2D, TE/TR = 6/290 ms, resolution 130\*130\*250  $\mu$ m, matrix size 140\*110\*28, 5 averages, acquisition time 2.5 minutes) were acquired to detect to MNPs in the brain.  $T_1$ -weighted images were acquired before the ultrasound protocol to be used as a references. As control, one mouse underwent injection of AgulX-Peg after BBB opening and one mouse underwent injection of AgulX-Peg without BBB opening.

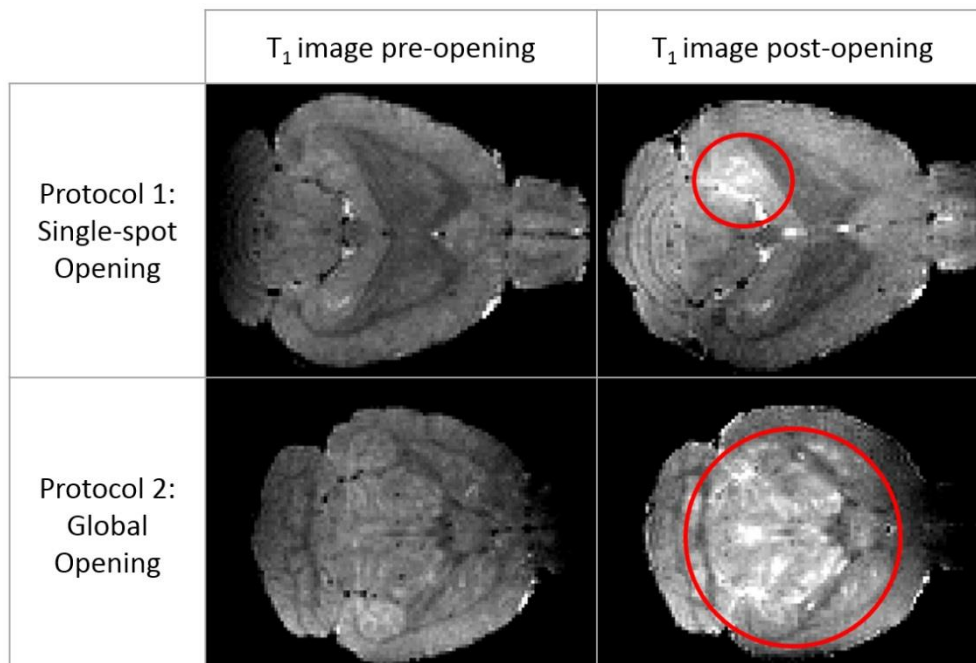
c) MR imaging

Figure 4-4:  $T_1$ -weighted images before BBB opening and after BBB opening and injection of the AgulX-Peg-PIB at 11.7 Tesla. For both protocols, the  $T_1$ -weighted images post opening show an increase of the intensity in the sonicated region (in red) demonstrating the delivery of AgulX-Peg-PIB to the brain.

Figure 4-4 shows T<sub>1</sub>-weighted images before and after the BBB opening and the injection AgulX-Peg-PIB. For the first protocol, the intensity clearly increases (in the red circled area) on the post-ultrasound image when compared with the contra-lateral side which was not open (+35 %). For the second protocol, the global intensity is also higher in the opened volume of brain on the post-ultrasound image when compared with the prefrontal cortex which was not open (+20 %). Those results suggest that both protocols were efficient in opening the BBB and allowed the nanoparticles to cross the BBB and reach the brain parenchyma. Also, that the first technique, more localized, provides a stronger opening than the second, more global. This was expected as the duty cycle per volume of brain is higher in the first experiment.

At the end of the MRI acquisition, approximately 2 hours after the BBB opening, mice sacrificed with exsanguino-perfusion to remove the blood from the vessels. Brains were harvested and kept in PFA.

### 4.1.3. Validation of the targeting with histology

The ability to target nanoparticles on amyloid plaques *in vivo* was verified by immunohistology. Those measurements were done by Jonathan Pansieri and Christel Marquette. The protocol they used is briefly explain here, more details are available on the article from *Pansieri et al.* (2018).

The brains were then cut using a microtom. Brain slices were pre-incubated with blocking buffer before incubation with mouse anti PEG antibody. Nanoparticles were then detected by treating tissues for 20 min with 0.05% 3,3'-diaminobenzidine (DAB) tetrachlorhydrate. Images were obtained using a Zeiss microscope Axiovert 200 M equipped with AxioCam ERc 5s camera (Carl Zeiss) and analyzed using Carl Zeiss AxioVision software.

Other frozen sections were processed for fluorescence immunohistochemistry with same anti PEG antibody and with Thioflavin-S for amyloid aggregates. Thereby, AgulX-Peg-PIB nanoparticles targeting amyloid plaques were evaluated through detection the fluorescence of secondary antibody conjugated with Alexia 594 ( $\lambda_{ex} = 590 \text{ nm}$ - $\lambda_{em} = 617 \text{ nm}$ ) and amyloid burden with ThS ( $\lambda_{ex} = 450 \text{ nm}$  -  $\lambda_{em} = 488 \text{ nm}$ ) (Sigma, #T1892) according to standard practice. Nuclei were revealed by Hoechst dye. Fluorescent images were recorded using Zeiss confocal LSM 800 microscope and analyzed using Carl Zeiss Zen software.

AgulX-Peg-PIB has been found in brain tissue, mainly in the thalamus nuclei (ventral, lateral and posterior lateral), geniculate nuclei, amygdaloid (basolateral, post-lateral, post-medium) nuclei, and piriform and enthorinal cortex (Figure 5A). Some nanoparticles appear to be associated with or close to the amyloid charge (Figure 5B-F), suggesting the need to follow the behavior of the MNPs at different times after injection, to distinguish specific and nonspecific targeting. Mice injected with control nanoparticles (without the PIB target) also cross the BBB and diffuse into the tissue (Figure 5G). However, no colocalization was evidenced between amyloid plaques and AgulX-Peg-PIB. Finally, the nanoparticles injected into mice which do not have prior ultrasound-induced BBB opening, remained in the cerebral vascular area (Figure 5H).

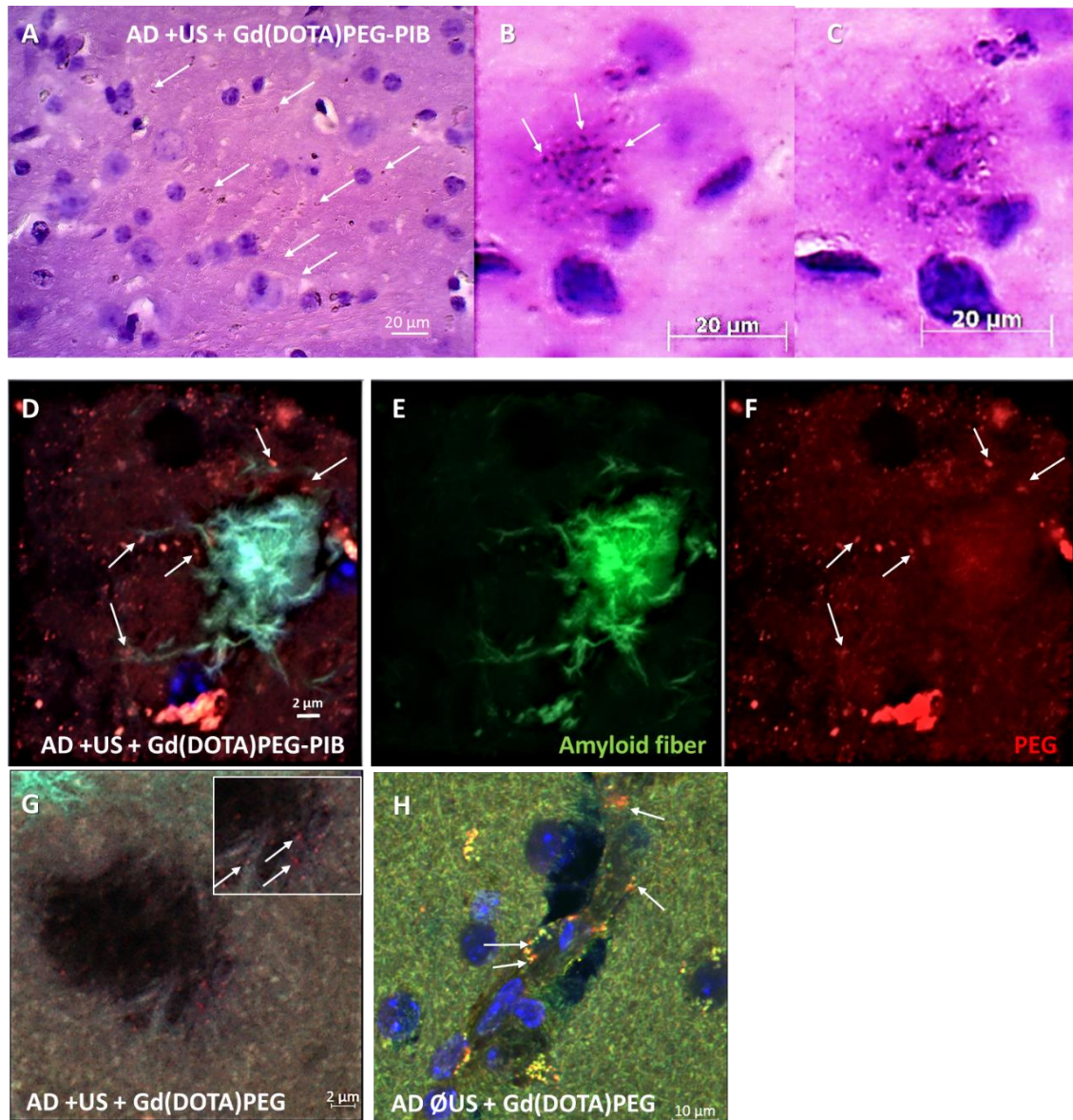


Figure 4-5: Immunohistological pictures of Gd(DOTA)PEG-PIB delivery inside cerebral tissue after BBB opening by ultrasound. (A-C) The images revealed the diffusion of MNPs into the brain using an antibody directed against the spacer PEG integrated in MNPs (brown spots) (A). Some of Gd(DOTA)PEG-PIB were located in the vicinity of amyloid plaques (hematoxylin-eosin counterstaining) (B,C). (D-F) Confocal microscopy observations confirmed a close colocalization (D) between amyloid fibers (E: thioflavin S staining (green)) and Gd(DOTA)PEG-PIB (F: anti-PEG antibody revealed by secondary conjugated antibody Alexa-594 (red)). (G,H) For control, others AD mice were injected with MNPs without the amyloid targeter-PIB with (G) or without (H) prior ultrasound opening BBB: respectively, MNPs either diffuse into the brain but none specific accumulation around amyloid aggregates was observed (G), suggesting they remained localized in the vessel (H).

## 4.2. *Ex vivo* imaging of Alzheimer's disease

In this section I will present a pipeline, which I developed, to quantify amyloid load on *ex vivo* images. This pipeline was used to quantify the amyloid load on mice of different age with results in accordance with the literature. This pipeline was also tried on *ex vivo* images of rats and *in vivo* on mice.

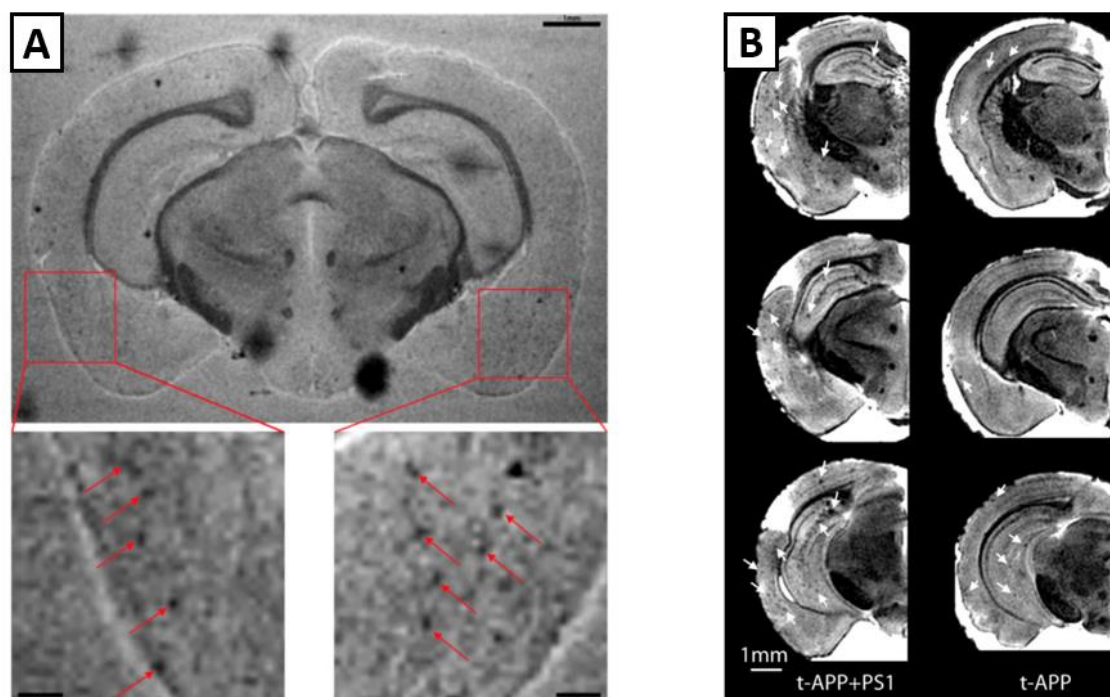


Figure 4-6: A – MGE image of a APP/PS1 mouse at 7 T, resolution:  $45 \times 45 \times 60 \mu\text{m}^3$  (from Meadowcort et al., 2009) B – MGE images of APP/PS1 and APP mice at 9.4 T, resolution:  $46 \times 62 \times 62 \mu\text{m}^3$  (from Zhang et al., 2004)

It was shown in the early 2000s' that amyloid plaques can be identify using  $T_2^*$  images in postmortem human hippocampus tissues (Benveniste et al., 1999). Amyloid plaques have iron in their core (James et al., 2016), as well as other metals, and iron is a ferromagnetic compound. Placed inside a magnetic field, iron will locally change the magnetic field. So, water molecules of the amyloid plaques have a disturbed magnetic field which shortens the  $T_2^*$  of those molecules, thus giving a hypo-signal on the  $T_2^*$  images.  $T_2^*$  based *ex vivo* imaging of amyloid plaques in transgenic mice has already been demonstrated (Meadowcort et al., 2009; Zhang et al., 2004) (Figure 4-6) and the increased transverse relaxation associated with  $A\beta$  plaques has largely been credited to focal iron deposition within the amyloid plaques (Chamberlain et al., 2011; Wengenack et al., 2011).

In this paragraph, I present the optimized MGE sequence I developed to detect amyloid plaques in APP/PS1 mice. The two constraints were i) to be isotropic for a better quantification of the amyloid load ii) the sequence should fit in an overnight scan so the total acquisition time had to be inferior to 12 hours.

#### 4.2.1. The MGE sequence

For *ex vivo* imaging, mice were exsanguino-perfused with PBS and PFA. The heads of the mice were stored in PFA at 4°C. 48 hours before imaging heads were re-hydrated in PBS. Then, heads were placed in small tubes filled with Fc40, a liquid that does not give any signal on MR images as it does not contain hydrogen. The head was placed inside a Cryo-probe: a two coils antenna that is cooled down to very low temperature in order to reduce the electronic noise. Brüker claims that this antenna has an increased sensitivity of 2.5 to 5.3 compared to standard room temperature RF-coils, which is really convenient for high resolution imaging. Then, the Cryo-probe was placed inside the 11.7 Tesla Brüker scanner for imaging (Figure 1-21).

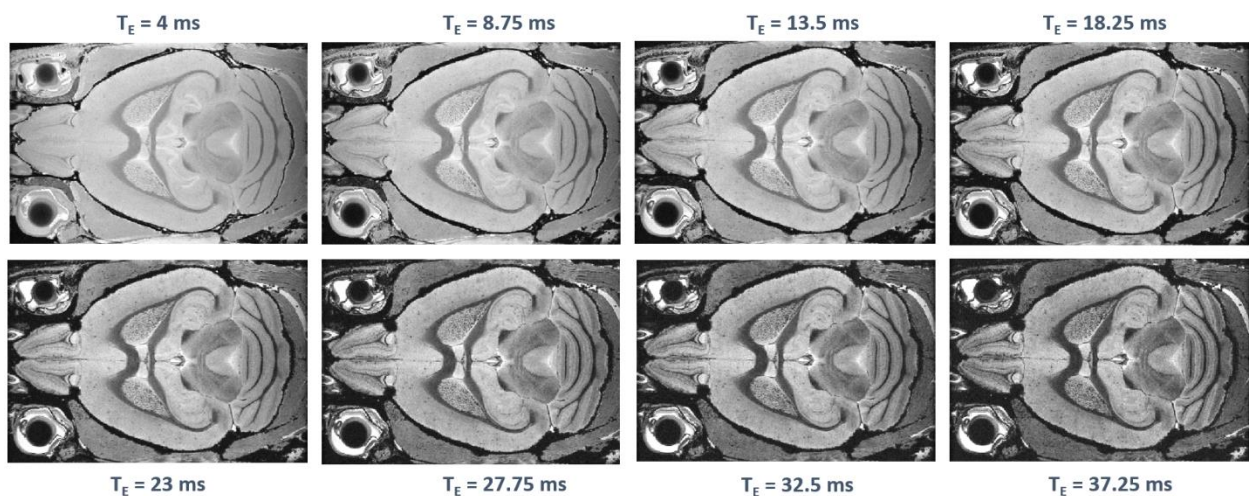


Figure 4-7: The 8 echoes of the MGE sequence

The sequence used for *ex vivo* imaging was a Multi Gradient Echoes (MGE). This sequence, with a short relatively short TE and a long TR, was  $T_2^*$ -weighted. The parameters of the sequence are the followings: TE 4 ms, TR 90 ms, echo spacing 4.75 ms, resolution  $40 \times 40 \times 40 \mu\text{m}^3$ , matrix size  $400 \times 270 \times 180$ , encoding 3D, number of echoes 8, number of averages 12, total acquisition time 12 hours. Before starting the sequence, the antenna was carefully tuned and matched and a second order shim was done in the brain. Saturation bands are placed around the field of view.

As shown on Figure 4-7 the first echoes (short TE) have a high SNR (signal to noise ratio) but a low CNR (contrast to noise ratio) between the amyloid plaques and the cortex. The last echoes (long TE) have a lower SNR but a higher CNR.

#### 4.2.2. Automatic plaque detection

In this section I present the post processing of the *ex vivo* images which leads to amyloid plaques quantification. The echoes are summed to give the best contrast, the cortex is segmented and finally, a homemade Matlab code detect and cluster the hypsignals.

a) Optimization of sum of the echoes

In order to obtain the best contrast between the amyloid plaques and the cortex, the optimum echo time  $TE_{optimum}$  was calculated. Figure 4-8 B shows the  $T_2^*$  decay of voxels from the cortex (in blue) and from amyloid plaques (in red), the  $T_2^*$  of the cortex ( $T_{2^*Co}$ ) and the  $T_2^*$  of the amyloid plaques ( $T_{2^*Pl}$ ) can be fitted. Indeed, for each voxel the signal decreases with TE as a mono-exponential with a time constant  $T_2^*$ . The maximum difference between the signal from the cortex and the plaques occurs at TE given by the following formula:

$$TE_{optimum} = \ln\left(\frac{T_{2^*Co}^*}{T_{2^*Pl}^*}\right) \cdot \frac{T_{2^*Co}^* \cdot T_{2^*Pl}^*}{T_{2^*Co}^* - T_{2^*Pl}^*} \quad (4.1)$$

The  $T_2^*$  map is shown on Figure 4-8 A. The  $T_2^*$  of the amyloid plaques was about 20 ms and the  $T_2^*$  of the cortex was about 37 ms. From the equation (4.1) the  $TE_{optimum}$  is estimated at 27 ms, which correspond to the sixth echo. So, when averaging the different echoes, more weight was given to the sixth echo and less to the other echoes. The weight of each echo is given on Figure 4-8 C.

This weighting was arbitrary and proved to function rather well. But it can be further optimized. The optimum image was also simulated (from  $M_{xy}(0)$  and  $T_2^*$ ) but contrast between plaques and cortex was not better. On the weighted sum of the MGE images, the SNR in the cortex was about 63 and the CNR between plaques and the cortex about 11.

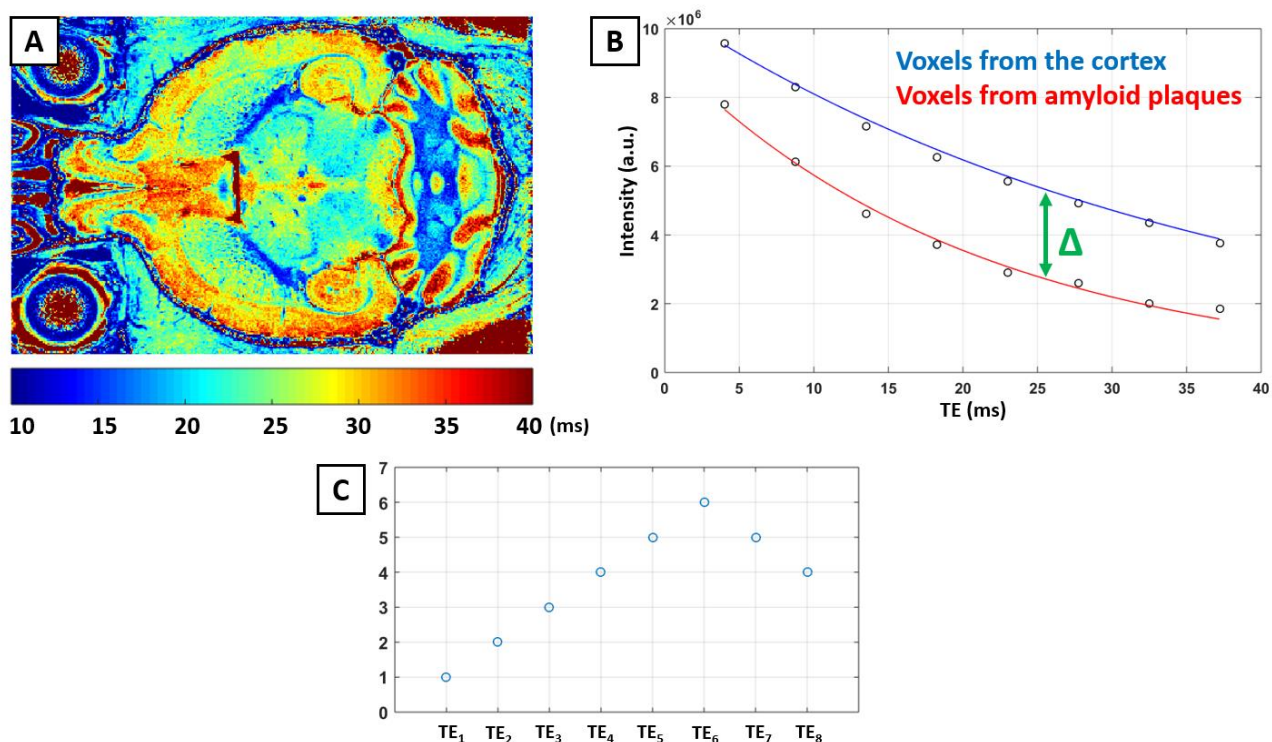


Figure 4-8: A –  $T_2^*$  map of a mouse brain fitted from the different echoes of the MGE sequence. B –  $T_2^*$  decay of the transverse magnetization for voxels from the cortex (blue) and voxels from the plaques (red). C – Weight given to the different echoes when summing them. More weights were given to the echoes around the echoes 6<sup>th</sup> because  $TE_{optimum}$  is estimated at 27 ms.

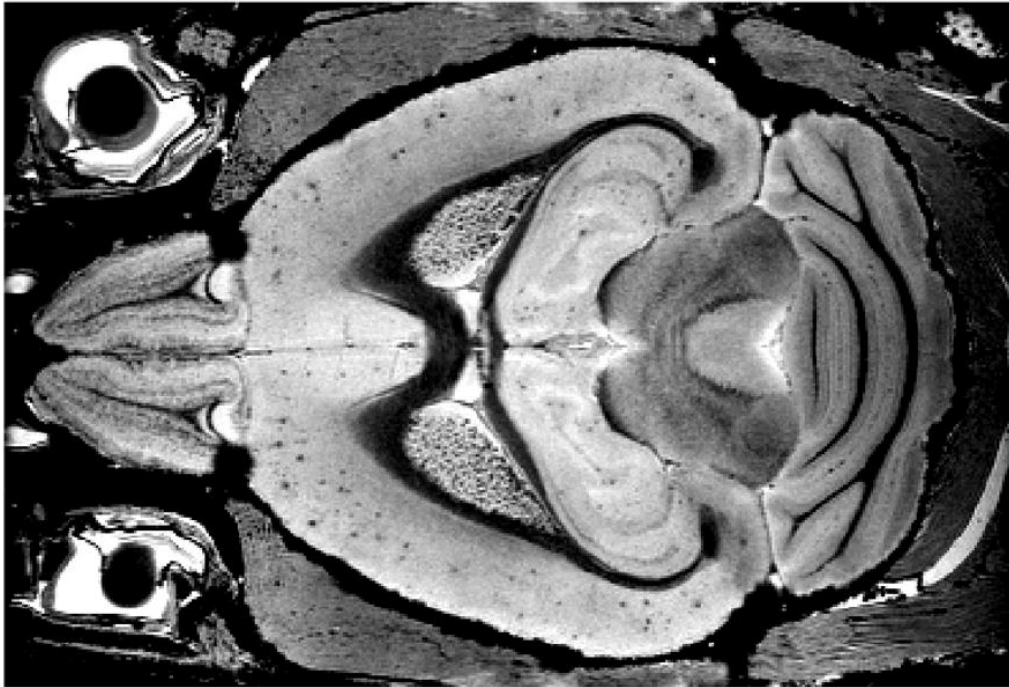


Figure 4-9: Weighted sum of the echoes.

The weighted sum of the echoes is given on Figure 4-9. A lot of amyloid plaques (black dots) are present in the cortex and few in the hippocampus. This is expected since this mouse is one year old and that this model exhibits amyloid plaques as early as 6 months.

b) Cortex segmentation

The cortex was the region with the higher amyloid plaque loaded. Moreover, it was the region where it was the easiest to detect them because of the relatively homogenous signal in the cortex (compare to hippocampus for example). So, in order to quantify the amyloid load in the cortex, the first step was to segment the cortex.

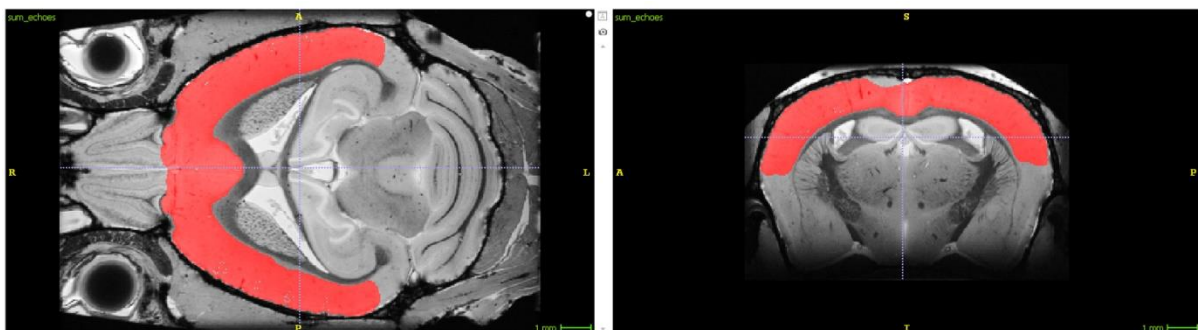


Figure 4-10: Segmentation of the cortex with the ITK-SNAP software. In red the resulting mask of the cortex.

The segmentation was done with the ITK-SNAP software (Yushkevich et al. 2006, [www.itksnap.org](http://www.itksnap.org)). ITK-SNAP provides semi-automatic segmentation using active contour methods. Firstly, the image was threshold with an upper and lower limit. Then, seeds are manually placed in the cortex to initialize the region growth. The lower threshold was set to exclude white matter, the upper threshold does not really matter but shall not exclude parts of the cortex. The seed radius typically 0.36 and approximately 50 seeds were placed in the cortex. The *region competition force* was set to 1 and the *smoothing force* to 0.75. An example of cortex segmentation is shown on Figure 4-10. The segmentation did not cover the back and the bottom of the cortex because of the difficulty to tune the algorithm. Including those parts always caused a leakage of the region growth outside of the cortex.

c) Detection of the hyposignals

The amyloid plaques detection was performed with a Matlab code which I developed. This code detects local minimums with a threshold. The threshold was automatically and locally adapted because the intensity of the image was not homogenous in the whole cortex. Indeed, the antenna used to acquire those images was a surface antenna, which means that the signal decreases with depth. In other words, the parts of the brains closer to the antenna gave more signal. The antenna being above the head, the bottom parts of the brains gave less signal. Moreover, when the tube containing the head was not perfectly horizontally aligned, the brain was tilted left-right and one of the hemispheres was closer to the antenna and thus gives more signal. For those reasons, the threshold was local, typically on a neighborhood of 15x15x15 voxels. Every voxel of the cortex below the local threshold was classified as amyloid plaque. But this method gave false positives due to wrongly perfused blood vessels. Indeed, as amyloid plaques, the blood contains iron which also give a hypo-intense signal on  $T_2^*$  images. To get rid of the blood vessels a clustering of the voxels below the threshold was done. Typically, an amyloid plaque is 50 to 100  $\mu\text{m}$  large, so with voxels of 40x40x40  $\mu\text{m}^3$ , biggest plaques contain a dozen of voxels. So, clusters bigger than 12 voxels were excluded: not classified as amyloid plaques but as remaining blood in the vessels.

Figure 4-11 shows an example of an automatic plaques detection on a one-year old APP/PS1 mouse. The amyloid plaques are shown in red. Even if amyloid plaques are present in other structures, only the amyloid plaques in the cortex are detected. And not all of them were detected because the masks did not cover the back and the bottom of the cortex. This code allows to quantify the amyloid load in the cortex of mice. It was used to compare different cohorts of different experiments. For each experiment the parameters of the different steps (intensity threshold, neighborhood size, cluster size...) are kept constant to compare the different cohorts, they will be reminded in the manuscript for each experiment.

It was reported that amyloid plaques do not induce susceptibility change (Dhenain et al., 2002), and therefore we cannot expect the enlargement effect in MRI. This observation implies that the plaque must be larger than the voxel size to be detected. We can assume that we do not detect small amyloid plaques inferior to 40  $\mu\text{m}$ .



Figure 4-11: Automatic detection of the amyloid plaques in the cortex. In red, overlaid on the anatomical image, pixels that were classified as amyloid plaques.

#### 4.2.3. Amyloid plaque load quantification

This pipeline was tested to quantify amyloid plaque load on APP/PS1 mice and TgF344-AD rats.

##### a) In mice

This quantification was done on 12 APP/PS1 mice (7 one-year old and 5 two-year old) and also on 2 one-year old wild type mice. For this study the threshold under which a voxel is classified as amyloid plaque was fixed at 85% of the mean intensity of the local neighborhood (15x15x15 voxels) and the threshold on the cluster above which the plaque is classified as a blood vessel was fixed at 15 voxels. Results are given on Figure 4-12.

The plaque load, in terms both of volume ratio and of number of plaques, was significantly higher ( $P=0.005$ , Wilcoxon test) for the two years old mice when compared with the one-year old mice. This result makes sense as APP/PS1 mice keep on developing amyloid plaques all their life. The detection process resulted in a lower plaque load for wild type mice when compared with APP/PS1 mice, even if it is not significant due to the small number of animals in this group (only two). The amyloid plaque detection in wild type animals gives the sensitivity of the method as no amyloid plaques are present in those animals. The hypsignals detected on wild type mice could only be artefacts (blood vessels,

edges of the mask, field inhomogeneity). The really low number of voxels classified as amyloid plaques in wild type animals attests for the robustness of the method.

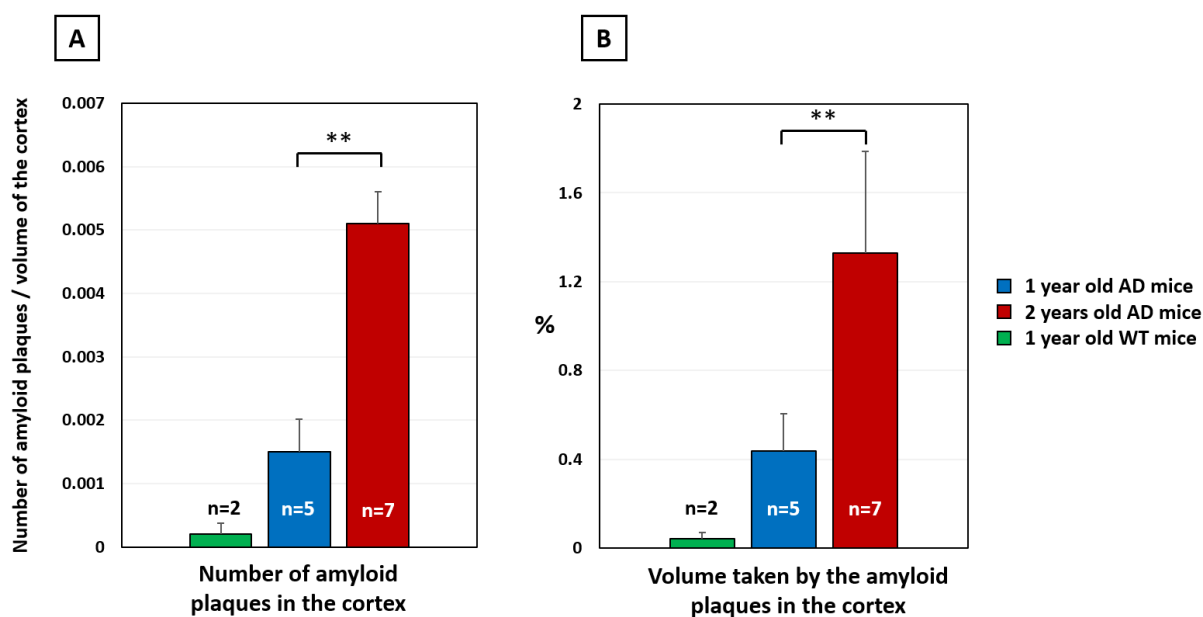


Figure 4-12: Quantification of the amyloid load on different mice. A – Number of amyloid plaques in the cortex normalized by the volume of the cortex. B – Volume ratio of the amyloid plaques in the cortex.

The amyloid plaque load in the two-year old mice is three times as high as in the one-year old mice in terms of volume ratio. This results is in good agreement with the study of *Babcock et al.* where they found a 2.5 fold increase in amyloid plaque load between transgenic mice of one year and transgenic mice of two years (Babcock et al., 2015). It has to be noticed that they quantified amyloid load with brain staining of the whole brain, so on 2D images whereas I did it on 3D images and on the cortex only.

#### b) In rats

I also tried amyloid plaque quantification on few rats. The setup at the 11.7 T was made for mice, so I had to adapt the sequence to our 7 T scanner (Bruker, Biospin, Germany) equipped with a surface antenna at room temperature. The modified MGE sequence had the following parameters: TE 3.5 ms, TR 90 ms, echo spacing 4.65 ms, resolution 80x80x80  $\mu\text{m}^3$ , matrix size 360x22x140, 10 echoes, 23 averages, acquisition time 17 hours. Moving from a 11.7 T to a 7 T scanner and from a cryo-probe to a room-temperature antenna induced a severe loss of SNR, even with a longer acquisition time.

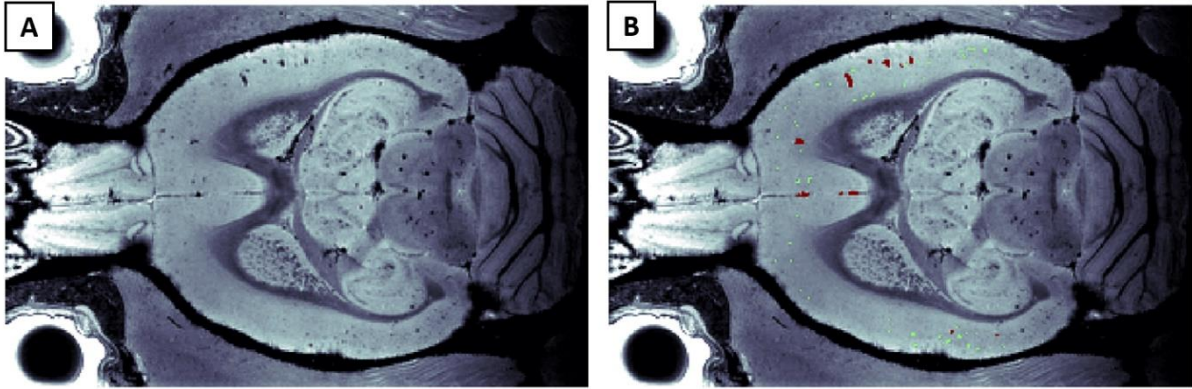


Figure 4-13: A – Sum of the echoes of the MGE image for the 18 months old TgF344-AD rat.  
B – Amyloid plaque detection on the same rat, amyloid plaques in green and blood vessels in red.

Figure 4-13 A shows the sum of the echoes of the MGE sequence on an eighteen-month old TgF344-AD rat. Big hyposignals were probably blood vessels not enough perfused. Figure 4-13 B shows the detection of amyloid plaques. In green what was classified as amyloid plaques and in red the hyposignals classified as blood vessel.

Amyloid plaque load quantification was performed in two Alzheimer's rats: one of nine months and one of eighteen months. For the nine-month rat, the volume ratio of amyloid plaques in the cortex was 0.007 and the number of plaques (normalized by the volume of the cortex) was 0.0025. For the eighteen-month rat, the volume ratio of amyloid plaques in the cortex was 0.017 and the number of plaques (normalized by the volume of the cortex) was 0.0048. For both indexes, we can observe a 2.4 and a 1.9-fold increase of the amyloid plaque load.

So, even if the resolution had to be degraded to image rats, it was still possible to detect amyloid plaques. The oldest rat had a lot of wrongly perfused blood vessels (where blood remains) but they were well classified as blood vessels with the criteria on the size of the cluster. As expected we found more amyloid plaques in the eighteen-month rat when compared to the nine-month old rat. Indeed, in this model the amyloid load increases with the age of the animals (Cohen et al., 2013).

#### 4.2.4. In vivo imaging

*In vivo* imaging was also tried. *In vivo* imaging is much more challenging due to *i)* the presence of blood in the vessels giving hyposignals similar to amyloid plaques and *ii)* to the total acquisition time which has to be strongly reduced and thus decreasing the signal-to-noise ratio. I will present here the protocol with the imaging of the same cohort of Alzheimer's mice at different ages and the evolution of the amyloid plaques quantification.

Seven male APP/PS1 mice were imaged at 8, 12 and 17 months at the 11.7 T scanner equipped with the cryo-probe. The sequence used was derivated from the sequence used *ex vivo*. The resolution was degraded in order to balance the loss of SNR resulting from a shorter acquisition time. The sequence was an 3D Multi Gradient Echoes with the following parameters: TE 4 ms, TR 90 ms, echo spacing 3 ms, resolution 60x60x60  $\mu\text{m}^3$ , matrix size 280x180x120, encoding 3D, number of echoes 8, number of

averages 1, total acquisition time 32 minutes. During imaging, mice were anesthetized with 2% isoflurane in a mixture of air and oxygen. Respiration rate and body temperature were monitored and controlled. Mice were scanned with the exact same protocol at 8, 12 and 17 months.

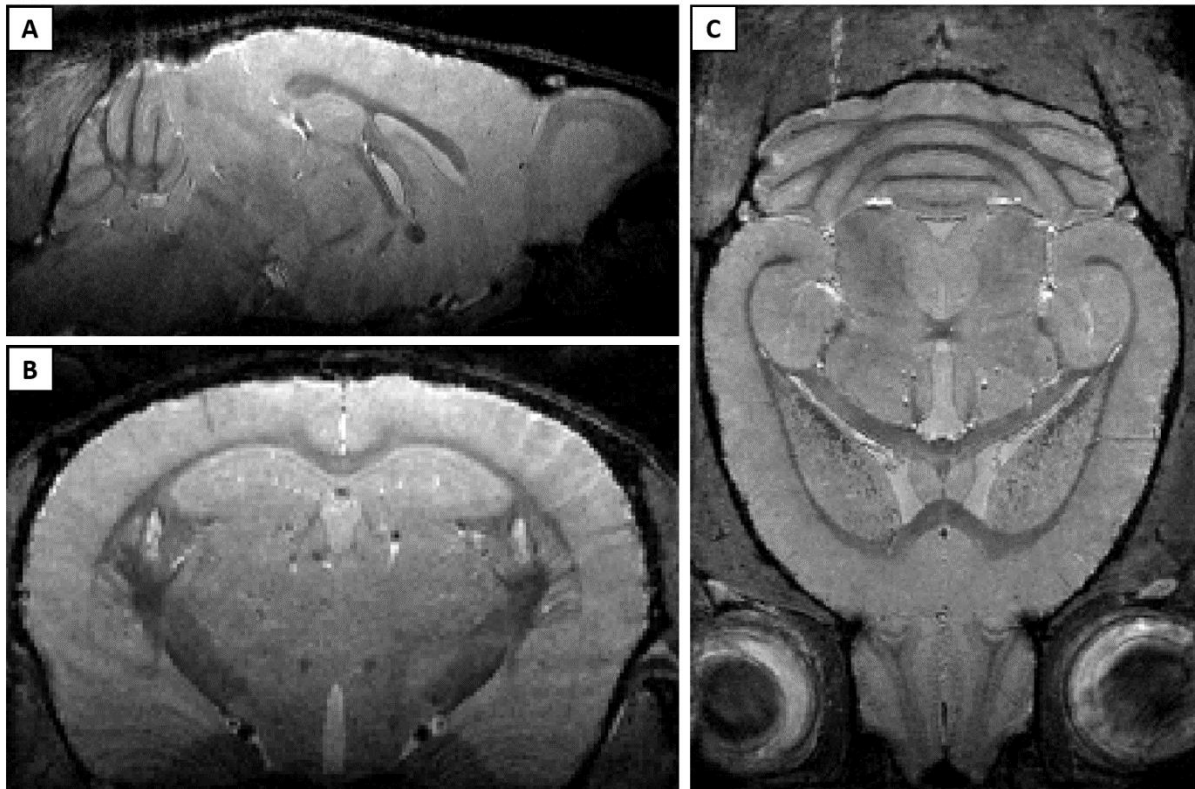


Figure 4-14: MGE sequence for *in-vivo* amyloid plaques imaging

Unfortunately, this setup and this sequence did not allow to image amyloid plaques *in vivo*. Figure 4-14 illustrates *in vivo* imaging on an APP/PS1 mice at 17 months. Despite APP/PS1 mice developing a lot of amyloid plaques at this age, we were unable to image them. All the hyposignals present in the cortex were blood vessels. It can easily be told as those hyposignals are continuous when going dynamically through the slices.

As I described earlier in this chapter, it has already been proven that *in vivo* amyloid plaques imaging is feasible but almost always with contrast agents. For example, a large variety of Superparamagnetic Iron Oxide Nanoparticles (SPIONs) has been designed for MRI, with both *ex vivo* and *in vivo* follow up. So far, SPIONs are mainly tested in rodent models, with amyloid plaques and tau tangles. Some of them can sufficiently penetrate the BBB, and act as promising *in vivo* contrast agents. On mouse models of AD, anti-A $\beta$  and anti-tau antibodies-coated SPIONs doubled the number of MRI-visible plaques with suggested spontaneous crossing of the BBB.

Alternatively, gadolinium-based contrast agents have also been tested to improve amyloid plaques detection. Concerning AD and cerebral amyloid angiopathy, the combination of gadolinium-based nanoparticles with targeting molecules (PIB, polyphenols, peptides and antibodies) remains the common strategy (André et al., 2017). Most of these works attempt to prove the *in vivo* concept, but

also needs *ex vivo* confirmation. Thus, in mice modeling AD, PUT–Gd–A $\beta$  (Le Duc et al., 2014) enhances the contrast of amyloid plaques on T<sub>1</sub>-weighted images with a low, but significant, contrast between plaques and tissue *in vivo*. Gd(DO3A)-PIB shows a specific recognition of A $\beta$  plaques, as Gd(DTPA) grafted with Amyloid  $\beta$  peptide<sup>52z</sup> or curcumin, and anti-A $\beta$  antibody IgG4.1 vectorized on Gd(DOTA). To overcome the limitation of the BBB, *Dudeffant et al.* intra-cranially injected, directly in the ventricles, a contrast agent (Dudeffant et al., 2017). The amyloid plaques being hydrophobic, the contrast agent penetrates the surrounding tissues and increases the signal given by these surrounding tissues. This resulted in an increased contrast between the amyloid plaques and the brain tissue. But this protocol is relatively invasive.

In this study, we wanted to remain totally non-invasive and without contrast agent. We chose a relatively short acquisition time (32 minutes) in order to preserve old transgenic animals, which are weaker than wild type, to perform several imaging sessions at different ages. One possible continuation of this work would be to try with a longer acquisition time, around two hours, as it has been done in some studies using contrast agent.

#### 4.2.5. An efficient method to quantify amyloid load

To summarize, this pipeline, which goes from imaging to a semi-automatic detection of the plaques on the image, was efficient in quantifying amyloid load. More plaques were detected on old mice when compared with young mice and almost no plaques were detected on wild type mice. Properly adapted, this pipeline also seems to be working for amyloid plaques quantification on rats. Unfortunately, amyloid plaques quantification was not successful *in vivo*. The sensitivity of this technique will be investigated in the next sections by comparison with X-ray phase-contrast imaging and histology.

### 4.3. Imaging AD with X-ray phase-contrast at the ESRF

During my PhD I had the opportunity to image few brains of APP/PS1 mice with X-ray phase-contrast imaging. This technique can image whole brain with a micrometric resolution and can ideally give contrast between brain tissue, gadolinium and amyloid plaques. The idea of this project was to perform a FUS-induced global opening of the BBB on old APP/PS1 mice and to inject a gadolinium-based contrast agent that targets amyloid plaques: the AgulX-Peg-PIB. Phase-contrast imaging would then allow to characterize the specificity of the targeting when compared to the relevant controls. The imaging took place at the European Synchrotron Radiation Facility in Grenoble. Image acquisitions were mainly performed by Lorenzo Massimi from the Alessia Cedola's team at the Sapienza University and Elena Longo from the Philippe Zeitoun's team at Ensta Paristech. Besides providing the samples, I assist them during the first two days of experiment (over 5 days). Image processing was done by Elena Longo.

### 4.3.1. Phase-contrast imaging

Unlike classic X-ray imaging, X-ray phase-contrast imaging does not rely on the decrease of the X-ray intensity (attenuation) by the sample but by the diffraction of the X-ray by this sample at interfaces when the refractive index changes. This diffraction creates interferences that are transformed into intensity variations, which then can be recorded by the detector. Like conventional computed tomography, several 2D phase-contrast images can be combined to obtain the 3D distribution of the real part of the refractive index of the sample.

Several phase-contrast imaging technics exist. The one we used is called propagation-based imaging or in-line holography as the X-ray source, the sample and the detector are aligned. The detector is not placed immediately behind the sample, but in some distance, so the radiation refracted by the sample can interfere with the unchanged beam and create “Fresnel fringes”. The recorded interference fringes are not proportional to the phase itself but to the second derivative of the phase. Therefore, the method is most sensitive to abrupt changes in the decrement of the refractive index (Wilkins et al., 1996). This leads to stronger contrast on the structural boundaries of the sample (such as the edge of the brain or plaques/brain interfaces) than a conventional radiogram. This technique is called edge enhancement.

### 4.3.2. AgulX delivery

The samples I brought at the ESRF are listed in Table 4-1. We only had enough AgulX-Peg-PIB to inject two mice and investigate the targeting of the AgulX-Peg-PIB on the amyloid plaques. All the other mice are controls. Table 4-1 summarizes the different groups and the different conditions. All mice were littermates, their ages go from 20 to 22 months.

The BBB opening protocol was the one presented in Chapter 2 where the permeabilisation is global (on a 6x6 mm square). The BBB openings were performed outside the MR scanner. Immediately after the opening, mice were i.v. injected with the contrast agents in the tail vein and moved inside the scanner for imaging. T<sub>1</sub>-weighted images were acquired in order to validate the penetration of the AgulX into the brain. The quantity of AgulX-Peg and AgulX-Peg-PIB injected was always 10 µmol.

Mice were sacrificed with ex-sanguino perfusion (with PBS and PFA) 3 to 4 hours after injection. We thought this timing was good to observe the specific targeting of the PIB. Indeed, you had to wait long enough so that AgulX-Peg-PIB not bound to amyloid plaques in washed out of the brain but not too long so some AgulX-Peg-PIB still remains bound to the plaques. This timing was more of a guess since we did not have any information on this.

Table 4-1: List of the brains brought to the ESRF for X-ray imaging.

Genotype	Number	BBB opening	Nanoparticles	Ex vivo MRI
APP/PS1	2	✓	AgulX-Peg-PIB	✓
APP/PS1	2	✓	AgulX-Peg	✓
APP/PS1	2	✗	Water	✓
WT	2	✗	Water	✗
WT	2	✓	AgulX-Peg	✗
WT	2	✓	AgulX-Peg	✗
APP/PS1	2	✓	AgulX-Peg	✓

Figure 4-15 shows the contrast enhancement caused by the penetration of AgulX to the brain after FUS-induced BBB opening. Figure 4-15 A shows a clear BBB opening done on an APP/PS1 mice injected with AgulX-Peg. Figure 4-15 B shows a weak BBB opening on an APP/PS1 mice injected with AgulX-Peg-PIB. For all control mice AgulX extravasation into the brain was obvious. Unfortunately, the imaging of the two mice injected with AgulX-Peg-PIB were not satisfactory. The first one had to undergo a retro-orbital injection of the compound because of a failed injection in the tail vein and died in the scanner 15 minutes after the injection while acquiring the  $T_1$ -weighted image. It was quickly removed for ex-sanguino perfusion but it was not sufficient to wash the blood from the vessels. Nevertheless, AgulX-Peg-PIB circulated in the blood stream for at least 15 minutes which is enough to extravagate in the brain even if it is not confirmed by MRI. The second one (Figure 4-15 B) shows only really weak contrast enhancement at some locations. This is can be due to a wrong targeting of the ultrasound or a miss injection of the microbubbles resulting in a weaker BBB opening.

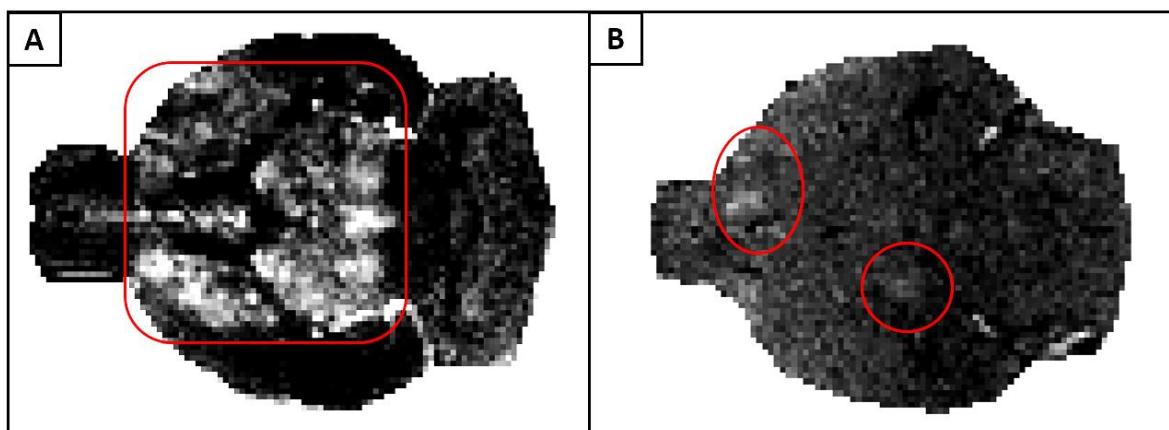


Figure 4-15:  $T_1$ -weighted images after BBB opening and injection of the contrast agent. A – Mouse injected with AgulX-Peg. B – Mouse injected with AgulX-Peg-PIB.

Due to a breakdown of the 11.7 T scanner during this experiment, *ex vivo* imaging was done at 7 T. The sequence was adapted with a degradation of the resolution to balance the loss of SNR. The parameters of the Multi Gradient Echoes sequences are the following: TE 3.5 ms, TR=90 ms, echo spacing 3.5 ms, 10 echoes, resolution 60x60x60  $\mu\text{m}^3$ , matrix size 266x180x120, 26 averages, acquisition time 14 hours. Figure 4-16 shows the *ex vivo* images of the same two mice as Figure 4-15.

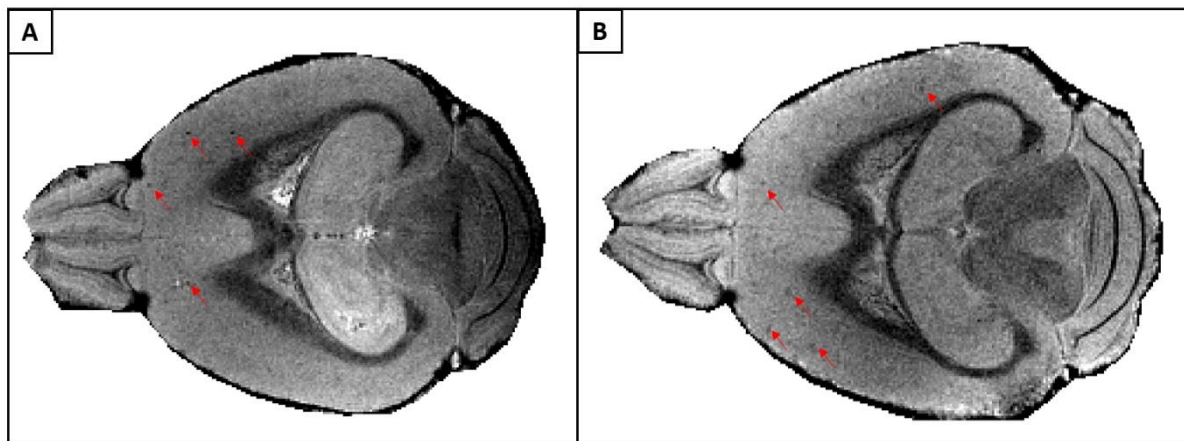


Figure 4-16: *Ex vivo* images acquired at the 7 Tesla scanner. A – Mouse injected with Aguix-Peg. B – Mouse injected with AguIX-Peg-PIB.

AguIX-Peg-PIB bound to amyloid plaques is supposed to lead to a better contrast between the plaques and the cortex on the *ex vivo* images. Indeed, gadolinium has a small  $T_2$  effect and could accentuate the susceptibility effect caused by the iron core of amyloid plaques and shorten even more the  $T_2^*$ . But it is difficult to tell if amyloid plaques are more visible on image B (when the mice was injected with AguIX-Peg-PIB) and with so few samples (only one *ex vivo* image of an APP/PS1 mice injected with AguIX-Peg-PIB can be exploited) it was not possible to push the analysis forward. However, it was possible to distinguish amyloid plaques even if we worked at 7 T without a cryo-probe. Amyloid plaques imaging is feasible with this setup but we see far fewer amyloid plaques compared to images from paragraph 4.2. Indeed, the SNR is 30 and the CNR (between plaques and cortex) is only 2. These values are clearly below the SNR of 63 and the CNR of 11 at 11.7 T with a cryo-probe.

### 4.3.3. Imaging of Alzheimer's mouse brains

Some data are still under reconstruction. The reconstruction process is very long because the imaging technique is not straightforward. Here, I present X-ray images that Elena Longo could provide me. I remind the very high resolution of these images, pixels are 6  $\mu\text{m}$  large. With this technique, metals give a really high signal because they create a strong refractive index discontinuity with the biologic tissue. This is why we expected signal from AguIX but also from the iron core of the amyloid plaques.

Figure 4-17 shows two brains imaged with this technique, one brain of a wild type mouse (A) and one brain of a one-year old APP/PS1 mouse (B). The cortex of the wild type mouse was clear from any bright spots whereas the cortex of the APP/PS1 mouse was filled with bright spots. These two mice did not undergo BBB opening or any injection of nanoparticles. We can assume that those bright spots

were the iron core of the amyloid plaques. Those bright spots were also present in the hippocampus of the Alzheimer's mouse, which is a common location for amyloid plaques. This strengthens the idea that those spots are amyloid plaques.

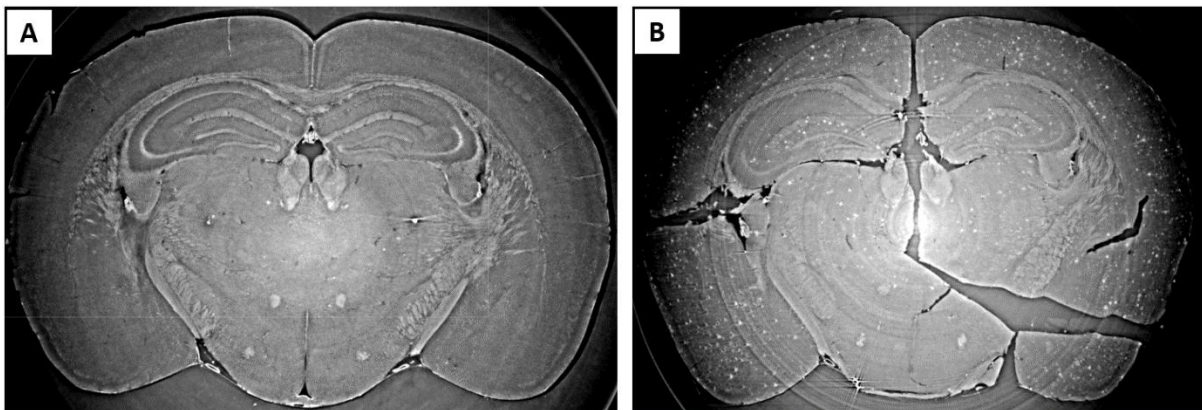


Figure 4-17: X-ray images of mice brains. A- Wild type mouse. B – Alzheimer's mouse.

Figure 4-18 shows the brain of a wild type mouse which underwent BBB opening and injection of AgulX-Peg. The objective, with these conditions, was to detect nanoparticles. Indeed, without amyloid plaques, all bright spots should come from nanoparticles. Some spots are extremely bright (yellow arrow), which could come from a high concentration in AgulX. Unfortunately, it seems that these spots were also present in the wild type mice without injection of AgulX (Figure 4-17 A), they could be iron from blood in the vessels. Other spots (red arrows) are more diffuse and seems to be away from blood vessels, these could be nanoparticles.

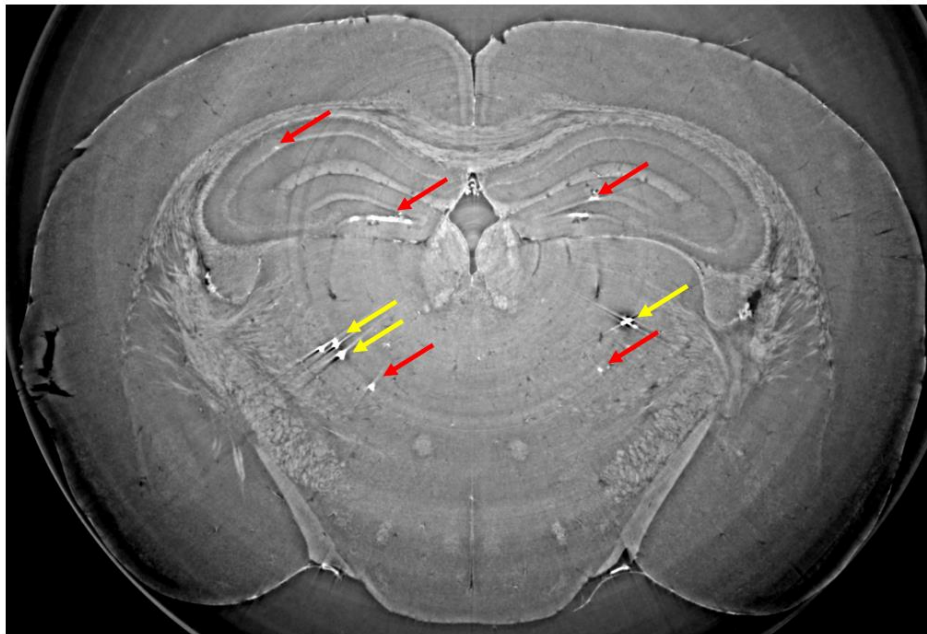


Figure 4-18: X-ray image of the brain of a wild type mouse which underwent BBB opening and injection of AgulX-Peg.

To answer the question whether or not AgulX could be imaged with this technique, the reconstruction of the other brains will be needed. As shown on Table 4-1, I performed the BBB opening experiments with many conditions but unfortunately, not all the brains could be imaged at the ESRF due to a shutdown of the electron beam. The reconstruction of the remaining imaged brains will be time consuming. Indeed, the brains from APP/PS1 mice that underwent BBB opening with injection of AgulX-Peg-PIB were imaged at two different energies in order to have different contrasts between gadolinium, iron and brain tissue. With a smart combination of the two images, we hope to tell amyloid plaques from AgulX-Peg-PIB and maybe study the targeting of those nanoparticles on the amyloid plaques but this is not trivial.

#### 4.3.4. Correlation with MRI

I had the opportunity to image on brain of an APP/PS1 mouse that did not undergo any protocol related to ultrasound but that has previously been imaged *ex vivo* at 11 T with a very high resolution. This was the opportunity to correlate high resolution MRI (40  $\mu\text{m}$ ) with X-ray phase contrast imaging. Figure 4-19 shows the correlation between MRI and X-ray. The right slice on the MR image was looked identify thank to big structures in the brain such as ventricles or blood vessels (green arrows). In red are big amyloid plaques that are detected both with MRI and X-ray.

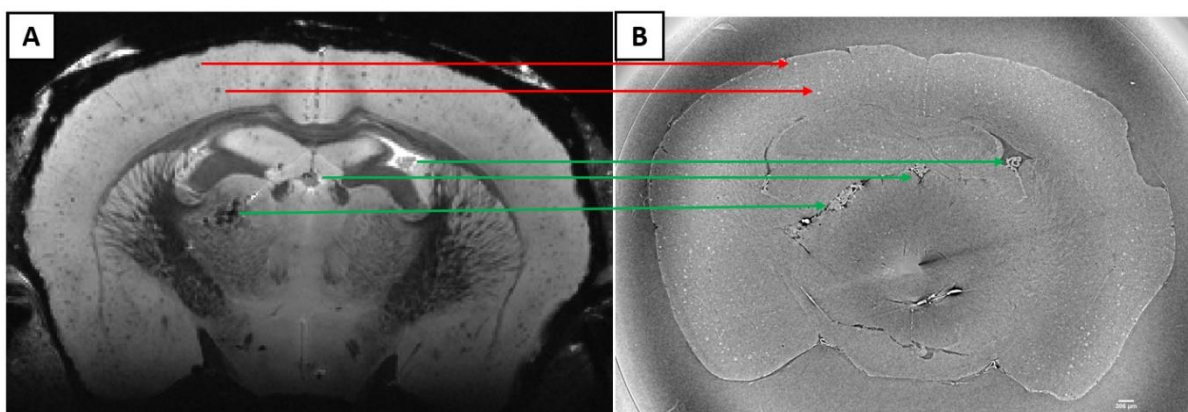


Figure 4-19: Correlation between MRI (A) and X-ray (B).

The correlation seems to work even if the two datasets are flipped. The red arrows show two big amyloid plaques, hyposignals on Figure 4-19 A, which correspond to two big hypersignals on Figure 4-19 B. So, these hypersignals are very probably amyloid plaques. With this correlation, the sensitivity of the *ex vivo* MRI could be investigated by looking at the distributions of amyloid plaques obtained with the two methods and see the fraction of amyloid plaques under 40  $\mu\text{m}$ .

As a conclusion, this X-ray phase contrast imaging allows a clear detection of amyloid plaques and looks like a promising tool to investigate the targeting of nanoparticles such AgulX-Peg-PIB. The fact that this technique is compatible with *ex vivo* MRI and even with histology as a last step gives a lot of possibilities when planning protocols.

## 4.4. Imaging Alzheimer's disease with histology

Histology is currently the gold standard to image the hallmark of Alzheimer's disease: amyloid plaques and tau tangles. It is with histology that Alois Alzheimer described and characterized the disease in the very first patient, August Deter. We have a histology lab at NeuroSpin where we study not only AD but also the effects of BBB opening on brain tissue or the targeting of cancerous cell with nanoparticles. In this section, I will mainly present results of amyloid plaques staining with Thioflavin and Perls'. Double staining of the same slices of brain can give information on the natures of the amyloid plaques. I will also present stains that are new in our team, for tau tangles and neuroinflammation.

The extraction of the brains was performed by Erwan Selingue. The section, staining and microscopic imaging of the brains was performed by Françoise Geffroy.

### 4.4.1. Amyloid plaques imaging

The images showed in the paragraph were obtained from APP/PS1 mice of 1 year. Two stains of the amyloid plaques are presented: one with Thioflavin-S which binds to A $\beta$  and one with Perls' which binds to the iron core of the amyloid plaques.

#### a) Imaging of A $\beta$ deposits: Thioflavin-S

Thioflavin-S (Kelényi, 1967) is one of the most used stain (with Congo Red) for amyloid deposits. Thioflavin-S is a homogenous mixture of compounds resulting from the methylation of dehydrothiotoluidine with sulfonic acid. It binds to amyloid fibrils, but not to soluble monomers and oligomers (Kayed et al., 2003). Thioflavin-S is a routine diagnostic compound for the presence of plaques and tangles in postmortem brain sections of AD patients (Choi et al., 2012) or of AD rodents (Urbanc et al., 2002).

The Figure 4-20 A shows a mosaic image (multiple field of view juxtaposed) of Thioflavin-S staining. This image is an RGB image on 8 bits. I optimized a Matlab code I wrote for automatic detection of the amyloid plaques. Amyloid plaques give strong hypersignals on the Green channel, the background noise was very low which makes thresholding easy. This image being very large (20 000 x 24 000 pixels), the code was tested on a ROI of this image (Figure 4-20 B). First, the Green channel was extracted and turned into a matrix of doubles between 0 and 256. Then the signal was thresholded, the threshold was fixed at 170 (out of 256 bits) but can be tuned depending on the experiment (the threshold has to be the same for all the animals of an experiment). Pixels above this threshold were classified as amyloid plaques. Then, the pixels were clustered and only clusters above 120 pixels are kept, the others small clusters were considered as noise.

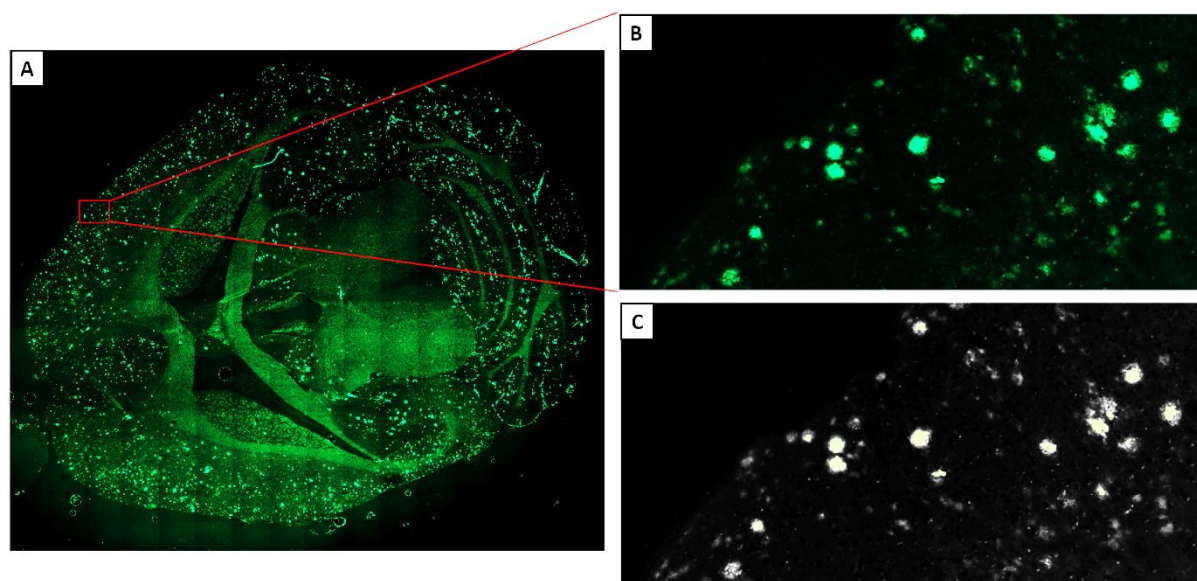


Figure 4-20: A – Mosaic image of the staining of an APP/PS1 mouse brain with Thioflavin-S. Amyloid plaques are stained in green. B – ROI to optimize the automatic detection code. C – Result of the automatic detection, in green the pixels that are classified as amyloid plaques.

Figure 4-20 C shows the results of this automatic detection. This image is an overlay of the Thioflavin-S image (in black and white) and of the detected amyloid plaques (in green). This stain is really robust and Francoise Geffroy managed to stain brains fixed for a really long time, which gives a lot a freedom in designing protocols. For example, brains can be fixed for *ex vivo* MRI and still be used for brain staining with Thioflavin-S. Moreover, the clustering process allows to quantify amyloid load in terms of number of plaques, size of plaques or surface ratio of plaques in the brain. This stain and this post-processing will be used in Chapter 5 to study the effect of BBB opening on the amyloid load.

#### b) Imaging of iron deposits: Perls'

Perls' is a common stain used by pathologists to detect the presence of iron in biopsy specimens. The technique is based on the conversion of ferrocyanide to insoluble crystals of Prussian blue in the presence of  $\text{Fe}^{3+}$  under acidic conditions. It is now extensively used in human and animal histology (Meguro, 2007), especially to detect the iron core of the amyloid plaques (Xian-Hui et al., 2015).

The Figure 4-21 A shows a mosaic image (multiple field of view juxtaposed) of Perls' staining. This image is an RGB image on 8 bits. The iron core of the amyloid plaques gives strong hypersignals on the Blue channel. This image being very large (20 000 x 24 000 pixels), the code was tested on a ROI of this image (Figure 4-21 B). First the Blue channel was extracted and turned into a matrix of doubles between 0 and 256. Then the signal was thresholded, the threshold was fixed at 150 but can be tuned depending on the experiment. Pixels above this threshold are classified as iron deposits. Then the pixels are clustered and only clusters above 120 pixels are kept, the others small clusters are considered as noise.

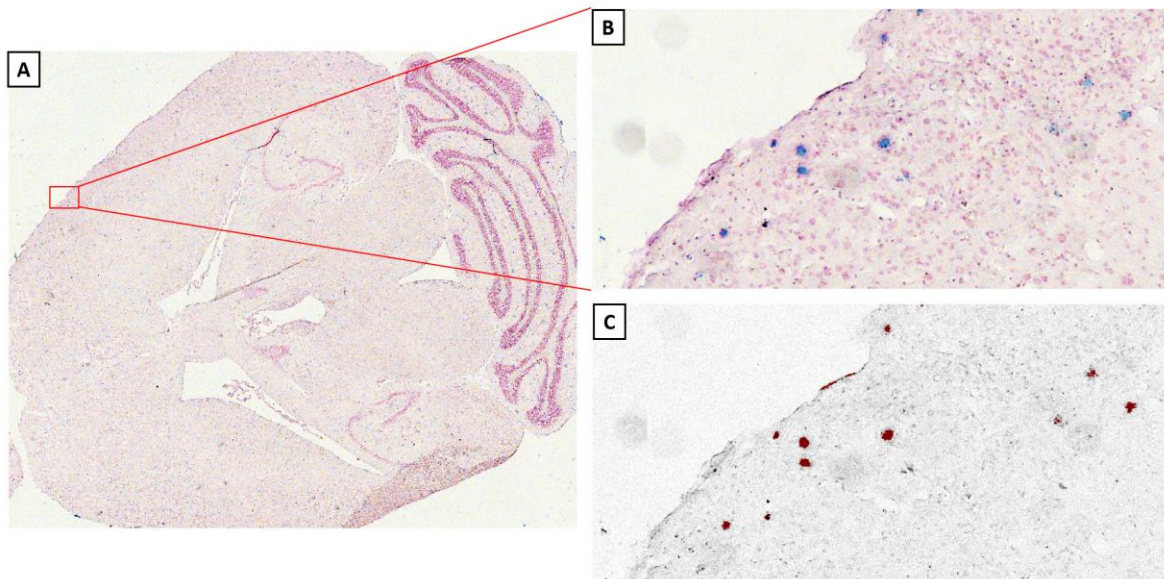


Figure 4-21: A – Mosaic image of the staining of an APP/PS1 mouse brain with Perls'. Iron deposits are stained in blue. B – ROI to optimize the automatic detection code. C – Result of the automatic detection, in red the pixels that are classified as iron deposits.

Figure 4-21 C shows the results of this automatic detection. This image is an overlay of the Perls' image (in black and white) and of the detected iron (in red).

### c) Correlation between iron and amyloid plaques

Because the Thioflavin staining was done after the Perls' staining on the exact same slice of brain, it was possible to correlate the two stainings. Unfortunately, the two images are not co-registered as they are not acquired with the same cameras. So, it was necessary to rotate the Perls' image and to resize it to get pixels of the same size. The same ROI was selected for the two images. Figure 4-22 shows, overlaid on the Perls' image in black and white, the two detections: in green the Thioflavin only, in red the Perls' only and in orange the pixels with both Perls' and Thioflavin staining.

The iron deposit seems to be located at the center of the amyloid plaques and to be smaller. This tendency is confirmed when the size of the iron core is plotted as a function of the amyloid plaque it belongs to (Figure 4-23). This scatter plot was done in ROI four times bigger than the ROI showed on Figure 4-20 B and Figure 4-21 B. In this ROI, the size of the amyloid plaque was always bigger than the size of the iron core (or equal in two cases). In few cases the amyloid plaque did not have an iron core (dots on the abscise axis). Of course, those results depend on the different thresholds used for the detection codes.

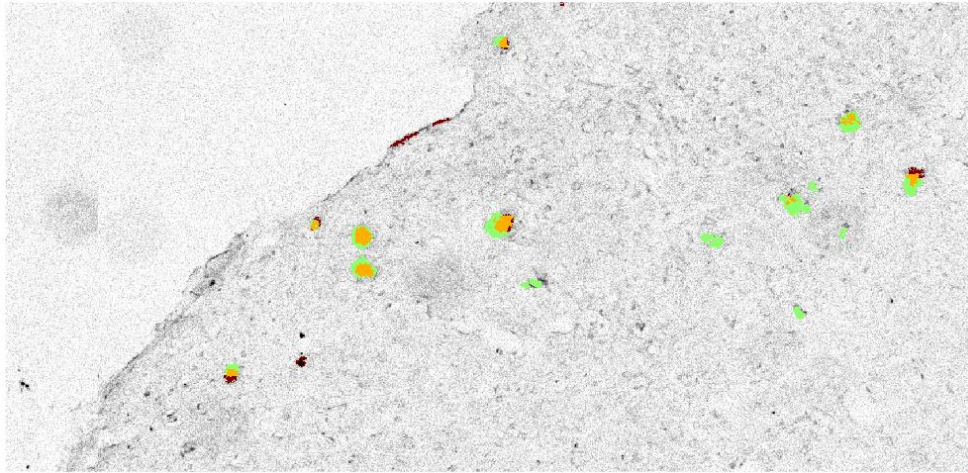


Figure 4-22: Re-alignment of the detection of iron deposit with the detection of amyloid plaques. In green pixels that are classified as amyloid plaques only, in red pixels as iron deposits only and in orange pixels that are both amyloid plaques and iron deposits. Results of the automatic detection are overlaid on the Perls' image.

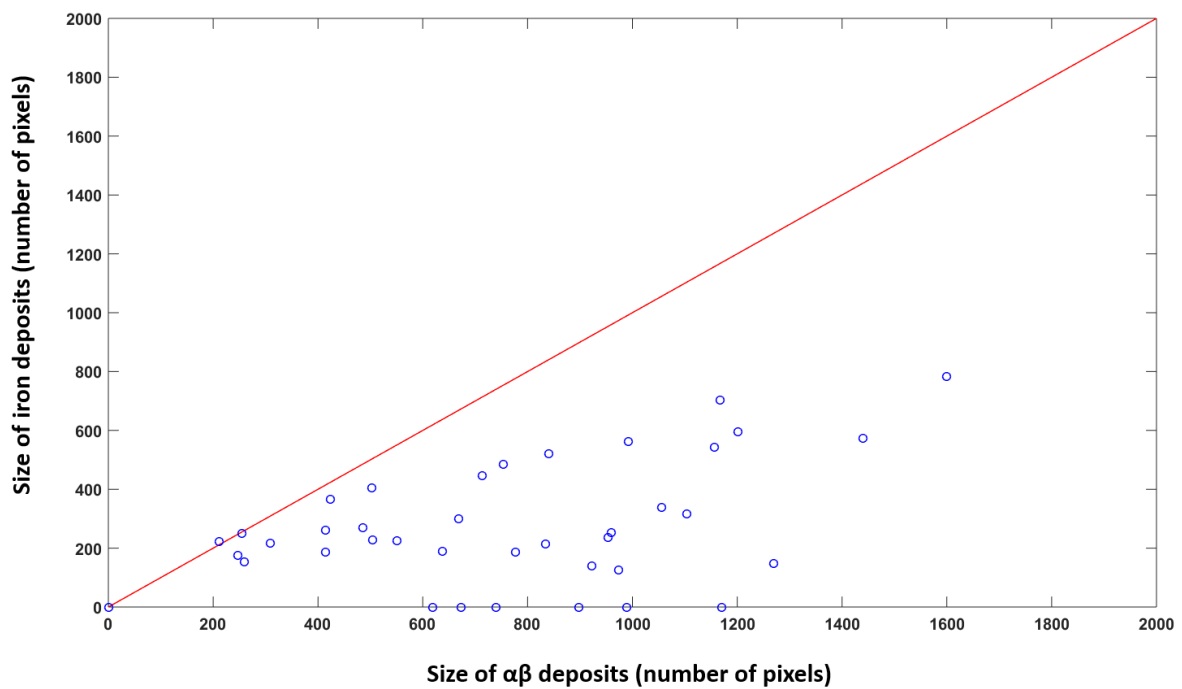


Figure 4-23: For each amyloid plaque, the size (in number of pixels) of the iron core as a function of the size (in number of pixels) of the amyloid plaque. For both images pixels are the same size.

#### 4.4.2. Other stains related to Alzheimer's disease

##### a) Tau protein imaging

The rat model of AD we have at our disposal is more complete than our mouse model. These rats develop, in addition to amyloid plaques, tau tangles. These tau tangles can also be imaged with histology. Francoise Geffroy stained tau proteins with Tau antibody 81268 (Yang et al., 2017).

Figure 4-24 shows the staining of the tau tangles. These results are preliminary and need further optimization. Tau proteins (in orange) can be seen close to the nucleus of the neurons (blue), they are located in the cytoplasm of the neurons. What seems to be an amyloid plaques, with a high density of tau proteins, can be seen in the center of the image. This stain could be an interesting tool to investigate the effect of FUS-induced BBB opening on tau tangles since FUS-induced BBB opening has recently been proven to reduce tauopathy (Nisbet et al., 2017).

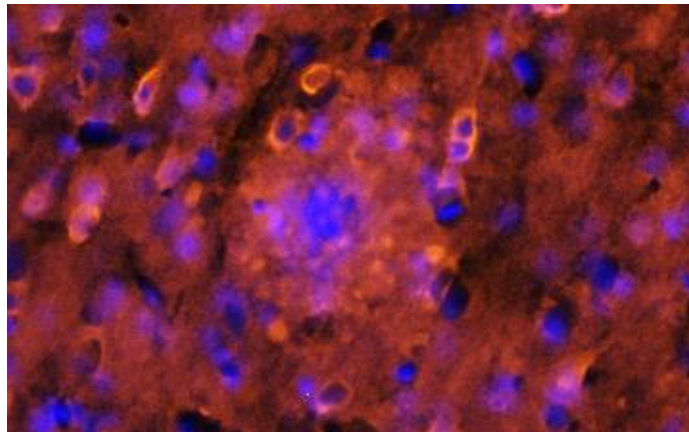


*Figure 4-24: Staining of the tau tangles in orange and on the neurons in blue.*

##### b) Neuroinflammation imaging

As it will be largely discussed in the next chapter, neuroinflammation has a leading role in the therapy for AD that are based on FUS-induced BBB opening. This makes imaging of the neuroinflammation a very important tool. Iba1 and GFAP are common stains to image (Kaufman et al., 2015; Kovacs et al., 2016; Sumbria et al., 2016).

Iba1 binds to microglia and GFAP binds to astrocytes. Figure 4-25 shows an innovative triple staining of amyloid plaques, microglia and astrocytes. This image is an ApoTome image displayed as a maximum intensity projection (MIP), which means that the full slice was imaged at different depths and that for each pixel, only the brighter depth is displayed. It can be seen that a lot activated microglia are present in the close neighborhood of the amyloid plaques. It has already clearly been proven that activated microglia surround amyloid plaques (Perlmutter et al., 1990; Stalder et al., 1999). The relationship between amyloid plaques and neuroinflammation will be discussed in more details in the next chapter.

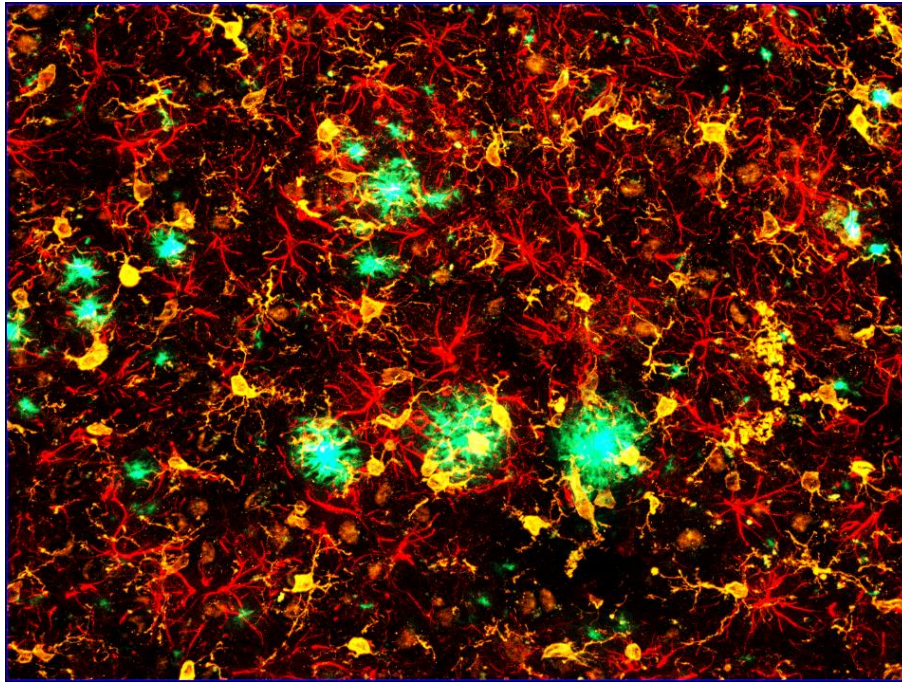


Figure 4-25: Triple staining of Amyloid plaques in green (Thioflavin), Microglia in orange (Iba1), Astrocytes in red (GFAP), in rats. MIP image.

#### 4.5. Conclusion

In this chapter, I presented different modalities I used during my PhD to image Alzheimer's disease. I began with a contrast agent grafted with PIB to target amyloid plaques (AgulX-Peg-PIB). The targeting could not be demonstrated *in vivo*. But thanks to FUS-induced BBB opening, it was successfully delivered to the brain of APP/PS1 mice and its targeting was confirmed with histology. Secondly, I proceeded with a pipeline for *ex vivo* imaging of heads of APP/PS1 mice. This pipeline was efficient in detecting and quantifying amyloid plaques. Thirdly, I described X-ray phase-contrast imaging, how it could be used to detect nanoparticles and amyloid plaques. Finally, I concluded with brain staining. I presented stains for amyloid plaques, for the iron core of the amyloid plaques, for the tau tangles and for neuroinflammation. These stains are tools that will be used in the next chapter to quantify amyloid load after therapies based on FUS-induced BBB opening.



CHAPTER 5.	<b>BLOOD-BRAIN BARRIER OPENING AS A THERAPY FOR ALZHEIMER'S DISEASE .....</b>	<b>129</b>
5.1.	<b>Ultrasound as a therapy for Alzheimer's disease: promising studies .....</b>	<b>129</b>
5.1.1.	<i>Preclinical studies.....</i>	<i>129</i>
5.1.2.	<i>The first clinical trial.....</i>	<i>133</i>
5.2.	<b>Assessment of memory deficits with behavior tests .....</b>	<b>134</b>
5.2.1.	<i>The Open Field test.....</i>	<i>135</i>
5.2.2.	<i>The Y-maze test.....</i>	<i>137</i>
5.2.3.	<i>The Barnes Maze test.....</i>	<i>140</i>
5.3.	<b>Therapeutic trials on mice .....</b>	<b>144</b>
5.3.1.	<i>A first trial without motorization .....</i>	<i>144</i>
a)	<i>Protocol.....</i>	<i>144</i>
b)	<i>Safety .....</i>	<i>146</i>
c)	<i>Behavior test .....</i>	<i>146</i>
d)	<i>Ex-vivo imaging.....</i>	<i>149</i>
e)	<i>Limits of this study .....</i>	<i>150</i>
5.3.2.	<i>A safety study.....</i>	<i>150</i>
a)	<i>Protocol and follow-up of the weights.....</i>	<i>150</i>
b)	<i>Results of the behavior tests.....</i>	<i>152</i>
5.3.3.	<i>A second trial on APP/sPS1 mice.....</i>	<i>153</i>
a)	<i>Behavior tests.....</i>	<i>154</i>
b)	<i>Histology .....</i>	<i>157</i>
5.4.	<b>Therapeutic trial on rats.....</b>	<b>160</b>
5.4.1.	<i>Ultrasound protocol .....</i>	<i>160</i>
5.4.2.	<i>Behavior tests results .....</i>	<i>161</i>
5.5.	<b>Study of the neuroinflammation with PET.....</b>	<b>164</b>
5.5.1.	<i>How to detect neuroinflammation.....</i>	<i>164</i>
a)	<i>Neuroinflammation in Alzheimer's disease .....</i>	<i>164</i>
b)	<i>A marker of neuroinflammation: the TSPO protein .....</i>	<i>165</i>
5.5.2.	<i>Ultrasound and PET protocol .....</i>	<i>166</i>
5.5.3.	<i>Follow-up of the neuroinflammation .....</i>	<i>167</i>
5.6.	<b>Conclusion.....</b>	<b>169</b>

## Chapter 5. **Blood-brain barrier opening as a therapy for Alzheimer's disease**

This Chapter is divided in five main sections. In the first one, I will describe the state-of-the art studies combining FUS-induced BBB opening and Alzheimer's disease. In the second section, I will present the different behavior tests that we used at NeuroSpin. The next two sections will be dedicated to my therapeutic trials, first on a mouse model of Alzheimer's disease and then on a rat model of AD. Finally, in the last section, I will present a short study on the neuroinflammation induced by BBB opening.

I introduce here two notations that will be extensively used in this Chapter. The animals that underwent repeated sessions of FUS-induced global BBB opening will be referred to as "SUS-treated" for Scanning UltraSound. The animals that underwent the same protocol than the SUS-treated animals without shooting the ultrasound will be referred to as "sham-treated", which means that they underwent anesthesia and microbubbles injections but without BBB opening. These notations are commonly used in the literature.

### 5.1. **Ultrasound as a therapy for Alzheimer's disease: promising studies**

As I briefly mentioned in Chapter 1, FUS-induced BBB opening by itself is now studied as a therapeutic tool for AD without injecting any drug. The studies are few, hence the need to keep on investigating. Preliminary results are convincing. In this section, I will summarize them in chronological order. They were all performed in mice. So we are the first, to our knowledge, to try it on TgF344-AD rats. I will finish by presenting the first and recent phase 1 clinical trial that is still on-going.

#### 5.1.1. **Preclinical studies**

##### *i) Jordao et al., 2013*

The first study showing the effect of FUS-induced BBB opening *in vivo* was done by *Jordao et al. (2013)*. They hypothesized that FUS-induced BBB opening only could reduce the amyloid plaque burden. They selected four months old TgCRND8 mice, this model already developed plaques at this age. Those mice underwent a single BBB opening in the cortex in one hemisphere. Mice were sacrificed 4 days later. Thank to brain straining, authors observed that after a single treatment, plaque size and total surface area were significantly reduced by 20% and 13%, in the cortex targeted with FUS compared to the untreated equivalent cortical region of the other hemisphere. The main results of this study are shown on Figure 5-1.

This finding was unprecedented. They explored two probable contributing factors: the delivery of blood-borne endogenous antibodies to the brain since endogenous antibodies injected in the brain have been shown to reduce amyloid load (Du et al., 2003), and glial activation (microglia and astrocytes), which have been implicated in the mechanism of antibody-mediated A $\beta$  clearance (Wilcock et al., 2003, 2004). They found that FUS-induced BBB opening increased the immuno-positive

signal (IgG levels were almost doubled in treated hemisphere) and protein expression of glial cell markers, specifically Iba1 for microglia and GFAP for astrocytes. Neuroinflammation was already identified as a contributing factor.

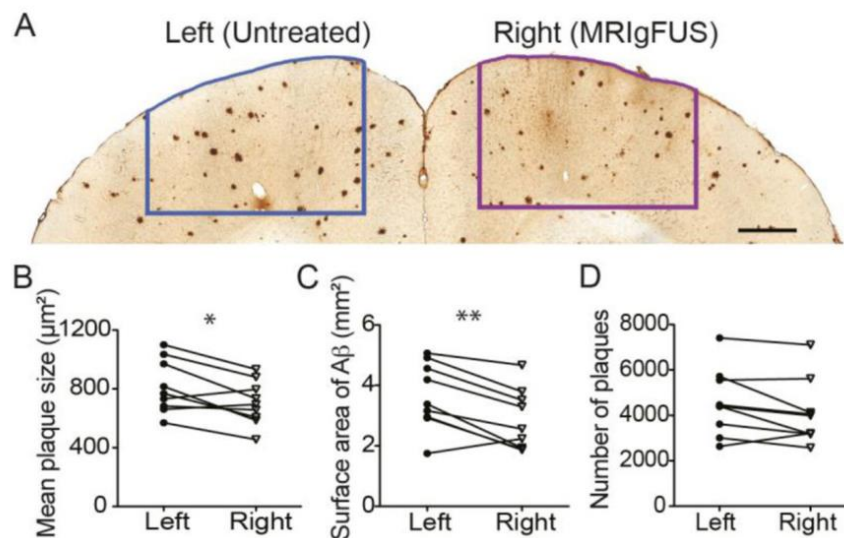


Figure 5-1: A – Brain staining of the cortex of the two hemispheres. B – Significant decrease of the mean plaque size in the FUS treated hemisphere. C – Significant decrease of surface ratio of plaques in the FUS treated hemisphere. D – No diminution in the number of plaques. (from Jordão et al. 2012)

ii) Burgess et al. 2014

The second study was done by Burgess et al. (2014). They worked on the same mice strain but on 8 months old animals. They performed three sessions, once per week, of FUS-induced BBB opening in four locations, two spots in each hippocampi, a structure severely affected in AD (Figure 5-2 A). In addition to amyloid plaque load quantification, they also performed a behavior test: the Y-maze. As shown on Figure 5-2 B, they found significant differences in the Y-maze performances between TgCRND8 untreated mice and wild type mice. Interestingly, those differences were not found between SUS-treated mice (TgCRND8 FUS) and the FUS treated wild type mice (non-Tg FUS). This results showed for the first time that FUS-induced BBB opening could restore memory in TgCRND8 mice. And they found both a memory improvement (Figure 5-2 B) and a 20% decrease of the amyloid plaque load (Figure 5-2 C) after FUS treatment.

To further investigate the correlation between behavior changes and biologic changes in the brain, authors characterized the immature neurons of the dentate gyrus in immunochemistry with immunochemistry. They showed that MR imaging-guided focused ultrasound increases the proliferation and maturation of newborn cells in the hippocampus, which could explain the behavioral changes in the FUS treated TgCRND8 mice.

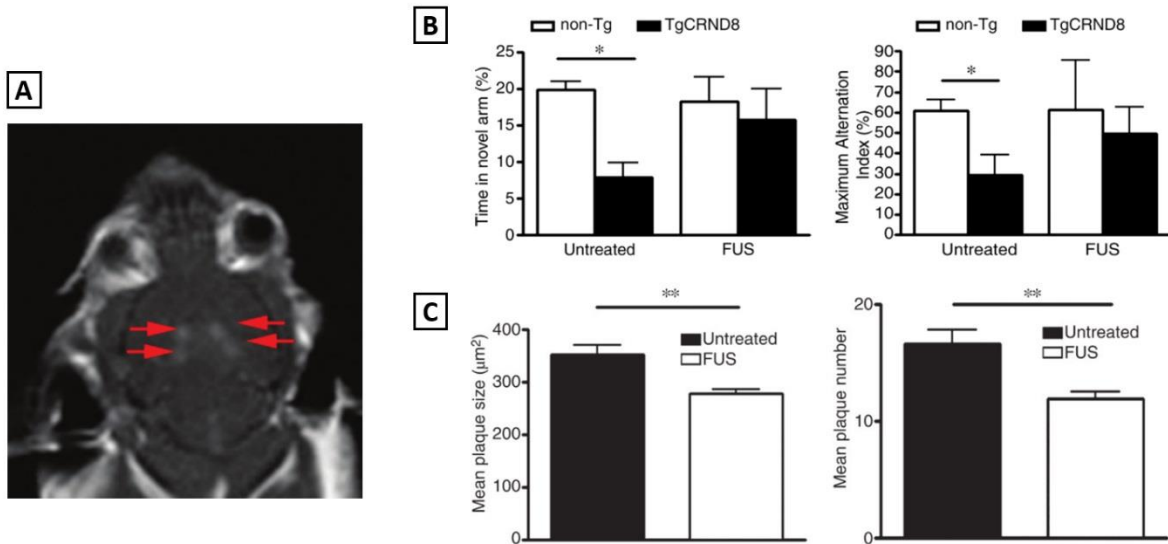


Figure 5-2: A –  $T_1$ -weighted image showing a contrast enhancement, after injection of a contrast agent, where the BBB is open. B – Results of the Y-maze showing a memory improvement on the FUS treated TgCRND8 mice. C – Significant reduction in the amyloid plaque load for the FUS treated TgCRND8 mice compared to the non-treated animals. (from Burgess et al. 2014)

iii) *Leinenga and Götz, 2015 and 2018*

The study probably the most complete was recently published by *Leinenga and Götz* (2015). They performed 7 sessions, once per week, of FUS-induced BBB opening on 15 months old APP23 mice. Parameters for the ultrasound delivery were 0.7 MPa acoustic pressure, 10-Hz pulse repetition frequency, 10% duty cycle, 1MHz center frequency, and 6 second sonication time per spot. A motorized positioning system moved the focus of the transducer in a grid with 1.5 mm between individual sites of sonication so that ultrasound was delivered sequentially to the entire brain. After ultrasound, mice were tested in the Active Place Avoidance (APA) task, followed by the Novel Object Recognition (NOR) test, in order to assess their memory. Then, they quantified amyloid load with Western Blot and ELISA tests.

As shown on Figure 5-3 C, APP23 mice that underwent FUS treatment received fewer shocks than sham-treated mice, meaning that they remember better the places to avoid. This results indicates a memory improvement due to FUS. Western Blot (Figure 5-3 D and E) and ELISA (Figure 5-3 F) both showed a significant reduction of the amyloid plaque load. With spinning disk confocal microscopy they investigated microglia-internalization of A $\beta$ . They observed a twofold increase of microglia-internalized A $\beta$  in SUS-treated APP23 mice compared to sham-treated APP23 mice. Their results revealed that FUS treatment engages microglia and promotes internalization of A $\beta$  into microglial lysosomes, thereby reducing A $\beta$  and plaque load in the APP23 transgenic mouse model of AD as well as restoring function in tests of spatial and recognition memory. But they did not find any astrogliosis. Finally they also underline that BBB opening could attenuate the deposition of newly generated A $\beta$ . To summarize, they proved that repeated session of FUS-induced BBB opening on old APP23 mice could restore memory (measured with several memory-related behavior test) and they correlated this improvement with a reduction of the amyloid load (measured with histology, Western Blot and ELISA).

Authors remind that the effect of the ultrasound were “modest” and that this technique should be coupled with injection of therapeutics to increase their delivery to the brain.

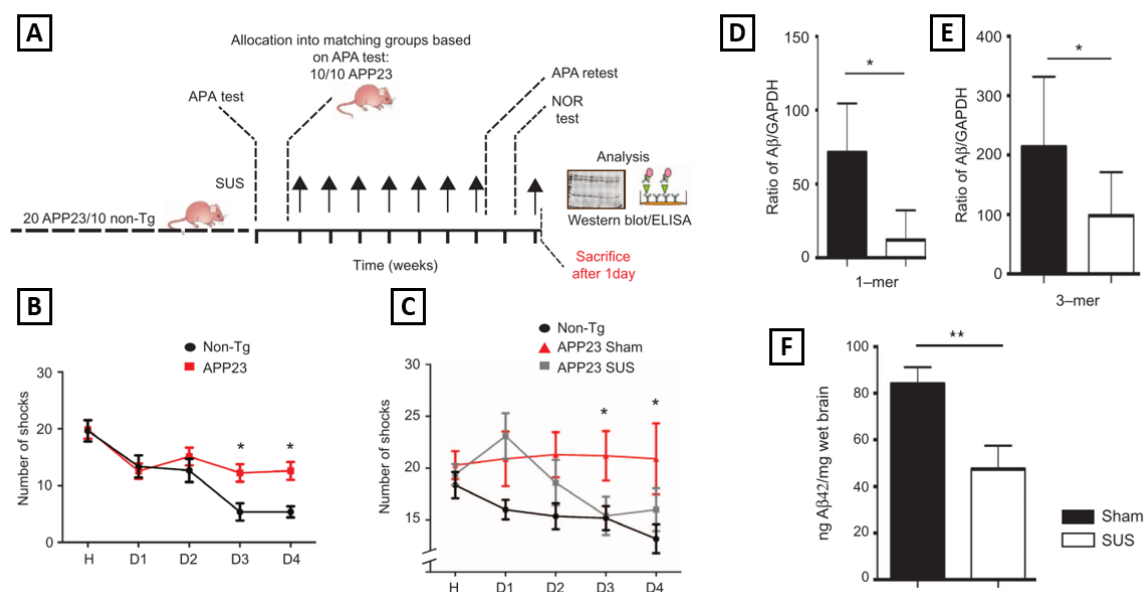


Figure 5-3: A – Treatment scheme. B – APP23 mice perform significantly worse than non-Tg mice in ATA. C – SUS-treated APP23 mice perform better than sham-treated mice. D and E – A significant decrease of the amyloid load in the FUS treated APP23 mice was measured with Western Blot. F – A significant decrease of the amyloid load in the FUS treated APP23 mice was also measured with ELISA. (from Leinenga & Götz 2015)

Leinenga and Götz recently completed their previous study by studying the effect of repeated FUS-induced BBB opening on old (two-year old) APP23 mice (Leinenga and Götz, 2018). In this study mice underwent 4 sessions of ultrasound over 8 weeks with the same protocol as their previous study. Surprisingly, they did not observe a reduction of the number of amyloid plaques, of the surface filled by amyloid plaques in the brain nor in the mean size of plaques (Figure 5-4 A, B and C). But they did find a shifting of the distribution of the plaques size toward small plaques and a clear 58% reduction of fibrillary amyloid (Figure 5-4 D and E). They also found a greater number of activated microglia around amyloid plaques in the SUS-treated mice when compared with the sham-treated mice, which highlight the role of neuroinflammation in amyloid plaque clearance (Figure 5-4 F).

Authors found more activated microglia around bigger amyloid plaques and suggest that microglia degrades large plaques. They think this is the mechanism responsible for the shifting of the distribution of plaques size toward small plaques. They explain the absence of amyloid load reduction by the fact that mice were treated only 4 times over 8 weeks and that sacrifices were performed 4 weeks after the last sonication compared to 4 days after for their previous study.

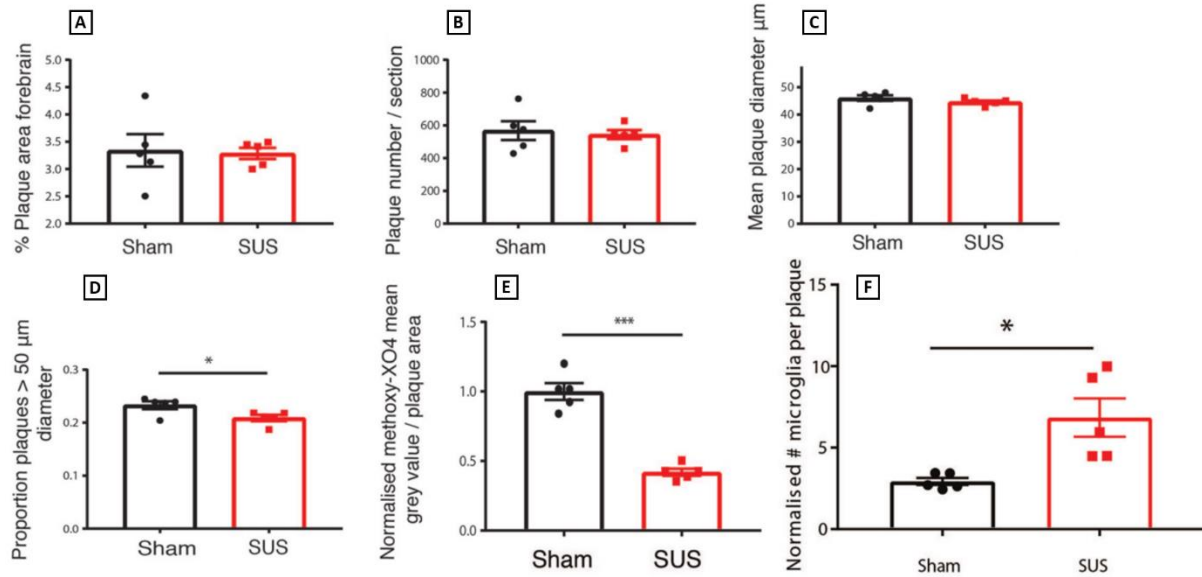


Figure 5-4: A, B and C – No differences in amyloid plaques load between the SUS-treated and the sham-treated mice. D – More small amyloid plaques in the SUS-treated mice. E – Decrease of fibrillary amyloid in the SUS-treated mice. F - Increase of the number of activated microglia in the SUS-treated mice. (from Leinenga & Götz 2018)

iv) Nisbet et al., 2017

Even if most studies have focused on amyloid, one was focused on the effect of repeated FUS-induced BBB opening on tau pathology. Nisbet et al. showed that, in the pR5 transgenic mouse model of tauopathy, hyperphosphorylated tau proteins could be partially cleared with this technique (Nisbet et al., 2017). They hypothesized that the mechanism of action is through the ubiquitin pathway as they proved that FUS-induced BBB opening reduces GSK3 levels. Even if those mice did not show a decrease of anxiety using the Elevated Plus maze on those mice, the effect of BBB opening on tauopathy is of great interest.

Those studies paved the way for a clinical translation of this technique. The first clinical BBB opening system from Insightec, the Exablate Neuro, just received the FDA approval for an Alzheimer's disease clinical trial using focused ultrasound. We will see in the next paragraph the first BBB opening trial on Alzheimer's patient.

5.1.2. The first clinical trial

This study, performed at the Sunnybrook hospital in Toronto, was a phase 1 clinical trial (Lipsman et al., 2018). Its goal was to assess the safety of the technique. FUS-induced BBB opening was performed in 5 Alzheimer's patients at a mild-to-moderate stage of the disease. The procedure was MR-guided thanks to the Exablate Neuro system (ExAblate Neuro, InSightec, Haifa, Israel) inserted in a 3T MR scanner. After injection of commercially approved microbubbles, BBB opening was performed in the

frontal lobe (area where patients proved to have amyloid deposition) and monitored with passive cavitation detection. The same way we use gadolinium-based contrast agent to validate our openings on rodents, they injected a contrast agent and to ensure the efficacy of the opening on T<sub>1</sub>-weighted images (Figure 5-5 B). The closure of the BBB was validated with a second scan 24h later. They found hypo-intense signals, which could be a sign of microhemorrhages, on two patients just after sonication. But those signals were resolved 24h later.

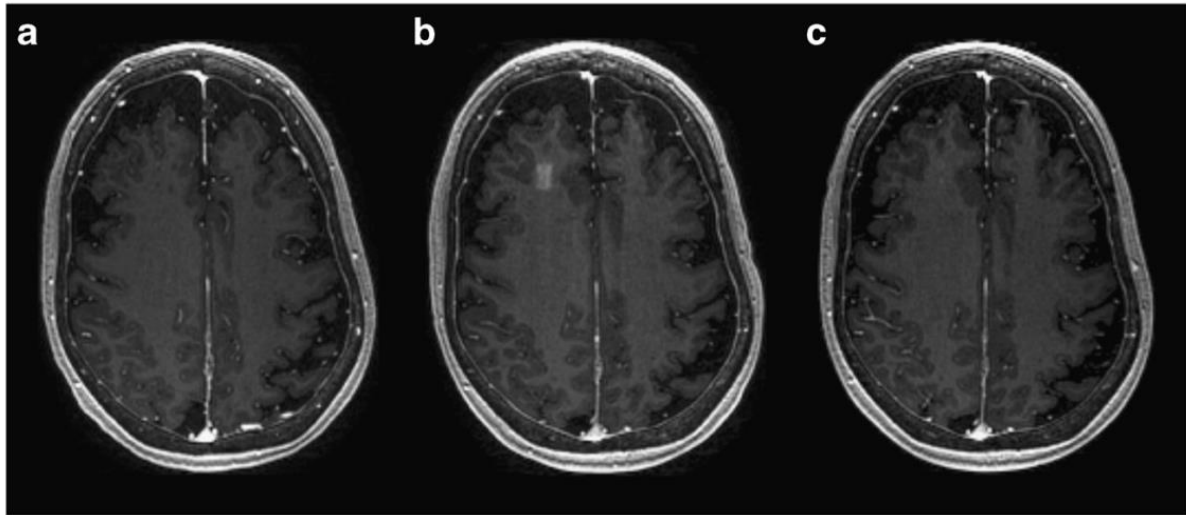


*Figure 5-5: A – Baseline scan. B – T<sub>1</sub>-weighted image after the FUS-induced BBB opening and the injection of the contrast agent. C – Scan 24h after the opening. (from Lipsman et al. 2018)*

As a general conclusion, this study proved the safety, efficacy and reversibility of FUS-induced BBB opening on humans. Those results encourage to keep on investigating this promising technique. Knowing that this technique can be transferred to clinic make all the preclinical studies aiming to understand the mechanisms of action even more relevant. This road is not a dead-end!

## 5.2. Assessment of memory deficits with behavior tests

In order to validate a therapy, quantifying a biomarker, such as the amyloid plaques, with imaging or biochemical analysis is not enough. What matters most is the beneficial phenotypic effects, which means, in the case of Alzheimer's disease, a beneficial impact on memory or on anxiety. This is why behavior tests must be used to validate therapeutic trials on animal models of Alzheimer's disease.

Although they require a high degree of rigor by the scientists to get reproducible data and are globally less sensitive than biological biomarkers, behavior tests are the only tools to assess complex cognitive functions such as anxiety, space orientation or memory. Those functions can be affected by many other factors external to our studies. Therefore, this creates large variability inside apparently homogeneous groups and decrease the sensitivity of detection of cognitive deficits or recoveries. To be able to significantly detect effects, behavioral studies thus require large cohorts of animals.

Behavior tests are many and the same maze can be used with many conditions to test the different kinds of memory. All our behavior tests were built by Jeremy Bernard, mechanical technician in

NeuroSpin. We choose them either for their ease to build, their ease to maintain or for the fact that they are reference tests in the literature. I will present the different behavior tests individually and for each of them show results before treatment that validate their use on our mice and rats models of Alzheimer's disease.

The help of Ashley Novais, a PhD Student from ICBS in Braga Portugal, was very precious in designing the apparatus, in setting up the exact protocols and in processing the data. All the behavior tests were performed either by Erwan Selingue, technician in our team or by myself. Animals are brought to the room at least 30 minutes before the test and left alone so they can get used to the room (brightness, smell, etc.). Between every trial the mazes were wiped with a 10 % alcohol solution to eliminate odors. Within one study, behavior test were always performed by the same experimenter because animals get used to its odor and its way of handling them. All the video analyzes were done with the Smart software (Panlab, Harvard Apparatus, USA). The center of mass of the animal was used as its position. After detecting the position of the animal through the whole test, the software automatically extracts the needed parameters such as the walked distance or the number of entries per arm. The only parameters which had to be count manually are the errors and the deviation for the Barnes maze.

For each behavior test, many parameters can be extracted from the videos in order to quantify the performances of the animals. They will be described when presenting the tests. But to keep the manuscript clear and not overload with figures, only the relevant parameters will be showed. For example, I will not present the "errors", the "deviation" and the "primary latency" for every Barnes maze test. When presenting the therapeutic trials, I will mainly show the parameters for which the effect of the FUS-treatment is observable, even though I will also show the parameters for which the effect is more modest to remain critical on the interpretations.

The most used statistic test in the literature is undoubtedly the *t*-test. Due to the small number of animals per study, the static test used to compare the performances of the groups was the Wilcoxon signed-rank test, which is a non-parametric test. With the Barnes maze, the training session was analyzed with 2-way ANOVA with days and genotype as parameters. Differences were considered significant and marked with \* when the *p* value was smaller than 0.05. Unless said otherwise, all the behavior results present in this Chapter will be presented as mean  $\pm$  standard error of the mean (sem).

### 5.2.1. The Open Field test

The Open Field allows to assess the anxiety of the animals and potential locomotion impairments. Since its development by Hall (Hall, 1936) it has become widely used in behavioral research, especially on rodents (mice and rats). Anxiety is measured through animals being more in the central or in the peripheral area of a box. The central area is more anxiogenic for rodents (Choleris et al., 2001). Indeed, in the nature, rodents fear open and bright areas. So the more anxious they are the closer to the wall they will stay. The total distance walked during the test can also be used to assess locomotion impairments, especially after ultrasound protocols. Indeed, changes in locomotion could mean damages due to ultrasound. The protocol is simple: under dim light, animals are placed in the center of the box and can freely explore it for 15 min.

Our Open Field (OF) is made of a simple box (Figure 5-6 A), 33x33x33 cm<sup>3</sup> for mice and 50x50x50 cm<sup>3</sup> for rats. For an easy video tracking of the animals, the contrast between the surface and the animals was improved by choosing a white material for the mouse apparatus (C57Bl/6 mice are black) and a black material for the rat apparatus (Fisher rats are white). A central area is defined as a square of half the size of the OF and placed at the center of the OF.



Figure 5-6: Open Field apparatus for mice.

Figure 5-7 shows results of an OF test on one-year old mice. The AD group was gender balanced and composed of 8 APP/PS1 mice and the WT of 9 wild type littermates and gender balanced too. On Figure 5-7 A, wild type mice spent more time in the central area than APP/PS1 mice and on Figure 5-7 B, APP/PS1 mice walked 32% more than their wild type littermates on average. These differences were not significant but show tendencies.

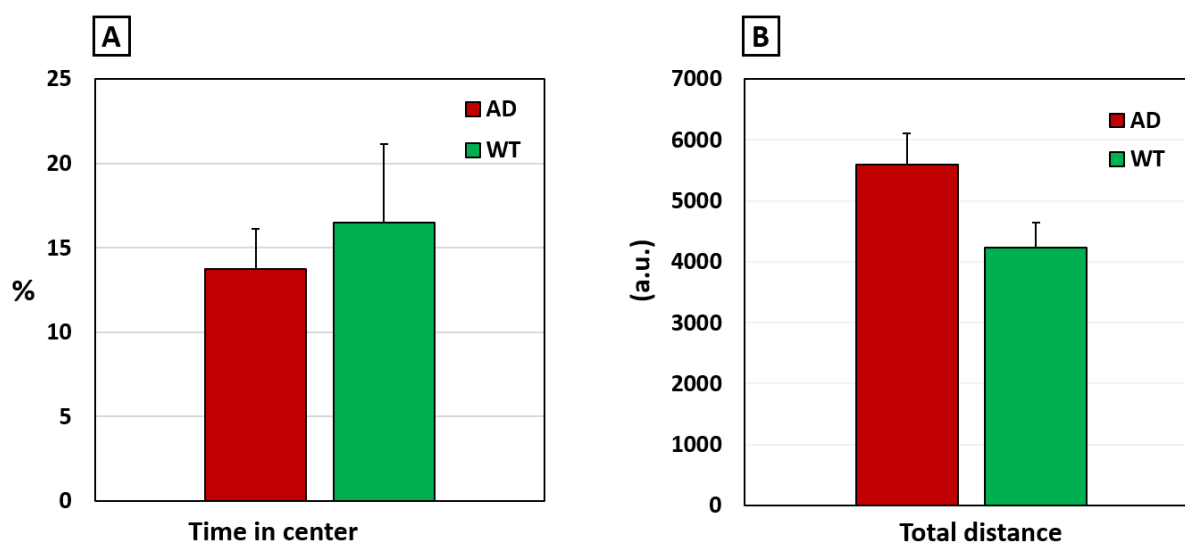


Figure 5-7: Open Field results on mice. A – Fraction of time spent in the central area. B – Total walked distance.

These results are consistent with the literature for APP/PS1dE9 models. Firstly, on anxiety: APP/PS1 mice walk less in the center than wild type at 12 months (Lalonde et al., 2005) and wild type mice spend significantly more time in the central area than APP/PS1 dE9 mice at 24 months (Huang et al., 2016). Secondly, on locomotion: one study showed a significantly higher exploratory activity at 8 and 15 months for APP/PS1 mice when compared with wild type (Hooijmans et al., 2009) and other studies showed a longer distance walked in the OF for APP/PS1 dE9 mice than for wild type mice (Huang et al., 2016; Lalonde et al., 2005). Groups showing significant results always used more than 14 animals per group.

The results being consistent with the literature, we consider that our apparatus and our protocol are efficient in assessing the anxiety and exploratory activity of mice.

Figure 5-8 shows results of an OF test in one-year old rats. The AD group was gender balanced and composed of 10 TgF344-AD rats and the WT was composed of 14 wild type littermates and gender balanced too. On Figure 5-8 A, wild type rats spent 78% more time in the central area than TgF344-AD rats on average. On Figure 5-8 B, wild type and TgF344-AD rats walk about the same distance during the trial. These differences are not significant but show tendencies. Unfortunately, only little literature is available on this rat model since it is relatively recent (2013).

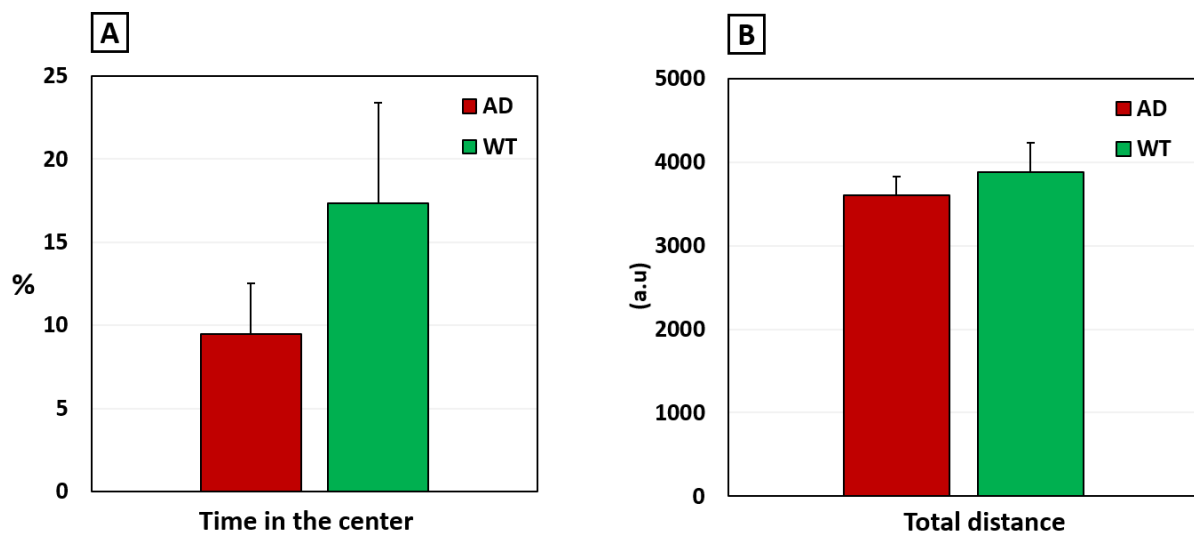


Figure 5-8: Open Field results on rats. A – Spend time in the central area. B – Total walked distance.

Because of the lack of literature, it is difficult to conclude on the efficacy of our OF test for rats. However, TgF344-AD rats seem more anxious than wild type littermates, as they spend less time in the central area, which is reported in many mice model of AD.

### 5.2.2. The Y-maze test

The Y-maze allows to assess the memory of the animals. The Y-maze is made of three arms, 40x8 cm<sup>2</sup> for mice (Figure 5-9 A) and 50x10 cm<sup>2</sup> for rats (Figure 5-9 A), walls are 20 cm high. The angle between

two arms is 120°. Visual cues are positioned at the end of the walls. Two protocols were used. The most used was a two-step trial, the other one was a one-step trial.

For the two-step trial, during the first step, the animal is allowed to visit two arms of the Y-maze, the third being blocked by a door. Animals start from the “start arm”. During the second step, the door is open, and the animal has free access to all three arms. Discrimination of novelty versus familiarity can then be studied by comparing exploration of the three arms. This two-step memory task, based on a free-choice exploration paradigm, was first validated on rats (Dellu et al., 1992) and is now also frequently used in mice (Dellu et al., 2000; Webster et al., 2014). Based on their natural tendency to explore what is new, rodents which remember the old arms (“start arm” and “old arm”) should explore more the “new arm”. This protocol assesses the spatial memory of the animals. The time between the first and the second trial was set to 1 hour. It has been shown on another transgenic mouse strain that longer intervals result in less difference between the APP/PS1 mice and their wild type littermates (Hyde et al., 2005). In our protocol, mice can freely explore two arms for 10 minutes. They return to their cage for 1 hour and then can freely explore the 3 arms for 5 minutes.

For the second protocol with only one step, the animal is placed at the center of the maze and can freely explore the 3 arms for 5 minutes. The ability to alternate between arms requires the animal to know which arms they have already visited. Spontaneous alternation behavior was defined as entries into all three arms on consecutive choices in overlapping triplet sets. If the arms are named A, B and C, spontaneous alternations are ABC, BCA etc. when ABA, CAC etc. are not. The percentage of spontaneous alternation behavior was calculated as the ratio of spontaneous alternation to the maximum number of possible alternations (defined as the total number of arm entries minus 2) multiplied by 100 (Zhu et al., 2017). This protocol assesses the short-term memory of the animals.

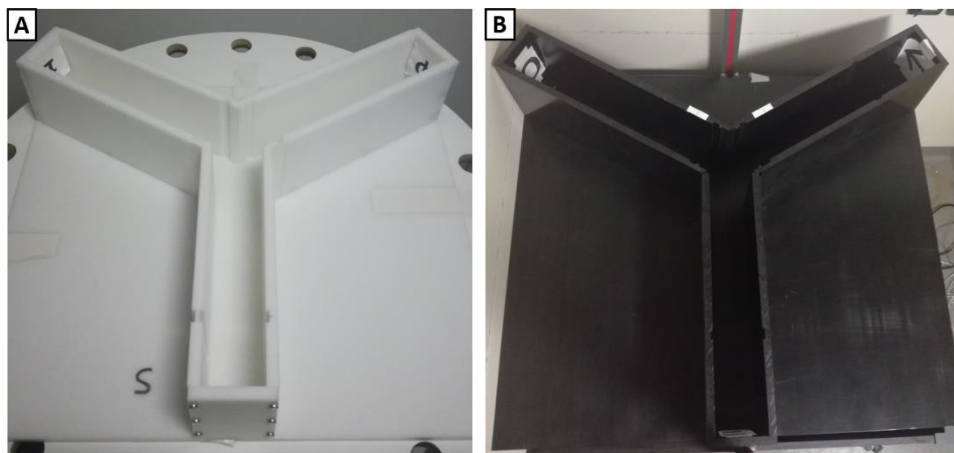


Figure 5-9: A – Y-maze for mice. B – Y-maze for rats.

Figure 5-10 shows results of the Y-maze on one-year old APP/PS1 mice and their wild type littermates. The AD group was composed of 7 APP/PS1 mice and the WT group of 8 wild type littermates. During the second trial of the first protocol, animals were video recorded and the exploration of the three arms was quantified with the video analysis software. Figure 5-10 A shows the percentage of distance walked in each arm. APP/PS1 mice did not seem to explore less than the wild type mice. However, significant differences in spent time in the new arm have been shown in those mice at 24 months with

14 animals per group (Huang et al., 2016). The incapacity of our protocol to exhibit differences between the AD and the WT group could come either from the age of the mice, which were maybe tested too young, or from the number of animals per group which was unfortunately relatively low. But as shown on Figure 5-10 C, at the beginning of the trial wild type mice chose the new arm three times more than the APP/PS1 mice ( $p=0.2$ , *Wilcoxon rank test*). Figure 5-10 B shows the results of the second protocol on the same mice. APP/PS1 mice made 20% less alternation than wild type mice. This means that this protocol can almost detect their impaired short-term memory ( $P=0.06$ , *Wilcoxon rank test*). It has been shown on another APP/PS1 transgenic strain that APP/PS1 mice make less alternation than their wild type littermates at 5, 9 and 12 months (Zhu et al., 2017). As a conclusion, the parameter “new arm visited first” for the first protocol and “alternation triplet” for the second protocol seem to be the most sensitive ones to discriminate our mice.

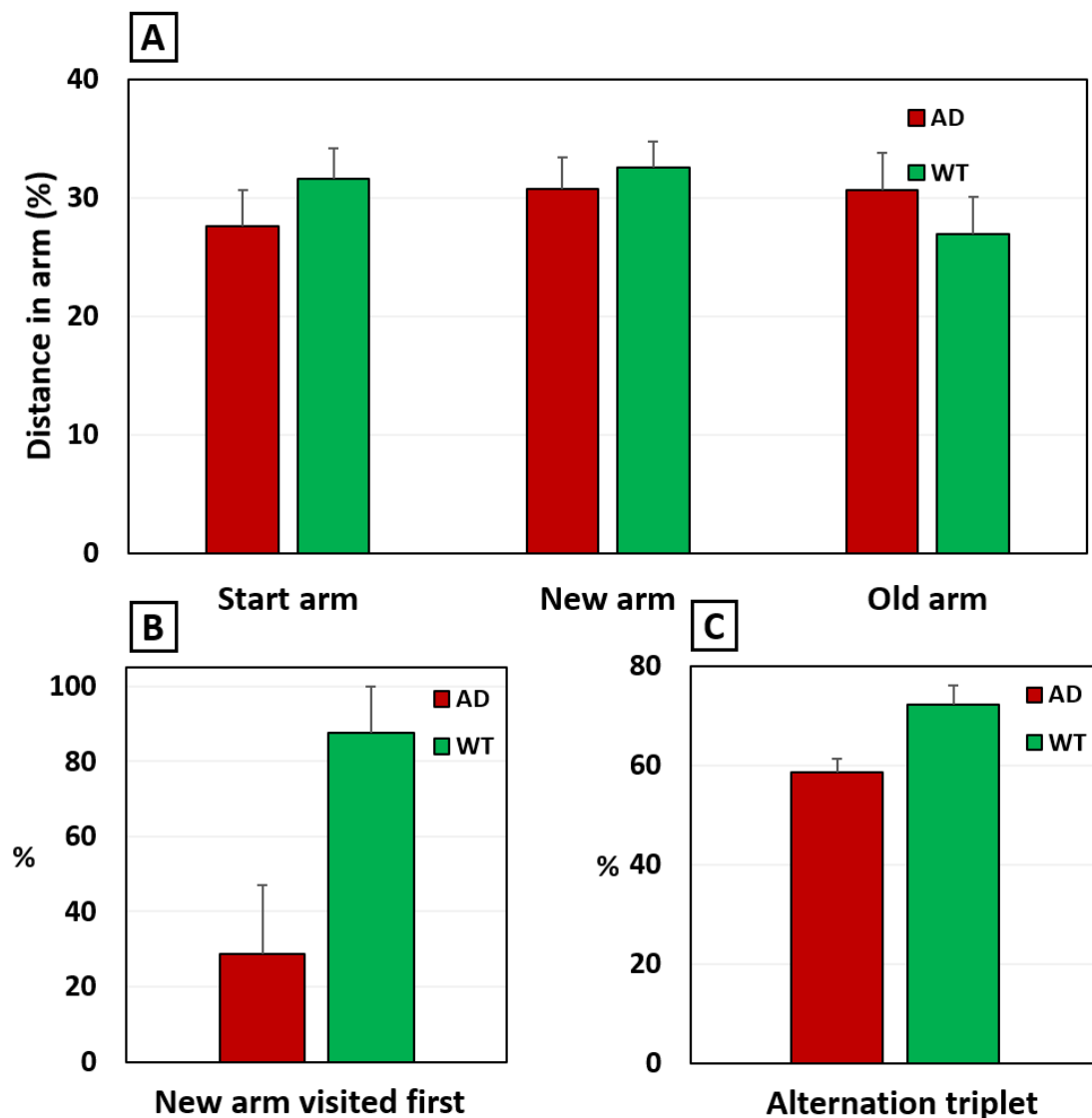


Figure 5-10: Y-maze results on mice. A – Distance in each arm expressed as percentage of the total distance. B – First arm choice. C – Alternation triplet.

Figure 5-11 shows the results of the Y-maze on one-year old rats. : 10 TgF344-AD rats and 14 WT littermates. There is a tendency showing better performances for wild type rats than TgF344-AD rats: they walked 20% more in the new arm (Figure 5-11 A) and chose 43% more the new arm at the beginning of the trial for the first protocol (Figure 5-11 B). Nevertheless, these differences are not significant and it is difficult to conclude on the efficacy of this test because to our knowledge no literature on Y-maze is available for this rat model. The second protocol could not be performed in rats during my PhD.

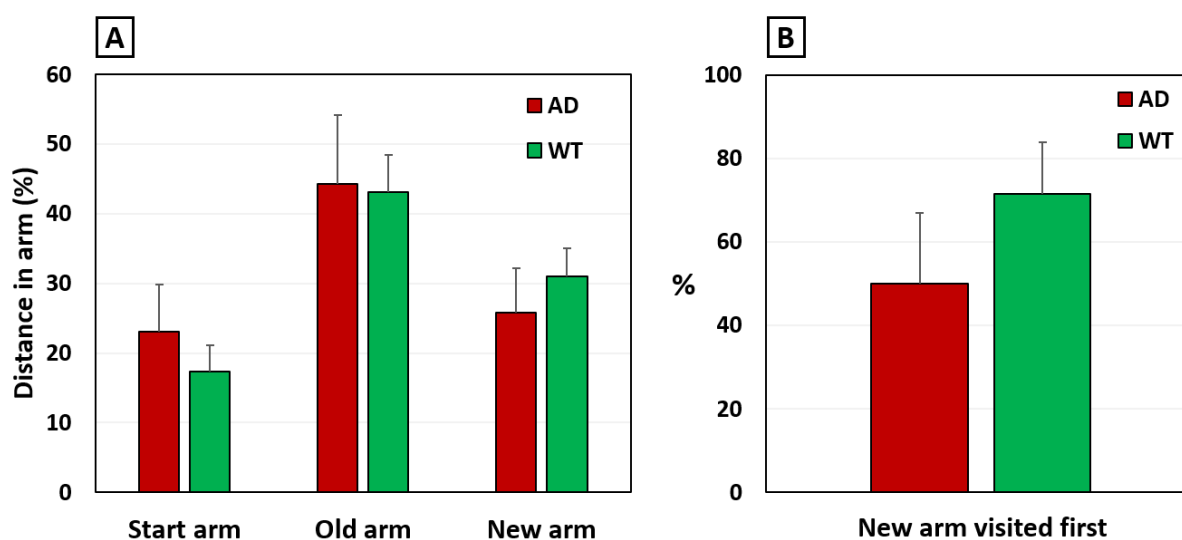


Figure 5-11: Y-maze results on rats. A – Walked distance in each arm. B - First arm choice.

### 5.2.3. The Barnes Maze test

The Barnes maze (BM) was designed to assess visuo-spatial learning and memory in aged rats (Barnes, 1979). Our BMs are made of a disk drilled in its periphery with a circle of 20 holes evenly spaced. The disk is 1 m large for mice (Figure 5-12 A) with holes of 5 cm diameter and the plateau is 1.20 m large for rats (Figure 5-12 B) with holes of 10 cm. Under one so called “escape hole”, an escape box is placed where animals can hide and feel comfortable. Although it was first designed for rats, this test also became really popular to assess memory of mice (Nguyen et al., 2000; O’Leary and Brown, 2012). Placed in the middle of the maze and exposed to weak stimuli (bright light and noise) for reinforcement (Koopmans et al., 2003), animals try to find the escape box.

After several trials per day over a few days (typically 5 to 9 days) animals learn the location of the escape hole thank to visual cues (such as a cross, a triangle, a square and a disk printed in black on a regular sheet of paper) placed on the 4 walls around the maze. These visuals cues were proved to be mandatory to optimize the cognitive performance of the animals (Barnes et al., 1980). The performances of the animals are quantified for each trial. Healthy animals performed better over the days (finding the escape hole faster for example). Rodents with hippocampal damage showed impaired performance in the BM, supporting the spatial nature of the task (Fox et al., 1998). The BM represents somehow a dry version of the very popular Morris water maze. Its advocates claim that

the BM is less physically taxing than swimming (Harrison et al., 2009) and the performances are not affected by the body temperature drop caused by the multiple training trials (Iivonen et al., 2003).

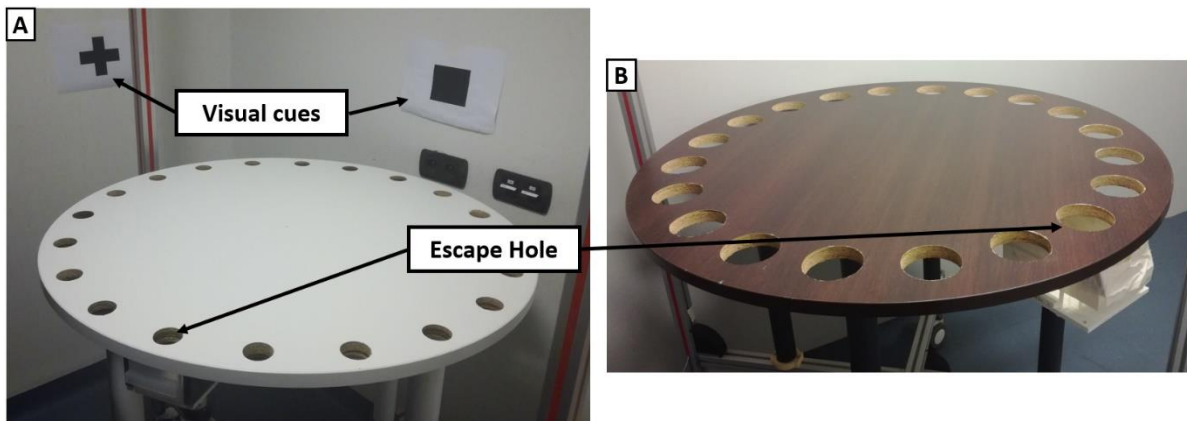


Figure 5-12: A – Barnes maze for mice. B – Barnes maze for rats.

The BM protocol starts with a training step called the learning session. In our case, we used a protocol with 2 trials per days for 4 days. For each trial, the rodent was first trapped under a black box placed at the center of the BM. Trials start when removing the box and turning on light and sound. Then, the animal was given 2 minutes to find the escape hole. When the animal entered the escape box, the light and the noise were turned off and the animal could stay 30 seconds in the escape box. The animal was then put back into its cage during maze cleaning before undergoing the second trial of the day. For each trial, animals were video recorded. Various parameters can be used to quantify their performance:

- Number of errors, i.e. number of holes in which the animal dips its head while they are not the escape hole
- Primary latency, i.e. time delay between the beginning of the trial and the finding of the escape hole
- Deviation, i.e. distance, in number of holes, between the first hole encountered and the escape hole
- Distance walked to find the escape hole.

Finally, on the fifth day also called “test day”, the escape box is removed and animals could explore the maze for 2 minutes, in the presence of the visual cues and of the external stimuli. Walked distance and spent time in each quadrant are quantified. The definition of the quadrant is shown on Figure 5-13.

Figure 5-14 shows results of a BM experiment on eighteen-month old male mice. The AD group was composed of 9 APP/PS1 mice and the WT group of 9 wild type littermates. During the learning session (Figure 5-14 A), the WT group performed better over the days: wild type mice found the escape hole twice as fast on Day 4 as on Day 1 ( $p=0.06$ , Wilcoxon rank test) but APP/PS1 mice did not seem to reduce their primary latency over the learning session. On the test day, both groups of mice walked much more distance in the quadrant of the escape hole (EH) and in the nearby quadrant than in the rest of the maze. This proves that both groups of mice did learn and remember the position of the escape hole, even though the primary latency did not decrease for the AD group.

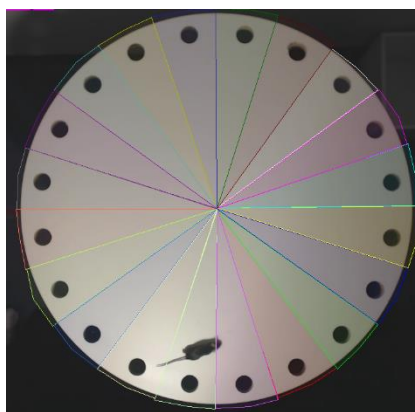


Figure 5-13: Definition of the 20 quadrants in which distance and time are quantified during the test day.

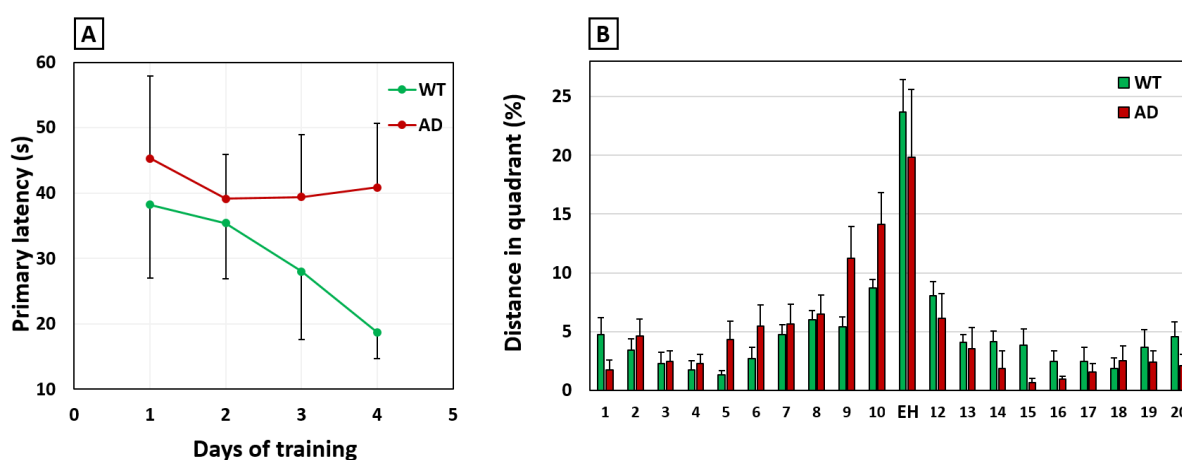


Figure 5-14: Barnes maze results on mice. A – Primary latency over the learning session. B – Distance in quadrant during the test on the 5<sup>th</sup> day. EH stands for the escape hole quadrant.

Wild type mice learned faster than APP/PS1 mice during the learning session: the difference in primary latency between the two groups is statistically significant ( $P=0.043$ , 2-ways ANOVA) when taking the whole learning curve into account. It is noticeable from Fig 5-14 that this difference clearly increases with the number of training days. However, during the test day, WT and TgF344-AD mice walked only 20% more in the quadrant of the escape hole than APP/PS1 mice. This could mean that they remembered better its position than the APP/PS1 mice. This tendency has been reported in the literature (O’Leary and Brown, 2009). In this study, sixteen-months old APP/PS1 mice spent twice as much time in the quadrant of the escape hole as their wild type littermates even though those differences were not significant. Significant differences in learning have already been reported in seven-months old APP/PS1 mice but only with a “cued-target” version of the maze where the hole in indicated with a piece of polystyrene fixed on the edge of the maze (Reiserer et al., 2007). As a conclusion, our BM protocol seems adequate to assess memory impairment on APP/PS1 mice.

Figure 5-15 shows results of a BM experiment on fourteen-month old male rats. The AD group was composed of 7 TgF344-TgF344-AD rats and the WT group of 7 wild type littermates. No statistical differences were found during the learning session although wild type rats seem to perform slightly better on the deviation criteria (Figure 5-15 A). But on the test day, wild type rats walked twice as

much in the quadrant of the escape hole as TgF344-AD rats and they also walked a distance three times as short as TgF344-AD rats to find the escape hole ( $P=0.07$ , Wilcoxon rank test), showing that they did remember better the position of the escape hole than their AD littermates ( $P=0.07$ , Wilcoxon rank test). More animals per group is certainly needed to get significant results.

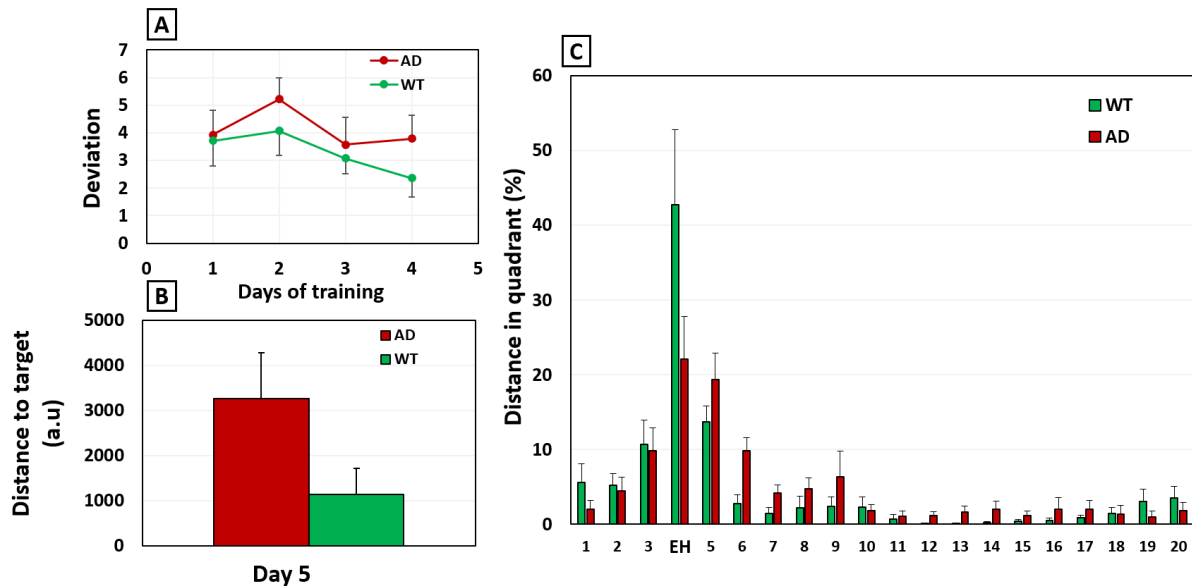


Figure 5-15: Barnes maze results on rats. A – Deviation over the learning session. B – Distance walk to find the escape hole on the 5<sup>th</sup> day. C – Time in quadrant during the test on the 5<sup>th</sup> day.

Only three studies have been published on this model. In one of them, Morris water maze was used instead of BM but it failed to exhibit memory deficit on six-months old TgF344-AD rats (Pentkowski et al., 2017). Literature on the BM for this model is still unclear as another study showed no differences at 15 months (Voorhees et al., 2017) but the main reference paper showed differences at 16 and 26 months (Cohen et al., 2013). *Cohen et al.* showed significant differences in the number of errors at 16 and 26 months during the last days of the learning session and on the test day. Moreover, they showed significant differences in the number of errors during the so called “reversal phase” that we did not perform here: after the test day, the maze can be turned 180° and a shorter learning session is done. Animals have to learn again the position of the escape hole.

In conclusion our BM protocol seems to succeed in observing differences between Alzheimer’s and wild type rats, especially by using the deviation parameter during the learning session and the “distance to target” and “distance in quadrant” during the test day.

In the two next sections, I will present a study where FUS-induced BBB opening was evaluated as a therapeutic tool on our two AD rodent models without addition of drug. The first goal is to limit or reverse the phenotype of AD, in particular the memory deficits. Indeed, reducing the amyloid load is only relevant if it leads to memory improvements. To do so, animals were tested with behavior test after the ultrasound protocol. The second and collinear goal is to demonstrate amyloid plaque clearance, which is thought to be one possible strategy for the restauration of memory on AD animal models. To do so, histology and biochemical analysis (Western Blot and ELISA) were tried. This therapeutic lead is worth investigating because of the current absence of therapy for AD and because

only few studies have evaluated the potential of focused ultrasound on Alzheimer's disease as summarized in paragraph 5.1, with only two of them having performed behavior tests. Here, I worked with AD transgenic models and behavior tests which are different from the ones used by previous studies. Biochemical analysis were based on *Leinenga's* work.

### 5.3. Therapeutic trials on mice

In this section, I will present a study where FUS-induced BBB opening is used as a therapeutic tool on APP/PS1 mice. The first goal is to counterbalance the memory deficits of Alzheimer's disease. To do so animals were tested with behavior test after the ultrasound protocol. The second and collinear goal is amyloid plaque clearance, which is thought to be the cause of the restoration of the memory on Alzheimer's animals. To do so histology and biochemical analysis (Western Blot and ELISA) were tried. This lead still needs to be studied because the absence of current therapy for AD makes every possible therapy worth investigating and because only few studies have investigated the effect of ultrasound on APP/PS1 mice (and only two have performed behavior test). Here I work with AD transgenic mice that were never tested with ultrasound before and I will perform different behavior tests. Biochemical analysis were based on *Leinenga's* work. On a first study I validate the safety of the protocol on wild type animals and on the second I try it as a therapy on Alzheimer animals.

#### 5.3.1. A first trial without motorization

Once a first group of mice was old enough, I tried to use FUS-induced BBB opening as a therapy for Alzheimer's disease. At that time, we did not have the 3-axis motorized system in our possession. So, openings were done by manually holding the transducer and changing the focus to cover the whole brain. We are aware that this protocol had a low reproducibility.

##### a) Protocol

For this study ten-month old mice were separated in three groups. The AD US group made of 8 APP/PS1 mice which underwent 6 sessions of ultrasound, one session a week for 6 weeks. As controls, we used one group of 8 Alzheimer littermates, the AD group, and one group of 8 wild type littermates, the WT group. Those two groups did not undergo anesthesia, they were not manipulated for the 6 weeks of treatment. The timeline of the protocol is showed on Figure 5-17.

Without motorization of the transducer, I used our old BBB opening set of parameters. Ultrasound were shot with a PNP of approximately 0.66 MPa *in situ*. The duty cycle was 3% with a repetition rate of 10 Hz. Ultrasound were shot for 5 minutes. 100  $\mu$ L of microbubbles were injected in retro-orbital right before the sonication, new microbubbles were used each week. During the sonication the transducer was manually moved over the skull to cover the whole brain with 10 seconds of sonication per location. An example of BBB opening is given on Figure 5-16.

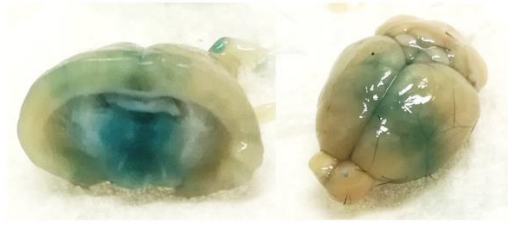


Figure 5-16: This protocol of BBB opening on mice was previously tested with injection of Evan's Blue (EB). This figure shows the brain of a mice after BBB opening, injection of EB and exsanguino-perfusion. EB is clearly present in the brain, more in sub-cortical areas but still in some part of the cortex. The repartition of EB is not homogenous.

After the 6 weeks of ultrasound, the three groups underwent behavior tests. Mice were first tested in the Open Field test to assess anxiety and locomotion impairment and then with Y-maze and Barnes maze to assess memory. Mice were given a full week of rest between the last session of ultrasound and the first behavior test. This delay is important. Indeed, isoflurane anesthesia has been reported to impact performances on memory-based behavior tests even if its effect is still unclear. For example extensive exposures, 6 hours, to isoflurane impairs memory of mice on the Morris water maze up to 2 weeks after anesthesia (Su et al., 2011). With an isoflurane anesthesia of 2 hours, memory deficits on the Y-maze have been reported on rats up to 48 hours after anesthesia (Yan et al., 2012). We are far from those exposure times to isoflurane as our animals were anesthetize at maximum 15 minutes. Moreover, for the next two trials presented in this Chapter, control groups also underwent anesthesia, which makes the comparison to control groups unquestionable.

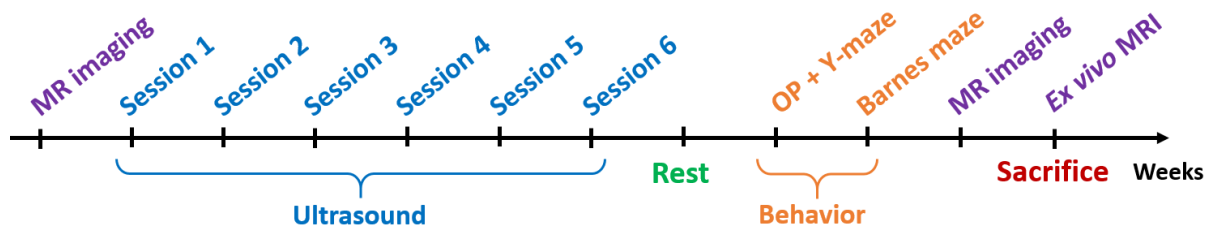


Figure 5-17: Protocol.

At the beginning of the protocol and before sacrifice, the AD US group was imaged with the 11.7 T MR scanner. High resolution  $T_2^*$  images (3D Multi Gradient Echoes, TE = 3 ms, TR = 90 ms, matrix size 280x180x120, resolution 60x60x60  $\mu\text{m}^3$ , echo spacing = 3 ms, 8 echoes, 1 average, total acquisition time 32 min) were acquired to assess damages.

At the end, mice were sacrificed by exsanguino-perfusion to remove blood from vessels. Head were fixed with PFA and placed in falcon tubes. Heads were imaged over night with the high-resolution sequence described in Chapter 4. I scanned as many heads as possible given the available time slots. This results in 4 brains from the AD US group, 3 from the AD group and 2 from the WT group.

b) Safety

Safety was assessed by four means: body mass follow-up, mortality, *in vivo* MR imaging, *ex vivo* MR imaging. BBB opening with those parameters (0.65 MPa, 3% duty cycle) has been used for a long time in our lab and is considered safe. What is new with this protocol is the frequency of the opening (6 openings in 6 months) and the retro-orbital injections of microbubbles.

Figure 5-18 A shows the body mass of the 8 mice of the AD US group over the 6 weeks. Except for some mice in the second week, animals did not suffer weight loss. The 3 curves in light blue represent 3 mice which died during the protocol. This mortality was quite high, but during this period we also reported the death of one mouse of the AD group. Moreover, *in vivo* imaging did not show any sign of damages in the brain. An example is given on Figure 5-18 B and C for one mice but all the remaining mice were imaged and none of them showed damages. Of course, this method has a bias as I could only image mice that survived. *Ex vivo* imaging also did not reveal damages (images are showed in the paragraph 5.3.1.d)

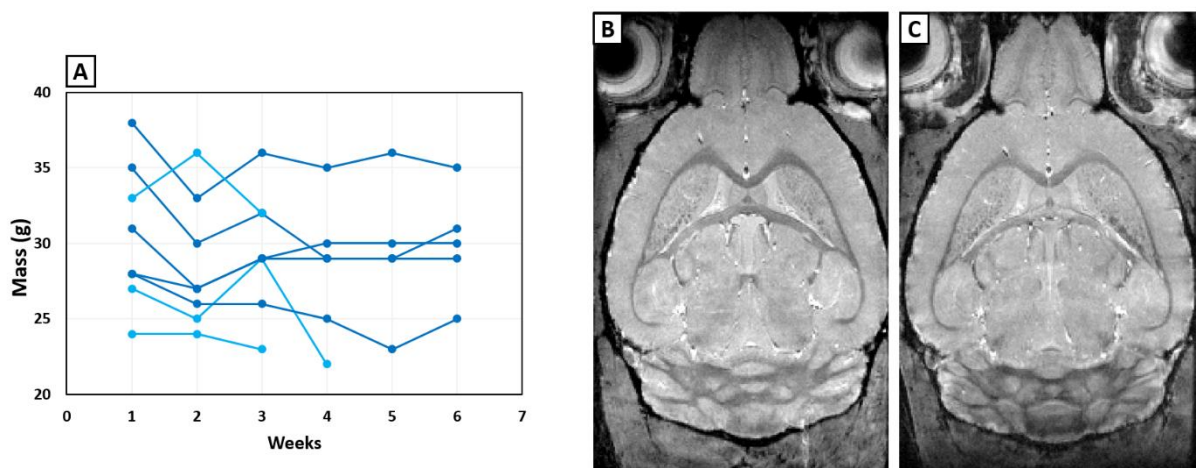


Figure 5-18: A – Follow-up of the body mass of the mice from the AD US group. Mice were weighted before each ultrasound session. B – *In vivo* imaging before the ultrasound. C – *In vivo* imaging of the same mice after the 6 weeks of ultrasound.

Although it is true that the acoustic pressure used was quite high, we think that those deaths were due to either repeated anesthesia or repeated injection in retro-orbital (or missed injections) in old APP/PS1 mice which are already weaker than wild type mice. Those three deaths occurred during the anesthesia of the animals, which advocates for this hypothesis.

c) Behavior test

After the ultrasound protocol, the three groups underwent behavior tests. The Open Field test to assess their anxiety and detect locomotion impairments and the Y-maze and Barnes maze to assess their memory.

Figure 5-19 A shows that SUS-treated APP/PS1 mice walked 30% less in the central area than mice of the AD group. This could mean that they were more anxious. This observation correlates with the fact that SUS-treated APP/PS1 mice walked more than mice of the two other groups (Figure 5-19 B). Maybe they explored more than non-treated APP/PS1 mice because there were more anxious. APP/PS1 mice still walked more than wild type, as previously described. These results might come from the fact that AD and WT groups were not sham-treated and were not handled for the 6 weeks. SUS-treated APP/PS1 mice underwent 6 sessions of ultrasound which might increase their anxiety.

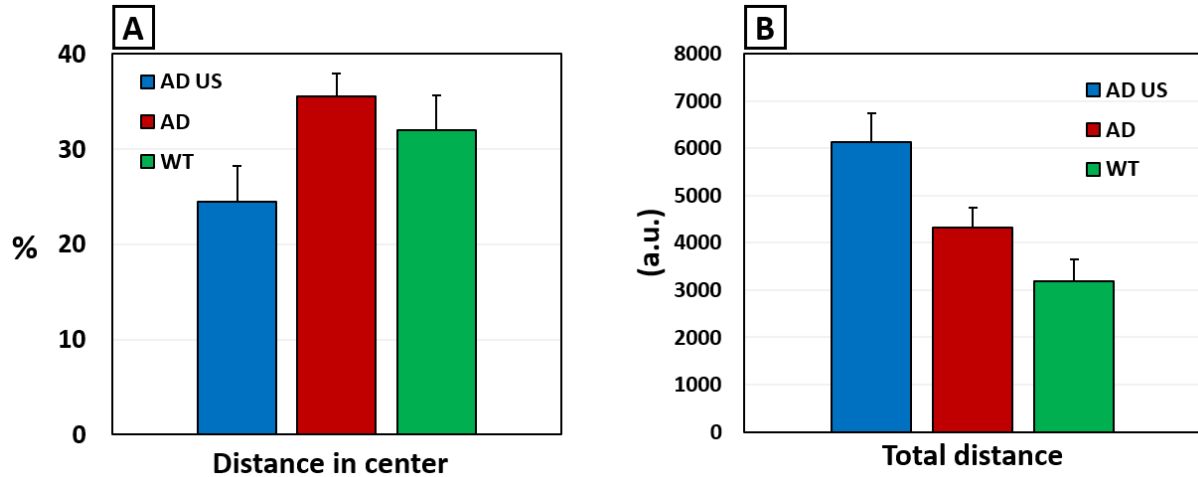


Figure 5-19: Open Field test results. A – Walked distance in the central area. B – Total walked distance.

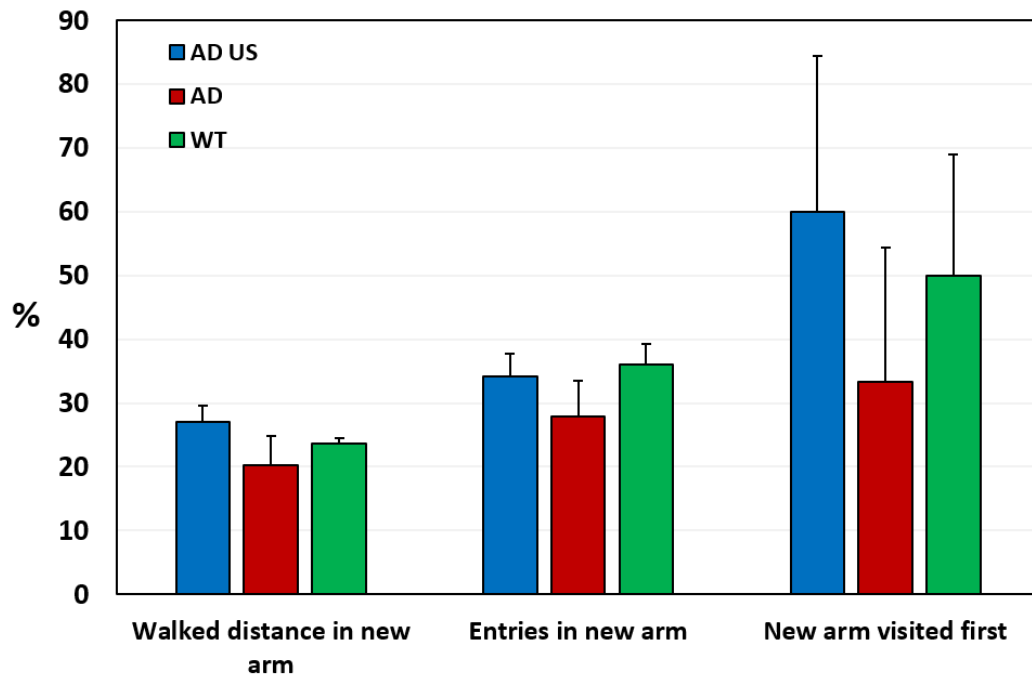


Figure 5-20: Y-maze results. Exploration of the new arm is quantified in three ways: the walked distance in the new arm the relative number of entries in the new arm and the choice of the new arm as first choice.

Figure 5-20 shows the results of the Y-maze, used with the two-step protocol. SUS-treated APP/PS1 mice exhibit a higher exploration of the new arm than the non-treated APP/PS1 mice. In fact, their level of exploration is similar to the WT group. They walked 35% more in the new arm, they entered the new arm 21% more and their first choice is the new arm 81% more than APP/PS1 mice. Those differences are not significant but gives a tendency toward a beneficial role of the ultrasound on the memory of the treated mice. It could even be said that this memory improvement is high as SUS-treated APP/PS1 mice retrieved the exploration level of the Wild type mice.

Mice were then tested with the Barnes maze for a week. Figure 5-21 shows one parameter, the number of errors, which can be used to quantify the learning of the animals. SUS-treated APP/PS1 mice did not seem to learn the position of the escape hole. Indeed, they made between 4 and 6 errors in average over the days 2 to 5 without showing a decrease. On the contrary non-treated APP/PS1 mice clearly reduced the number of errors they made between day 2 and 5 to finish with less than 1 errors on day 5. Wild type mice seem to learn during the first 3 days, but did not improve afterward. The others parameters used to quantify learning (deviation or primary latency) gave similar results and on the first day SUS-treated APP/PS1 mice explore almost equally each one of the 20 quadrants while APP/PS1 mice explore more around the escape hole (data not shown). So, this test does not show any kind of memory improvement for the SUS-treated APP/PS1 mice.

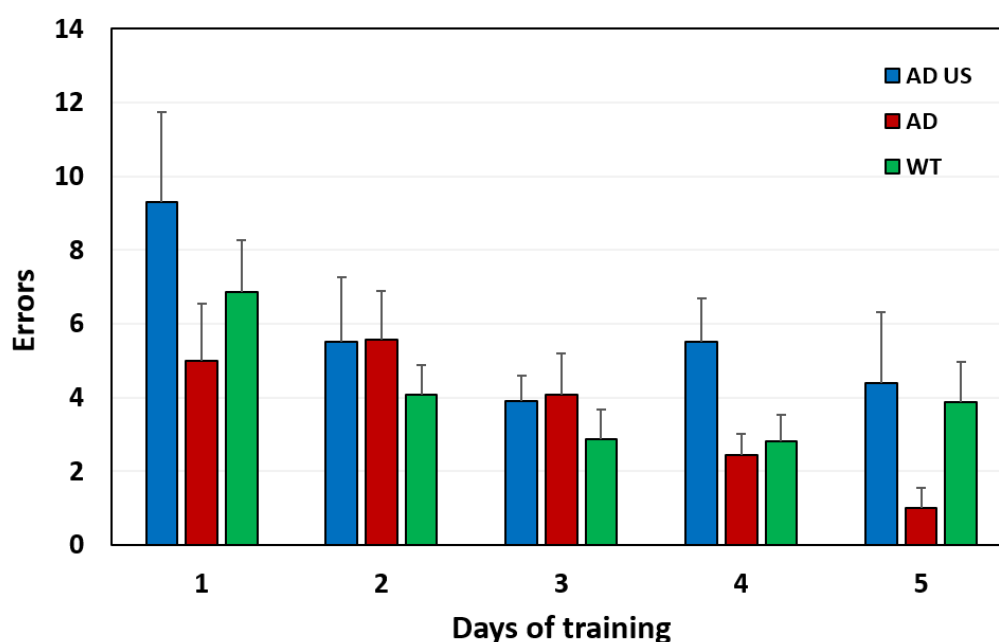


Figure 5-21: Results of the Barnes maze with the number of errors for each day of training.

As a conclusion, these encouraging results regarding memory improvement on the Y-maze have to be interpreted really carefully. Firstly, because this tendency was not confirmed with the Barnes maze. Secondly, because the number of mice per group was really small: only 5 mice in the AD US group and 7 in the AD group. On the Y-maze, one mouse of the AD group explored really little the new arm and decreases the performance of the whole group. The number of mice per group was clearly too small for behavior tests, having groups of at least 8 animals is highly recommended and, of course, the more the better.

But behavior tests characterize a macroscopic phenomenon, behavior resulting from a lot of different factor. So, despite the small number of animals per group, it might be possible to exhibit differences between the AD US and the AD group with other techniques such as imaging.

d) Ex-vivo imaging

After behavior, as many mice as possible (4 AD US, 3 AD and 2 WT) were imaged *ex vivo* with the sequence described in Chapter 4. An example of an ultrasound treated mice is given on Figure 5-22.

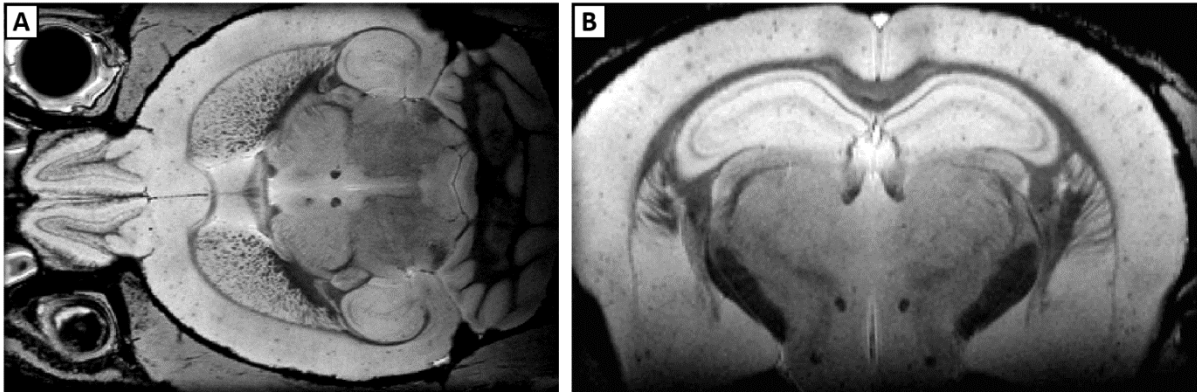


Figure 5-22: *Ex vivo* imaging of a mouse of the AD US group. A – Horizontal view. B – Coronal view.

Amyloid plaques were then quantified with the homemade software I presented in Chapter 4. SUS-treated APP/PS1 mice have in average 23% more plaques than non-treated APP/PS1 mice (in number of plaques, data not shown) and amyloid plaques filled a volume of the cortex 23% higher (Figure 5-23). So no there is no effect on the amyloid plaque load which could be due to ultrasound.

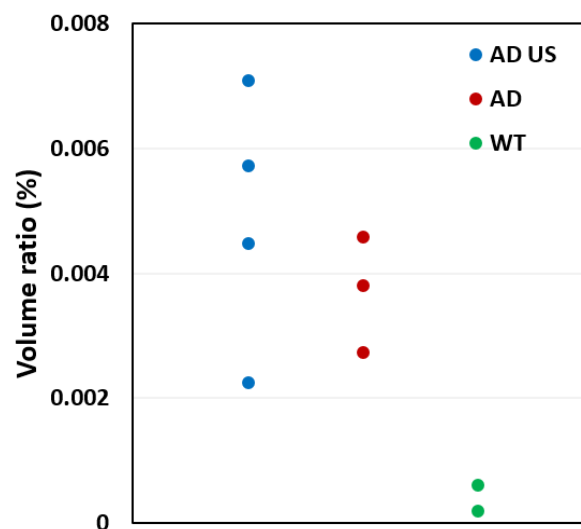


Figure 5-23: Amyloid plaques quantification with the volume of the cortex filled with amyloid plaques.

It not possible to say that ultrasound had an impact on the amyloid plaques load. Even with imaging of the remaining animals, it is difficult to expect differences between the AD US and the AD group. We have to remind here, that the amyloid load was only quantified in the upper parts of the cortex (not in the temporal part), as illustrated on Figure 4-10 with the mask of the cortex. Amyloid plaque clearance in other regions could not be detected.

e) Limits of this study

This study was a first trial performed with the tools available at this time. Despite interesting results showing a tendency to memory improvement with the Y-maze, amyloid plaques clearance was not observed and Y-maze results were not confirmed with Barnes maze.

One limit of this study is the reliability of the FUS-induced BBB opening protocol. Indeed, the transducer was manually handed, which can cause variability between the animals. Moreover, the BBB opening was stronger deep in the brain and lighter in the cortex and subcortical regions. As illustrated on Figure 5-22, amyloid plaques are mainly present in the cortex and in subcortical regions such as the hippocampus, so in the upper half of the brain. This distinction between the regions we opened and the area where amyloid plaques were quantified proves that it was necessary to develop a more systematic way of opening the BBB on mice, which I did using the 3-axis motorized system.

In addition to improving the ultrasound protocol, this study also allowed us to train skills such as retro-orbital injections or animal handling and to practice with behavior test and tune some of their parameters.

**5.3.2. A safety study**

The goal of this study is to validate the safety of this new protocol with the 3-axis motorized system. It was necessary for me to do so because the sonication is different, it uses continuous wave combined with a displacement of the transducer. The safety of such an opening was already tested in the Chapter 2. Here I assess the safety regarding behavior tests.

a) Protocol and follow-up of the weights

Sixteen-month old females were used in this study. The protocol is presented on Figure 5-24. Mice were separated in two groups: the WT group made of 8 mice which received a sham treatment (ultrasound were shot but with an amplitude of 0) and the WT US group made of 7 mice which received an ultrasound treatment. Mice underwent 6 sessions of ultrasound, once a week for 6 weeks. At each session, mice were anesthetized with isoflurane in a mixture of air and oxygen. They were shaved and placed in a stereotaxic frame. 50  $\mu$ L on microbubbles (new ones each week) were injected in retro-orbital and ultrasound shot right after with the motorized trajectory presented in Chapter 2.



Figure 5-24: Protocol.

Based on a preliminary study, the transmission factor for sixteen-month old mice was thought to be around 65%. Ultrasound were shot at 16% of the benchtop amplitude which corresponds to 0.7 MPa *in-situ*. This pressure turned out to be relatively high. Indeed, the transmission factor was under estimated. With measurement done on more skull samples, the transmission factor turned out to be around 80-85% for mice of this age. Such a pressure might create damages like edema of micro-hemorrhages, we are here at the limit of the safety window described in Chapter 1. But being at the limit of the safety window makes a lot of sense for a safety study. We are here studying the worst-case scenario.

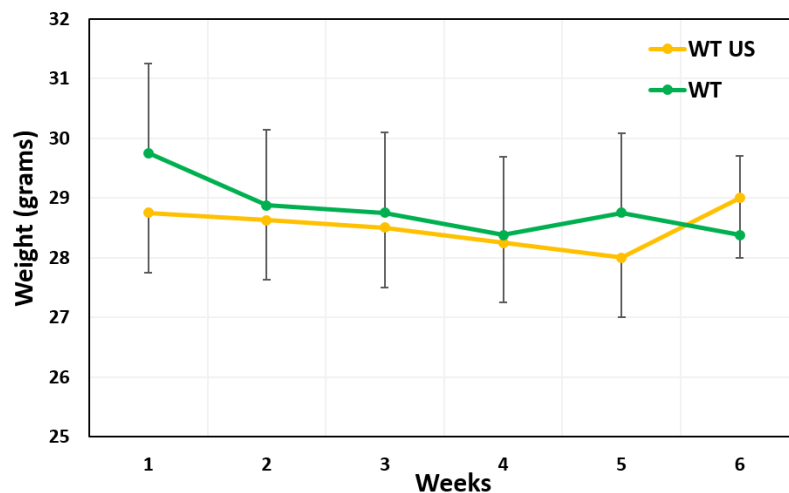


Figure 5-25: Follow-up of the body mass (mean  $\pm$  s.d.) of the two groups.

Figure 5-25 shows the evolution of the weights of mice of the two groups. All animals were weighted before the ultrasound session. Week 1 is actually the reference weighting before the protocol. The variation of mass for the WT US group is small. Indeed, the mean mass does not change more than 1 gram (only 3% of the total body mass), with a slow decrease at the beginning and an increase at the end. This decrease is similar to the one of the WT group, which received only a sham treatment. This leads us to think that this body mass loss is more likely to come from the effect of repeated anesthesia than from ultrasound itself. This result is a first argument in favor of the safety of the technique. Indeed, even at the limit of the safety window, body mass loss does not differ between the ultrasound-treated and the sham-treated mice.

b) Results of the behavior tests

After the 6 ultrasound sessions, the three behavior tests in our possession were performed in these mice. I will here present the relevant results.

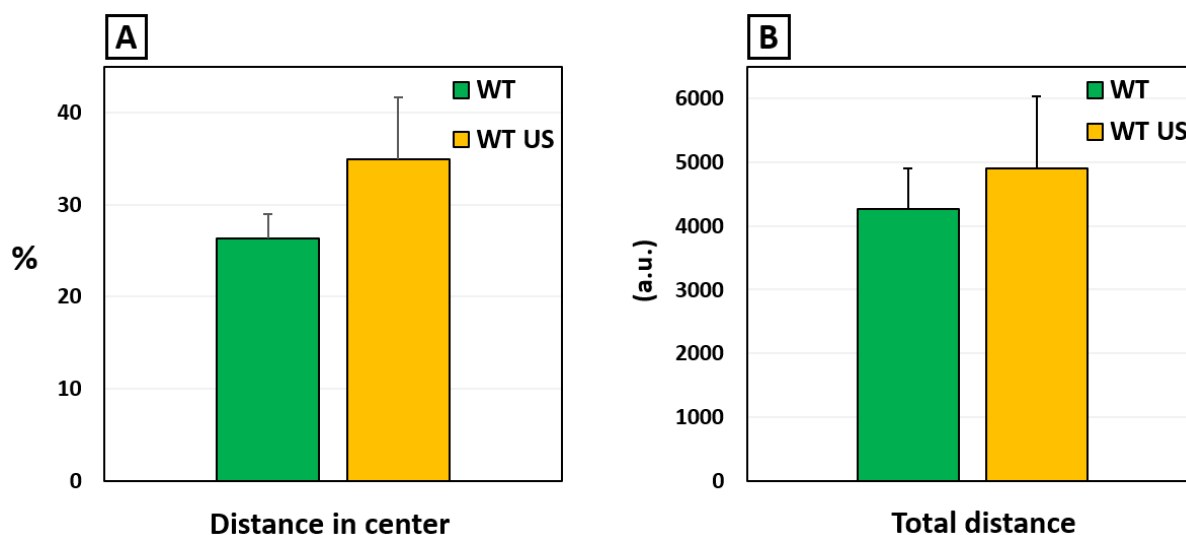


Figure 5-26: Open Field results. A – Walked distance in the central area. B – Total walked distance.

Firstly, the Open Field test. The results of the test are presented on Figure 5-26. Mice of the WT US group walked more time in the central area (A) and walked more distance overall (B). It can be concluded from this test is that SUS-treated wild type mice are not more anxious or to have more locomotion impairment when compared to their sham-treated littermate. This result is another argument in favor of the safety of the technique. Indeed, even at the limit of the safety window, ultrasound do not cause deleterious effects on basic behaviors such as anxiety or locomotion.

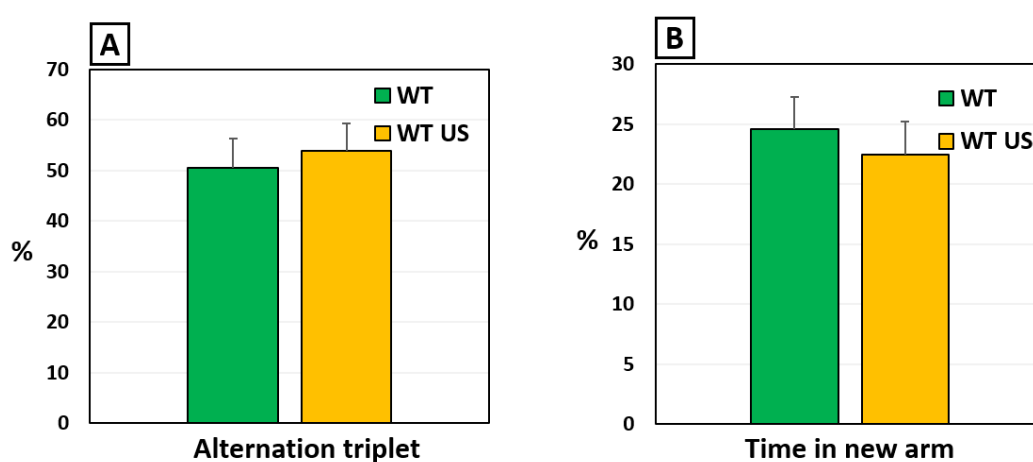


Figure 5-27: Y-maze results. A – Alternation triplet. B – Time in new arm.

Secondly the Y-maze test. The results of the test are presented on Figure 5-27. Performances of the two groups were much alike. Indeed, on the one hand SUS-treated mice explored a little bit more the new arm (B) but on the other hand they made little bit less alternation triplets (A). Those differences were really small and not significant, so it can be said that those two groups performed similarly.

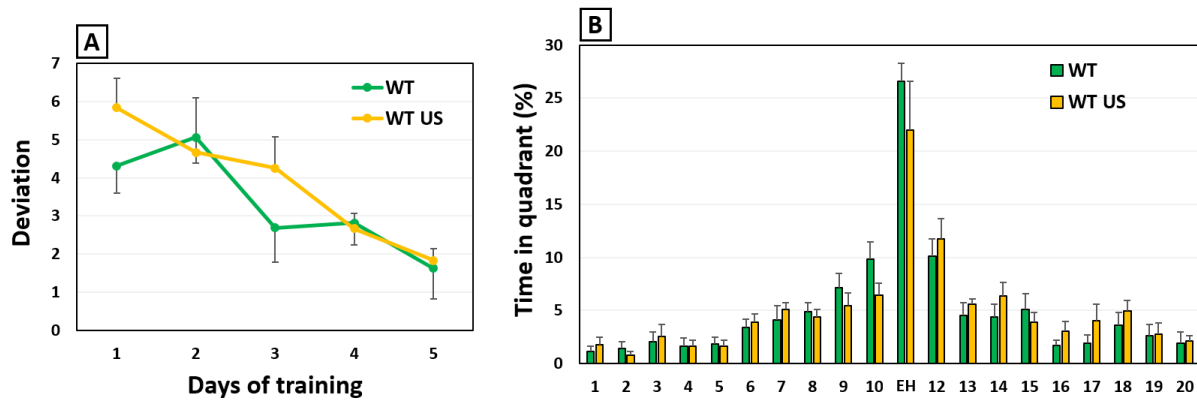


Figure 5-28: Results of the Barnes maze. A – Deviation over the learning session. B – Time in quadrant during the test on the 5<sup>th</sup> day.

Thirdly, the Barnes maze test. The results of the test are presented on Figure 5-28. SUS-treated and sham-treated mice performed similarly during the learning session. Even if the deviation of the SUS-treated mice is higher at the beginning, both deviation scores decreased over the week and were almost identical on Day 4 and 5. On the test day, SUS-treated mice spent 20% less time in the quadrant of the escape hole but not significantly less.

These two last tests show no differences on the memory of the animals. It means that cognitive functions are not altered by the ultrasound. This is an important result because I will later on use this protocol on APP/PS1 mice in order to restore memory impairments and decrease the amyloid load. It would have been contradictory to try restoring memory with a protocol inducing memory impairments.

Overall this protocol seems safe regarding the physical condition and the behavior of the animals. I remind here once more that I was here at the limit of the safety window, which means that those conclusions remain valid for the following study done at 0.5 MPa *in-situ*.

### 5.3.3. A second trial on APP/PS1 mice

The objective of this study was to test the new protocol of FUS-induced BBB opening as a therapy on APP/PS1 mice. Mice were one-year old at the beginning of the ultrasound protocol and fourteen-months old for the behavior. We believe that this age is relevant because, according to literature, they have already developed amyloid plaques and they start to show memory impairments. It is our hypothesis that an early therapy would be more beneficial than a late therapy when memory impairments are already severe. The idea is more to prevent than to cure. Indeed, according to the amyloid cascade hypothesis, memory impairments are at the end of the cascade which starts with

amyloid plaques deposition. So, it would be already too late when memory impairments are severe. Too late therapies might be the reason why many people think that phase 3 clinical studies have failed.

Mice were spread in three groups. One group with 8 APP/PS1 mice that were treated with ultrasound: the AD US group. One group with 9 APP/PS1 mice that received a sham treatment (ultrasound shot with an amplitude of 0 MPa): the AD group. One group with 9 wild type mice that received a sham treatment: the WT group. The protocol is presented on Figure 5-29. It is similar to the protocol for the safety study but ultrasound are shot with a lower pressure, in order to have 0.5 MPa *in-situ*. Moreover, at the end of the behavior test, mice were sacrificed for amyloid plaques quantification. Animals were exsanguino-perfused with PBS, one hemisphere was then fixed with PFA for histology and the other hemisphere was frozen at -80°C for western blot and histology.

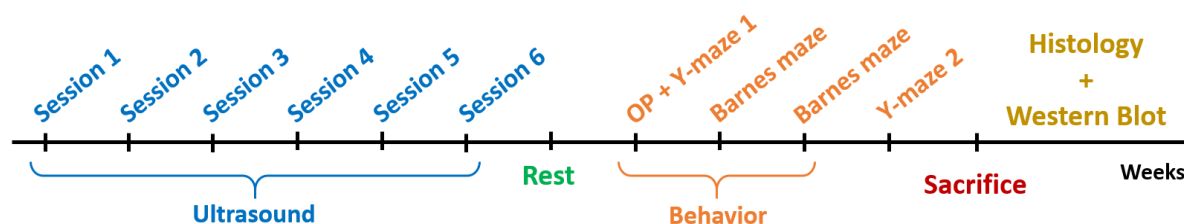


Figure 5-29: Timeline of the protocol.

Compared to the last protocol, a second week of test was also added to the Barnes maze. After the first 5 days and 2 days of rest, the maze is rotated 180° so the escape hole is at the other side of the maze. This phase is called the reversal phase. For 3 days mice underwent another learning session with 2 trials per days, like during the first week. On the 4<sup>th</sup> day of the reversal phase, the escape box removed and mice can freely explore the maze for 2 minutes. The time and distance in each quadrant is quantified. The behavior tests were performed by Erwan Selingue.

#### a) Behavior tests

After the 6 weeks of ultrasound, mice underwent behavior tests. First the Open Field test to assess anxiety and locomotion impairments. Then they were tested on the Y-maze and Barnes maze to assess their memory.

Figure 5-30 shows the results of the Open Field test. SUS-treated APP/PS1 mice explored 40% more the central part of the maze than the sham-treated APP/PS1 mice ( $P=0.049$ , Wilcoxon test) (A). This tendency suggests that the ultrasound treatment reduce the anxiety of the APP/PS1 mice. SUS-treated APP/PS1 mice walked as much as sham-treated mice, which suggests that ultrasound have no effects on locomotion (B). The two groups of APP/PS1 mice both walked more than wild type mice but this is well reported in the literature and already described in the paragraph 5.2.1.

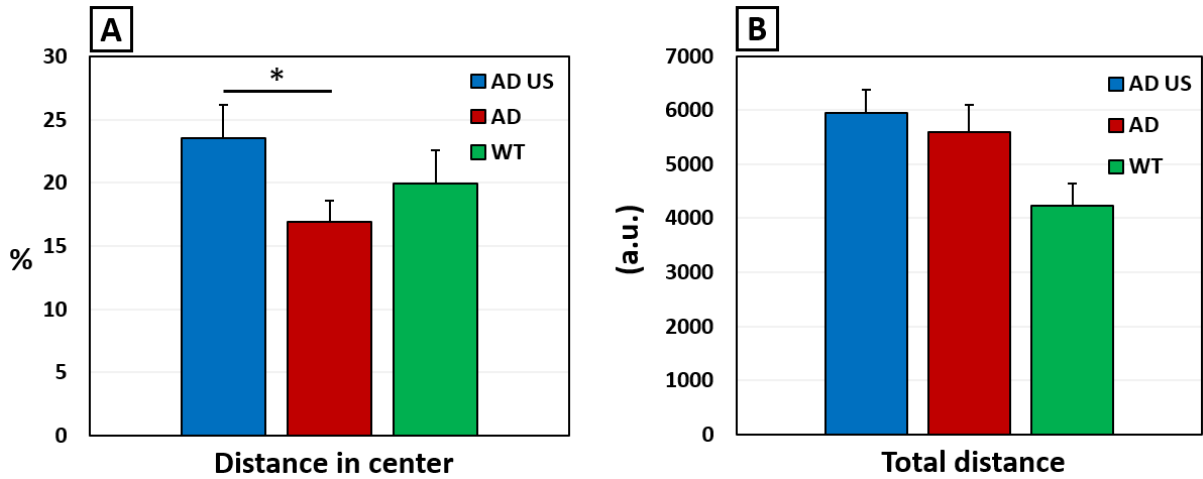


Figure 5-30: Open Field results. A – Walked distance in the central area. B – Total distance walked.

Figure 5-31 shows the results of the Y-maze test. During the two-step trial (A), when mice can explore the three arms, ultrasound-treated APP/PS1 mice went 50% more for the new arm than the sham-treated APP/PS1 mice (but still less than sham-treated wild type mice). This could mean that they remembered better than the sham-treated APP/PS1 mice that they have not explore this arm yet. During the one-step trial (B), SUS-treated APP/PS1 mice made 17% more alternation triplet than sham-treated APP/PS1 mice which could mean that they have a better short memory. Unfortunately, mice of the WT group, which are the control mice, did as much alternation triplets as mice of the AD group. This questions the efficacy of this test. These differences between the AD US and the AD groups are interesting, they are not statistically significant but show a tendency which is supported by the next test: a reduction of the memory impairments.

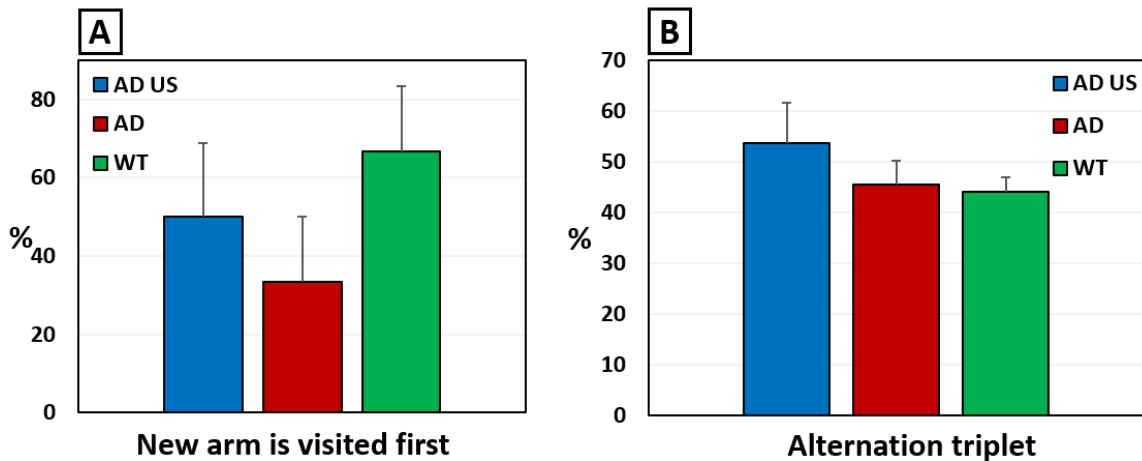


Figure 5-31: Y-maze results. A – First arm choice. B – Alternation triplets.

Figure 5-32 shows results of the Barnes maze test. Figure 5-32 A shows the mean number of errors of each group. The effect of learning was not clear during the classic phase (Days 1 to 5). Indeed, the number of errors done by the WT group, which is the control group, did not decrease over the 5 first days.

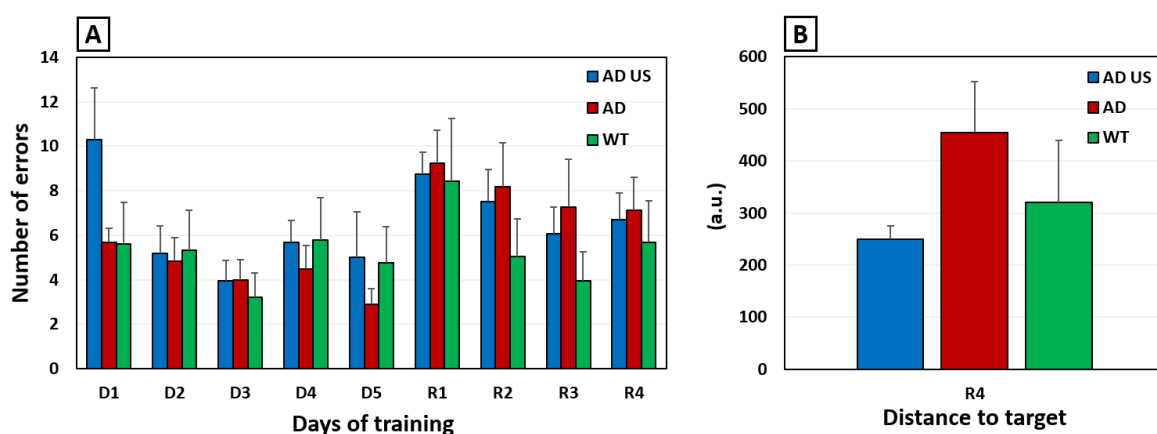


Figure 5-32: Barnes maze results. A – Number of errors over the learning session. B – Distance to target on day R4.

Nevertheless, during the reversal phase mice learned again the position of the escape hole. Interestingly there was a constant tendency for the days R1 to R4, the SUS-treated APP/PS1 mice did fewer errors than the sham-treated APP/PS1 mice. When the results of days R1 to R4 are tested with 2-ways ANOVA, the effect of days is clearly significant ( $P=0.00008$ ), which shows that mice re-learned the position of the escape hole, and the effect of group is almost significant ( $P=0.07$ ). SUS-treated APP/PS1 mice and sham-treated APP/PS1 mice performed quite differently ( $P=0.08$ , Tukey post-hoc test), while SUS-treated APP/PS1 mice and wild type mice performed more similarly ( $P=0.68$ , Tukey post-hoc test). This result was strengthened by the fact that the sham-treated wild type mice did fewer errors than the two other groups. Moreover, on R4, SUS-treated APP/PS1 mice walked 45% less than sham-treated APP/PS1 mice ( $P=0.15$ , Wilcoxon test) to find the escape hole and around the same distance than the wild type mice (Figure 5-32 B). This result could suggest that SUS-treated APP/PS1 mice learned or remembered better the new position of the escape hole than the sham-treated APP/PS1 mice. Even if those differences were not significant, this could be a sign of memory improvement due to the ultrasound.

Figure 5-33 shows the time mice spend in each quadrant on D5. Mice of the three groups did explore more the quadrant of the escape hole. But the SUS-treated APP/PS1 mice and the wild type mice did not spend more time in the quadrant of the escape hole than the sham-treated APP/PS1 mice. Those results did not suggest any sign of memory improvements in the SUS-treated APP/PS1 mice. But the results of the test day could be seen as less relevant than direct quantification of the escape hole during the learning session such as errors, deviation, time or distance to find the escape hole. Indeed, once the escape hole is found and its absence checked by the animals, curious animals explore more the other holes and stay less in the quadrant of the escape hole. This is why some studies present only direct quantification such as errors (Bach et al., 1995; Cohen et al., 2013) or primary latency (Voorhees et al., 2017).

It also has to be noticed that mice of the three groups made much more errors on R1 than on D5. Results are not shown but the deviation was almost doubled on R1 (6.1 in average for the three group) when compared with D5 (3.1 in average for the three group). Those results prove that mice really

oriented themselves with the extra-maze visual cues. On R1, mice went more to the old position of the escape hole. This result confirms the good functioning of the Barnes maze.

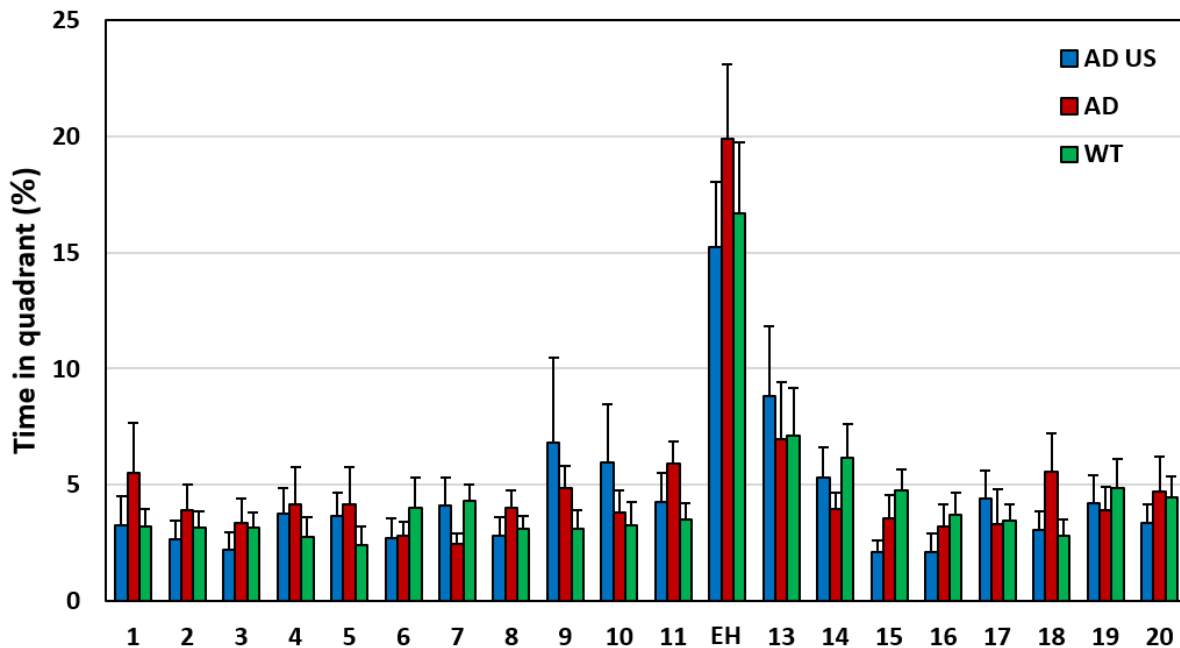


Figure 5-33: Barnes maze results on APP/PS1 mice. Time in quadrant during the test on the 5<sup>th</sup> day.

As a conclusion it can be said first that ultrasound seems to have an effect on the anxiety of the animals. This point is relevant as increased anxiety is one of the first symptoms of clinical AD and requires a lot of means to take care of the patients. And secondly, all together, the results presented on Figure 5-31 and Figure 5-32, could show signs of memory improvements in the SUS-treated APP/PS1 mice when compared to the non-treated APP/PS1 mice. This tendency will have to be correlated with amyloid plaque clearance which will be studied by histology and biochemical analysis (biochemical analysis are still undergoing).

## b) Histology

After behavior test, mice were sacrificed. Mice were exsanguino-perfused with PBS to remove blood from the vessels. One hemisphere was fixed in PFA for histology and the other was frozen for biochemical analysis. Brains were stained with Thioflavin-S as described in Chapter 4. For each mouse, approximately 10 axial slices equally distributed in the brain were stained. Examples of this staining are given on Figure 5-34. So far, 8 mice of the AD US group and 6 mice of the AD group have been analyzed.

For each mouse, two slices at the beginning of the hippocampus were selected. Slices were specifically selected in this region because this region is at the center of the ultrasound trajectory. For each sonication the transducer was manually positioned at the top of the skull. Intrinsic errors of positioning could shift the trajectory few millimeters forward the nose or toward the cerebellum. But even with these errors, the region at the beginning of the hippocampus is always covered by the trajectory.

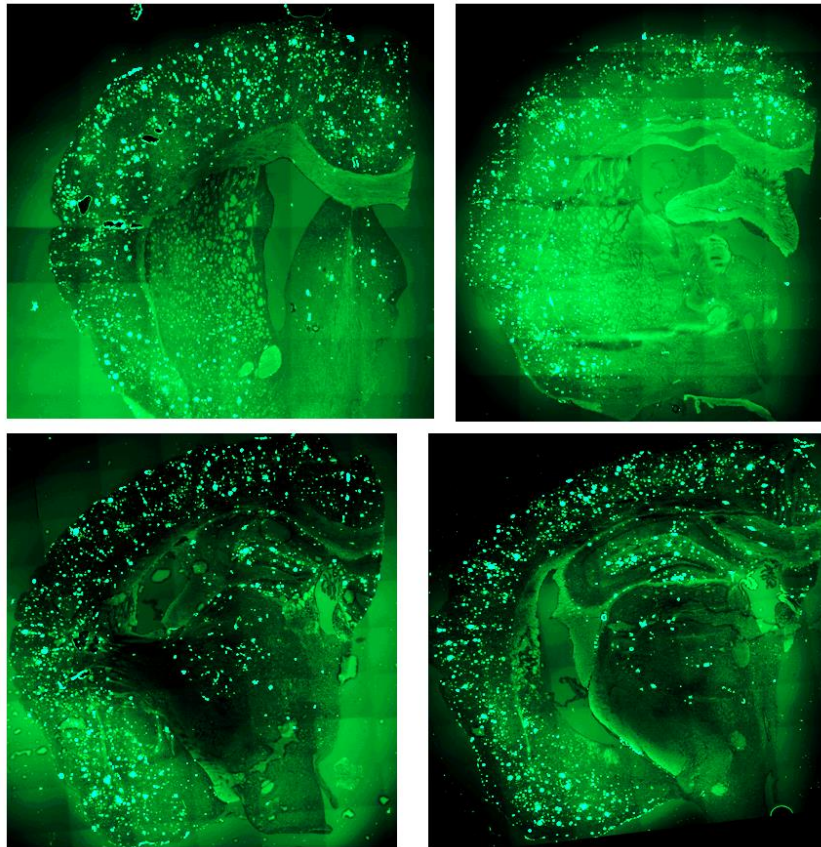


Figure 5-34: Thioflavin-S staining

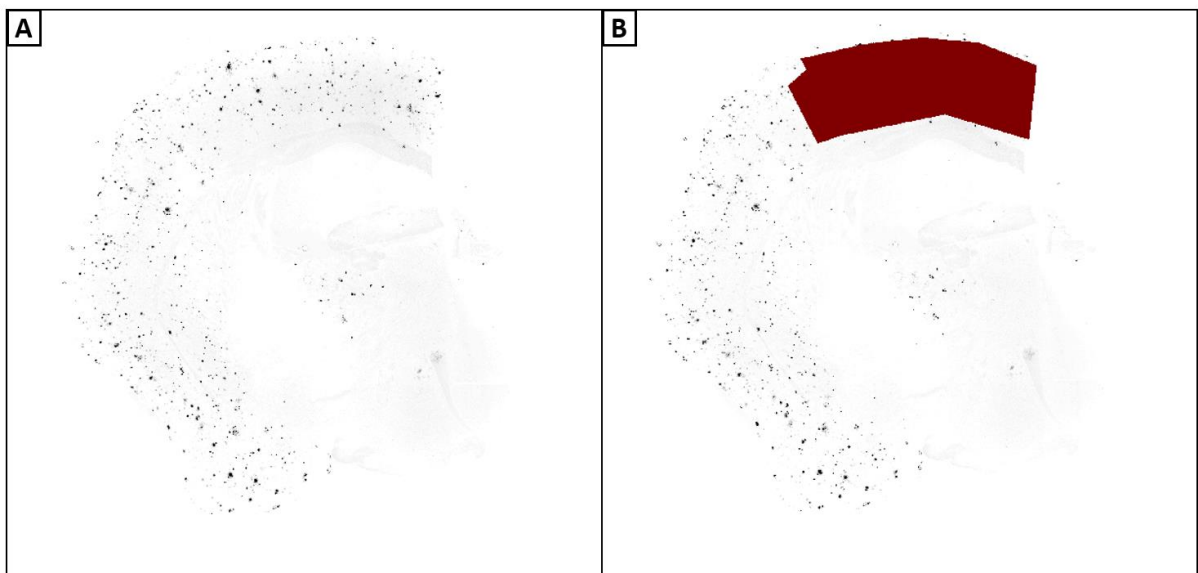


Figure 5-35: Black and white images of the Thioflavin-S. A – Original image. B – Mask of the upper cortex in red.

On these selected slices, the upper part of the cortex was masked out, as illustrated on Figure 5-35. The mask, in red on Figure 5-35 B, was approximately 3 mm wide. This size corresponds to half the width of the trajectory which is center in the middle of the brain. Then amyloid plaques were quantified in the masked region according to the data processing presented in Chapter 4. For this dataset, the threshold was set at 220 (out of 256 bits) and cluster smaller than 5 pixels were excluded.

After analysis of all the available animals, no differences, between the AD US group and AD, in the amyloid plaques load were found. The number of plaques, surfaces of plaques and mean size of plaques were similar (data not showed).

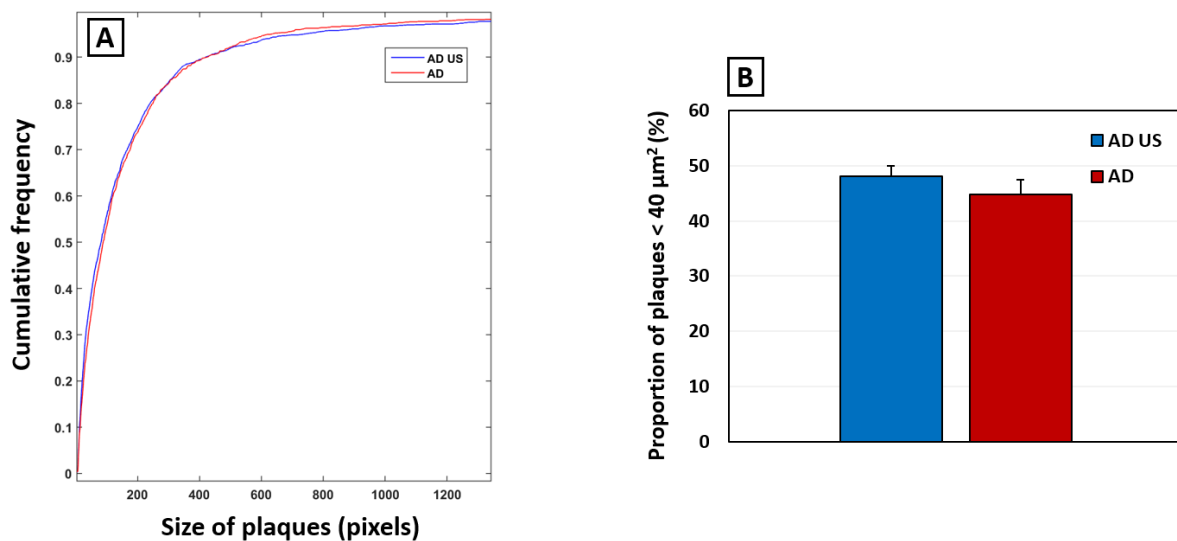


Figure 5-36: A – Cumulative frequency of the size of the amyloid plaques. B – Fraction of plaques smaller than 40  $\mu\text{m}^2$ .

SUS-treated mice seems to have smaller amyloid plaques. Figure 5-36 A shows the cumulative frequency of the plaques size. Under 400 pixels, the cumulative frequency of the SUS-treated group is always higher compared with the sham-treated groups. Figure 5-36 B shows the proportion of plaques smaller than 40  $\mu\text{m}^2$ . This proportion is 7% higher in the SUS-treated mice when compared to the sham-treated mice. The effect is small and not statistically significant.

Such a small effect could be explained by the fact that mice were sacrificed one months after the last BBB opening session, which is considered late by some authors (Leinenga and Götz, 2018). In most studies, sacrificed in done within a week (Burgess et al., 2014; Jordão et al., 2013; Leinenga and Götz, 2015), which leaves less time for behavior and implies for the animals to undergo behavior without rest after the last ultrasound sessions.

## 5.4. Therapeutic trial on rats

In this section I will present a therapeutic trial on TgF344-AD rats. Due to the difficulty to breed these animals in our facility, I got animals old enough to start a therapy only by the end of my PhD. So, I could perform only on trial.

### 5.4.1. Ultrasound protocol

Animals were one-year old at the beginning of the protocol. Rats were spread in three groups. One group with 9 TgF344-AD rats that were treated with repeated session of FUS-induced BBB opening: the AD US group. One group with 11 TgF344-AD rats that received a sham treatment (ultrasound shot with a PNP of 0 MPa): the AD group. One group with 14 wild type rats that received a sham treatment: the WT group.

The protocol was identical to the protocol used on APP/PS1 mice (see Figure 5-29). The two protocols were performed in parallel. Rats underwent 6 weeks of ultrasound with one session per week. Ultrasound sessions for mice and rats were on the same days. I performed the behavior tests on rats when Erwan Selingue was performing those on mice.

The ultrasound protocol slightly differed from the one used on mice. Because the rat brains are much larger than mice brains, the trajectory was not a 6 by 6 mm square but was extended to a 8.4 by 8 mm<sup>2</sup> rectangle (Figure 5-37). The trajectory was not extended farther because the lifetime of the microbubbles in the blood is limited and we want to ensure a sufficient number of repetition of the transducer on the sonicated area. The electrical voltage transmitted to the transducer was increased to 21% of the maximum voltage in order to have 0.6 MPa in-situ. Previously, this protocol was tested and optimized with injection of a contrast agent and MR imaging.

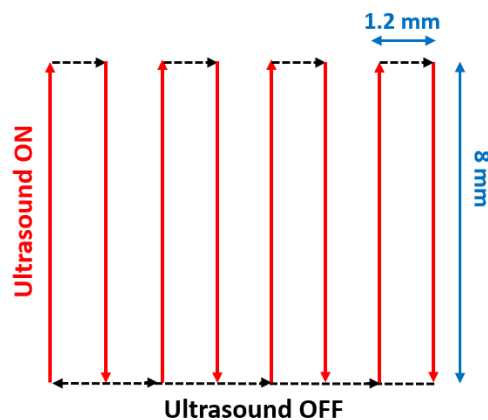
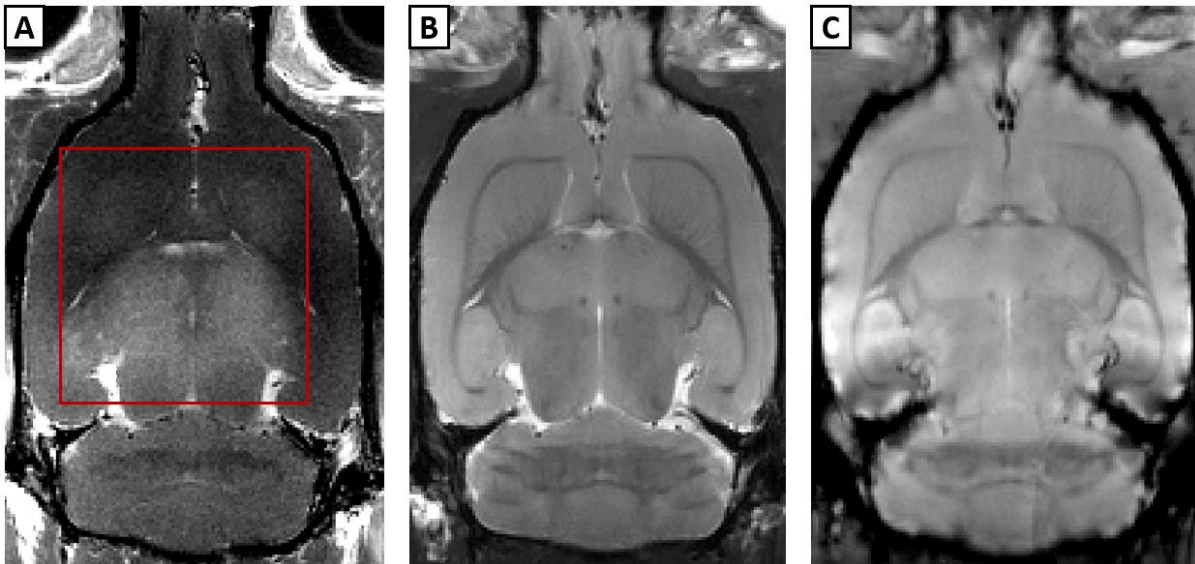


Figure 5-37: Ultrasound trajectory chosen for the repeated BBB opening protocol.

Rats were headshaved and anesthetized with isoflurane. This FUS-induced BBB opening was performed with the benchtop and the 3-axis motorized positioning system. 200  $\mu$ L of microbubbles were injected in retro-orbital before sonication. After sonication rats were placed in the MR scanner

and a gadolinium-based contrast agent (Dotarem) was injected through a catheter in the tail vein.  $T_1$ -weighted images were acquired to evaluate the extent of the BBB opening. Figure 5-38 shows the results of the optimization of the ultrasound trajectory. Different size of the opening region and different acoustic pressure have been tested. A safe and efficient trajectory has been found with the parameter described above: an 8.4 by 8 mm rectangle and a 21% amplitude. As shown on Figure 5-38 A the BBB opening is quite homogeneous, especially in the hippocampus. Opening the BBB in this region is of great interest because hippocampus is a region closely correlated with memory. Damages were looked for at 24h after BBB opening. No edema (B) nor hemorrhages (C) were found.



*Figure 5-38: Optimization of the trajectory for BBB opening on rats. A –  $T_1$ -weighted image with the open area in the red square, where contrast agent has extravagated. B –  $T_2$ -weighted image 24 hours after opening, edema would have appeared as hypersignals. C –  $T_2$  star weighted image 24 hours after opening, hemorrhages would have appeared as hyposignals.*

Surprisingly, many animals died during the 6 weeks of ultrasound: 4 rats of the AD US group and 3 rats of the AD groups. Whether or not this was due to ultrasound is unclear. Indeed, the BBB opening protocol was tested and considered safe and sham-treated rats died too. When ultrasound-treated rats died, their brains were extracted and no hemorrhages were found. Therefore we think that the death of rats was due to weakness of the transgenic rats combined with the repeated anesthesia and microbubbles injections. TgF344-AD rats were autopsied and a lot of them were in poor condition, we found big tumors in the liver or spleen, stomachs filled with air or bladder with blood. This makes us think that the deaths were more probably due to the phenotype, transgenic animals seems weaker and might not have born repeated anesthesia.

#### 5.4.2. Behavior tests results

After the 6 weeks of ultrasound, rats underwent behavior tests. First the Open Field test to assess anxiety and locomotion impairments. Then they were tested on the Y-maze and Barnes maze to assess their memory.

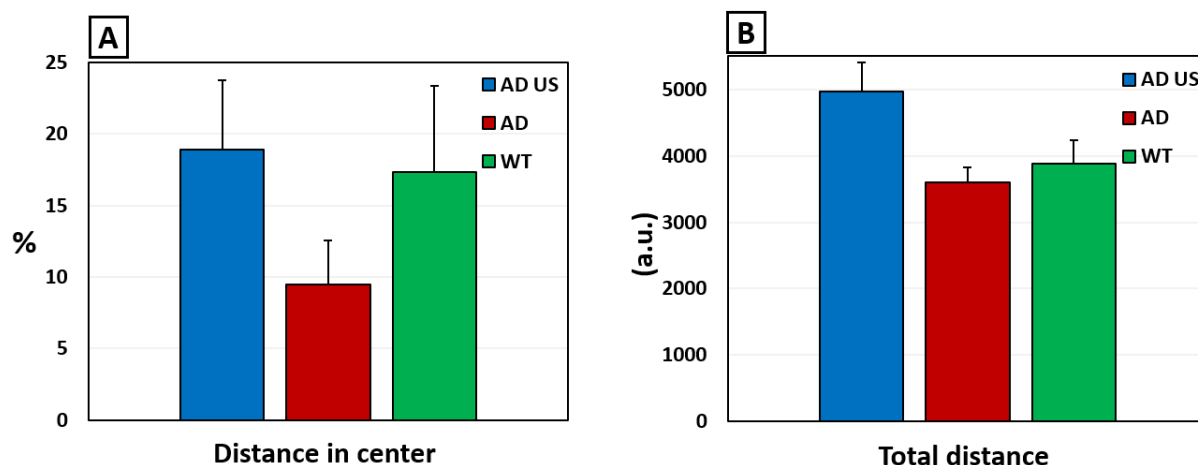


Figure 5-39: Open Field results. A – Walked distance in the central area. B – Total distance walked.

Figure 5-39 shows the results of the Open Field test. Ultrasound-treated TgF344-AD rats explored the central part of the maze twice as much as the sham-treated TgF344-AD rats (A) and as much as the wild type rats. This tendency suggests that the ultrasound treatment reduces the anxiety of the TgF344-AD rats. Ultrasound-treated TgF344-AD rats walked more than the sham-treated rats, which suggests that ultrasound did not cause any locomotion impairments (B).

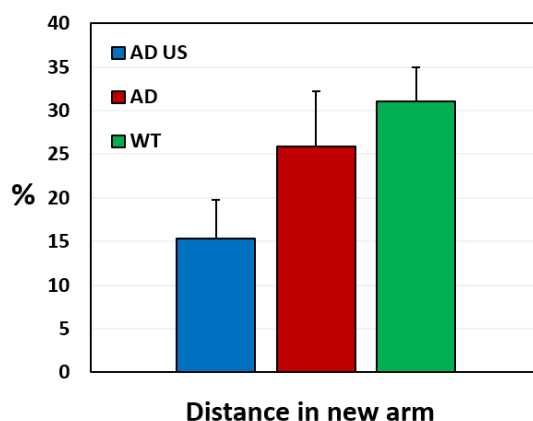


Figure 5-40: Y-maze results on TgF344-AD rats after ultrasound. Ultrasound-treated TgF344-AD rats do not explore more the new arm than non-treated TgF344-AD rats.

Figure 5-40 shows the result of the Y-maze test. This test was disappointing as many rats did not take part, they just stayed in the start arm or at best crossed the maze once. In these conditions, it is difficult to quantify the exploration of the rats and to conclude anything on their memory. As a comparison, rats walked on average 680 units and did 6 arms entries during the 5 minutes of the test when mice walked 2050 units and did 25 arms entries on the same time. 3 rats of the AD US group, 3 rats of the AD group and 4 rats of the WT groups did 3 or less arms entries. This makes it impossible to quantify alternation triplets. Indeed, it is often considered that animals performing less than 8 arms entries should be excluded from analysis (Wolf et al., 2016).

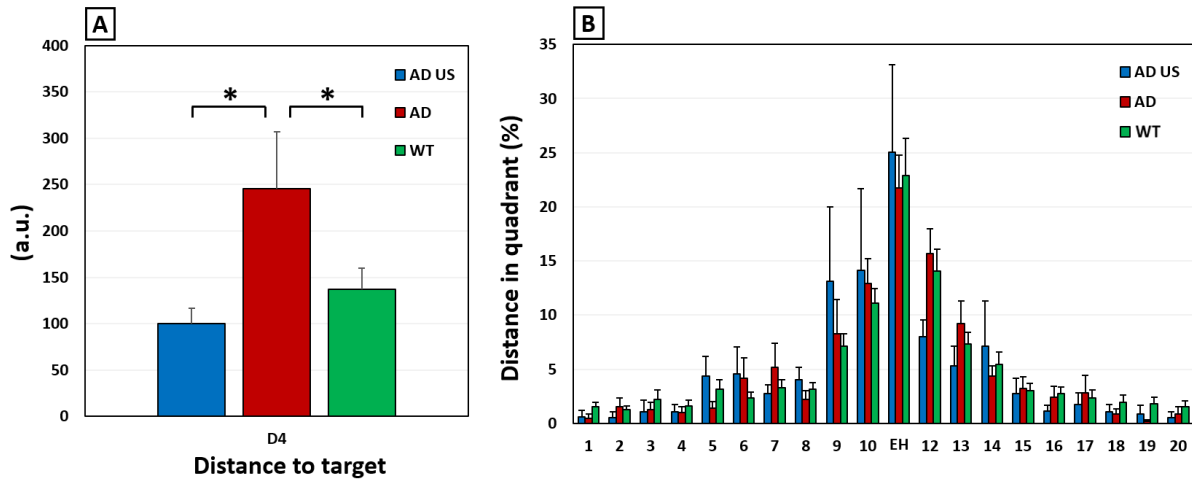


Figure 5-41: Barnes maze results. A – Distance to target on Day 4. B - Distance in quadrant on Day 5.

Figure 5-41 shows results of the Barnes maze test. Rats not performing the test were not taken into account. Rats not moving away from the center during the first minutes were excluded. For example, on D4, this results in 5, 10 and 14 rats performing the task. Figure 5-41 A shows the mean distance that rats walked to find the escape hole. On Day 4, SUS-treated TgF344-AD rats walked significantly less to find the escape hole than sham-treated TgF344-AD rats ( $P=0.013$ , Wilcoxon rank test). Sham-treated TgF344-AD rats walk also significantly more than wild type rats ( $P=0.02$ , Wilcoxon rank test) and there were no differences between the AD US and WT groups ( $P=0.78$ , Wilcoxon rank test). Figure 5-41 B shows the results of the test day on Day 5. All rats walked more in the quadrant of the escape hole and there are no differences between groups.

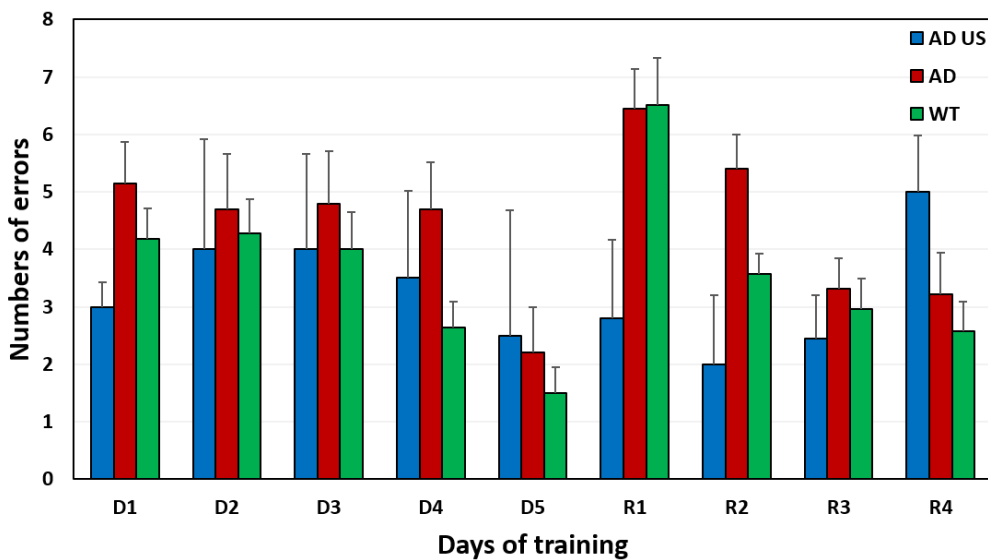


Figure 5-42: Number of errors over the learning session. The effect of learning is clearer on the first phase.

Figure 5-42 shows the mean number of errors over the 9 days of test. There is a pattern present on day D1 D2 D3 D4 R2 and R3: SUS-treated TgF344-AD rats and wild type rats made fewer errors than sham-treated TgF344-AD rats. When tested with 2-ways ANOVA (with the days of training and the

groups as parameters) there is a significant effect of group ( $P=0.008$ ). There is also a clear effect of days between D1 and D5 ( $P=0.0007$ ) and between day R1 and R4 ( $P=0.012$ ) showing that rats learned and re-learned the position of the escape hole. SUS-treated TgF344-AD rats and sham-treated TgF344-AD rats performed significantly differently ( $P=0.025$ , Tukey post-hoc test) as well as sham-treated TgF344-AD rats and wild type rats ( $P=0.018$ , Tukey post-hoc test) but SUS-treated TgF344-AD rats and wild type did not perform differently ( $P=0.78$ , Tukey post-hoc test).

Once again, many TgF344-AD rats were reluctant to do the test. Few of them did not perform the maze at all (they just stayed in the middle for 2 minutes). Other started exploring after 30 seconds or one minutes. This lack of motivation is the reason why the latency to find the escape hole was less relevant than the number of errors or the distance to find the escape hole.

Together, the results of the Barnes maze shown on Figure 5-41 A and Figure 5-42 suggest that the ultrasound treatment improves the memory of the SUS-treated TgF344-AD rats. Indeed, SUS-treated TgF344-AD rats performed more like the wild type animals than like the sham-treated AD animals. This result will have to be correlated with amyloid plaque clearance which will be studied by histology and biochemical analysis.

## 5.5. Study of the neuroinflammation with PET

As we saw in the first section of this Chapter, neuroinflammation has long been identified as a very possible cause for the amyloid plaques clearance due to repeated FUS-induced BBB openings. In this section, I will present a preliminary study aiming to investigate the neuroinflammation triggered by the ultrasound. This was done *in vivo* with PET imaging and dedicated radiotracer. This protocol is extremely innovative because it is the first time FUS-induced neuroinflammation is studied *in vivo*. Indeed, past studies only looked at neuroinflammation *ex vivo* with brain staining. In a first part, I will quickly remind how neuroinflammation can be imaged with PET and in a second part I will present the results of this study.

### 5.5.1. How to detect neuroinflammation

#### a) Neuroinflammation in Alzheimer's disease

Neuroinflammation has been proven to play an important role in Alzheimer's disease (Akiyama et al., 2010; Hamelin et al., 2016; Heneka and O'Banion, 2007; Rogers et al., 1999). Neuroinflammation is the activation of glial cells (microglia and astrocytes) and the release of pro- and anti-inflammatory factors. Microglia are the macrophages of the brain (Kettenmann et al., 2011) and, at the same time, contribute to the protection and remodeling of synapses for proper maintenance and plasticity of neuronal circuits (Ji et al., 2013). Astrocytes provide trophic support for neurons, promote formation and function of synapses, reshape synapses by phagocytosis and can also, like microglia, respond to pathological stimuli through reactive gliosis (Sofroniew and Vinters, 2010). In AD, microglia are able to bind to soluble A $\beta$  oligomers and A $\beta$  fibrils (Paresce et al., 1996), which results in activation of microglia which start to produce pro-inflammatory cytokines and chemokines. Microglia also start to

absorb A $\beta$  fibrils by phagocytosis. Similarly, active astrocytes can be found near plaques degrading them (Pihlaja et al., 2011). The activation of the astrocytes has been shown to increase in parallel with the severity of the disease (Simpson et al., 2010). As a consequence of the glial activation, these fibrils enter the endosomal/lysosomal pathway, leading to A $\beta$  clearance. In sporadic cases of AD, inefficient clearance of A $\beta$  has been identified as a major pathogenic pathway (Mawuenyega et al., 2010). It has been suggested that increased cytokine levels are responsible for the insufficient microglial phagocytic capacity by downregulating A $\beta$  phagocytosis receptors (Hickman et al., 2009). However, as other inflammatory mechanisms in the body, glial activation appears to be both beneficial and detrimental.

Upon exposure to a pathogen, microglial activation aims at the removal of this recognized pathogen. Under normal circumstances such a reaction quickly resolves pathology with an immediate benefit to the nearby environment. In AD however, several mechanisms including the ongoing formation of A $\beta$  and the positive feedback loops between inflammation and APP processing prevent the inflammation decrease. Instead, the further accumulation of A $\beta$  establish a chronic, non-resolving inflammation. The sustained exposure to A $\beta$ , chemokines, cytokines, and other inflammatory mediators seems responsible for the persistent functional impairment of microglia observed at plaque sites (Krabbe et al., 2013; Streit et al., 2009). The same way, astrocyte activation appears to be initially beneficial but could be harmful later on due to disease-specific alterations (Ben Haim et al., 2015).

On the one hand, there are multiple evidences suggesting that the pro-inflammatory environment present in the brain of AD patients and in transgenic mouse models of cerebral amyloidosis assumes damaging proportions (Heppner et al., 2015). For instance, risk for conversion from MCI to AD is higher in subjects with elevated CSF presence of the pro-inflammatory cytokine TNF- $\alpha$  and decreased anti-inflammatory TGF- $\beta$  levels (Tarkowski et al., 2003). Activated astrocytes are thought to lose their support functions of the neurons which could lead to neuronal death (Liddel et al., 2017). On the other hand, stimulation of some pro-inflammatory signaling pathways seems to be a beneficial approach in AD mouse models. Transgenic expression of IL-1 $\beta$  in APP/PS1 led to robust neuroinflammation and a reduction of amyloid plaque pathology (Jin et al., 2008; Shaftel et al., 2007). These results suggest that certain “good” forms of pro-inflammatory glial activation are potentially beneficial for reducing AD pathology in transgenic mouse models. Interestingly, overexpression of IL-1 $\beta$  seems to have opposite effects on amyloid plaques and on neurofibrillary tangles as it reduces amyloid load but increase tau pathology (Ghosh et al., 2013).

Our hypothesis, which has already been partly validated by the studies presented in the first section of this chapter, is that FUS-induced BBB opening triggers a beneficial neuroinflammation – the “good” form of inflammation.

#### b) A marker of neuroinflammation: the TSPO protein

To study this hypothesis, we used Positron Emission Tomography (PET) and a radio-tracer of the Translocator protein (TSPO): <sup>18</sup>F-DPA-714, which we will referred to as DPA. The TSPO is a membrane protein present on mitochondria. Its role is to transport cholesterol across the membrane. Expressed on glial cells, TSPO is overexpressed in case of neuroinflammation (Crawshaw and Robertson, 2017), which makes it a valuable biomarker to follow neuroinflammation. On APP/PS1 mice, a significant increase in DPA uptake has been shown seen in the hippocampus and cortex of 18 months old APP/PS1

mice when compared to wild type littermates and to 6 months old APP/PS1 mice, which supports the role of neuroinflammation in AD (Chaney et al., 2017).

This “good” neuroinflammation hypothesis is supported by both preclinical and clinical studies. *Kovacs et al.* (2016) showed that FUS-induced BBB opening led to an early release of pro-inflammatory cytokines, probably by the activated microglia, that could lead to a late release of anti-inflammatory cytokines. Those pro-inflammatory cytokines could be the origin of the therapeutic effects of the ultrasound observed on APP/PS1 mice. From a clinical point of view, *Hamelin et al.* (2016) showed that patients with a higher expression of TSPO, so with more neuroinflammation, have a slower cognitive decline than patients with a lower expression of TSPO.

### 5.5.2. Ultrasound and PET protocol

8 ten-month old mice, 4 APP/PS1 mice and 4 wild type littermates, underwent 6 weeks of FUS-induced BBB opening with one ultrasound session per week. The opening was global on a 6x6 mm<sup>2</sup> trajectory. The transmitted electrical voltage was set so to have 0.6 MPa in the brain at focus. Mice were anesthetized with 2% isoflurane in oxygen and received a 50 µL bolus of microbubbles (SonoVue, Bracco, Italia) in retro-orbital before the sonication. Every week, 5 days after BBB opening, mice were imaged with PET. They received a DPA injection in order to quantify the expression of TSPO, so to have a picture of their neuro-inflammatory state. Before the first ultrasound session mice were also imaged with PET for baseline.

Ultrasound were performed 5 days before the DPA injection and PET imaging. Here, what we are looking at is the neuroinflammation and not the leakage of the DPA through an open BBB. Our hypothesis is that this delay between ultrasound and PET allows us to see only the neuroinflammation induced by the ultrasound.

For this study, PET acquisitions were done by Charles Truillet and Venetia Cardona. Reconstruction and analysis of the PET images were done by Venetia Cardona. For PET imaging, mice were anesthetized with 2% isoflurane in oxygen, respiration frequency is monitored and kept above 60 Hz. All groups received an equivalent dose of DPA, which was i.v. injected, and its uptake in the brain was followed by 60 minutes of PET dynamic acquisitions. PET scans were performed under using an Inveon<sup>®</sup> microPET-CT system (Siemens, Germany). PET images are co-registered with CT scans and then aligned with an MRI atlas to segment the brains in regions of interest (ROIs) with the PMOD software (PMOD Technologies LLC, Switzerland). Three main ROIs were investigated: cortex + hippocampus, cerebellum and subcortical regions. Radioactivity was quantified on the last 30 minutes of the dynamic PET scan, when the radioactivity has plateaued because the equilibrium reflecting the specific fixation of DPA on TSPO is reached. Values are corrected for the injected dose and normalized by the values in the cerebellum, which is a pseudo-reference region for TSPO (Graeber et al., 2011). DPA signal is then expressed in NUV<sub>cb</sub> (Normalized – to the cerebellum – Uptake Values).

It has to be noticed that mice did not undergo PET imaging on week 5. Indeed, repeated injections (once a week) in the tail vein make the followings injections harder due to the scarring process. Also tail veins of black mice are already difficult to see. This is why, on week 5, we preferred not to inject and let the tails scar better to be sure to inject on week 6.

### 5.5.3. Follow-up of the neuroinflammation

The results presented in this section are the NUVcb in the cortex + hippocampus ROI. According to the global opening performed in mice in Chapter 2, this is where we expect the BBB opening. Figure 5-43 A shows the NUVcb of the 8 mice for the whole protocol. For each week (week 0 being the baseline) before the ultrasound protocol started, the NUVcb averaged on the 8 mice (mean $\pm$ s.d.) are displayed. As shown on the Figure 5-43 A, the NUVcb seems to increase over the weeks, especially between the weeks 3 and 6. The NUVcb was also high on week 1, just after the first session of ultrasound but decreases up to week 3.

We can also look to the difference between the baseline and the last session of PET, after the 6 weeks of ultrasound. Figure 5-43 B shows the NUVcb for each individual mouse on week 0 and on week 6 after the ultrasound protocol. On week 6, the values are significantly higher than on week 0 ( $P=0.04$ , Wilcoxon rank test).

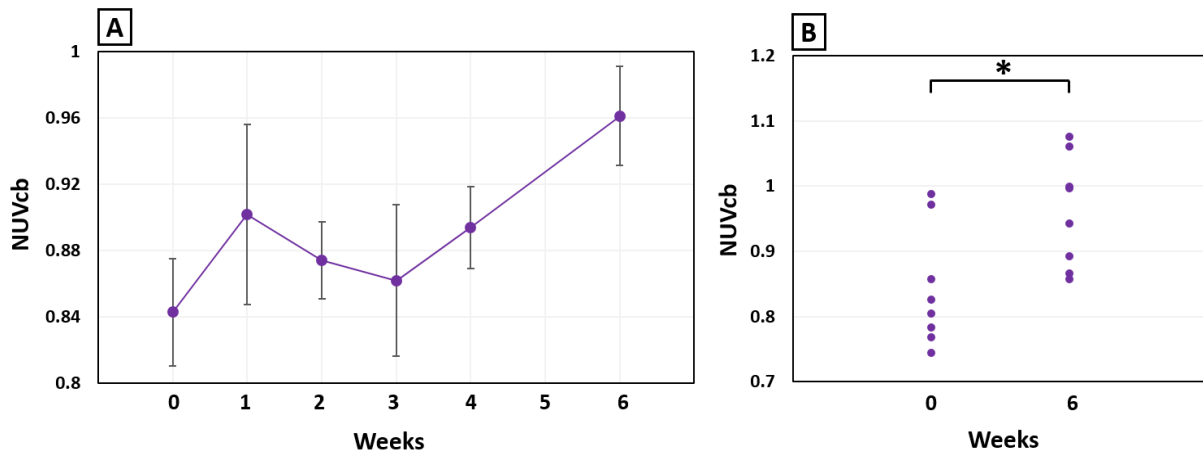


Figure 5-43: A – Mean ( $\pm$ s.d.) DPA signal for the 8 mice in the cortex + hippocampus ROI over the 6 weeks of protocol. B – Individual DPA signal before and after the ultrasound protocol.

Those results suggest an increase of the neuroinflammation, detected by an increase of the DPA signal, between weeks 0 and 6. This increase is subtle, only 15 % on average, but statistically significant.

We hypothesize that this neuroinflammation was due to the ultrasound. We miss a sham-treated control group to definitely conclude on this. The absence of increase in the DPA signal for this group would have disqualified anesthesia as a possible cause of neuroinflammation. The role of anesthesia on neuroinflammation is unclear. *Wu et al.* showed increases levels of pro-inflammatory TNF- $\alpha$ , IL-6 and IL-1  $\beta$  in neurons but not in glial cells with anesthesia of 2 hours (*Wu et al.*, 2012). On the contrary, *Cibelli et al.* showed no effect of anesthesia on the levels of IL-6 and IL-1  $\beta$  (*Cibelli et al.*, 2016). In any case, this isoflurane-induced neuroinflammation is not thought to last more than 48h (*Luo et al.*, 2014; *Zhang et al.*, 2015). In our case, neuroinflammation was assessed with DPA 5 days after the anesthesia due to the BBB opening and 7 days after the anesthesia due to PET imaging. For sure a sham-treated group is the next step to this study, but so far, we strongly believed that what we observed are not chronic effect of anesthesia but are due to the FUS-induced BBB openings.

The group of 8 mice was composed of 4 APP/PS1 mice and 4 wild type mice. Figure 5-44 shows the individual variations between week 0 and week 6 for the APP/PS1 mice (in blue) and the Wild type mice (yellow).

Interestingly, AD and WT did not seem to respond the same way to the ultrasound treatment. Indeed, NUVcb increase as much as 22% for the AD US group and only of 9% for the WT US group, on average. So, ultrasound induced neuroinflammation seems higher in the APP/PS1 mice.

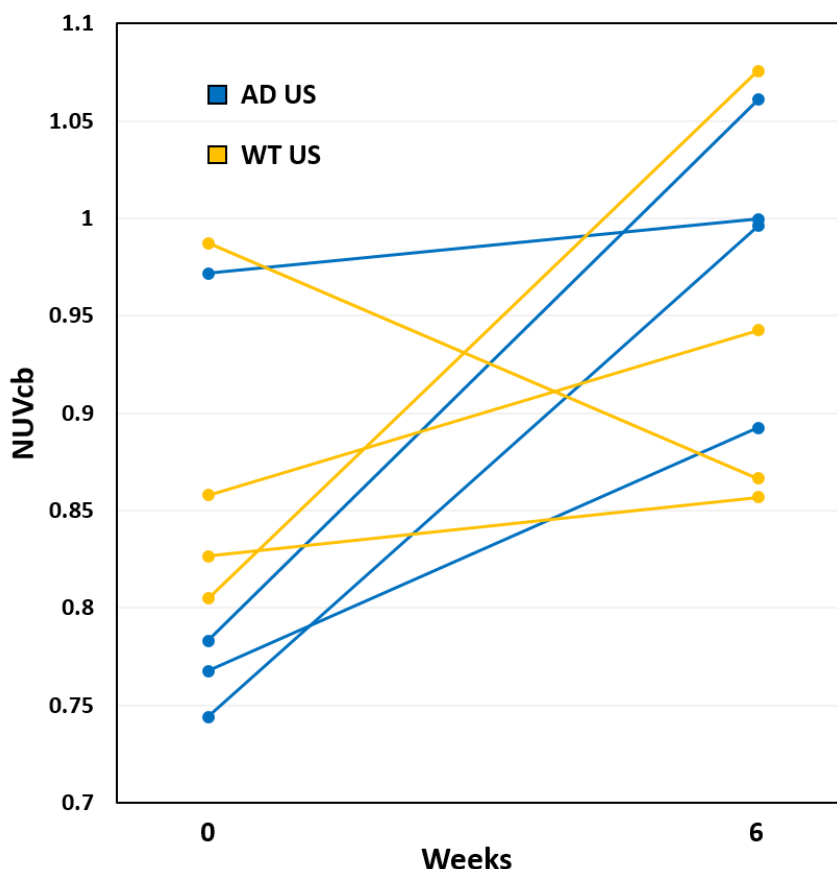


Figure 5-44: Individual DPA signal before and after the ultrasound protocol with a distinction between the Alzheimer's (blue) and the wild type (yellow) mice.

One hypothesis to explain this discrepancy between APP/PS1 and wild type mice is that the neuroinflammation induced by the ultrasound is maintained by the presence of amyloid plaques. As we already saw for example on the Chapter 4 with the histology, neuroinflammation is already present around amyloid plaques (activated astrocytes and microglia). It may be possible that the neuroinflammation brought by the ultrasound is maintained by the plaques and that it resorbs in the wild type animals.

As a conclusion, we could show, for the first time *in vivo*, neuroinflammation induced by the BBB opening. Neuroinflammation was significantly higher after the 6 weeks of the BBB opening protocol. Interestingly, neuroinflammation was higher in the APP/PS1 mice than in the wild type mice.

## 5.6. Conclusion

In this Chapter, I started by reviewing the literature on the link between FUS-induced BBB opening and Alzheimer's disease. The studies are few and the impact of many parameters such as the age of treatment, the number of BBB opening, the delay between the end of the ultrasound and the behavior test or even the rodent model, has to be studied. Then, I presented our behavior tests and how they can exhibit differences between transgenic and wild type animals. In the next two sections, I described the therapeutic trials I conducted on mice and rats. The impact of repeated FUS-induced BBB opening on behavior was not clear but some tests showed a reduced anxiety and a memory improvement on transgenic animals between the SUS-treated and the sham-treated. Finally, I presented a short preliminary study. In this study we imaged the neuroinflammation due to the BBB opening and for the first time *in vivo*.

## General conclusion

In my PhD work, innovative developments have been made in the field of ultrasound-induced blood-brain barrier (BBB) opening. These developments allowed us to successfully deliver various compounds to the brain, including drugs and contrast agents, and could even allow to investigate properties of the brain. Then, a specific focus was made on Alzheimer's disease, especially on imaging amyloid plaques and on using ultrasound-induced BBB opening as a novel potential therapy for Alzheimer's disease.

The first part of my PhD was dedicated to developments of methods on the BBB opening technique. A study on rat skulls demonstrated a clear linear dependency of the acoustic transmission factor of the skulls on the body mass of the animals. For the first time, the spatial dependency of the acoustic transmission factor was also described with a transmission factor which can be 50% lower at the back of the skull than at the front. These results were extensively used in my PhD for a proper calibration of the ultrasound beam during *in vivo* experiments. But the application of these results are broader than my own work as a precise control of the intensity at focus is also required in other techniques such as neurostimulation, thermal ablation or photoacoustic imaging. Direct *in vivo* estimation of the acoustic pressure would surely be a big step toward a better personalized dosimetry and one possible lead has been explored in this manuscript with MR acoustic radiation force imaging. Ultrasound-induced BBB opening holds unanswered questions. This is why new techniques, combining an accurate control of the ultrasound dose with quantified MR images of contrast agents in the brain, have been proposed in this manuscript to investigate the effects of the acoustic parameters on blood-brain opening. One main result on my work is that stronger openings lead to longer openings, increasing the pressure of 20% leads to an opening 60% longer. More pressure conditions and a better temporal sampling would be needed to complete this study.

Strengthened by these developments, ultrasound-induced BBB opening was used to deliver compounds to rodent brains. We investigated the impact of ultrasound-induced BBB opening on the efflux pumps and found out that opening the tight junctions was not enough to deliver drugs that are substrates of the efflux pumps. Erlotinib, an anti-cancer drug, failed to be delivered to the brain even with ultrasound-induced BBB opening. The general message here is that opening the BBB by loosening the tight junctions can be insufficient to deliver a drug if this one is actively transferred to the blood by active transporters at the surface of the endothelial cells. However, we were able to deliver promising drugs to the brain such as gold nanoparticles or monoclonal antibodies (up to +40%). Ultrasound-induced BBB opening was also used to study the diffusion of contrast agents in the brain. Indeed, delivering drugs or contrast agent in the brain parenchyma is a first step but compounds need also to diffuse to reach their targets. The coherent tortuosity values of the brain are one more argument in favor of the safety of the technique when appropriately tuned. We also showed that the delivery of drugs to brain tumors could be improved with ultrasound (up to +100%). This result is of great interest as brain tumors are thought to be one of the first clinical application of the technique due to the lack of efficient therapy and the short life expectancy of the patients diagnosed with malignant tumors. These successful deliveries remain preclinical results but could pave the way for clinical applications.

Progresses in imaging of Alzheimer's disease are more than welcome. On the one hand, efficient imaging techniques are key to an early detection of the patients and, on the other hand, they help quantifying the results of therapeutic studies. Here, a semi-automatic pipeline for the detection and quantification of amyloid plaques in mouse cortex was introduced. This protocol has the advantage of

being full 3D when the gold standard technique, brain staining, is 2D and images only part of the brain. This pipeline proved to be robust in telling young APP/PS1 mice from old APP/PS1 mice and from wild type mice. A 2.5 fold increase of the amyloid load was found when comparing one-year old APP/PS1 mice to two-year old APP/PS1 mice. It could be a relevant alternative to brain staining. The process is time saving as scans can be acquired overnight and non-destructive, so, it can even be combined with histology or biochemical analysis (western blots). Further optimization of the pipeline on the weighting of the echoes or on the parameters of the code such as the threshold or the size of the local neighborhood could improve this technique. With the help of biologists, we also developed several standard brain stainings to image amyloid plaques, tau tangles or neuroinflammation. As for the MRI protocol, a specific image processing has been set up for quantification, especially of the amyloid plaques. These developments do not represent strong innovations regarding brain stainings but will provide our laboratory with the gold standard techniques for amyloid plaques quantification.

At last, a therapeutic approach of the ultrasound-induced BBB opening technique was tested on rodent models of Alzheimer's disease. The results, showing a slight improvement of the memory of the animals (for example ultrasound-treated transgenic animals walk less than non-treated transgenic animals to find the exit of the Barnes maze), have to be replaced in the context of promising new studies on this topic. Only few parameters have been investigated so far. First, among all the animal models of AD, can these results be applied to other species than mice? We were the first to test this protocol on rats. Most studies have been limited to an evaluation of the effects within days after the therapy when we tested the animals for several weeks. Is this technique relevant if the benefits are brief? At what stage of the disease animal should be treated? All studies were performed in mice that had already a heavy amyloid load, in order to observe a decrease of it. But this approach could be more interesting with an early treatment to prevent amyloid plaques formation and slow down or stop this amyloid cascade. This approach is highly promising, even more since no current treatment seems efficient for Alzheimer's disease. More studies will be needed to clearly state its efficacy and understand the underlying mechanisms. For now, a beneficial neuroinflammation triggered by the ultrasound is thought to be the cause. Nevertheless, ultrasound-induced BBB opening carries great hopes for an Alzheimer's disease therapy. The best proof of this is that the Food and Drug Administration recently approved the initiation of an Alzheimer's disease clinical trial using this technique.

Of course, numerous studies presented in this manuscript need further investigations. My PhD work is one link in a chain which started few years ago in our laboratory with the development and the first experiments of MR-guided ultrasound-induced BBB opening on rats and which will continue with a deep study of the impact of BBB opening on rodent models of Alzheimer's disease with a specific focus on neuroinflammation. My PhD work also started many collaborations which have already led to publications and which opened the door to new exciting scientific discoveries.

# Scientific communications

## Publications in international scientific journals

- Acoustic transmission factor through the rat skull as a function of body mass, frequency and position. Gerstenmayer M, Fellah B, Magnin R, Selingue E, Larrat B. *Ultrasound in Medicine and Biology*, 2018.
- Biomedical applications implying magnetic nanoparticles in amyloidoses. Pansieri J, Gerstenmayer M, Forge V, Larrat B, Marquette C. *Nanomaterials*, 2018.
- Physical blood-brain barrier disruption induced by focused ultrasound does not overcome the transporter-mediated efflux of erlotinib. Goutal S, Gerstenmayer M, Auvity S, Caillé F, Mériaux S, Buvat I, Larrat B, Tournier N. *Journal of Controlled Release*, Accepted.
- Gadolinium-based nanoparticles diffusion within the brain tissue following ultrasound induced Blood Brain Barrier permeabilisation. Magnin R, Conti A, Gerstenmayer M, Della Penna S, Romani G L, Dumont E, Mériaux S, Le Bihan D, Larrat B. In preparation.

## Communications in international congresses

### *Oral presentations*

- Weekly ultrasound induced blood-brain barrier openings seem to restore memory in APP/PS1dE9 amyloid mice model. Gerstenmayer M, Selingue E, Geffroy F, Mériaux M, Larrat B. IEEE – UFFC, 2017. Washington.
- Ultrasound-induced delivery of Erlotinib to the brain: not enough to counter efflux pumps. Gerstenmayer M, Goutal S, Auvity S, Caillé F, Mériaux S, Buvat I, Larrat B, Tournier N. IEEE – UFFC, 2017. Washington.
- Magnetic resonance guided ultrasound induced blood brain barrier opening in rats: influence of the acoustic pressure. Gerstenmayer M, Magnin R, Mériaux S, Le Bihan D, Larrat B. IEEE – UFFC, 2016. Tours.
- Relationship between acoustic pressure used for blood-brain barrier disruption and amount of MRI contrast agent delivered to the brain. Gerstenmayer M, Magnin R, Mériaux S, Le Bihan D, Larrat B. *International Society for Therapeutic Ultrasound*, 2016. Tel-Aviv.
- Magnetic resonance acoustic radiation force imaging for *in vivo* estimation of ultrasonic transmission factor through rat skulls. Gerstenmayer M, Fellah B, Magnin R, Le Bihan D, Larrat B. *International Society for Therapeutic Ultrasound*, 2016. Tel-Aviv.

- Gadolinium-based nanoparticles diffusion within the brain tissue following ultrasound induced Blood Brain Barrier permeabilisation. Gerstenmayer M, Magnin R, Conti A, Lux F, Tillement O, Della Penna S, Romani G L, Dumont E, Mériaux S, Le Bihan D, Larrat B. European Nanomedicine Meeting, 2015. Grenoble.
- MRI guided ultrasound induced blood-brain barrier disruption for the delivery of large molecules to the rodent brain. Larrat B, Magnin R, Conti A, Marty B, Geffroy F, Gerstenmayer M, Dumont E, Le Bihan D, Mériaux S. Cerebro-Vascular Biology international meeting 2015, Paris.

#### *Posters*

- Comparison of high resolution ex vivo multi gradient echo sequences at 7T and 11.7T for amyloid load quantification in an Alzheimer's disease mouse model. Gerstenmayer M, Geffroy F, Mériaux M, Larrat B. ISMRM, 2018. Paris.
- Comparison of single spot and volume ultrasound sonications for efficient nanoparticle delivery to glioblastoma model in rats Conti A, Gerstenmayer M, Geffroy F, Tillement O, Lux F, Mériaux S, Larrat B. IEEE – UFFC, 2017. Washington.

## Bibliography

(Inserm), I. national de la santé et de la recherche médicale (2007). *Maladie d'Alzheimer: Enjeux scientifiques, médicaux et sociétaux*.

Abbott, N.J., Rönnbäck, L., and Hansson, E. (2006). Astrocyte-endothelial interactions at the blood-brain barrier. *Nat. Rev. Neurosci.* *7*, 41–53.

Abbott, N.J., Patabendige, A.A.K., Dolman, D.E.M., Yusof, S.R., and Begley, D.J. (2010). Structure and function of the blood-brain barrier. *Neurobiol. Dis.* *37*, 13–25.

Agarwal, S., Sane, R., Oberoi, R., Ohlfest, J.R., and Elmquist, W.F. (2011). Delivery of molecularly targeted therapy to malignant glioma, a disease of the whole brain. *Expert Rev. Mol. Med.* *13*, e17.

Agrawal, M., Ajazuddin, Tripathi, D.K., Saraf, S., Saraf, S., Antimisiaris, S.G., Mourtas, S., Hammarlund-Udenaes, M., and Alexander, A. (2017). Recent advancements in liposomes targeting strategies to cross blood-brain barrier (BBB) for the treatment of Alzheimer's disease. *J. Control. Release* *260*, 61–77.

Aisen, P.S., Cummings, J., Jack, C.R., Morris, J.C., Sperling, R., Frölich, L., Jones, R.W., Dowsett, S.A., Matthews, B.R., Raskin, J., et al. (2017). On the path to 2025: Understanding the Alzheimer's disease continuum. *Alzheimer's Res. Ther.* *9*, 1–10.

Akiyama, H., Barger, S., Barnum, S., Bradt, B., Bauer, J., Cole, G.M., Cooper, N.R., Eikelenboom, P., Fiebich, B.L., Finch, C.E., et al. (2010). Inflammation and Alzheimer's disease. *Neurobiol. Aging* *21*, 383–421.

Al-Bataineh, O., Jenne, J., and Huber, P. (2012). Clinical and future applications of high intensity focused ultrasound in cancer. *Cancer Treat. Rev.* *38*, 346–353.

André, S., Ansciaux, E., Saidi, E., Larbanoix, L., Stanicki, D., Nonclercq, D., Vander Elst, L., Laurent, S., Muller, R.N., and Burtea, C. (2017). Validation by Magnetic Resonance Imaging of the Diagnostic Potential of a Heptapeptide-Functionalized Imaging Probe Targeted to Amyloid- $\beta$  and Able to Cross the Blood-Brain Barrier. *J. Alzheimer's Dis.* *60*, 1547–1565.

Annold, N.A.M.C.D., Hang, Y.O.Z., and Ykhodtseva, N.A. V (2017). The effects of oxygen on ultrasound-induced blood-brain barrier disruption in mice. *Ultrasound Med. Bio* *43*, 469–475.

Aoki, J., Shibazaki, K., Saji, N., Uemura, J., Sakamoto, Y., and Kimura, K. (2014). Risk of Intracerebral Hemorrhage After Thrombolysis in Patients with Asymptomatic Hemorrhage on T2\*. *Cerebrovasc. Dis.* *38*, 107–116.

Arvanitis, C.D., Livingstone, M.S., Vykhodtseva, N., and McDannold, N. (2012). Controlled Ultrasound-Induced Blood-Brain Barrier Disruption Using Passive Acoustic Emissions Monitoring. *PLoS One* *7*.

Arvanitis, C.D., Crake, C., McDannold, N., and Clement, G.T. (2016). Passive Acoustic Mapping with the Angular spectrum method. *IEEE Trans. Med. Imaging* *36*, 983–993.

Aryal, M., Arvanitis, C.D., Alexander, P.M., and McDannold, N. (2014). Ultrasound-mediated blood-brain barrier disruption for targeted drug delivery in the central nervous system. *Adv. Drug Deliv. Rev.* *72*, 94–109.

Aryal, M., Fischer, K., Gentile, C., Gitto, S., Zhang, Y.-Z., and McDannold, N. (2017). Effects on P-Glycoprotein Expression after Blood-Brain Barrier Disruption Using Focused Ultrasound and Microbubbles. *PLoS One* *12*.

Attwell, D., Buchan, A.M., Charpak, S., Lauritzen, M., MacVicar, B.A., and Newman, E.A. (2010). Glial and neuronal control of brain blood flow. *Nature* *468*, 232–243.

Babcock, A.A., Ilkjær, L., Clausen, B.H., Villadsen, B., Dissing-Olesen, L., Bendixen, A.T.M., Lyck, L., Lambertsen, K.L., and Finsen, B. (2015). Cytokine-producing microglia have an altered beta-amyloid load in aged APP/PS1 Tg mice. *Brain. Behav. Immun.* *48*, 86–101.

Bach, M.E., Hawkins, R.D., Osman, M., Kandel, E.R., and Mayford, M. (1995). Impairment of spatial but not contextual memory in CaMKII mutant mice with a selective loss of hippocampal LTP in the range of the theta

frequency. *Cell* *81*, 905–915.

Bahce, I., Smit, E.F., Lubberink, M., van der Veldt, A.A.M., Yaqub, M., Windhorst, A.D., Schuit, R.C., Thunnissen, E., Heideman, D.A.M., Postmus, P.E., et al. (2013). Development of [(11)C]erlotinib positron emission tomography for in vivo evaluation of EGF receptor mutational status. *Clin. Cancer Res. An Off. J. Am. Assoc. Cancer Res.* *19*, 183–193.

Ballabh, P., Braun, A., and Nedergaard, M. (2004). The blood-brain barrier: An overview: Structure, regulation, and clinical implications. *Neurobiol. Dis.* *16*, 1–13.

Ballard, P., Yates, J.W.T., Yang, Z., Kim, D.-W., Yang, J.C.-H., Cantarini, M., Pickup, K., Jordan, A., Hickey, M., Grist, M., et al. (2016). Preclinical Comparison of Osimertinib with Other EGFR-TKIs in EGFR-Mutant NSCLC Brain Metastases Models, and Early Evidence of Clinical Brain Metastases Activity. *Clin. Cancer Res. An Off. J. Am. Assoc. Cancer Res.* *22*, 5130–5140.

Barnes (1979). Memory deficits associated with senescence: a neurophysiological and behavioral study in the rat. *J Comp Physiol Psychol.*

Barnes, C.A., Nadel, L., and Honig, W.K. (1980). Spatial memory deficit in senescent rats. *Can. J. Psychol.* *34*, 29–39.

Baseri, B., Choi, J.J., Tung, Y.-S., and Konofagou, E.E. (2010). Multi-Modality Safety Assessment of Blood-Brain Barrier Opening Using Focused Ultrasound and Definity Microbubbles: A Short-Term Study. *Ultrasound Med. Biol.* *36*, 1445–1459.

Bellavance, M.-A., Blanchette, M., and Fortin, D. (2008). Recent Advances in Blood–Brain Barrier Disruption as a CNS Delivery Strategy. *AAPS J.* *10*, 166–177.

Benveniste, H., Einstein, G., Kim, K.R., Hulette, C., and Johnson, G. a (1999). Detection of neuritic plaques in Alzheimer’s disease by magnetic resonance microscopy. *Proc. Natl. Acad. Sci. U. S. A.* *96*, 14079–14084.

Bercoff, J., Tanter, M., and Fink, M. (2004a). Supersonic shear imaging: A new technique for soft tissue elasticity mapping. *IEEE Trans. Ultrason. Ferroelectr. Freq. Control* *51*, 396–409.

Bercoff, J., Tanter, M., Muller, M., and Fink, M. (2004b). The role of viscosity in the impulse diffraction field of elastic waves induced by the acoustic radiation force. *IEEE Trans. Ultrason. Ferroelectr. Freq. Control* *51*, 1523–1536.

Bhojani, N., and Lingeman, J.E. (2013). Shockwave Lithotripsy–New Concepts and Optimizing Treatment Parameters. *Urol. Clin. North Am.* *40*, 59–66.

Blanchard, V., Moussaoui, S., Czech, C., Touchet, N., Bonici, B., Planche, M., Canton, T., Jedidi, I., Gohin, M., Wirhth, O., et al. (2003). Time sequence of maturation of dystrophic neurites associated with A $\beta$  deposits in APP/PS1 transgenic mice. *Exp. Neurol.* *184*, 247–263.

Bloembergen, N., Purcell, E., and Pound, R. (1948). Relaxation effects in nuclear magnetic resonance absorption. *Phys. Rev.* *73*, 679–715.

Braak, H., and Braak, E. (1997). Frequency of stages of Alzheimer-related lesions in different age categories. *Neurobiol. Aging* *18*, 351–357.

Brem, H., and Gabikian, P. (2001). Biodegradable polymer implants to treat brain tumors. *J. Control. Release* *74*, 63–67.

Brown, R.W., Cheng, Y.C.N., Haacke, E.M., and Thompson, M. R., & Venkatesan, R. (2014). *Magnetic Resonance Imaging: Physical Principles and Sequence Design: Second Edition*. (Wiley Blackwell).

Buldyrev, S. V, Cruz, L., Gomez-Isla, T., Gomez-Tortosa, E., Havlin, S., Le, R., Stanley, H.E., Urbanc, B., and Hyman, B.T. (2000). Description of microcolumnar ensembles in association cortex and their disruption in Alzheimer and Lewy body dementias. *Proc. Natl. Acad. Sci. U. S. A.* *97*, 5039–5043.

Burgess, A., Sonam, D., Sharon, Y., Olivia, H., Naomi, E., Isabelle, A., and Kullervo, H. (2014). Alzheimer Disease in a Mouse Model: MR Imaging–guided Focused Ultrasound Targeted to the Hippocampus Opens the Blood-

Brain Barrier and Improves Pathologic Abnormalities and Behavior. *Radiology* 273, 736–745.

Burgess, A., Shah, K., Hough, O., and Hynynen, K. (2016). Focused ultrasound-mediated drug delivery through the blood-brain barrier. *Expert Rev Neurother.* 15, 477–491.

Busto, R., and Ginsberg, M.D. (1996). Quantitative evaluation of blood-brain barrier permeability following middle cerebral artery occlusion in rats. 739, 88–96.

C. Irizarry, M., Mcnamara, M., Fedorchak, K., Hsiao, K., and T. Hyman, B. (1997). APPSW Transgenic Mice Develop Age-related A $\beta$  Deposits and Neuropil Abnormalities, but no Neuronal Loss in CA1. *J. Neuropathol. Exp. Neurol.* 56, 965–973.

Calhoun, M.E., Burgermeister, P., Phinney, a L., Stalder, M., Tolnay, M., Wiederhold, K.H., Abramowski, D., Sturchler-Pierrat, C., Sommer, B., Staufenbiel, M., et al. (1999). Neuronal overexpression of mutant amyloid precursor protein results in prominent deposition of cerebrovascular amyloid. *Proc. Natl. Acad. Sci. U. S. A.* 96, 14088–14093.

Camidge, D.R., Pao, W., and Sequist, L. V. (2014). Acquired resistance to TKIs in solid tumours: learning from lung cancer. *Nat. Rev. Clin. Oncol.* 11, 473–481.

Carpentier, A., Canney, M., Vignot, A., Reina, V., Beccaria, K., Horodyckid, C., Karachi, C., Leclercq, D., Lafon, C., Chapelon, J., et al. (2016). Clinical trial of blood-brain barrier disruption by pulsed ultrasound. *Sci Transl Med.* 8.

Cedernaes, J., Schiöth, H.B., and Benedict, C. (2014). Efficacy of antibody-based therapies to treat Alzheimer's disease: Just a matter of timing? *Exp. Gerontol.* 57, 104–106.

Chamberlain, R., Wengenack, T.M., Poduslo, J.F., Garwood, M., and Jack Jr., C.R. (2011). Magnetic resonance imaging of amyloid plaques in transgenic mouse models of Alzheimer's disease. *Curr Med Imaging Rev.* 7.

Chaney, A., Bauer, M., Bochicchio, D., Smigova, A., Kassiou, M., Davies, K.E., Williams, S.R., and Boutin, H. (2017). Longitudinal investigation of neuroinflammation and metabolite profiles in the APP<sup>swE</sup>  $\times$  PS1 <sup>$\Delta$ e9</sup> transgenic mouse model of Alzheimer's disease. *J. Neurochem.* 318–335.

Chavhan, G.B., Babyn, P.S., Thomas, B., Shroff, M.M., and Haacke, E.M. (2009). Principles, techniques, and applications of T2\*-based MR imaging and its special applications. *Radiographics* 29, 1433–1449.

Chi, O.Z., Wei, H.M., Lu, X., and Weiss, H.R. (1996). Increased Blood-Brain Permeability with Hyperosmolar Mannitol Increases Cerebral O<sub>2</sub> Consumption and O<sub>2</sub> Supply/Consumption Heterogeneity. *J. Cereb. Blood Flow Metab.* 16, 327–333.

Cho, E.E., Drazic, J., Ganguly, M., Stefanovic, B., and Hynynen, K. (2011). Two-photon fluorescence microscopy study of cerebrovascular dynamics in ultrasound-induced blood-brain barrier opening. *J. Cereb. Blood Flow Metab.* 31, 1852–1862.

Cho, H., Lee, H.-Y., Han, M., Choi, J.-R., Ahn, S., Lee, T., Chang, Y., and Park, J. (2016). Localized Down-regulation of P-glycoprotein by Focused Ultrasound and Microbubbles induced Blood-Brain Barrier Disruption in Rat Brain. *Sci. Rep.* 6.

Choi, J.J., Feshitan, J.A., Baseri, B., Wang, S., Tung, Y.S., Borden, M.A., and Konofagou, E.E. (2010). Microbubble-size dependence of focused ultrasound-induced blood-brain barrier opening in mice in vivo. *IEEE Trans. Biomed. Eng.* 57, 145–154.

Choi, J.J., Selert, K., Gao, Z., Samiotaki, G., Baseri, B., and Konofagou, E.E. (2011). Noninvasive and localized blood-brain barrier disruption using focused ultrasound can be achieved at short pulse lengths and low pulse repetition frequencies. *J. Cereb. Blood Flow Metab.* 31, 725–737.

Choi, S.R., Schneider, J.A., Bennett, D.A., Beach, T.G., Bedell, B.J., Zehntner, S.P., Krautkramer, M., Kung, H.F., Skovronsky, D.M., Hefti, F., et al. (2012). Correlation of amyloid PET ligand florbetapir F 18 (18 F-AV-45) binding with  $\beta$ -amyloid aggregation and neuritic plaque deposition in postmortem brain tissue. *Alzheimer Dis Assoc Disord* 50, 294–306.

Choleris, E., Thomas, A.W., Kavaliers, M., and Prato, F.. (2001). A detailed ethological analysis of the mouse

- open field test: effects of diazepam, chlordiazepoxide and an extremely low frequency pulsed magnetic field. *Neurosci. Biobehav. Rev.* 25, 235–260.
- Cibelli, M., Fidalgo, A.R., Feldmann, M., Takata, M., Lever, I.J., Nanchahal, J., Fanselow, M.S., Maze, M., Care, I., Hospital, W., et al. (2016). Role of Interleukin-1 in Postoperative Cognitive Dysfunction. *68*, 360–368.
- Cleveland, R.O., and McAteer, J.A. (2007). Chapter 38 The physics of shock wave lithotripsy. *Smith's Textb. Endourol.* 1, 529–558.
- Cobbold, R.S. (2007). *Foundations of Biomedical Ultrasound. Nonlinear Ultrasonics.* Oxford Univ. Press.
- Coey, J.M.D., Skumryev, V., and Gallagher, K. (1999). Is gadolinium really ferromagnetic? *Nature* 401, 35.
- Cohen, R.M., Rezai-Zadeh, K., Weitz, T.M., Rentsendorj, a., Gate, D., Spivak, I., Bholat, Y., Vasilevko, V., Glabe, C.G., Breunig, J.J., et al. (2013). A Transgenic Alzheimer Rat with Plaques, Tau Pathology, Behavioral Impairment, Oligomeric A , and Frank Neuronal Loss. *J. Neurosci.* 33, 6245–6256.
- Coluccia, D., Fandino, J., Schwyzer, L., O'Gorman, R., Remonda, L., Anon, J., Martin, E., and Werner, B. (2014). First noninvasive thermal ablation of a brain tumor with MR-guided focused ultrasound. *J. Ther. Ultrasound* 2, 1–7.
- Crassard, I., and Boussier, M.G. (2006). Thromboses veineuses cérébrales: Mise au point. *Rev. Med. Interne* 27, 117–124.
- Crawshaw, A.A., and Robertson, N.P. (2017). The role of TSPO PET in assessing neuroinflammation. *J. Neurol.* 264, 1825–1827.
- Crouch, S.D., Hill, D., and Bridwell, D. (2008). New Technology for the Treatment of Peripheral Arterial and Venous Occlusions: Ultrasound Accelerated Thrombolysis. *J. Radiol. Nurs.* 27, 14–21.
- Culjat, M.O., Goldenberg, D., Tewari, P., and Singh, R.S. (2010). A review of tissue substitutes for ultrasound imaging. *Ultrasound Med. Biol.* 36, 861–873.
- Cummings, B.J., Su, J.H., Cotman, C.W., White, R., and Russell, M.J. (1993).  $\beta$ -Amyloid accumulation in aged canine brain: A model of early plaque formation in Alzheimer's disease. *Neurobiol. Aging* 14, 547–560.
- Cummings, J., Lee, G., Mortsdorf, T., Ritter, A., and Zhong, K. (2017). Alzheimer's disease drug development pipeline: 2017. *Alzheimer's Dement. Transl. Res. Clin. Interv.* 3, 367–384.
- Davson, H., Kleeman, C.R., and Levin, E. (2015). The blood-brain barrier. *Cold Spring Harb Perspect Biol* 7, 1–24.
- Deffieux, T., Younan, Y., Wattiez, N., Tanter, M., Pouget, P., and Aubry, J.F. (2013). Low-intensity focused ultrasound modulates monkey visuomotor behavior. *Curr. Biol.* 23, 2430–2433.
- Deichmann, R., and Haase, a (1992). Quantification of T 1 values by SNAPSHOT-FLASH NMR imaging. *J. Magn. Reson.* 612, 608–612.
- Deike-Hofmann, K., Thü nemann, D., Breckwoldt, M.O., Schwarz, D., Radbruch, A., Enk, A., Bendszus, M., Hassel, J., Schlemmer, H.-P., and Bä umer, P. (2018). Sensitivity of different MRI sequences in the early detection of melanoma brain metastases. *PLoS One* 1–13.
- Delatour, B., Guégan, M., Volk, A., and Dhenain, M. (2006). In vivo MRI and histological evaluation of brain atrophy in APP/PS1 transgenic mice. *Neurobiol. Aging* 27, 835–847.
- Dellu, F., Mayo, W., Cherkaoui, J., Lemoal, M., and Simon, H. (1992). A Two Trial Memory Task with Automated Recording: Study in Young and Aged Rats. *Brain Res.* 588, 132–139.
- Dellu, F., Contarino, A., Simon, H., Koob, G.F., and Gold, L.H. (2000). Genetic Differences in Response to Novelty and Spatial Memory Using a Two-Trial Recognition Task in Mice. *Neurobiol. Learn. Mem.* 73, 31–48.
- Dervishi, E., Larrat, B., Pernot, M., Adam, C., Marie, Y., Fink, M., Delattre, J.-Y., Boch, A.-L., Tanter, M., and Aubry, J.-F. (2013). Transcranial high intensity focused ultrasound therapy guided by 7 TESLA MRI in a rat brain tumour model: A feasibility study. *Int. J. Hyperth.* 29, 598–608.

- Dhenain, M., Privat, N., Duyckaerts, C., and Jacobs, R.E. (2002). Senile plaques do not induce susceptibility effects in T2\*-weighted MR microscopic images. *NMR Biomed.* *15*, 197–203.
- Downs, M.E., Buch, A., Sierra, C., Karakatsani, M.E., Chen, S., Konofagou, E.E., and Ferrera, V.P. (2015). Long-Term Safety of Repeated Blood-Brain Barrier Opening via Focused Ultrasound with Microbubbles in Non-Human Primates Performing a Cognitive Task. *PLoS One* 1–26.
- Du, Y., Wei, X., Dodel, R., Sommer, N., Hampel, H., Gao, F., Ma, Z., Zhao, L., Oertel, W.H., and Farlow, M. (2003). Human anti- $\beta$ -amyloid antibodies block  $\beta$ -amyloid fibril formation and prevent  $\beta$ -amyloid-induced neurotoxicity. *Brain* *126*, 1935–1939.
- Le Duc, G., Roux, S., Paruta-Tuarez, A., Dufort, S., Brauer, E., Marais, A., Truillet, C., Sancey, L., Perriat, P., Lux, F., et al. (2014). Advantages of gadolinium based ultrasmall nanoparticles vs molecular gadolinium chelates for radiotherapy guided by MRI for glioma treatment. *Cancer Nanotechnol.* *5*, 1–14.
- Dudeffant, C., Vandesquille, M., Herbert, K., Garin, C.M., Alves, S., Blanchard, V., Comoy, E.E., Petit, F., and Dhenain, M. (2017). Contrast-enhanced MR microscopy of amyloid plaques in five mouse models of amyloidosis and in human Alzheimer’s disease brains. *Sci. Rep.* *7*, 1–13.
- Durmo, F., Lätt, J., Rydelius, A., Engelholm, S., Kinhult, S., Askaner, K., Englund, E., Bengzon, J., Nilsson, M., Björkman-Burtscher, I.M., et al. (2018). Brain Tumor Characterization Using Multibiometric Evaluation of MRI. *Tomography* *4*, 14–25.
- Durmus, S., Hendrikx, J.J.M.A., and Schinkel, A.H. (2015). Apical ABC transporters and cancer chemotherapeutic drug disposition. *Adv. Cancer Res.* *125*, 1–41.
- Duyckaerts, C., Potier, M.-C., and Delatour, B. (2007). Alzheimer disease models and human neuropathology: similarities and differences. *Acta Neuropathol.* *115*, 5–38.
- Van Dyck, C.H. (2018). Anti-Amyloid- $\beta$  Monoclonal Antibodies for Alzheimer’s Disease: Pitfalls and Promise. *Biol. Psychiatry* *83*, 311–319.
- E Treeby, B., and Cox, B.T. (2010). k-Wave: MATLAB toolbox for the simulation and reconstruction of photoacoustic wave fields.
- Eimer, W.A., Vijaya Kumar, D.K., Navalpur Shanmugam, N.K., Rodriguez, A.S., Mitchell, T., Washicosky, K.J., György, B., Breakefield, X.O., Tanzi, R.E., and Moir, R.D. (2018). Alzheimer’s Disease-Associated  $\beta$ -Amyloid Is Rapidly Seeded by Herpesviridae to Protect against Brain Infection. *Neuron* *99*, 56–63.e3.
- Elias, W.J., Lipsman, N., Ondo, W.G., Ghanouni, P., Kim, Y.G., Lee, W., Schwartz, M., Hynynen, K., Lozano, A.M., Shah, B.B., et al. (2016). A Randomized Trial of Focused Ultrasound Thalamotomy for Essential Tremor. *N. Engl. J. Med.* *375*, 730–739.
- Endocrine, T.C., Res, J.L.F.C., Moss, R., Nicholson, C., Syková, E., and Nicholson, C. (1998). Extracellular space structure revealed by diffusion analysis. *Trends Neurosci.* 207–215.
- Engelhardt, B. (2003). Development of the blood-brain barrier. *Cell Tissue Res.* *314*, 119–129.
- Farwell, M.D., Chong, D.J., Iida, Y., Bae, S.A., Easwaramoorthy, B., and Ichise, M. (2013). Imaging P-glycoprotein function in rats using [(11)C]-N-desmethyl-loperamide. *Ann. Nucl. Med.* *27*, 618–624.
- Fox, G.B., Fan, L., Levasseur, R.A., and Faden, A.I. (1998). Effect of Traumatic Brain Injury on Mouse Spatial and Nonspatial Learning in the Barnes Circular Maze. *J. Neurotrauma* *15*, 1037–1046.
- Francis, D., Richards, G.M., Forouzannia, A., Mehta, M.P., and Khuntia, D. (2009). Motexafin gadolinium: a novel radiosensitizer for brain tumors. *Expert Opin. Pharmacother.* *10*, 2171–2180.
- Frederick, B.B., Satlin, A., Yurgelun-Todd, D. a, and Renshaw, P.F. (1997). In vivo proton magnetic resonance spectroscopy of Alzheimer’s disease in the parietal and temporal lobes. *Biol. Psychiatry* *42*, 147–150.
- Gabathuler, R. (2010). Approaches to transport therapeutic drugs across the blood-brain barrier to treat brain diseases. *Neurobiol. Dis.* *37*, 48–57.

- Garcia-Alloza, M., Robbins, E.M., Zhang-Nunes, S.X., Purcell, S.M., Betensky, R. a., Raju, S., Prada, C., Greenberg, S.M., Bacskai, B.J., and Frosch, M.P. (2006). Characterization of amyloid deposition in the APPsw/PS1dE9 mouse model of Alzheimer disease. *Neurobiol. Dis.* *24*, 516–524.
- Gerstenmayer, M., Fellah, B., Magnin, R., Selingue, E., and Larrat, B. (2018). Acoustic Transmission Factor through the Rat Skull as a Function of Body Mass, Frequency and Position. *Ultrasound Med. Biol.*
- Ghosh, S., Wu, M.D., Shaftel, S.S., Kyrkanides, S., LaFerla, F.M., Olschowka, J.A., and O’Banion, M.K. (2013). Sustained Interleukin-1 $\beta$  overexpression exacerbates tau pathology despite reduced amyloid burden in an Alzheimer’s mouse model. *J Neurosci.* *33*, 1–12.
- Goutal, S., Langer, O., Auvity, S., Andrieux, K., Coulon, C., Caillé, F., Gervais, P., Cisternino, S., Declèves, X., and Tournier, N. (2018). Intravenous infusion for the controlled exposure to the dual ABCB1 and ABCG2 inhibitor elacridar in nonhuman primates. *Drug Deliv. Transl. Res.*
- Graeber, M.B., Li, W., and Rodriguez, M.L. (2011). Role of microglia in CNS inflammation. *FEBS Lett.* *585*, 3798–3805.
- Grignon, Y., Duyckaerts, C., Bannic, M., and Hauw, J.J. (1998). Cytoarchitectonic alterations in the supramarginal gyrus of late onset Alzheimer’s disease. *Acta Neuropathol.* *95*, 395–406.
- Guillaume, D.J., Doolittle, N.D., Gahramanov, S., Hedrick, N.A., Delashaw, J.B., and Neuwelt, E.A. (2010). Intra-arterial chemotherapy with osmotic blood-brain barrier disruption for aggressive oligodendroglial tumors: Results of a phase I study. *Neurosurgery* *66*, 48–58.
- Gustke, N., Steiner, B., Mandelkow, E.M., Biernat, J., Meyer, H.E., Goedert, M., and Mandelkow, E. (1992). The Alzheimer-like phosphorylation of tau protein reduces microtubule binding and involves Ser-Pro and Thr-Pro motifs. *FEBS Lett.* *307*, 199–205.
- Guthkelch, A.N., Carter, L.P., Cassady, J.R., Hynynen, K.H., Iacono, R.P., Johnson, P.C., Obbens, E.A.M.T., Roemer, R.B., Seeger, J.F., Shimm, D.S., et al. (1991). Treatment of malignant brain tumors with focused ultrasound hyperthermia and radiation: results of a phase I trial. *J. Neurooncol.* *10*, 271–284.
- Hahn, E.L. (1950). Spin Echoes. *Phys. Rev.* *80*, 580–594.
- Ben Haim, L., Carrillo-de Sauvage, M.-A., Ceylan, K., and Escartin, C. (2015). Elusive roles for reactive astrocytes in neurodegenerative diseases. *Front. Cell. Neurosci.* *9*, 1–27.
- Hall, C.S. (1936). Emotional behavior in the rat. III. The relationship between emotionality and ambulatory activity. *Am. Psychol. Assoc.* 20002.
- Hall, W.A., Doolittle, N.D., Daman, M., Bruns, P.K., Muldoon, L., Fortin, D., and Neuwelt, E.A. (2006). Osmotic blood-brain barrier disruption chemotherapy for diffuse pontine gliomas. *J. Neurooncol.* *77*, 279–284.
- Hamelin, L., Lagarde, J., Dorothée, G., Leroy, C., Labit, M., Comley, R.A., de Souza, L.C., Corne, H., Dauphinot, L., Bertoux, M., et al. (2016). Early and protective microglial activation in Alzheimer’s disease: a prospective study using 18 F-DPA-714 PET imaging. *Brain* *139*, 1252–1264.
- Hamelin, L., Lagarde, J., Dorothée, G., Potier, M.C., Corlier, F., Kuhnast, B., Caillé, F., Dubois, B., Fillon, L., Chupin, M., et al. (2018). Distinct dynamic profiles of microglial activation are associated with progression of Alzheimer’s disease. *Brain.*
- Hardy, J., Duff, K., Hardy, K.G., Perez-Tur, J., and Hutton, M. (1998). Genetic dissection of Alzheimer’s disease and related dementias: amyloid and its relationship to tau. *Nat. Neurosci.* *1*, 355–358.
- Harrison, F.E., Hosseini, A.H., and McDonald, M.P. (2009). Endogenous anxiety and stress responses in water maze and Barnes maze spatial memory tasks. *Behav. Brain Res.* *198*, 247–251.
- Hebert, L.E., Weuve, J., Scherr, P.A., and Evans, D.A. (2013). Alzheimer disease in the United States (2010–2050) estimated using the 2010 census. *Neurology* *80*, 1778 LP-1783.
- Heneka, M.T., and O’Banion, M.K. (2007). Inflammatory processes in Alzheimer’s disease. *J. Neuroimmunol.* *184*, 69–91.

- Hennig, J., Nauerth, A., and Friedburg, H. (1986). RARE imaging: a fast imaging method for clinical MR. *Magn Reson Med* 3, 823–833.
- Heppner, F.L., Ransohoff, R.M., and Becher, B. (2015). Immune attack: The role of inflammation in Alzheimer disease. *Nat. Rev. Neurosci.* 16, 358–372.
- Hickman, S.E., Allison, E.K., and Khoury, J. El (2009). Microglial dysfunction and defective  $\beta$ -amyloid clearance pathways in aging Alzheimer's disease mice. *J Neurosci.* 28, 8354–8360.
- Hooijmans, C.R., Van der Zee, C.E.E.M., Dederen, P.J., Brouwer, K.M., Reijmer, Y.D., van Groen, T., Broersen, L.M., Lütjohann, D., Heerschap, A., and Kiliaan, A.J. (2009). DHA and cholesterol containing diets influence Alzheimer-like pathology, cognition and cerebral vasculature in APP<sup>swe</sup>/PS1<sup>dE9</sup> mice. *Neurobiol. Dis.* 33, 482–498.
- How, J., Mann, J., Laczniak, A.N., and Baggstrom, M.Q. (2017). Pulsatile Erlotinib in EGFR-Positive Non-Small-Cell Lung Cancer Patients With Leptomeningeal and Brain Metastases: Review of the Literature. *Clin. Lung Cancer* 18, 354–363.
- Huang, H., Nie, S., Cao, M., Marshall, C., Gao, J., Xiao, N., Hu, G., and Xiao, M. (2016). Characterization of AD-like phenotype in aged APP<sup>swe</sup>/PS1<sup>dE9</sup> mice. *Age (Omaha)*. 38, 303–322.
- Huang, Q., Deng, J., Xie, Z., Wang, F., Chen, S., Lei, B., Liao, P., Huang, N., Wang, Z., Wang, Z., et al. (2018). Effective Gene Transfer into Central Nervous System Following Ultrasound-Microbubbles-Induced Opening of the Blood-Brain Barrier. *Ultrasound Med. Biol.* 38, 1234–1243.
- Hyde, L.A., Kazdoba, T.M., Grilli, M., Lozza, G., Brussa, R., Zhang, Q., Wong, G.T., McCool, M.F., Zhang, L., Parker, E.M., et al. (2005). Age-progressing cognitive impairments and neuropathology in transgenic CRND8 mice. *Behav. Brain Res.* 160, 344–355.
- Hynynen, K., McDannold, N., Vykhodtseva, N., and Jolesz, F. a (2001). Noninvasive MR imaging-guided focal opening of the blood-brain barrier in rabbits. *Radiology* 220, 640–646.
- Hynynen, K., McDannold, N., Sheikov, N.A., Jolesz, F.A., and Vykhodtseva, N. (2005). Local and reversible blood-brain barrier disruption by noninvasive focused ultrasound at frequencies suitable for trans-skull sonications. *Neuroimage* 24, 12–20.
- Ibrahim, E.-S.H., Khalifa, A.M., and Eldaly, A.K. (2016). Influence of the analysis technique on estimating hepatic iron content using MRI. *J. Magn. Reson. Imaging* 44, 1448–1455.
- Iivonen, H., Nurminen, L., Harri, M., Tanila, H., and Puoliväli, J. (2003). Hypothermia in mice tested in Morris water maze. *Behav. Brain Res.* 141, 207–213.
- Ilyas, A., Chen, C.-J., Ding, D., Romeo, A., Buell, T.J., Wang, T.R., Kalani, M.Y.S., and Park, M.S. (2018). Magnetic resonance-guided, high-intensity focused ultrasound sonolysis: potential applications for stroke. *Neurosurg. Focus* 44, E12.
- Iqbal, K., and Grundke-Iqbal, I. (2005). Metabolic/signal transduction hypothesis of Alzheimer's disease and other tauopathies. *Acta Neuropathol.* 109, 25–31.
- Irizarry, M.C., Soriano, F., McNamara, M., Page, K.J., Schenk, D., Games, D., and Hyman, B.T. (1997). Abeta deposition is associated with neuropil changes, but not with overt neuronal loss in the human amyloid precursor protein V717F (PDAPP) transgenic mouse. *J. Neurosci.* 17, 7053–7059.
- Jack, C., Petersen, R., C O'Brien, P., and G Tangalos, E. (1992). MRI-based hippocampal volumetry in the diagnosis of Alzheimer's disease. *Neurology* 42, 183–188.
- Jack Jr, C.R., Wengenack, T.M., Reyes, D.A., Garwood, M., Curran, G.L., Borowski, B.J., Lin, J., Preboske, G.M., Holasek, S.S., Adrian, G., et al. (2005). In Vivo Magnetic Resonance Microimaging of Individual Amyloid Plaques in Alzheimer's Transgenic Mice. *J. Neurosci.* 25, 10041–10048.
- Jackson, R.J., Rudinskiy, N., Herrmann, A.G., Croft, S., Kim, J.S.M., Petrova, V., Ramos-Rodriguez, J.J., Pitstick, R., Wegmann, S., Garcia-Alloza, M., et al. (2016). Human tau increases amyloid  $\beta$  plaque size but not amyloid  $\beta$ -mediated synapse loss in a novel mouse model of Alzheimer's disease. *Eur. J. Neurosci.* 44, 3056–3066.

- James, S.A., Churches, Q.I., de Jonge, M.D., Birchall, I.E., Streltsov, V., McColl, G., Adlard, P.A., and Hare, D.J. (2016). The iron, copper and zinc concentration in A $\beta$  plaques in the APP/PS1 mouse model of Alzheimer's disease correlates with metal levels in the surrounding neuropil. *ACS Chem. Neurosci.*
- Jankowsky, J.L., Fadale, D.J., Anderson, J., Xu, G.M., Gonzales, V., Jenkins, N.A., Copeland, N.G., Lee, M.K., Younkin, L.H., Wagner, S.L., et al. (2004). Mutant presenilins specifically elevate the levels of the 42 residue  $\beta$ -amyloid peptide in vivo: Evidence for augmentation of a 42-specific  $\gamma$  secretase. *Hum. Mol. Genet.* *13*, 159–170.
- JC, M., Storandt, M., Miller, J., and al, et (2001). Mild cognitive impairment represents early-stage alzheimer disease. *Arch. Neurol.* *58*, 397–405.
- Jensen, J.A. (1996). FIELD: A Program for Simulating Ultrasound Systems. *Med. Biol. Eng. Comput.* *34*, 351–352.
- Jensen, J.A., and Svendsen, N.B. (1992). Calculation of Pressure Fields from Arbitrarily Shaped, Apodized, and Excited Ultrasound Transducers. *262 IEEE Trans. Ultrason. Ferroelectr. Freq. Control* *39*, 262–267.
- Ji, K., Akgul, G., Wollmuth, L.P., and Tsirka, S.E. (2013). Microglia Actively Regulate the Number of Functional Synapses. *PLoS One* *8*.
- Jin, J.J., Kim, H.D., Maxwell, J.A., Li, L., and Fukuchi, K.I. (2008). Toll-like receptor 4-dependent upregulation of cytokines in a transgenic mouse model of Alzheimer's disease. *J. Neuroinflammation* *5*, 1–10.
- JohnHardy, and Selkoe, D.J. (2002). The Amyloid Hypothesis of Alzheimer's Disease: Progress and Problems on the Road to Therapeutics. *Source Sci. New Ser.* *297*, 353–356.
- Johnson, K.A., Jones, K., Holman, B.L., Becker, J., Spiers, P.A., Satlin, A., and Albert, M. (1998). Preclinical prediction of Alzheimer's disease using SPECT. *Neurology* *50*, 1563–1571.
- Johnson, K.A., Lopera, F., Jones, K., Becker, A., Sperling, R., Hilson, J., Londono, J., Siegert, I., Arcos, M., Moreno, S., et al. (2001). Presenilin-1-associated abnormalities in regional cerebral perfusion. *Neurology* *56*, 1545 LP-1551.
- Jordão, J.F., Thévenot, E., Markham-Coultres, K., Scarcellia, T., Weng, Y.Q., Xhima, K., O'Reilly, M., Huang, Y., McLaurin, J., Hynynen, K., et al. (2013). Amyloid- $\beta$  plaque reduction, endogenous antibody delivery and glial activation by brain-targeted, transcranial focused ultrasound. *Exp Neurol.* *29*, 997–1003.
- Kamimura, H.A.S., Flament, J., Valette, J., Cafarelli, A., Aron Badin, R., Hantraye, P., and Larrat, B. (2018). Feedback control of microbubble cavitation for ultrasound-mediated blood–brain barrier disruption in non-human primates under magnetic resonance guidance. *J. Cereb. Blood Flow Metab.*
- Kamphuis, W., Mamber, C., Moeton, M., Kooijman, L., Sluijs, J.A., Jansen, A.H.P., Verveer, M., de Groot, L.R., Smith, V.D., Rangarajan, S., et al. (2012). GFAP isoforms in adult mouse brain with a focus on neurogenic astrocytes and reactive astrogliosis in mouse models of Alzheimer disease. *PLoS One* *7*.
- Kannan, P., Brimacombe, K.R., Zoghbi, S.S., Liow, J.-S., Morse, C., Taku, A.K., Pike, V.W., Halldin, C., Innis, R.B., Gottesman, M.M., et al. (2010). N-desmethyl-loperamide is selective for P-glycoprotein among three ATP-binding cassette transporters at the blood-brain barrier. *Drug Metab. Dispos.* *38*, 917–922.
- Katzman, R., Terry, R., Deteresa, R., Brown, T., Davies, P., Fuld, P., Renbing, X., and Peck, A. (1988). Neurochemical Changes in Dementia : A Subgroup with Preserved Mental Status and Numerous Neocortical Plaques. *138–144*.
- Kaufman, A.C., Salazar, S. V., Haas, L.T., Yang, J., Kostylev, M. a., Jeng, A.T., Robinson, S. a., Gunther, E.C., van Dyck, C.H., Nygaard, H.B., et al. (2015). Fyn inhibition rescues established memory and synapse loss in Alzheimer mice. *Ann. Neurol.*
- Kayed, R., Head, E., Thompson, J.L., Mcintire, T., Milton, S.C., Cotman, C.W., and Glabe, C.G. (2003). Common Structure of Soluble Amyloid Oligomers Implies Common Mechanism of Pathogenesis . *Science (80-. )*. *486*, 486–490.
- Kelényi, G. (1967). Thioflavin S fluorescent and congo red anisotropic stainings in the histologic demonstration of amyloid. *Acta Neuropathol.* *7*, 336–348.

- Kettenmann, H., Hanisch, U.-K., Noda, M., and Verkhratsky, A. (2011). Physiology of Microglia. *Physiol. Rev.* *91*, 461–553.
- Kiessling, F., Fokong, S., Koczera, P., Lederle, W., and Lammers, T. (2012). Ultrasound Microbubbles for Molecular Diagnosis, Therapy, and Theranostics. *J. Nucl. Med.* *53*, 345–348.
- Kim, Y.S. (2015). Advances in MR image-guided high-intensity focused ultrasound therapy. *Int. J. Hyperth.* *31*, 225–232.
- Kiricuta Jr., I.C., and Simplaceanu, V. (1975). Tissue water content and nuclear magnetic resonance in normal and tumor tissues. *Cancer Res* *35*, 1164–1167.
- Klunk, W.E., Engler, H., Nordberg, A., Wang, Y., Blomqvist, G., Holt, D.P., Bergström, M., Savitcheva, I., Huang, G.F., Estrada, S., et al. (2004). Imaging Brain Amyloid in Alzheimer's Disease with Pittsburgh Compound-B. *Ann. Neurol.* *55*, 306–319.
- Knopman, D., Jack, C.J., Wiste, H., Weigand, S., Vemuri, P., Lowe, V., Kantarci, K., Gunter, J., Senjem, M., Mielke, M., et al. (2016). Age neurodegeneration imaging biomarkers in persons with Alzheimer's disease dementia. *Neurology* *87*, 691–698.
- Kobus, T., Vykhodtseva, N., Pilatou, M., Zhang, Y., and McDannold, N. (2015). Safety Validation of Repeated Blood-Brain Barrier Disruption Using Focused Ultrasound. *Ultrasound Med. Biol.* *42*, 481–492.
- Von Koch, C.S., Zheng, H., Chen, H., Trumbauer, M., Thinakaran, G., Van Der Ploeg, L.H.T., Price, D.L., and Sisodia, S.S. (1997). Generation of APLP2 KO mice and early postnatal lethality in APLP2/APP double KO mice. *Neurobiol. Aging* *18*, 661–669.
- Kodaira, H., Kusuhara, H., Ushiki, J., Fuse, E., and Sugiyama, Y. (2010). Kinetic analysis of the cooperation of P-glycoprotein (P-gp/Abcb1) and breast cancer resistance protein (Bcrp/Abcg2) in limiting the brain and testis penetration of erlotinib, flavopiridol, and mitoxantrone. *J. Pharmacol. Exp. Ther.* *333*, 788–796.
- Koopmans, G., Blokland, A., Van Nieuwenhuijzen, P., and Prickaerts, J. (2003). Assessment of spatial learning abilities of mice in a new circular maze. *Physiol. Behav.* *79*, 683–693.
- Kort, A., Sparidans, R.W., Wagenaar, E., Beijnen, J.H., and Schinkel, A.H. (2015a). Brain accumulation of the EML4-ALK inhibitor ceritinib is restricted by P-glycoprotein (P-GP/ABCB1) and breast cancer resistance protein (BCRP/ABCG2). *Pharmacol. Res.* *102*, 200–207.
- Kort, A., Durmus, S., Sparidans, R.W., Wagenaar, E., Beijnen, J.H., and Schinkel, A.H. (2015b). Brain and Testis Accumulation of Regorafenib is Restricted by Breast Cancer Resistance Protein (BCRP/ABCG2) and P-glycoprotein (P-GP/ABCB1). *Pharm. Res.* *32*, 2205–2216.
- Kovacs, Z.I., Kim, S., Jikaria, N., Qureshi, F., Milo, B., Lewis, B.K., Bresler, M., Burks, S.R., and Frank, J.A. (2016). Disrupting the blood–brain barrier by focused ultrasound induces sterile inflammation. *Proc. Natl. Acad. Sci.* *114*, E75–E84.
- Krabbe, G., Halle, A., Matyash, V., Rinnenthal, J.L., Eom, G.D., Bernhardt, U., Miller, K.R., Prokop, S., Kettenmann, H., and Heppner, F.L. (2013). Functional Impairment of Microglia Coincides with Beta-Amyloid Deposition in Mice with Alzheimer-Like Pathology. *PLoS One* *8*.
- Krewson, C.E., Klarman, M.L., and Saltzman, W.M. (1995). Distribution of nerve growth factor following direct delivery to brain interstitium. *Brain Res.* *680*, 196–206.
- Krizanac-Bengez, L., Mayberg, M.R., and Janigro, D. (2004). The cerebral vasculature as a therapeutic target for neurological disorders and the role of shear stress in vascular homeostasis and pathophysiology. *Neurol. Res.* *26*, 846–853.
- Kumari, A., Singla, R., Guliani, A., and Yadav, S.K. (2014). Nanoencapsulation for drug delivery. *EXCLI J.* *13*, 265–286.
- De la Torre, J.C., and Mussivan, T. (1993). Can disturbed brain microcirculation cause Alzheimer's disease? *Neurol. Res.* *15*, 146–153.

- Lalonde, R., Kim, H.D., Maxwell, J.A., and Fukuchi, K. (2005). Exploratory activity and spatial learning in 12-month-old APP 695SWE/co + PS1/ $\Delta$ E9 mice with amyloid plaques. *Neurosci. Lett.* 390, 87–92.
- Lalonde, R., Fukuchi, K., and Strazielle, C. (2013). Neurologic and motor dysfunctions in APP transgenic mice. *Rev Neurosci* 23, 363–379.
- Larrat, B. (2010). PhD Thesis. <https://pastel.archives-ouvertes.fr/pastel-0056038>.
- Larrat, B., Chan, Q.C., Yang, X.F., Li, G., Yang, E.S., Fink, M., and Sinkus, R. (2007). Anisotropic viscoelastic properties of the corpus callosum - Application of high-resolution 3D MR-elastography to an Alzheimer mouse model. *Proc. - IEEE Ultrason. Symp.* 676–679.
- Larrat, B., Pernot, M., Aubry, J.-F., Dervishi, E., Sinkus, R., Seilhean, D., Marie, Y., Boch, A.-L., Fink, M., and Tanter, M. (2010a). MR-guided transcranial brain HIFU in small animal models. *Phys. Med. Biol.* 55, 365–388.
- Larrat, B., Pernot, M., Montaldo, G., Fink, M., and Tanter, M. (2010b). MR-guided adaptive focusing of ultrasound. *IEEE Trans. Ultrason. Ferroelectr. Freq. Control* 57, 1734–1747.
- Lauffer, R.B. (1987). Paramagnetic Metal Complexes as Water Proton Relaxation Agents for NMR Imaging: Theory and Design. *Chem. Rev.* 87, 901–927.
- Lavaud, J., Henry, M., Coll, J.L., and Josserand, V. (2017). Exploration of melanoma metastases in mice brains using endogenous contrast photoacoustic imaging. *Int. J. Pharm.* 532, 704–709.
- Leinenga, G., and Götz, J. (2015). Scanning ultrasound removes amyloid- $\beta$  and restores memory in an Alzheimer's disease mouse model. *Sci. Transl. Med.* 7.
- Leinenga, G., and Götz, J. (2018). Safety and efficacy of scanning ultrasound treatment of aged APP23 mice. *Front. Neurosci.* 12, 1–10.
- Levy, E., Carman, M., Fernandez-Madrid, I., Power, M., Lieberburg, I., van Duinen, S., Bots, G., Luyendijk, W., and Frangione, B. (1990). Mutation of the Alzheimer's disease amyloid gene in hereditary cerebral hemorrhage, Dutch type. *Science* (80-. ). 248, 1124–1126.
- Liddelow, S.A., Guttenplan, K.A., Clarke, L.E., Bennett, F.C., Bohlen, C.J., Schirmer, L., Bennett, M.L., Münch, A.E., Chung, S., Peterson, T.C., et al. (2017). Neurotoxic reactive astrocytes are induced by activated microglia. *Nature* 541, 481–487.
- Lipsman, N., Meng, Y., Bethune, A., Huang, Y., Lam, B., Masellis, M., Herrmann, N., Heyn, C., Aubert, I., Boutet, A., et al. (2018). Blood-brain barrier opening in Alzheimer's disease using MR-guided focused ultrasound. *Nat. Commun. in press*, 1–8.
- Luo, X., Yang, L., Chen, X., and Li, S. (2014). Tau hyperphosphorylation: A downstream effector of isoflurane-induced neuroinflammation in aged rodents. *Med. Hypotheses* 82, 94–96.
- Macdonell, J., Patel, N., Rubino, S., Fischer, G., Burdette, E.C., Hwang, R., Pilitsis, G., Therapeutics, E., and Program, E. (2018). Magnetic resonance-guided interstitial high-intensity focused ultrasound for brain tumor ablation. *Neurosurg. Focus* 44.
- Mace, E., Cohen, I., Montaldo, G., Miles, R., Fink, M., and Tanter, M. (2011). In Vivo Mapping of Brain Elasticity in Small Animals Using Shear Wave Imaging. *IEEE Trans. Med. Imaging* 30, 550–558.
- Magnin, R. (2016). PhD Thesis. <https://tel.archives-ouvertes.fr/tel-01277073>.
- Magnin, R., Rabusseau, F., Salabartan, F., Mériaux, S., Aubry, J.-F., Le Bihan, D., Dumont, E., and Larrat, B. (2015). Magnetic resonance-guided motorized transcranial ultrasound system for blood-brain barrier permeabilization along arbitrary trajectories in rodents. *J. Ther. Ultrasound* 3, 22.
- Martin, K.H., and Dayton, P.A. (2014). Current Status and Prospects for Microbubbles in Ultrasound Theranostics. 5, 1–23.
- Marty, B. (2012). PhD Thesis. <http://www.theses.fr/16155234X>.
- Marty, B., Larrat, B., Van Landeghem, M., Robic, C., Robert, P., Port, M., Le Bihan, D., Pernot, M., Tanter, M.,

- Lethimonnier, F., et al. (2012a). Dynamic study of blood–brain barrier closure after its disruption using ultrasound: a quantitative analysis. *J. Cereb. Blood Flow Metab.* *32*, 1948–1958.
- Marty, B., Djemaï, B., Robic, C., Port, M., Robert, P., Valette, J., Boumezbeur, F., Le Bihan, D., Lethimonnier, F., and Mériaux, S. (2012b). Hindered diffusion of MRI contrast agents in rat brain extracellular micro-environment assessed by acquisition of dynamic T1 and T2 maps. *Contrast Media Mol. Imaging* *8*, 12–19.
- Matsuoka, Y., Picciano, M., Maleste, B., LaFrancois, J., Zehr, C., Daeschner, J.A.M., Olschowka, J.A., Fonseca, M.I., O'Banion, M.K., Tenner, A.J., et al. (2001). Inflammatory responses to amyloidosis in a transgenic mouse model of Alzheimer's disease. *Am. J. Pathol.* *158*, 1345–1354.
- Mattsson, N., Zetterberg, H., Hansson, O., and al, et (2009). Csf biomarkers and incipient Alzheimer disease in patients with mild cognitive impairment. *JAMA* *302*, 385–393.
- Mawuenyega, K.G., Sigurdson, W., Ovod, V., Munsell, L., Kasten, T., Morris, J.C., Yarasheski, K.E., and Bateman, R.J. (2010). Decreased Clearance of CNS Amyloid- $\beta$  in Alzheimer's Disease. *Science* (80-. ). *330*, 1774.
- McDannold, N., and Maier, S.E. (2008). Magnetic resonance acoustic radiation force imaging. *Med. Phys.* *35*, 3748–3758.
- McDannold, N., Vykhodtseva, N., and Hynynen, K. (2008). Effects of acoustic parameters and ultrasound contrast agent dose on focused-ultrasound induced blood-brain barrier disruption. *Ultrasound Med Biol* *34*, 930–937.
- McDannold, N., Zhang, Y., Power, C., and Vykhodtseva, N. (2018). Blood-brain barrier disruption and delivery of irinotecan in a rat model using a clinical transcranial MRI-guided focused ultrasound system. *ISMRM*.
- McDannold, N., Vykhodtseva, N., and Hynynen, K. (2006). Targeted disruption of the blood-brain barrier with focused ultrasound: association with cavitation activity. *Phys. Med. Biol.* *51*, 793–807.
- McDannold, N., Vykhodtseva, N., and Hynynen, K. (2008). Blood-brain barrier disruption induced by focused ultrasound and circulating preformed microbubbles appears to be characterized by the mechanical index. *Ultrasound Med Biol* *34*, 834–840.
- McDannold, N., Zhang, Y., and Vykhodtseva, N. (2012a). Blood-brain barrier disruption and vascular damage induced by ultrasound bursts combined with microbubbles can be influenced by choice of anesthesia protocol. *Ultrasound Med Biol* *29*, 997–1003.
- McDannold, N., Arvanitis, C.D., Vykhodtseva, N., and Livingstone, M.S. (2012b). Temporary disruption of the blood-brain barrier by use of ultrasound and microbubbles: Safety and efficacy evaluation in rhesus macaques. *Cancer Res.* *72*, 3652–3663.
- Mckhann, G., Drachman, D., and Folstein, M. (1984). Clinical diagnosis of Alzheimer's disease: Report of the NINCDS-ADRDA Work Group under the auspices of Department of Health and Human Services Task Force on Alzheimer's Disease. *Neurology* *34*, 939–944.
- McMahon, D., Bendayan, R., and Hynynen, K. (2017). Acute effects of focused ultrasound-induced increases in blood-brain barrier permeability on rat microvascular transcriptome. *Sci. Rep.* *7*, 45657.
- McRobbie, D.W., Moore, E.A., Graves, M.J., and Prince, M.R. (2006). *MRI from Picture to Proton* (Cambridge: Cambridge University Press).
- Mead, B.P., Kim, N., Miller, G.W., Hodges, D., Mastorakos, P., Klivanov, A.L., Mandell, J.W., Hirsh, J., Suk, J.S., Hanes, J., et al. (2017). Novel Focused Ultrasound Gene Therapy Approach Noninvasively Restores Dopaminergic Neuron Function in a Rat Parkinson's Disease Model. *Nano Lett.* *17*, 3533–3542.
- Meadowcort, M.D., Connor, J.R., Smith, M.B., and Yang, Q.X. (2009). Magnetic Resonance Imaging and Histological Analysis of Beta- Amyloid Plaques in Both Human Alzheimer's Disease and APP/ PS1 Transgenic Mice. *J Magn Reson Imaging* *29*, 997–1007.
- Meguro, R. (2007). Full-TextNonhem-iron histochemistry for light and electron microscopy: a historical, theoretical and technical review. *Arch Histol Cytol* *70*, 1–19.

- Mesulam, M.-M. (1999). Neuroplasticity Failure in Alzheimer's Disease. *Neuron* 24, 521–529.
- Mohandas, E., Rajmohan, V., and Raghunath, B. (2009). Neurobiology of *Alzheimer's disease*. *Indian J. Psychiatry* 51, 55.
- Muthupillai, R., Lomas, D., Rossman, P., Greenleaf, J., Manduca, A., and Ehman, R. (1995). Magnetic resonance elastography by direct visualization of propagating acoustic strain waves. *Science* (80-. ). 269, 1854–1857.
- Nelson, P.T., Greenberg, S.G., and Saper, C.B. (1994). Neurofibrillary tangles in the cerebral cortex of sheep. *Neurosci. Lett.* 170, 187–190.
- Nelson P. T. et al (2013). Correlation of Alzheimer Disease Neuropathologic Changes With Cognitive Status: A Review of the Literature. *J Neuropathol Exp Neurol.* 71, 362–381.
- Nguyen, P. V., Abel, T., Kandel, E.R., and Bourtchouladze, R. (2000). Strain-dependent differences in LTP and hippocampus-dependent memory in inbred mice. *Learn. Mem.* 7, 170–179.
- NIA (1997). Consensus Recommendations for the Postmortem Diagnosis of Alzheimer's Disease. *Neurobiol. Aging* 18, 1–2.
- Nicholson, C. (2001). Diffusion and related transport mechanisms in brain tissue. *Reports Prog. Phys.* 64.
- Nisbet, R.M., Van Der Jeugd, A., Leinenga, G., Evans, H.T., Janowicz, P.W., and Götz, J. (2017). Combined effects of scanning ultrasound and a tau-specific single chain antibody in a tau transgenic mouse model. *Brain* 140, 1220–1230.
- O'Leary, T.P., and Brown, R.E. (2009). Visuo-spatial learning and memory deficits on the Barnes maze in the 16-month-old APP<sup>swe</sup>/PS1<sup>dE9</sup> mouse model of Alzheimer's disease. *Behav. Brain Res.* 201, 120–127.
- O'Leary, T.P., and Brown, R.E. (2012). The effects of apparatus design and test procedure on learning and memory performance of C57BL/6J mice on the Barnes maze. *J. Neurosci. Methods* 203, 315–324.
- O'Reilly, M.A., and Hynynen, K. (2012). Feedback-controlled Focused Ultrasound Disruption by Using an Acoustic Emissions – based Controller 1. *Radiology* 263.
- O'Reilly, M.A., and Hynynen, K. (2016). Emerging Non-Cancer Applications of Therapeutic Ultrasound. *Int J Hyperth.* 31, 310–318.
- O'Reilly, M.A., Waspe, A.C., Ganguly, M., and Hynynen, K. (2011). Focused-Ultrasound Disruption of the Blood-Brain Barrier Using Closely-Timed Short Pulses: Influence of Sonication Parameters and Injection Rate. 25, 713–724.
- O'Reilly, M.A., Muller, A., and Hynynen, K. (2012). Ultrasound insertion loss of rat parietal bone appears to be proportional to animal mass at sub-megahertz frequencies. *Changes* 29, 997–1003.
- Oby, E., and Janigro, D. (2006). The Blood – Brain Barrier and Epilepsy. *Epilepsia* 47, 1761–1774.
- Oddo, S., Caccamo, A., Shepherd, J.D., Murphy, M.P., Golde, T.E., Kaye, R., Metherate, R., Mattson, M.P., Akbari, Y., and LaFerla, F.M. (2003). Triple-transgenic model of Alzheimer's Disease with plaques and tangles: Intracellular A $\beta$  and synaptic dysfunction. *Neuron* 39, 409–421.
- OECD (2017). Health at a Glance 2017.
- Olumolade, O.O., Wanga, S., Samiotakia, G., and Elisa E. Konofagou, B. (2017). Longitudinal Motor and Behavioral assessment of Blood-Brain Barrier Opening With Transcranial Focused Ultrasound. *Ultrasound Med* 42, 2270–2282.
- Pan, H., Zhou, Y., Sieling, F., Shi, J., Cui, J., and Deng, C. (2004). Sonoporation of cells for drug and gene delivery. *Conf. Proc. IEEE Eng. Med. Biol. Soc.* 5, 3531–3534.
- Pansieri, J., Gerstenmayer, M., Lux, F., Mériaux, S., Tillement, O., Forge, V., Larrat, B., and Marquette, C. (2018). Magnetic Nanoparticles Applications for Amyloidosis Study and Detection: A Review. *Nanomaterials* 8, 740.

- Pardridge, W.M. (2005). The blood-brain barrier: Bottleneck in brain drug development. *NeuroRx* 2, 3–14.
- Paresce, D.M., Ghosh, R.N., and Maxfield, F.R. (1996). Microglial cells internalize aggregates of the Alzheimer's disease amyloid  $\beta$ -protein via a scavenger receptor. *Neuron* 17, 553–565.
- Patwardhan, M.B., McCrory, D.C., Matchar, D.B., Samsa, G.P., and Rutschmann, O.T. (2004). Alzheimer disease: operating characteristics of PET--a meta-analysis. *Radiology* 231, 73–80.
- Paul, B., Thomas, F., Raymond, A., and Pfeifer Leah (1998). A review of normal tissue hydrogen NMR relaxation times and relaxation mechanisms from 1–100 MHz: Dependence on tissue type, NMR frequency, temperature, species, excision, and age. *Med. Phys.* 11, 425–448.
- Pauly, K.B., Diederich, C.J., Rieke, V., Bouley, D., Chen, J., Nau, W.H., Ross, A.B., Kinsey, A.M., and Sommer, G. (2006). Magnetic resonance-guided high-intensity ultrasound ablation of the prostate. *Top. Magn. Reson. Imaging* 17, 195–207.
- Pentkowski, N.S., Berkowitz, L.E., Thompson, S.M., Drake, E.N., Olguin, C.R., and Clark, B.J. (2017). Anxiety-like behavior as an early endophenotype in the TgF344-AD rat model of Alzheimer's disease. *Neurobiol. Aging* 61, 169–176.
- Perlmutter, L.S., Barron, E., and Chui, H.C. (1990). Morphologic association between microglia and senile plaque amyloid in Alzheimer's disease. *Neurosci. Lett.* 119, 32–36.
- Pihlaja, R., Koistinaho, J., Kauppinen, R., Sandholm, J., Tanila, H., and Koistinaho, M. (2011). Multiple cellular and molecular mechanisms Are involved in human A $\beta$  clearance by transplanted adult astrocytes. *Glia* 59, 1643–1657.
- Pitt, W.G., Hussein, G.A., and Staples, B.J. (2004). Ultrasonic drug delivery--a general review. *Expert Opin. Drug Deliv.* 1, 37–56.
- Plissonneau, M., Pansieri, J., Heinrich-Balard, L., Morfin, J.-F., Stransky-Heilkron, N., Rivory, P., Mowat, P., Dumoulin, M., Cohen, R., Allémann, É., et al. (2016). Gd-nanoparticles functionalization with specific peptides for  $\beta$ -amyloid plaques targeting. *J. Nanobiotechnology* 14, 60.
- Poduslo, J.F., Wengenack, T.M., Curran, G.L., Wisniewski, T., Sigurdsson, E.M., Macura, S.I., Borowski, B.J., and Jack, C.R. (2002). Molecular targeting of Alzheimer's amyloid plaques for contrast-enhanced magnetic resonance imaging. *Neurobiol. Dis.* 11, 315–329.
- Pottier, G., Marie, S., Goutal, S., Auvity, S., Peyronneau, M.-A., Stute, S., Boisgard, R., Dollé, F., Buvat, I., Caillé, F., et al. (2016). Imaging the Impact of the P-Glycoprotein (ABCB1) Function on the Brain Kinetics of Metoclopramide. *J. Nucl. Med. Off. Publ. Soc. Nucl. Med.* 57, 309–314.
- Rapoport, S.I. (1970). Effect of concentrated solutions on blood-brain barrier. *Am. J. Physiol.* 219, 270–274.
- Reiserer, R.S., Harrison, F.E., Syverud, D.C., and McDonald, M.P. (2007). Impaired spatial learning in the APPSwe + PSEN1DeltaE9 bigenic mouse model of Alzheimer's disease. *Genes. Brain. Behav.* 6, 54–65.
- Rogers, J.T., Leiter, L.M., McPhee, J., Cahill, C.M., Zhan, S.S., Potter, H., and Nilsson, L.N.G. (1999). Translation of the Alzheimer amyloid precursor protein mRNA is up-regulated by interleukin-1 through 5' untranslated region sequences. *J. Biol. Chem.* 274, 6421–6431.
- Samiotaki, G., and Konofagou, E.E. (2013). Dependence of the Reversibility of Focused-Ultrasound-Induced Blood-Brain Barrier Opening on Pressure and Pulse Length In Vivo. *IEEE Trans Ultrason Ferroelectr Freq Control* 60, 2257–2265.
- Sancey, L., Lux, F., Kotb, S., Roux, S., Dufort, S., Bianchi, A., Crémillieux, Y., Fries, P., Coll, J.-L., Rodriguez-Lafresse, C., et al. (2014). The use of theranostic gadolinium-based nanoprobe to improve radiotherapy efficacy. *Br. J. Radiol.* 87.
- Sanden, B. Van Der, Klein, J., Laurent, B., Dugourd, P., Perriat, P., Motto-ros, V., Tillement, O., Lyon-cnrs, U.C.B., Lyon, U. De, Inserm, G.I.N., et al. (2015). Long-Term in Vivo Clearance of Gadolinium-Based AGuIX Nanoparticles and Their Biocompatibility after Systemic Injection. 2477–2488.

- Sarvazyan, A.P., Rudenko, O. V., Swanson, S.D., Fowlkes, J.B., and Emelianov, S.Y. (1998). Shear Wave Elasticity Imaging : A new ultrasonic technology of medical diagnostic. *Ultrasound Med. Biol.* *24*, 1419–1435.
- Scarpini, E., Schelterns, P., and Feldman, H. (2003). Treatment of Alzheimer’s disease: current status and new perspectives. *Lancet Neurol* *2*, 539–547.
- Schneider, M. (1999). SonoVue, a new ultrasound contrast agent. *Eur. Radiol.* *9*, S347–S348.
- Selim, M., Fink, J., Linfante, I., Kumar, S., Schlaug, G., and LR, C. (2002). Diagnosis of cerebral venous thrombosis with echo-planar t2\*-weighted magnetic resonance imaging. *Arch. Neurol.* *59*, 1021–1026.
- Shaftel, S.S., Carlson, T.J., Olschowka, J.A., Kyrkanides, S., Matousek, S.B., and O’Banion, M.K. (2007). Chronic Interleukin-1 Expression in Mouse Brain Leads to Leukocyte Infiltration and Neutrophil-Independent Blood Brain Barrier Permeability without Overt Neurodegeneration. *J. Neurosci.* *27*, 9301–9309.
- Shang, X., Wang, P., Liu, Y., Zhang, Z., and Xue, Y. (2011). Mechanism of Low-Frequency Ultrasound in Opening Blood–Tumor Barrier by Tight Junction. *J. Mol. Neurosci.* *43*, 364–369.
- Sheikov, N., McDannold, N., Vykhodtseva, N., Jolesz, F., and Hynynen, K. (2004). Cellular mechanisms of the blood-brain barrier opening induced by ultrasound in presence of microbubbles. *Ultrasound Med. Biol.* *30*, 979–989.
- Sheikov, N., McDannold, N., Sharma, S., and Hynynen, K. (2008). Effect of focused ultrasound applied with an ultrasound contrast agent on the tight junctional integrity of the brain microvascular endothelium. *Ultrasound Med Biol* *34*, 1093–1104.
- Shin, J., Kong, C., Cho, J.S., Lee, J., Koh, C.S., Yoon, M.-S., Na, Y.C., Chang, W.S., and Chang, J.W. (2018). Focused ultrasound–mediated noninvasive blood-brain barrier modulation: preclinical examination of efficacy and safety in various sonication parameters. *Neurosurg. Focus* *44*, E15.
- Siemers, E.R., Sundell, K.L., Carlson, C., Case, M., Sethuraman, G., Liu-Seifert, H., Dowsett, S.A., Pontecorvo, M.J., Dean, R.A., and DeMattos, R. (2016). Phase 3 solanezumab trials: Secondary outcomes in mild Alzheimer’s disease patients. *Alzheimer’s Dement.* *12*, 110–120.
- Simpson, J.E., Ince, P.G., Lace, G., Forster, G., Shaw, P.J., Matthews, F., Savva, G., Brayne, C., and Wharton, S.B. (2010). Astrocyte phenotype in relation to Alzheimer-type pathology in the ageing brain. *Neurobiol. Aging* *31*, 578–590.
- Soderberg (1987). The precursor of Alzheimer’s disease amyloid A4 protein resembles a cell-surface receptor. *Nature* *325*, 733–736.
- Sofroniew, M. V., and Vinters, H. V. (2010). Astrocytes: Biology and pathology. *Acta Neuropathol.* *119*, 7–35.
- Solomon (1955). Relaxation Processes in a System of Two Spins. *Phys. Rev.* *953*.
- Spuch, C., and Navarro, C. (2011). Liposomes for Targeted Delivery of Active Agents against Neurodegenerative Diseases (Alzheimer’s Disease and Parkinson’s Disease). *J. Drug Deliv.* *2011*, 1–12.
- Stalder, M., Phinney, A., Probst, A., Sommer, B., Staufenbiel, M., and Jucker, M. (1999). Association of microglia with amyloid plaques in brains of APP23 transgenic mice. *Am. J. Pathol.* *154*, 1673–1684.
- Streit, W.J., Braak, H., Xue, Q.S., and Bechmann, I. (2009). Dystrophic (senescent) rather than activated microglial cells are associated with tau pathology and likely precede neurodegeneration in Alzheimer’s disease. *Acta Neuropathol.* *118*, 475–485.
- Struble, R.G., Price, D.L., Cork, L.C., and Price, D.L. (1985). Senile plaques in cortex of aged normal monkeys. *Brain Res.* *361*, 267–275.
- Su, D., Zhao, Y., Wang, B., Xu, H., Li, W., Chen, J., and Wang, X. (2011). Isoflurane-Induced Spatial Memory Impairment in Mice is Prevented by the Acetylcholinesterase Inhibitor Donepezil. *PLoS One* *6*.
- Suh, C.H., Jung, S.C., Kim, K.W., and Pyo, J. (2016). The detectability of brain metastases using contrast-enhanced spin-echo or gradient-echo images: a systematic review and meta-analysis. *J. Neurooncol.* *129*, 363–

371.

Sumbria, R.K., Grigoryan, M.M., Vasilevko, V., Krasieva, T.B., Scadeng, M., Dvornikova, A.K., Paganini-Hill, A., Kim, R., Cribbs, D.H., and Fisher, M.J. (2016). A murine model of inflammation-induced cerebral microbleeds. *J. Neuroinflammation* *13*, 1–12.

Sun, T., Zhang, Y., Power, C., Alexander, P.M., Sutton, J.T., Aryal, M., Vykhodtseva, N., Miller, E.L., and McDannold, N.J. (2017). Closed-loop control of targeted ultrasound drug delivery across the blood–brain/tumor barriers in a rat glioma model. *Proc. Natl. Acad. Sci.* *114*, E10281–E10290.

Swift, T.J., and Connick, R.E. (1962). NMR-Relaxation mechanisms of O17 in aqueous solutions of paramagnetic cations and the lifetime of water molecules in the first coordination sphere. *J. Chem. Phys.* *37*, 307–320.

T. Hyman, B., Marzloff, K., and V. Arriagada, P. (1993). The Lack of Accumulation of Senile Plaques or Amyloid Burden in Alzheimer’s Disease Suggests a Dynamic Balance Between Amyloid Deposition and Resolution. *J. Neuropathol. Exp. Neurol.* *52*, 594–600.

Takashima, A. (2009). Amyloid- $\beta$ , tau, and dementia. *J. Alzheimer’s Dis.* *17*, 729–736.

Talu, E., Powell, R.L., Longo, M.L., and Dayton, P. a (2009). Needle Size and Injection Rate Impact Microbubble Contrast Agent Population. *34*, 1182–1185.

Tarkowski, E., Andreasen, N., Tarkowski, A., and Blennow, K. (2003). Intrathecal inflammation precedes development of Alzheimer’s disease. *J. Neurol. Neurosurg. Psychiatry* *74*, 1200–1205.

van Tellingen, O., Yetkin-Arik, B., de Gooijer, M.C., Wesseling, P., Wurdinger, T., and de Vries, H.E. (2015). Overcoming the blood-brain tumor barrier for effective glioblastoma treatment. *Drug Resist. Updat. Rev. Comment. Antimicrob. Anticancer Chemother.* *19*, 1–12.

Torr, G.R. (1984). The acoustic radiation force. *Am. J. Phys.* *52*, 402–408.

Tosaka, M., Sato, N., Hirato, J., Fujimaki, H., Yamaguchi, R., Kohga, H., Hashimoto, K., Yamada, M., Mori, M., Saito, N., et al. (2007). Assessment of hemorrhage in pituitary macroadenoma by T2\*-weighted gradient-echo MR imaging. *Am. J. Neuroradiol.* *28*, 2023–2029.

Tournier, N., Goutal, S., Auvity, S., Traxl, A., Mairinger, S., Wanek, T., Helal, O.-B., Buvat, I., Soussan, M., Caillé, F., et al. (2017). Strategies to Inhibit ABCB1- and ABCG2-Mediated Efflux Transport of Erlotinib at the Blood-Brain Barrier: A PET Study on Nonhuman Primates. *J. Nucl. Med. Off. Publ. Soc. Nucl. Med.* *58*, 117–122.

Traxl, A., Wanek, T., Mairinger, S., Stanek, J., Filip, T., Sauberer, M., Müller, M., Kuntner, C., and Langer, O. (2015). Breast Cancer Resistance Protein and P-Glycoprotein Influence In Vivo Disposition of 11C-Erlotinib. *J. Nucl. Med. Off. Publ. Soc. Nucl. Med.* *56*, 1930–1936.

Upadhyay, R.K. (2014). Drug delivery systems, CNS protection, and the blood brain barrier. *Biomed Res. Int.* *2014*.

Urbanc, B., Cruz, L., Le, R., Sanders, J., Ashe, K.H., Duff, K., Stanley, H.E., Irizarry, M.C., and Hyman, B.T. (2002). Neurotoxic effects of thioflavin S-positive amyloid deposits in transgenic mice and Alzheimer’s disease. *Proc. Natl. Acad. Sci. U. S. A.* *99*, 13990–13995.

Verheijen, R.B., Yaqub, M.M., Sawicki, E., van Tellingen, O., Lammertsma, A.A., Nuijen, B., Schellens, J.H.M., Beijnen, J.H., Huitema, A.D.R., Hendrikse, N.H., et al. (2017). Molecular Imaging of ABCB1/ABCG2 Inhibition at the Human Blood Brain Barrier using Elacridar and 11C-Erlotinib PET. *J. Nucl. Med. Off. Publ. Soc. Nucl. Med.*

Vieira, D.B., and Gamarra, L.F. (2016). Getting into the brain: Liposome-based strategies for effective drug delivery across the blood–brain barrier. *Int. J. Nanomedicine* *11*, 5381–5414.

Voges, J., Reszka, R., Gossmann, A., Dittmar, C., Richter, R., Garlip, G., Kracht, L., Coenen, H.H., Sturm, V., Wienhard, K., et al. (2003). Imaging-guided convection-enhanced delivery and gene therapy of glioblastoma. *Ann Neurol* *54*, 479–487.

Volianskis, A., Køstner, R., Mølgaard, M., Hass, S., and Jensen, M.S. (2010). Episodic memory deficits are not related to altered glutamatergic synaptic transmission and plasticity in the CA1 hippocampus of the

- APPswe/PS1dE9-deleted transgenic mice model of B-amyloidosis. *Neurobiol. Aging* *31*, 1173–1187.
- Voorhees, J.R., Remy, M.T., Cintrón-Pérez, C.J., El Rassi, E., Kahn, M.Z., Dutca, L.M., Yin, T.C., McDaniel, L.M., Williams, N.S., Brat, D.J., et al. (2017). (-)-P7C3-S243 protects a rat model of Alzheimer's disease from neuropsychiatric deficits and neurodegeneration without altering amyloid deposition or reactive glia. *Biol. Psychiatry*.
- Wadghiri, Y.Z., Li, J., Wang, J., Hoang, D.M., Sun, Y., Xu, H., Tsui, W., Li, Y., Boutajangout, A., Wang, A., et al. (2013). Detection of Amyloid Plaques Targeted by Bifunctional USPIO in Alzheimer's Disease Transgenic Mice Using Magnetic Resonance Microimaging. *PLoS One* *8*, 1–10.
- Waldemar, G., Dubois, B., Emre, M., Georges, J., McKeith, I.G., Rossor, M., Scheltens, P., Tariska, P., and Winblad, B. (2007). Recommendations for the diagnosis and management of Alzheimer's disease and other disorders associated with dementia: EFNS guideline. *Eur. J. Neurol.* *14*, 1–26.
- Walker, M.T., and Fram, E.K. (2010). Fast , Versatile , and Cost-Effective FSE MR Imaging : Technical Considerations and Clinical Applications Authors. *Barrow Q.* *16*.
- Wanek, T., Römermann, K., Mairinger, S., Stanek, J., Sauberer, M., Filip, T., Traxl, A., Kuntner, C., Pahnke, J., Bauer, F., et al. (2015). Factors Governing P-Glycoprotein-Mediated Drug-Drug Interactions at the Blood-Brain Barrier Measured with Positron Emission Tomography. *Mol. Pharm.* *12*, 3214–3225.
- Wang, X., Jia, Y., Wang, P., Liu, Q., and Zheng, H. (2017). Current status and future perspectives of sonodynamic therapy in glioma treatment. *Ultrason. Sonochem.* *37*, 592–599.
- Watson, T. (2008). Ultrasound in contemporary physiotherapy practice. *Ultrasonics* *48*, 321–329.
- Watzlawik, J., Skora, L., Frense, D., Griesinger, C., Zweckstetter, M., Schulz-Schaeffer, W.J., and Kramer, M.L. (2006). Prion protein helix1 promotes aggregation but is not converted into  $\beta$ -sheet. *J. Biol. Chem.* *281*, 30242–30250.
- Waubant, E. (2006). Biomarkers indicative of blood-brain barrier disruption in multiple sclerosis. *Dis. Markers* *22*, 235–244.
- Weber, B., Winterdahl, M., Memon, A., Sorensen, B.S., Keiding, S., Sorensen, L., Nexø, E., and Meldgaard, P. (2011). Erlotinib accumulation in brain metastases from non-small cell lung cancer: visualization by positron emission tomography in a patient harboring a mutation in the epidermal growth factor receptor. *J. Thorac. Oncol. Off. Publ. Int. Assoc. Study Lung Cancer* *6*, 1287–1289.
- Webster, S.J., Bachstetter, A.D., Nelson, P.T., Schmitt, F. a., and Van Eldik, L.J. (2014). Using mice to model Alzheimer's dementia: An overview of the clinical disease and the preclinical behavioral changes in 10 mouse models. *Front. Genet.* *5*, 1–23.
- Weinmann, H.-J., Brasch, R.C., Press, W.-R., and Wesbey, G.E. (1983). Characteristics of Complex Systems. *J. Qual. Particip.*
- Weiss, N., Miller, F., Cazaubon, S., and Couraud, P. (2009). Biochimica et Biophysica Acta The blood-brain barrier in brain homeostasis and neurological diseases. *BBA - Biomembr.* *1788*, 842–857.
- Wengenack, T.M., Reyes, D. a., Curran, G.L., Borowski, B.J., Lin, J., Preboske, G.M., Holasek, S.S., Gilles, E.J., Chamberlain, R., Marjanska, M., et al. (2011). Regional differences in MRI detection of amyloid plaques in AD transgenic mouse brain. *Neuroimage* *54*, 113–122.
- Wilcock, D.M., DiCarlo, G., Henderson, D., Jackson, J., Clarke, K., Ugen, K.E., Gordon, M.N., and Morgan, D. (2003). Intracranially administered anti-A $\beta$  antibodies reduce beta-amyloid deposition by mechanisms both independent of and associated with microglial activation. *J. Neurosci.* *23*, 3745–3751.
- Wilcock, D.M., Rojiani, A., Rosenthal, A., Levkowitz, G., Subbarao, S., Alamed, J., Wilson, D., Wilson, N., Freeman, M.J., Gordon, M.N., et al. (2004). Passive Amyloid Immunotherapy Clears Amyloid and Transiently Activates Microglia in a Transgenic Mouse Model of Amyloid Deposition. *J. Neurosci.* *24*, 6144–6151.
- Wilkins, S.W., Gureyev, T.E., Gao, D., Pogany, A., and Stevenson, A.W. (1996). Phase-contrast imaging using polychromatic hard X-rays. *Nature* *384*, 335–338.

- Wilkinson, D. (2005). REVIEW: Is there a double standard when it comes to dementia care? *Int. J. Clin. Pract.* *59*, 3–7.
- Winkler, E.A., Bel, R.D., and Zlokovic, B. V (2014). Central nervous system pericytes in health and disease. *Nat Neurosci* *14*, 1398–1405.
- Wolf, A., Bauer, B., Abner, E.L., Ashkenazy-Frolinger, T., and Hartz, A.M.S. (2016). A comprehensive behavioral test battery to assess learning and memory in 129S6/ Tg2576 mice. *PLoS One* *11*, 1–23.
- Wu, X., Lu, Y., Dong, Y., Zhang, G., Zhang, Y., Xu, Z., Culley, D.J., Crosby, G., Marcantonio, E.R., Tanzi, R.E., et al. (2012). The inhalation anesthetic isoflurane increases levels of proinflammatory TNF- $\alpha$ , IL-6, and IL-1 $\beta$ . *Neurobiol. Aging* *33*, 1364–1378.
- Xian-Hui, D., Wei-Juan, G., Tie-Mei, S., Hong-Lin, X., Jiang-Tao, B., Jing-Yi, Z., and Xi-Qing, C. (2015). Age-related changes of brain iron load changes in the frontal cortex in APPswe/PS1 $\delta$ E9 transgenic mouse model of Alzheimer's disease. *J. Trace Elem. Med. Biol.* *30*, 118–123.
- Yan, X. Bin, Ouyang, W., Li, G., and Duan, K.M. (2012). Involvement of neuronal nitric oxide synthase in cognitive impairment in isoflurane-treated rats. *Neurosci. Lett.* *506*, 240–244.
- Yang, F.Y., Fu, W.M., Chen, W.S., Yeh, W.L., and Lin, W.L. (2008). Quantitative evaluation of the use of microbubbles with transcranial focused ultrasound on blood-brain-barrier disruption. *Ultrason. Sonochem.* *15*, 636–643.
- Yang, F.Y., Lin, Y.S., Kang, K.H., and Chao, T.K. (2011). Reversible blood-brain barrier disruption by repeated transcranial focused ultrasound allows enhanced extravasation. *J. Control. Release* *150*, 111–116.
- Yang, S., Lee, D.K., Shin, J., Lee, S., Baek, S., Kim, J., Jung, H., Hah, J., and Kim, Y. (2017). Nec-1 alleviates cognitive impairment with reduction of A $\beta$  and tau abnormalities in APP/PS1 mice. *EMBO Mol. Med.* *9*, 61–77.
- Yuan, Y., Yan, J., Ma, Z., and Li, X. (2016). Noninvasive focused ultrasound stimulation can modulate phase-amplitude coupling between neuronal oscillations in the rat hippocampus. *Front. Neurosci.* *10*, 1–7.
- Yushkevich, P.A., Piven, J., Hazlett, H.C., Smith, R.G., Ho, S., Gee, J.C., and Gerig, G. (2006). User-guided 3D active contour segmentation of anatomical structures: Significantly improved efficiency and reliability. *Neuroimage* *31*, 1116–1128.
- Zenaro, E., Piacentino, G., and Constantin, G. (2016). The blood-brain barrier in Alzheimer's disease. *Neurobiol. Dis.*
- Zhang, J., Yarowsky, P., Gordon, M.N., Carlo, G. Di, Munireddy, S., Zijl, P.C.M. Van, and Mori, S. (2004). Detection of Amyloid Plaques in Mouse Models of Alzheimer ' s Disease by Magnetic Resonance Imaging. *457*, 452–457.
- Zhang, J., Tan, H., Jiang, W., and Zuo, Z. (2015). The Choice of General Anesthetics May Not Affect Neuroinflammation and Impairment of Learning and Memory After Surgery in Elderly Rats. *J. Neuroimmune Pharmacol.* *10*, 179–189.
- Zhao, Z., Nelson, A.R., Betsholtz, C., Zlokovic, B. V, and Angeles, L. (2015). Establishment and Dysfunction of the Blood-Brain Barrier. *Cell* *163*, 1064–1078.
- Zhu, S., Wang, J., Zhang, Y., He, J., Kong, J., Wang, J.-F., and Li, X.-M. (2017). The role of neuroinflammation and amyloid in cognitive impairment in an APP/PS1 transgenic mouse model of Alzheimer's disease. *CNS Neurosci. Ther.* 1–11.



**Titre : Perméabilisation de la barrière hémato-encéphalique par ultrasons chez le rongeur : de la délivrance de nanoparticules à une thérapie pour la maladie d'Alzheimer**

**Mots clés :** Ultrasons, Barrière hémato-encéphalique, IRM, Maladie d'Alzheimer

**Résumé :** La barrière hémato-encéphalique (BHE) régule finement l'apport en oxygène et en nutriments du cerveau et le protège d'éventuels pathogènes, notamment en bloquant le passage des molécules de poids moléculaire supérieur à 400 Da. Malheureusement, cette barrière est un obstacle à la délivrance de nombreux médicaments. Les ultrasons focalisés de basse intensité, combinés avec des microbulles, représentent un outil de choix pour perméabiliser la BHE, de façon sûre et réversible, et ainsi permettre de délivrer efficacement des médicaments ou des agents de contraste dans le cerveau.

Dans la première partie de ma thèse, j'ai développé de nouvelles stratégies ultrasonores de perméabilisation de la BHE chez le rongeur. J'ai mesuré l'atténuation du faisceau ultrasonore par le crâne et étudié l'influence des paramètres acoustiques sur l'intensité et la durée de la perméabilisation. Ces développements m'ont ensuite permis de délivrer des nanoparticules dans le cerveau de rongeurs et d'observer cette délivrance par imagerie par résonance magnétique (IRM), tomographie par émission de positrons, imagerie de contraste de phase par rayons-X, spectrométrie de masse ou encore histologie.

La seconde partie de mon travail a porté sur l'application de cette technologie ultrasonore à la maladie d'Alzheimer (MA). J'ai tout d'abord optimisé un protocole IRM  $T_2^*$  à très haute résolution permettant l'imagerie *ex vivo* des plaques amyloïdes de souris modèles de la MA. J'ai développé un traitement semi-automatique des images pour détecter et quantifier la charge amyloïde dans le cortex. Enfin, j'ai évalué la perméabilisation répétée de la BHE en tant que thérapie pour la MA et démontré que des perméabilisations répétées de la BHE pouvaient avoir un effet bénéfique sur la mémoire de rongeurs modèles de la maladie.

**Title: Ultrasound induced blood-brain barrier opening on rodents: from nanoparticles delivery to a therapy for Alzheimer's disease**

**Keywords:** Ultrasound, Blood-brain barrier, MRI, Alzheimer's disease

**Abstract:** The blood-brain barrier (BBB) plays a crucial role in maintaining the hemostasis of the brain and protects it from pathogens. The BBB prevents molecules with a molecular weight higher than 400 Da to enter the brain. Crucial, the BBB becomes a limit to deliver drugs to the brain. Low intensity focused ultrasound and microbubbles are a unique tool to open the BBB, in a safe and reversible way, to deliver drugs that do not naturally cross the BBB to the brain.

The first part of the PhD was dedicated to developing new strategies for BBB opening. To do so, I measured the attenuation of the ultrasound beam by the skull and studied the dependency of the intensity and of the duration of the BBB opening on the acoustic parameters. Thanks to these developments, I was able to deliver many kinds of nanoparticles to rodent brains and I could observe their delivery with techniques such as magnetic resonance imaging (MRI), positron emission tomography, phase-contrast X-ray imaging, mass spectroscopy or histology.

The second part of my PhD was focused on applying this technology to Alzheimer's disease (AD). I optimized a  $T_2^*$  MRI protocol at very high resolution for *ex vivo* imaging of amyloid plaques in the cortex of mice modeling AD. I developed a semi-automatic image treatment to detect and quantify the amyloid load. Finally, I tested a repeated BBB opening as a therapy for AD and showed that repeated BBB openings could have a beneficial impact on the memory on rodents modeling AD.

